UNIVERSITÀ DEGLI STUDI DI MILANO

Dipartimento di Fisica

Corso di Dottorato in Fisica, Astrofisica e Fisica Applicata
Ciclo XXIX

Positronium laser excitation in the AE$\bar{g}$IS experiment

Settore Scientifico Disciplinare FIS/03

Supervisore: Dottor Fabrizio CASTELLI
Co-Supervisore: Dottor Marco Giulio GIAMMARCHI

Coordinatore: Professor Francesco RAGUSA

Tesi di Dottorato di:
Zeudi MAZZOTTA

Anno Accademico 2016

Final examination:

Date:
19th of January 2017

Department of Mathematics "Federigo Enriques", Università degli Studi di Milano, Via Saldini 50, 20133 Milano, Italy

Abstract

The AEgIS experimental program on antimatter systems involves the formation of antihydrogen atoms for gravitational and CPT studies. One of the key ingredients of the AEgIS strategy for the synthesis of antihydrogen atoms is the creation and manipulation of Positronium (Ps) atoms laser excited to Rydberg states ($n > 15$).

In AEgIS, Ps is produced in bunched mode and the Rydberg excitation is achieved with a two laser pulse technique, by passing through a $n = 3$ intermediate level. Because excitation on Ps $n = 3$ state has never been proposed before, in AEgIS a dedicated experimental apparatus and several detection strategies have been studied in order to observe the first measurement ever on this interesting process. In this work we present and discuss the experimental findings about the successful Ps $n = 3$ excitation.

Moreover, in this thesis, a study of the impact of involved nonlinear processes on the excitation efficiency of a Doppler broadened atomic cloud is carried out. Presented simulation results show that, by exploiting properly nonlinear processes in the generation of the desired wavelength, it is possible to improve the excitation efficiency of a laser pulse. It is crucial, in AEgIS, the use of a periodically poled crystal in quasi phase matching regime. This gives a broadband continuous output spectrum whose wings survive to the spectral cutting of the last nonlinear crystal of the chain (which has insufficient spectral acceptance). This means that, at high laser energies, these wings can be amplified and the spectrum gaps can be filled in, leading to high reachable saturation efficiencies. On the contrary, in a laser pulse with a comb-shaped spectrum with a Gaussian envelope, both wings and gaps drop rapidly to zero, and amplification hardly occurs at usually employed energy regimes.

The presented model is finally used to fit AEgIS Ps $n = 3$ excitation experimental data.

To my parents, always believing in my choices, even without understanding them. "We believe in you", this is the fuel you gave me to go on.

Ai miei genitori, che hanno sempre creduto nelle mie scelte seppur non comprendendole appieno. "Crediamo in te", è stato questo il carburante di cui ho sempre avuto bisogno per andare avanti, e voi me lo avete sempre donato.

Contents

List of Figures

List of Tables

Introduction

Our Universe, vast and cold. What is it made of? How did it start? What is its destiny? For thousands of years mankind has been wondering about these questions.
Everything started at the moment of the big bang, 13.8 billion years ago.
Time and space begin when a tiny point full of energy starts expanding at incredible rate. And only a marginal amount of energy transforms into matter and antimatter. But shortly after, all antimatter is disappeared and only a tiny fraction of matter is left. Still enough for all stars and planets in our universe.
In the first three minutes, protons and neutrons form the lightest nuclei, while the universe continues to expand and cool down. But it takes almost 400 thousand years until hydrogen and helium matters can form. Now the universe has become transparent. Light from this era can be still seen today as the cosmic background radiation.
Gravity begins to pull hydrogen and helium together: stars are born. Fusion inside the stars forms every nuclei, the base of life. And these building blocks are thrown into space when stars die in giant explosions.
After 9 billion years gravity put some of this remanence together to form our solar system, with our planet Earth, where evolution gives rise to life, intelligence and consciousness.[1]

Since its first steps in this universe, humankind is wondering about its origins. Today we are developing the tools to give answers. At CERN, scientists from all around the world are working in experiments that might soon allow us to answer some of these big questions. The recent discoveries of the Higgs particle [1, 2] (responsible for giving mass to all particles) and of gravitational waves [3], answer only two of countless questions...
Will we find the reason why antimatter and matter did not destroy each other completely?
Will we understand the primordial state of matter before protons and neutrons formed?
Will we find the particles that make up the mysterious dark matter?
Particle and quantum physics experiments will bring us closer to answering such questions.

Will we find the reason why antimatter and matter did not destroy each other completely in the Early Universe?

Antimatter is a hot topic in contemporary physics, as it plays a crucial role in our understanding of fundamental interactions. Precision spectroscopy measurements on an-

[1] Inspired by CERN globe "Universe of particles" exhibition

timatter are useful for testing the validity of the CPT theorem[2]. A possible violation of the theorem is contemplated in some extensions of the Standard Model [4]. Another issue concerns the gravitational interaction on antimatter. The Weak Equivalence Principle (WEP), or "universality of free-fall trajectories", states that *all test particles at the same spacetime point, in a given gravitational field, will undergo the same acceleration, independent of their properties, including their rest mass*. Several careful tests have verified the WEP at 10^{-13} level for ordinary matter [5]. Indirect arguments have been raised against a different acceleration of antimatter with respect to matter; however, some attempts either to formulate quantum theories of gravity [6], or to unify gravity with all other forces [7, 8] introduce the possibility of a non-identical gravitational interaction between matter and antimatter, which could even repel each other instead of being self-attractive [9, 10]. This possible gravitational repulsion might be consistent with the standard formulation of general relativity and would not imply any modification of the theory [11].
The theoretical prediction of antigravity between matter and antimatter supports cosmological models attempting to explain the observed accelerated expansion of the Universe through such a repulsion between equal amounts of the two components [12, 13, 14]. This gravitational repulsion would prevent the mutual annihilation of isolated and alternated systems of matter and antimatter. These new cosmological scenarios could also eliminate the uncomfortable presence of an unidentified dark energy, and maybe also of cosmological dark matter, which, according to the Λ-CDM concordance model [16], would together represent more than the 95% of the Universe content [11, 15].
Nevertheless, there are disagreements with the idea of an universe with equal separated amounts of matter and antimatter [12]. It is necessary, then, to find a way to solve this puzzling doubt.

Study of gravitational interaction between matter and antimatter
Gravitational measurements with charged antimatter are very complicated, due to the overwhelming effect of residual electromagnetic forces [17]. Therefore, neutral antimatter, i.e. antiatoms, are of great interest and necessary to investigate the gravitational interaction. In particular, a measurement of the earth's gravitational acceleration $\bar{g}$ on the simplest stable anti-atom, the anti-hydrogen $\overline{H}$, even with a few percent precision, might be scientifically relevant as it will represent the first direct measurement of the gravitational interaction between matter and antimatter.

This is the aim of the AE$\bar{g}$IS experiment: our hope is to help find an answer to the question at the beginning of this paragraph. Do we actually have just matter in the whole universe? Or there are separated regions of matter and antimatter? By studying how they interact gravitationally with each other, we might understand whether they are ruled by usual gravitational laws or not. Whatsoever result will be crucial: will we discover new physics? Will we have a hint on what is the right path to follow among all current theories?

The AEgIS experimental program on antimatter systems involves the formation of antihydrogen atoms for gravitational and CPT studies. One of the key ingredients of the AE$\bar{g}$IS strategy for the synthesis of antihydrogen atoms is the creation and manipulation of Positronium (Ps) atoms laser excited to Rydberg states ($n > 15$). Ps is very interesting in its own right. Ps is indeed a truly "elementary atom", a purely leptonic system holding important possibilities for modern research topics such as Ps Bose-Einstein condensates [18, 19, 20] or higher-order bound state QED corrections [21]. In AE$\bar{g}$IS, Ps is produced in bunched mode and the Rydberg excitation is achieved with a two laser pulse technique,

[2]CPT theorem says that CPT symmetry (Charge, Parity and Time reversal Symmetry) holds for all physical phenomena.

by passing through a $n = 3$ intermediate level. Because excitation on Ps $n = 3$ state has never been proposed before, in AEgIS several detection strategies have been studied in order to observe the first measurement ever on this interesting process.

Thesis overview

Almost the full body of the present thesis is dedicated to the AEgIS experiment, with special emphasis on my contribution on positronium excitation process.
Being fundamental ingredients of Ps excitation, Positrons, positronium and lasers will be investigated in dedicated chapters. In the opening chapter about the AEgIS experiment, antiprotons and antihydrogen will have dedicated a suitable space, due to the fact that I helped trap experts work with antiprotons and positron manipulation during several antiproton runs at the Antiproton Decelerator at CERN.
After this general chapter, I will describe the ingredients for positronium excitation: we have positrons, packed in small bunches (both in time and space), and we have a correlated (within nanoseconds) pulsed laser. Positrons are the tool to generate positronium, laser is our tool to excite it.
Two chapters will be dedicated to the laser topic. The first one is a theoretical chapter, the second one is a description of the AEgIS laser system, including a spectral analysis of the radiation generated through nonlinear crystals.
Afterwards, I will report results of my simulations on positronium $n = 3$ excitation and detection, and make a comparison between the efficiencies of two spectrally different exciting pulses. Finally, results of Ps $n = 3$ and Rydberg excitation measurements (in which I was directly involved) are shown.
During my training in the Milano laboratories, I was involved in a new quantum mechanics experiment. I took care of both theoretical and experimental aspects of the measurement, making this period of great impact to my research path. But, being it unlinked from the AEgIS work, I describe this parallel activity with the Milano Quantum Optics Group in the appendix.
Here a schematic view of the thesis structure:

Chapter 1: The AEgIS experiment: I describe the experimental apparatus and the task of each component. I explain the whole story of our elementary ingredients, positrons and antiprotons, starting from their origin towards anti-hydrogen production and free fall in the earth gravitational field.

Chapter 2: Positron system: I describe how we generate small bunches of positrons, to be used for positronium production. Production, trapping, accumulation and bunching of positrons are explained.

Chapter 3: Positronium: I explain the positronium synthesis process in silica targets, positronium emission in vacuum and the issue of its velocity distribution. The way we detect positronium atom generation is shown, together with experimental results.

Chapter 4: Lasers, nonlinear optics and frequency generation: A theoretical treatment of lasers and nonlinear optics, necessary to understand how we generate the right wavelengths for positronium excitation and their spectral properties, is presented.

Chapter 5: The AEgIS laser system: a spectral analysis: I describe the AEgIS strategy for the generation of the required wavelengths for positronium excitation together with the AEgIS laser apparatus. A spectral analysis of the generated radiations will be reported.

Chapter 6: A geometrical simulation of Ps excitation: I describe my geometrical Montecarlo simulation on the excitation process. I explain how it can be used to extrapolate information about the optimal Ps configuration for the excitation measurement.

Chapter 7: Ps $n = 3$ excitation spectral simulation: In this chapter I describe my `Labview` simulation of the $n = 3$ excitation process from the spectral point of view. I put special emphasis on the effects of the spectral properties of the exciting radiation on the excitation efficiency.

Chapter 8: Positronium excitation measurements: I report our latest experimental results on positronium excitation. I perform a new data analysis with my spectral simulation, in the light of new elements and information at our disposal.

Appendix A: A two-photon interference experiment: I describe what is quantum interference between two entangled photons, and how it is affected by changes in the phase function of one of the two photons with respect to the other one.

Appendix B: Thesis tools: I deepen concepts that can help understand better some topics in the thesis body.

CHAPTER 1

The AEgIS experiment

In this chapter, I report an overview of the AEgIS experiment and a brief description of the tasks of each part.

1.1 The AEgIS experiment scheme

The AEgIS collaboration (Antimatter Experiment: Gravity, Interferometry, Spectroscopy) began in 2007 in order to study fundamental physics with antimatter systems. The primary aim is to measure the gravitational acceleration $\bar{g}$ on antihydrogen ($\overline{H}$). The first experimental goal is to produce $\overline{H}$ with energies below 1 K and to measure $\overline{H}$ free fall in the earth's gravitational field, with a precision of 1%.
The idea is to form a beam of cold $\overline{H}$ atoms, launch them horizontally and measure the vertical deflection in their flight through a classical deflectometer. There are few essential steps to take in the whole process (see Fig.1.1):

- capture and accumulate antiprotons ($\bar{p}$) coming from the A.D. (Antiproton Decelerator) at CERN;
- cool $\bar{p}$ down to sub-K temperatures;
- produce, trap and accumulate positrons;
- produce and cool positronium down;
- laser excite positronium to Rydberg levels, in order to increase $\overline{H}$ generation cross section ;
- produce $\overline{H}$ via a charge exchange reaction between antiprotons and positronium atoms according to the scheme: $Ps^* + \bar{p} \longrightarrow \bar{H}^* + e^-$; [1]
- extract and guide $\overline{H}$ atoms via inhomogeneous electric fields (Stark acceleration);
- measure $\overline{H}$ beam deflection due to gravitational acceleration in a classical device called *moiré deflectometer*;

The body of the AEgIS apparatus consists of four main parts: an antiproton trapping system, a positron system, a laser system and a gravity measurement system. For antiproton trapping we use an ultra high vacuum cryogenic system, containing two magnets (4.46 T and 1 T), wherein a complex series of traps is installed. Here antiprotons

[1] The star indicates an atom in a Rydberg state

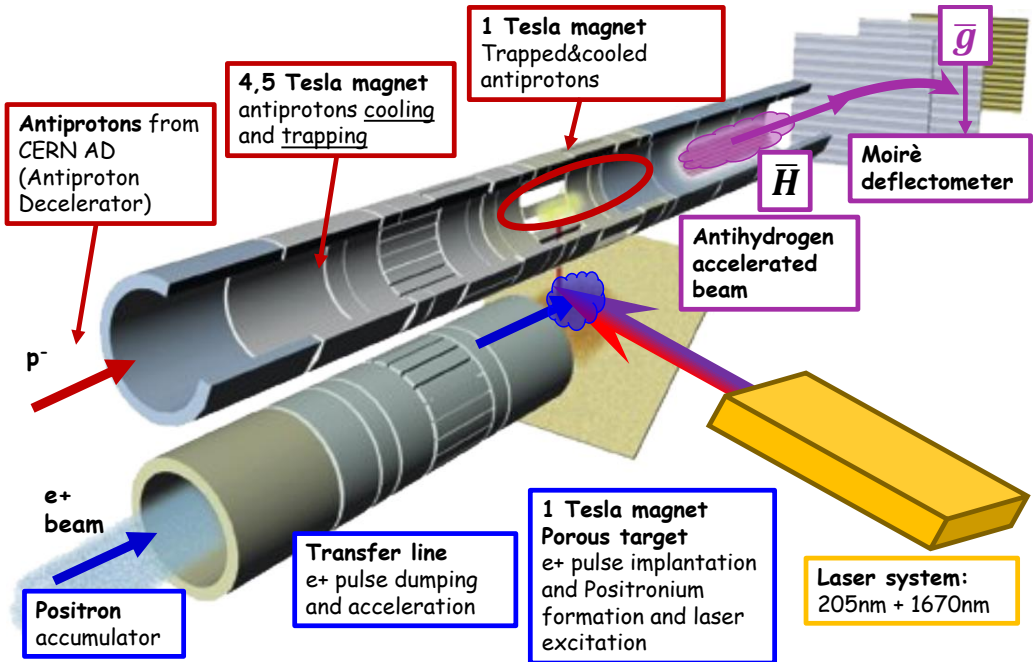

Figure 1.1: AEgIS simplified apparatus sketch: particles go from the left rightwards. Two parallel lines merge into one inside the 1 Tesla trap, where Antihydrogen will be produced and then sent into the moiré deflectometer. Image ©INFN/Internosei

from A.D. are trapped, cooled down and stored. The storage step is necessary to synchronize $\bar{p}$ with Ps production. The positron system deals with positron production, bunching and transfer into the 1 T magnet. Here Ps is generated by implanting positrons in a mesoporous silica converter. Then Ps is emitted in vacuum. A pulsed laser system is used to bring Ps to Rydberg levels immediately after its emission in vacuum, before it reaches the antiproton cloud in the antiproton storage trap. The final system is a gravity module (the moiré deflectometer), located at the exit of the 1 T magnet, to receive the $\overline{H}$ beam and measure the beam vertical deflection.

1.2 A more detailed view of the AEgIS apparatus

In Fig.1.2 there is a more detailed schematic view of the apparatus.

1.2.1 Antiproton system

Antiprotons are sent from A.D. in bunches of about 3×10^7 particles and 200 ns duration every 110 s, with an axial energy of 5.3 MeV. An energy degrading system is used to lower the energy of antiprotons, via dE/dx losses in subsequent aluminum foils. Since the 2015 run, the beam position at the entrance of the apparatus is monitored by a beam monitor detector - MIMITO [2] - a reduced-thickness version of the MIMOTERA detector [22]. This detector allows online non-destructive beam monitoring and imaging of the

[2] based on the MIMO detection method: multiple-input, multiple-output. MIMITO is a monolithic pixel detector for real-time beam imaging and profilometry.

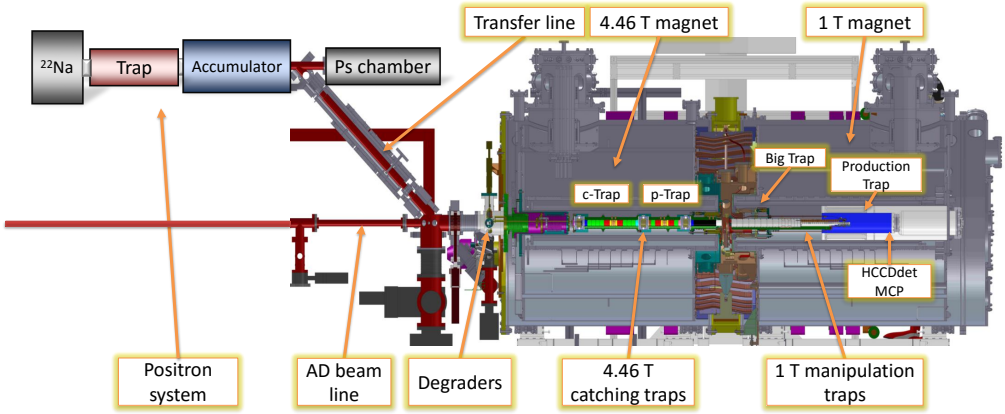

Figure 1.2: AEgIS apparatus detailed scheme

antiproton beam. This is helpful to achieve precise beam steering and focusing. An example frame captured by MIMITO is given in Fig.1.3.

The AEgIS main cryostat has two magnets: a 4.46 T magnet, used to catch antiprotons coming from AD and cool them down, and the 1 T magnet, used to compress and store antiprotons after the catching step, to guide positrons for Ps production and to subsequently host $\overline{\mathrm{H}}$ production.
The AEgIS catching hardware is composed of a 75 cm long set of Penning-Malmberg traps, terminated by pulsable high-voltage electrodes. Antiprotons entering the trap are stopped with the final high-voltage electrode, previously set to a constant negative bias. Once all the $\bar{\mathrm{p}}$ bunch is inside the trap, a pulsable high-voltage electrode on their back acts as an entrance endcap, preventing bounced antiproton to exit the trap (4.46 T c-trap in Fig.1.2). Cooling of antiprotons in the trap is performed by using the sympathetic technique involving electromagnetically cooled electrons. An electron plasma, emitted from a heated thermoelectric filament, is loaded several seconds before antiproton capture in a smaller low voltage trap, placed in the center of the capture region. After cooling, antiprotons have to be moved in the 1 T big trap, by manipulating the potential of the end-cups of both traps.
A more complex trap system, formed by four Penning-Malmberg traps, is located in the 1 T magnet. The first trap compresses the particles coming from the 4.46 T magnet by means of a rotating wall electrodes system [23]. Then, two traps follow: an off axis trap used to send positrons towards the Ps converter, and an on-axis trap used to transfer $\bar{\mathrm{p}}$ into the $\overline{\mathrm{H}}$ production trap, where $\bar{\mathrm{p}}$ cooling to the final temperatures takes place. Here, cooled $\bar{\mathrm{p}}$ wait for Ps to make $\overline{\mathrm{H}}$ via charge exchange reaction.

Latest performances of antiproton manipulation [24]

In 2014 and early 2015 runs with A.D., trapping and cooling conditions of the first commissioning AEGIS run in 2012 were reproduced with ease: a maximum of 1.24×10^5 antiprotons per shot at 9 kV catching voltage was achieved (see [101]).
Catching conditions were then improved by optimizing more accurately the aluminum

degrader foil thickness for antiproton moderation. Two sets of calibrated aluminum foils (thickness spanning from 0 μm, that means no foil, to 50 μm, with a few μm step) were used to study the optimal degrader thickness around a given yield, the maximum one identified in the 2012 run. This optimization, together with the 9 kV trapping potential (now routinely used) increased substantially the number of captured antiprotons per A.D. shot. With nominal A.D. luminosity (3.0×10^7antiproton/shot delivered), an average of 3.6×10^5 antiprotons per shot were captured, and then observed on outer external scintillators (see Fig. 1.3, left panel).

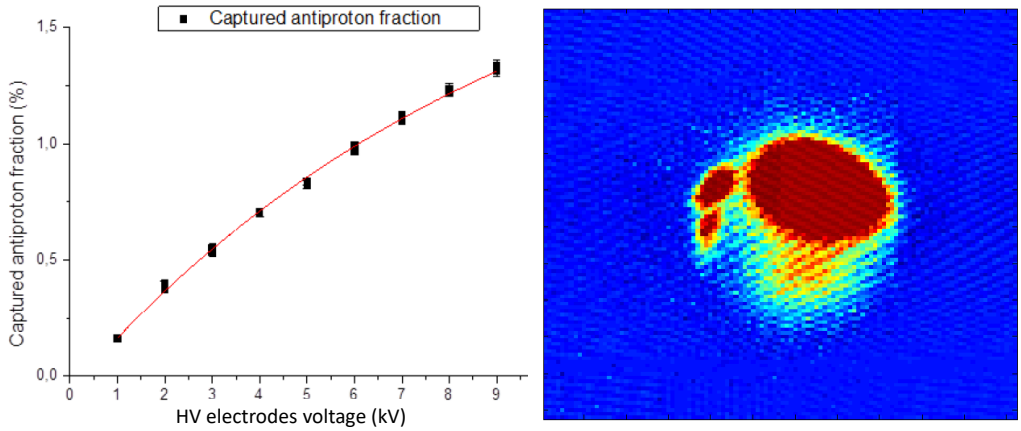

Figure 1.3: Left: fraction of the incoming A.D. beam intensity captured per shot, as a function of the catching voltage. Annihilation signals are observed on external plastic scintillators acquired by two photomultipliers in coincidence. Right panel: An example section of the antiproton beam captured by the MiMITO beam monitor detector. This example image was chosen - besides the poor beam quality in this particular A.D. shot - to emphasize the beam imaging capabilities of the MIMOTERA detector [22].

Electron cooling of antiprotons was then reproduced and optimized. The plasma of electrons, emitted from a heated thermoelectric filament, was loaded several seconds before capture in a smaller low voltage trap in the center of the capture region. Depending on the current in the filament and the potential used for capture, dense plasmas of 10^7 to 10^9 electrons were obtained. Lower densities were achieved by selectively removing a part of the electrons from the trap with a partial opening of one of the Malmberg-trap endcaps. Cooling efficiencies up to 90% in about 60 s were obtained by optimizing the electron loading procedure. The best configuration is the electron cloud almost completely overlapping the antiprotons' one.

A critical parameter for the lifetime of cold antiprotons in trap was the pressure of the residual gas. The vacuum level in AEGIS is barely measurable with commercial ion gauges only in the warm section of the vacuum chamber when the experiment is at its nominal 4K temperature. The inner ultra-high vacuum pressure level goes under 10^{-13} mbar, so the only available diagnostic for the vacuum quality is the antiproton lifetime in the trap itself. In fact, the number of antiproton annihilations per second depends on the collision probability with the atoms of the residual gas in the traps. During 2014 run, AEGIS reached a lifetime of about 740 sec in the catching traps at the beginning of the run (see Fig. 1.4, right panel). During lifetime measurements, the radius of the antiproton plasma was kept monitored by imaging the plasma with a microchannel plate

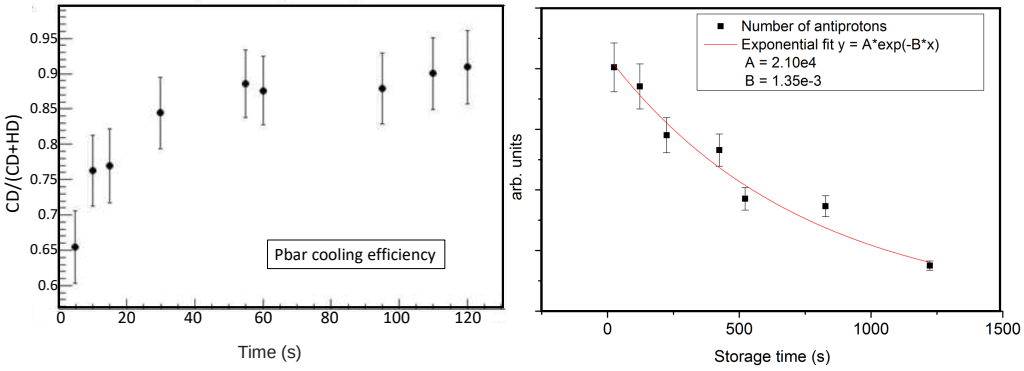

Figure 1.4: Left panel: fraction of cold antiprotons observed in the final opening of the cooling trap as a function of the time spent together with electrons, before lowering the high-voltage catching electrodes to low-voltage. This operation, denoted hot ejection (HD, hot dump, in the plot), makes the remaining hot fraction of antiprotons leave the trap before being cooled by electrons. Then, only the cold antiprotons could survive in the trap, until the final opening of the low-voltage electrodes, named cold ejection (CD, cold dump, in the plot). The total amount of caught antiprotons is estimated by summing the fraction observed in the hot and cold ejections (CD + HD). All annihilation signals are detected by the external scintillators. Right panel: number of cold antiprotons surviving in the trap as a function of the storage time, in arbitraty units.

detector, to exclude radial annihilations on the walls due to the radial enlargement of the cloud. Antiprotons were observed by selectively removing electrons from the trap before the antiproton ejection, by using a sequence of fast voltage pulses opening the trap for a time sufficiently short to be negligible with respect to the characteristic times of the antiproton cloud evolution.

1.2.2 Positron system

Positrons are produced outside the main cryostat, via the following radioactive decay of a ^{22}Na source (9 mCi)

$$^{22}Na \longrightarrow ^{22}Ne + e^{+} + \nu_e + \gamma \tag{1.1}$$

They are immediately slowed down by a solid Ne moderator and then captured in a Surko-type trap [26]. Subsequently, a magnetic buffer-gas accumulator stores the positrons with a well established experimental technique (see [27]). A magnetic transfer line tilted by 45° carries positrons down from the accumulator to the antiproton beam line, so to share the same catching hardware of antiprotons (Fig. 1.2). Then, positrons are magnetically guided to the 1 T region: a positron plasma is first prepared in a 2.2 cm radius trap (1 T Big trap in Fig. 1.2), then moved out of the main axis of the experiment by exciting its autoresonant diocotron mode via radiofrequencies (a first result was obtained with electrons [28]). Here they are accelerated towards a dedicated target for Ps production.

Latest performances of positron manipulation [24]

Significant progresses in storing positrons in the accumulator and transferring in the main experiment were carried out during 2015. A large number of positrons was col-

lected in the accumulator by carefully optimizing trap potentials and rotating wall [3] parameters. Positrons were kept accumulating for around 6 min before being transferred to the main catching traps in the 4.46 T region by a magnetic transfer line. Lossless positron transfer was achieved after optimization of the transfer line parameters: around 2.5×10^7 positrons were routinely transferred and trapped per shot. Positrons were transferred with an axial velocity corresponding to 300 eV: when the number of transferred positrons exceeded an experimentally determined threshold ($\sim 1.3 \times 10^7$ positrons per shot) this energy was dissipated in a fraction of a second. Below this limit, probably because the cooling rate was too low with respect to the plasma expansion rate at such low density, lossless cooling conditions were only seldom found. With higher number of positrons, almost 100% cooling efficiency was routinely obtained, and no significant losses due to the vacuum quality were observed.
In order to reach the goal value of 10^8 positrons for anti-hydrogen production, several shots from the accumulator had been collected and stacked into the catching traps. With the current ^{22}Na source, around 9 mCi of activity at the time of the experiment, 10^8 positrons were obtained by stacking 8 shots, corresponding to around 45 min of accumulation time.
A new, more intense source of 50 mCi will replace the present one soon, nominally allowing 10^8 positrons to be reached in about 8 min.

1.2.3 Positronium formation and thermalization

Being a bound state of a positron and an electron, positronium is a purely leptonic atom. It exists in two different states: the singlet state, called para-Ps and the triplet state called orto-Ps. Para-Ps has a really short mean life (0.125 ns) and annihilates mostly[4] into two gamma rays; ortho-Ps has a longer mean life (142 ns) and it mostly[5] annihilates into three gamma rays.
A positronium converter is a target made of a special material able to efficiently transform incoming positrons into positronium. In AEgIS a positronium converter made of mesoporous silica is placed about 1.7 cm above the anti-hydrogen production trap facing downwards, looking at the antiproton storage trap (see Fig. 1.5, right panel). A bunched positron beam is implanted at keV energies inside the porous silicon target. In this way, some positrons capture an electron from the material and form Positronium at around $1-3$ eV kinetic energy [30]. Atoms exit the target through the pores and, while bouncing on the walls, loose their kinetic energy. As a result, we have outside the target a Ps cloud with a thermalized percentage. This percentage depends on how deep was the implantation of positrons, and therefore on their implantation energy. In AEgIS, the use of a cloud of thermalized Ps atoms is preferable because thermalized atoms are more likely to be efficiently excited by a suitable synchronized laser pulse, and in turn this helps increase the $\overline{\mathrm{H}}$ production cross section. The positronium emission in vacuum efficiency is about 9% (see [31]), that is also dependent on the implantation energy.

1.2.4 AEgIS Laser and Positronium excitation

Ps atoms play a fundamental role in the AEgIS experiment. The main reason is that it is the actual responsible of the large cross section of the charge exchange reaction: the

[3] A "Rotating Wall" (RW) is a rotating electric field that counteracts the radial expansion of a non-neutral plasma [29]

[4] It can decay into four, six etc gamma rays.

[5] It can decay into five, seven etc gamma rays.

cross section depends on the fourth power of Ps principal quantum number[6] ($\sigma \propto n^4 \pi a_0^2$) [32, 33]. For this reason, we can drastically increase it by exciting Ps to Rydberg levels. Reaching too high Rydberg levels is dangerous because the presence of high fields inside the production trap can induce ionization processes. This is the reason why we planned not to exceed the principal quantum number $n = 24$. Positronium excitation to these high-n levels can be obtained either via collisions [34] or via photoexcitation. In [32, 33] Ps excitation was proposed and tested through Cs excitation by light and a successive charge exchange reaction with positrons. In the AEgIS experiment the photoexcitation strategy has been chosen, i.e. a direct Ps excitation via a two-step process in which two photons, coming from two simultaneous laser pulses with different wavelengths [35], are absorbed. The goal is to reach a very efficient excitation process, more controllable and with a simpler and more compact experimental setup than the one achieved via collisions with atoms (see, for example, the experimental setup for collisions with Rydberg Cs atoms in [33]). The laser system will be described in Chapter 5.
In the AEgIS 1 T trap the Ps excitation will be then achieved with the following strategy: a first excitation to the $n = 3$ level and a second one from $n = 3$ level to the selected Rydberg level. The wavelengths of the two lasers for the in-cascade transition are, respectively, $\lambda = 205$ nm for excitation from the ground to the $n = 3$ state, and λ between $1650 - 1700$ nm (see Fig. 1.5, left panel) for excitation from $n = 3$ to a selected Rydberg level. The choice of this particular excitation pattern was suggested by theoretical studies. It has been simulated that, in AEgIS working conditions [35, 36], a higher excitation efficiency is achieved with respect to the alternative pattern involving $n = 2$ as intermediate level. In fact, this choice seems more adequate than the other possible two step sequence $1 \rightarrow 2$ and $2 \rightarrow$ high-n because the level $n = 2$ has a three time shorter lifetime than the $n = 3$ level (3 ns against 10.5 ns) and, in addition, population losses become dynamically relevant.

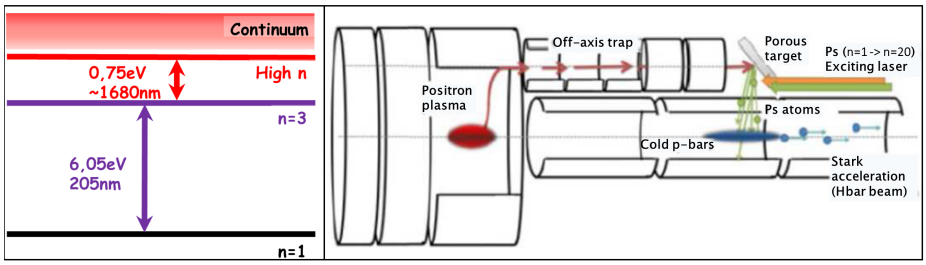

Figure 1.5: Left panel: Positronium Rydberg excitation strategy in AEgIS. Right panel: schematic drawing of AEgIS experimental layout to produce $\overline{\mathrm{H}}$ via charge exchange with Rydberg-excited Ps

Two prisms transfer these laser pulses in front of the converter, to excite the emitted fraction of Ps to Rydberg levels, thus allowing the excited atoms to fly towards the antiproton storage trap and perform charge exchange with the cold antiproton plasma.

[6] We know that $E \propto -\frac{1}{r}$ and $E \propto -\frac{1}{n^2}$. Therefore $r \propto n^2$. As $\sigma \propto r^2$, we have $\sigma \propto n^4$

1.2.5 Antihydrogen formation and gravity measurements

A bit of history [37]

The first productions of $\overline{\mathrm{H}}$ occurred in 1995 at CERN [38] and two years later at Fermilab [39]. Confinement of antihydrogen was however impossible, the energies being of the order of a few GeV[7]. In 2002, ATHENA [40] and ATRAP [41] experiments obtained for the first time $\overline{\mathrm{H}}$ with low kinetic energy (actually, around 1 meV, corresponding to a temperature of about 10 K). Nowadays, four experiments (ALPHA [42], ASACUSA [43], ATRAP and AEGIS [44]) are running at CERN, with the aim to produce antihydrogen for other goals (e.g. cold $\overline{\mathrm{H}}$ for spectroscopy studies), by using the A.D. facility.
At the basic level, the formation of an antihydrogen atom is the conversion of an initially unbound antiproton and positron pair into a single bound state. However, some mechanism must exist to carry away the excess energy and momentum, be it a third particle or a photon. The most efficient method of producing antihydrogen atoms (in terms of number of atoms produced) demonstrated so far is the interaction of antiprotons with a plasma of positrons. Combination of clouds or plasmas of antiprotons and positrons has become commonly known as "mixing". ALPHA, ASACUSA and ATRAP collaborations produce antihydrogen by means of the following mixing reactions:

$$e^+ + \bar{p} \longrightarrow \bar{H} + \gamma \tag{1.2a}$$

$$e^+ + e^+ + \bar{p} \longrightarrow \bar{H} + e^+ \tag{1.2b}$$

Equation (1.2a) represents the so-called "*Radiative recombination*" (RR): a positron incident on an antiproton can be captured into a bound state with the emission of a photon, the time-reversed analogue of the photoionisation process. Equation (1.2b) represents the so-called "*Three body recombination*" (TBR): two positrons scatter in the field of an antiproton, with one becoming bound, and the other carrying away the excess energy.
Positrons and $\bar{\mathrm{p}}$ are first confined into electromagnetic nested Penning traps [45], then they are mixed, so that reactions (1.2a) and (1.2b) take place. These two reactions are in competition: depending on density and temperature of the positron cloud, a reaction prevails on the other one.
Concerning the density dependence, the RR (1.2a) has a linear dependence on the positron cloud spatial density, while the TBR (1.2b) has a quadratic dependence. In fact, the rate R of recombined particles via RR in a volume V is given by a convolution of the experimental phase space overlap between positrons and antiprotons [46][8]:

$$R = \int_V \int_v n_{e^+}(\vec{r}) n_{\bar{p}}(\vec{r}) \sigma(v) v f(\vec{v}) \mathrm{d}^3 v \mathrm{d}^3 r \tag{1.3}$$

where n_{e^+} and $n_{\bar{p}}$ are the positron and antiproton spatial densities respectively, $\vec{v}$ the vector of relative velocity, v its absolute value, $f(\vec{v})$ the relative velocity distribution[9] and $\sigma(v)$ the cross section of the reaction. Usually[10], the integral over the velocity distribution can be carried out separately by introducing a rate coefficient α, so as to obtain:

$$R = \alpha \int_V n_{e^+}(\vec{r}) n_{\bar{p}}(\vec{r}) \mathrm{d}^3 r \qquad \text{with} \qquad \alpha := \int_v \sigma(v) v f(\vec{v}) \mathrm{d}^3 v \tag{1.4}$$

[7] This, together with the TRAP measurements, motivated the construction of the AD facility

[8] Their deal with electrons interacting with positively charged ions. Given the CPT symmetry, we can use that model for positrons and antiprotons as well.

[9] The distribution function f is dominated by the electron velocity distribution because of the large mass difference between electrons and ions.

[10] By assuming $f(\vec{v})$ independent on $\vec{r}$

Intuitively, for the TBR, we would have another n_{e^+} factor inside the spatial integral. By assuming a uniform spatial distribution, we obtain straightforwardly the linear and quadratic dependence on the positron spatial density of the RR and TBR rates respectively, as mentioned above. Therefore, the higher the positron density, the more TBR is likely to enhance the total recombination rate.
As far as the dependence of R on the positron temperature is concerned, in [46] the total α rate coefficient is reported. It is defined as

$$\alpha := \alpha_{\mathrm{RR}} + \alpha_{\mathrm{TBR}} + \alpha_{\mathrm{corr}} \tag{1.5}$$

where α_{corr} results from the complex interplay of three-body and radiative processes. In fig. 1.6 the dependence of each term is plotted as a function of the thermal energy (and therefore on the temperature) of the positron cloud. The plot shows how, at low

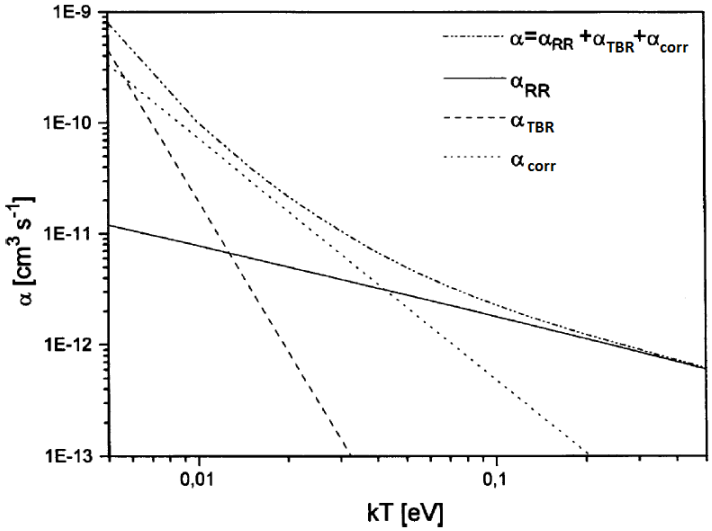

Figure 1.6: Total 2-body and 3-body recombination rates for protons with free electrons at a density $n_{e^+} = 10^7$ cm^{-3}, calculated as a function of temperature from the formulas provided by Stevefelt et al. [47]. Picture from [46].

temperatures, TBR dominates RR.

In ALPHA intense magnetic fields (about 3 T) and pulsed electric fields assure respectively the radial and axial confinement of $\bar{\mathrm{p}}$, which are cooled through sympathetic scattering with low energy electrons inserted into the trap. Positrons are guided by means of a magnetic field in the Penning trap, where they are manipulated to reach the suitable energy and density to interact with antiprotons and produce antihydrogen. $\overline{\mathrm{H}}$ confinement is achieved by means of a radial magnetic multipole trap which is superimposed on the axial magnetic solenoid field for plasma confinement. In 2011 ALPHA reported the longest achieved $\overline{\mathrm{H}}$ confinement, 1000 s, together with the first measurement of the energy distribution of the trapped antiatoms [48]; this result was obtained by means of an octupolar radially non-homogeneous magnetic field. Two years later ALPHA attempted a first gravitational test on neutral trapped antimatter. $\overline{\mathrm{H}}$ atoms in a trap were released and the up-down asymmetry of the annihilations was measured allowing the

collaboration to find a constraint (at 95% confidence level) of $-65 < \frac{M_g}{M_i} < 110$ for the ratio between the gravitational and the inertial mass of $\overline{\mathrm{H}}$ [49].

Charge exchange reaction

A conceptually different antihydrogen production mechanism ("*Charge exchange reaction*") involves transfer of a positron from an atom of positronium to an antiproton (see Eq. (1.6b)). the production of normal hydrogen via charge exchange $Ps + p- > H + e^+$ was demonstrated in [50]. For $\overline{\mathrm{H}}$ it has been demonstrated by the ATRAP experiment [51]: they generated $\overline{\mathrm{H}}$ through the interaction of $\bar{\mathrm{p}}$ (collected in a Penning trap) with positronium produced by means of Cs atoms in Rydberg state (that is, highly excited atoms, denoted with an asterisk) which interact with positrons accumulated in a second Penning trap. The whole process can be described by the following charge exchange reactions:

$$Cs^* + e^+ \longrightarrow Ps^* + Cs^+ \tag{1.6a}$$

$$Ps^* + \bar{p} \longrightarrow \bar{H}^* + e^- \tag{1.6b}$$

Antihydrogen production via positronium charge exchange has the advantage that, although the efficiency of the entire process (1.6) is lower than that of reaction (1.2), antihydrogen can be produced with lower energy (depending on $\bar{\mathrm{p}}$ temperature), therefore it can be trapped and manipulated more easily via electric field gradients.
When positronium atoms in high-n (Rydberg) states pass through the antiproton cloud, antihydrogen is also formed in high-n states via the charge exchange reaction ((1.6b)). The production of antihydrogen in AEḡIS is planned by using only reaction (1.6b), because this scheme is advantageous for the controlled pulsed production (the antihydrogen is formed within about 100 ns) allowing a time of flight measurement, and because of the fact that antiprotons, trapped and cooled before the reaction, determine the antihydrogen temperature. Moreover, Rydberg antihydrogen will allow for manipulation, being H^* atoms more sensitive to electric field variations. Note that, in the usual antihydrogen production via recombination of antiprotons and positrons in nested traps [40, 41, 61], antihydrogen is continuously produced during the time antiprotons spend in the nested trap (hundreds of ms or seconds). The temperature of the resulting antihydrogen depends on the competition between antiproton cooling and recombination rates [61, 71, 72]. On the contrary, the AEḡIS strategy foresees the production of low temperature $\overline{\mathrm{H}}$ in Rydberg states, possible because it is directly dependent on the low $\bar{\mathrm{p}}$ temperature; then, by quickly applying suitable voltages to the trap electrodes, an inhomogeneous electric field will be generated, producing and steering (see [63]) a beam of antihydrogen with a horizontal velocity of a few hundred m/s: thus anti-atoms will be accelerated in the horizontal direction [62] towards the gravity module.

Also the GBAR experiment at the AD facility will take advantage of the charge exchange reaction in order to make an antihydrogen beam and perform CPT tests like the measurement of the Lamb shift of $\overline{\mathrm{H}}$ and the determination of the antiproton radius [64].

Moiré deflectometer

The design of the moiré deflectometer will take advantage of the experience gained on a compact prototype device, working with antiprotons [65], formed by two parallel gratings (spaced by 25 mm) and an emulsion detector at a distance of 25 mm from the second grating [66] (Fig.1.7). It is a classical device, and, when a beam of particles passes

through, it produces a fringe pattern on the detector. This fringe pattern gets shifted in the presence of a transverse force. To infer the force, a comparison with a near-field in-

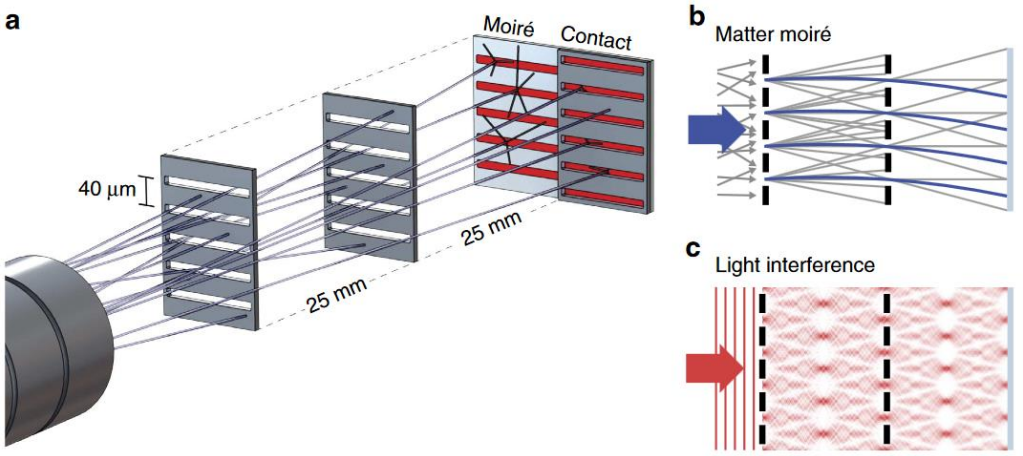

Figure 1.7: (a) An uncollimated antiproton beam impinges on two subsequent gratings that restrict the transmitted particles to well-defined trajectories. This leads to a shadow fringe pattern as indicated in b, which is shifted in the presence of a force (blue trajectories). Finally, the antiprotons are detected with a spatially resolving emulsion detector. To infer the force, the shifted position of the moiré pattern has to be compared with the expected pattern without force. (c) This is measured using light and near-field interference, the shift of which is negligible. A grating in direct contact with the emulsion is used to reference the antimatter and the light measurements

terference pattern produced by light is carried out. An additional transmission grating in direct contact with the emulsion is illuminated simultaneously with the moiré deflectometer, with antiprotons as well as with light. This provides a reference for alignment, since the pattern behind the contact grating cannot show any dependence on a force. The results showed a shift in the moiré pattern with respect to the interference pattern due to the light, which corresponds to a force acting on $\bar{\mathrm{p}}$ of about 530 ± 50 aN (stat) ± 350 aN (syst). By identifying such a force with a Lorentz force due to a magnetic field, a magnetic induction B ~ 7.4 G was found, which is good agreement with the magnetic induction ~ 10 G measured at the position of the deflectometer and normal to the direction of motion of antiprotons. These results are essential for the final design of the deflectometer working with $\overline{\mathrm{H}}$. Indeed, the $\overline{\mathrm{H}}$ fringe pattern due to gravity is expected to be comparable to the one observed in the case of antiprotons. It is true that the gravitational force acting on $\overline{\mathrm{H}}$ is 10 orders of magnitude smaller than the sensitivity level reached with the prototype device, but the resolution of the setup will be improved by scaling up the deflectometer and the detector. Furthermore, the velocity of $\overline{\mathrm{H}}$ will be four orders of magnitude smaller than the velocity of the $\bar{\mathrm{p}}$ used in the experiment described above.

How $\overline{\mathrm{H}}$ stark levels affect the gravity measurement

The kinetic energy $\overline{\mathrm{H}}$ atoms acquire via Stark acceleration depends on the Stark level the atom is in after the charge exchange reaction [67]. Different kinetic energies mean different shifts at the end of the moiré deflectometer. Blurry fringes are then expected,

affecting unfavourably the gravity measurement. In AEgIS the time of flight detection strategy [70] will be used to circumvent the problem. Position and time binning of incoming $\overline{H}$ atoms permits to obtain $\bar{g}$ by fitting the data of the dependence of the $\overline{H}$ gravitational shift on the time of flight (as depicted in Fig. 1.8). A parabolic dependence is calculated in [70], and the value of $\bar{g}$ is calculated from the curvature of the parabolic fit.

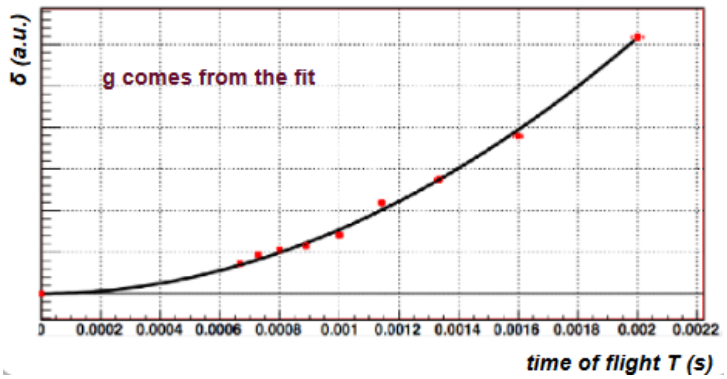

Figure 1.8: $\overline{H}$ gravitational shift as a function of the measured time of flight. The value of $\bar{g}$ comes from the parabolic fit of the data.

Latest developments The application of this method to the AEGIS experiment is challenging, due to the severe experimental conditions (vacuum and low temperatures) for the emulsions. To cope with these problems a new kind of emulsion gel was developed, which can be used in vacuum. Measurements with a 100 keV antiproton beam showed successful reconstructions of the $\bar{p}$ annihilation events with a resolution of ~ 1 μm, by using the ionizing secondary tracks [68]. The achievable precision in the measurement of $\bar{g}$ (gravitational acceleration of antimatter in the earth gravitational field) is strongly related to the spatial resolution: to get $\bar{g}$ with 1% uncertainty, less than 1000 events are required, with the given resolution [69]. For the sake of comparison, more than 10^4 events would be required with a spatial resolution of 10 μm. The influence of the temperature on the background and sensitivity of the emulsions are at present under investigation.

1.3 An external chamber for Positronium excitation tests

A new apparatus (see Fig.1.9) has been designed and built in order to study Ps formation in vacuum and Ps excitation to Rydberg states, in both tunable magnetic field and free field environments. A test chamber (henceforth called Bread Box), kept in a vacuum of $\sim 10^{-8}$ mbar, receives positron bunches sent from the accumulator. These bunches are further compressed before entering the chamber, and at the entrance they are focused on the porous target placed at the center.
Ps is thus generated and emitted in vacuum, so to study its excitation to Rydberg states outside the main cryostat. This chamber is connected to the accumulator through a transfer line of its own, connected in turn to the first section of the AEgIS positrons transfer line (shown in Fig.1.9), already described in the subsection 1.2.2. The picture shows how the transfer line is seen when one works in the experimental zone. By comparing it with

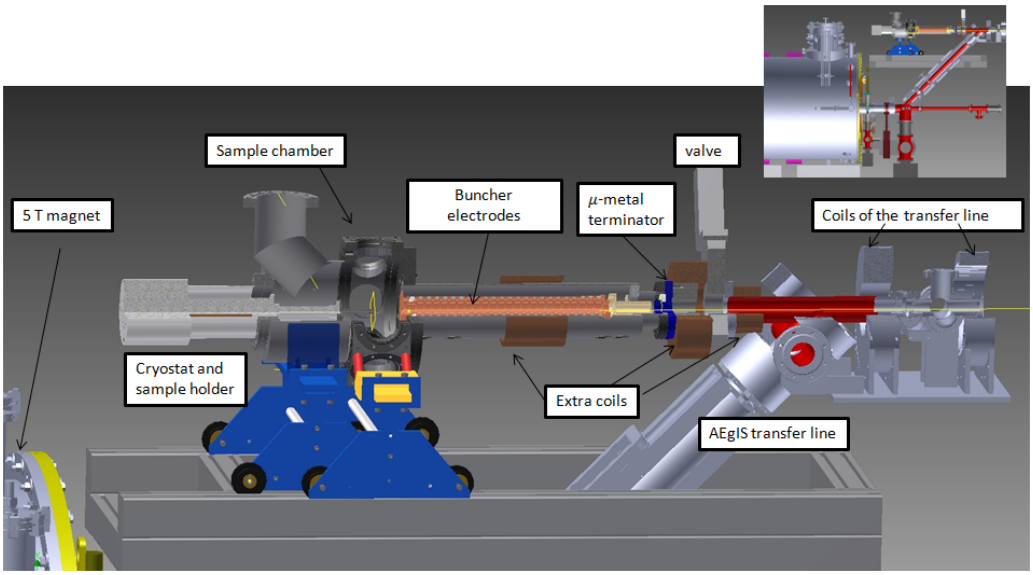

Figure 1.9: Positrons arrive from the right and, instead of going downwards they can go straight, towards the Bread Box to hit the converter placed in the center of the chamber, after a further bunching process

Fig. 1.2 (in which e^+ flew from the left to the right while here from the right to the left), it is clear how this part of the apparatus is embedded in the main AEgIS apparatus in Fig. 1.2 (just above the $45°$ tilted positron magnetic transfer line). This elongation of the transfer line was designed to accelerate positrons up to 9 keV and to obtain, at the target region, positrons pulses with a time duration of 5 ns, with a spot diameter lower than 3 mm FWHM.
The constraint of keeping the target in a free field region, or being able to control it, allows one to produce Ps and perform spectroscopy measurements in a controlled environment.
In fact, even though the chamber is placed outside the main cryostat, stray fields still pervade it. These stray fields come from the AEgIS 4.46 T and 1 T magnets, but we have also residual from magnetic fields used in A.D. experiments surrounding the AEgIS experimental zone. For this reason, in recent times we placed two grids inside the chamber, close to the target, in order to define a free field region in front of it. In addition, a mu-metal chamber has been made in order to shield all this new section of the apparatus from stray magnetic fields. The next step will be to put it in place. It is really important for us to be able to control fields inside the chamber, because it is a highly influential parameter in all Ps laser excitation processes.

My work in the AEgIS experiment

In the first months of my PhD I have been trained on positron transfer towards the Bread Box , and this allowed me to get confident with the Bread Box positron system. During the training I wrote a manual, in order to allow new users to have reference document. In the meanwhile I started implementing a Montecarlo simulation on Positronium formation, emission in vacuum and laser excitation. Ever since my second year, I also started dealing with lasers, thus participating at its maintenance and its setting up towards Ps

excitation measurements, that I contributed in the first person. As I already said at the beginning of this chapter, during these three years of PhD, I spent several weeks doing shifts: I helped to measure antiproton capture and cooling as well as positron transfer and stacking in the main cryostat traps.

In the following of the thesis, topics related to my work in the AEgIS experiment will be explained. More precisely, these topics are positrons, positronium and lasers, each of them related to the Bread Box line and not to the main cryostat.
The starting point will be the description of the positron transfer towards the converter, placed in the Bread Box . Then there will be some Ps physics: generation and cooling. At that point, a deep theoretical and practical excursion on the AEgIS laser will be done: my hope is for everyone who would like to work with it to get information on how to do it. I'll also describe all the problems I had during my work on the laser apparatus and its latest performances. After all this, I'll discuss my simulations on Ps excitation process, including a study on excitation efficiency's dependence on the exciting laser spectral properties. Finally, I'll show our experimental results.

CHAPTER 2

Positron system

On August 2, 1932, during the course of photographing cosmic-ray tracks produced in a vertical Wilson chamber (magnetic field of 15000 *Gauss designed in the summer of 1930 by Professor R. A. Millikan and the writer, the tracks shown in Fig. 1 were obtained, which seemed to be interpretable only on the basis of the existence in this case of a particle carrying a positive charge but having a mass of the same order of magnitude as that normally possessed by a free negative electron. Later study of the photograph by a whole group of men of the Norman Bridge Laboratory only tended to strengthen this view. The reason that this interpretation seemed so inevitable is that the track appearing on the upper half of the figure cannot possibly have a mass as large as that of a proton for as soon as the mass is fixed the energy is at once fixed by the curvature. The energy of a proton of that curvature comes out 300,000 volts, but a proton of that energy according to well established and universally accepted determinations' has a total range of about 5 mm in air while that portion of the range actually visible in this case exceeds 5 cm without a noticeable change in curvature. The only escape from this conclusion would be to assume that at exactly the same instant (and the sharpness of the tracks determines that instant to within about a fiftieth of a second') two independent electrons happened to produce two tracks so placed as to give the impression of a single particle shooting through the lead plate. This assumption was dismissed on a probability basis, since a sharp track of this order of curvature under the experimental conditions prevailing occurred in the chamber only once in some 500 exposures, and since there was practically no chance at all that two such tracks should line up in this way. We also discarded as completely untenable the assumption of an electron of 20 million volts entering the lead on one side and coming out with an energy of 60 million volts on the other side. A fourth possibility is that a photon, entering the lead from above, knocked out of the nucleus of a lead atom two particles, one of which shot upward and the other downward. But in this case the upward moving one would be a positive of small mass so that either of the two possibilities leads to the existence of the positive electron. In the course of the next few weeks other photographs were obtained which could be interpreted logically only on the positive-electron basis, and a brief report was then published*[2] *with due reserve in interpretation in view of the importance and striking nature of the announcement.*

C. D. Anderson 1933

[2]Here Anderson cites [75]

The idea of positron was postulated following the early work of Dirac [73], as reinterpretation of the "negative" energy extension of his theory of electron energy levels. Anderson's discovery (quoted in the previous page) followed soon afterwards, and the historic cloud-chamber photograph of his 1933 paper [74] is reproduced in Fig.2.1. The positron, which is the antiparticle of the electron, has the same mass within current experimental limits ($510.9989461(13)$ keV/c^2, [76]) and the same spin ($\frac{1}{2}$), but the opposite charge and magnetic moment. It should be stable in vacuum (like the electron: $\tau > 2 \times 10^{21}$ yr, [77]). In metals it rapidly slows down, and annihilates with an electron predominantly via $2-\gamma-$ray decay ($\sim$ 511 keV) with a mean lifetime that is typically only a few hundred picoseconds (ps).

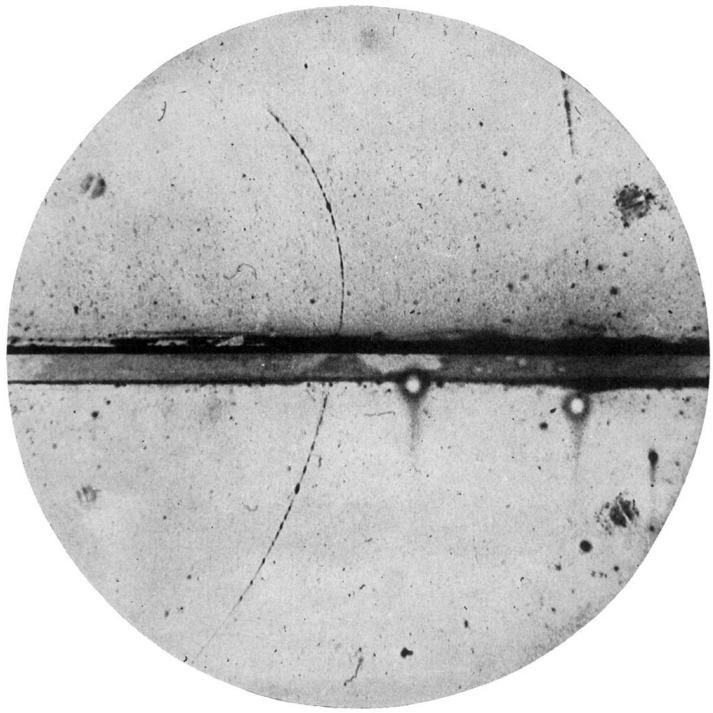

Figure 2.1: (called Fig. 1 in the quotation) One of Anderson's (1933) original photographs illustrating the historic discovery of the positron. In the cloud chamber, there is a lead plate 6 mm thick and a magnetic field of 1.5 T oriented in the page. The change of energy (63 MeV below the plate to 23 MeV above) with the known thickness of lead and magnitude of the field proves that the particle is positive and of the same mass as the electron.

Organizational note

In this chapter I'm going to describe the manner we produce and deliver positrons inside the Bread Box to form positronium and perform spectroscopy studies, while the description of how we produce positronium is postponed to next chapter.
I will describe the system designed to re-bunch positron pulses delivered by an accumulator supplied by a positron source and a Surko-trap. Positron pulses from the accumulator are magnetically guided in a 0.085 T field and are injected into a region free of magnetic fields, through a mu-metal field terminator. Here positrons are temporally

compressed, electrostatically guided and accelerated towards a porous silicon target for the production and emission of positronium into vacuum. Positrons are focused in a spot of less than 4 mm FWTM (Full Width at Tenth of Maximum) in bunches of ~ 8 ns FWHM.
The whole path includes therefore the following steps:

1. Positron (henceforth also called e^+) production and moderation
2. Positron trapping and compression
3. Positron accumulation and dumping
4. Positron transfer towards the target region
5. Positron re-bunching
6. Positron focusing
7. The Bread Box chamber: Positronium formation and excitation

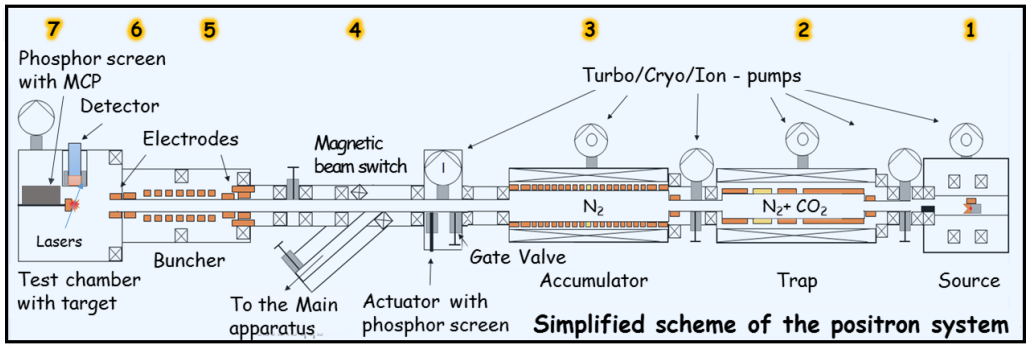

Figure 2.2: Here a simplified scheme of the positron system. Positrons go from the right leftwards passing through two main processes: accumulation (1+2+3), transport (4+5+6+7).

Each apparatus is separated by valves in order to preserve a good vacuum. Each segment is prepumped by roughing and turbo pumps. The source area is pumped with a roughing pump for a pre-vacuum and an ion pump for an Ultra High Vacuum (UHV, $\sim 10^-8$ mbar) while the trap and the accumulator are pumped by roughing pumps (pre-vacuum) and cryo-pumps (UHV). The transfer line between the accumulator and the Bread Box itself are pumped with a roughing pump (pre-vacuum) and turbo + ion each (UHV).

The chapter will be divided into three main parts: description of the whole accumulation process (1+2+3 in Fig.2.2), description of the transfer line (4+5+6 in Fig.2.2) and description of the Bread Box (7 in Fig.2.2).

The first two parts will be predominant: the former provides a ~ 20 ns long positron bunch (FWHM), the latter steers this bunch towards the target and compress it in time to obtain the ~ 8 ns time width. I'll describe the task of each section and which were the parameters we used to carry out an optimum positron transport towards the target, in view of the excitation measurements.

At the end I will describe the Bread Box hosting the excitation process.

2.1 Accumulation process

The positron Surko-type accumulator system is divided into three parts; source, trap and accumulator and is where the positron plasma pulse is processed. The positrons

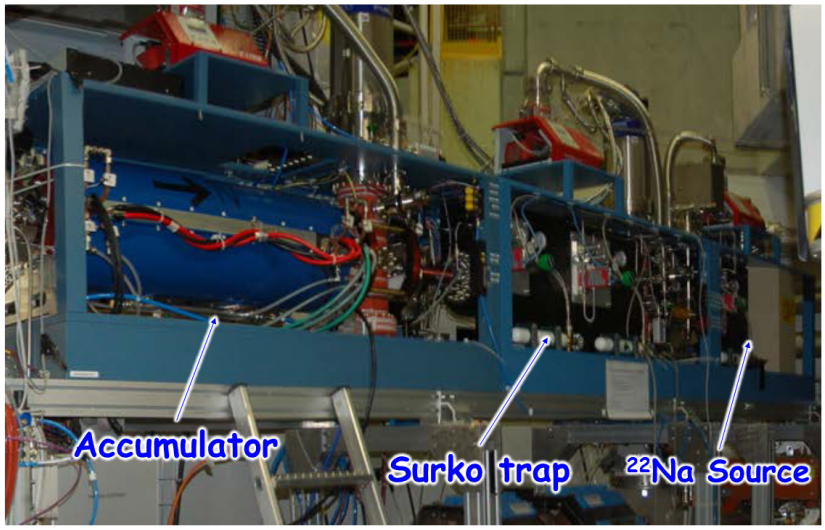

Figure 2.3: Positron accumulation system. From right to left we have positron generation, trapping and accumulation.

generated from the source (shown at right in Fig.2.3) are guided and transported with magnetic fields to the trap. In the trap, the continuous positron stream is divided, by means of electrodes, into small pulses, each containing 10^4 positrons. These small pulses are then accumulated in the accumulator. The accumulated positrons can be dumped all at once to either go the test chamber or to the main traps.
All these transfers between the connected sections are heavily affected by stray fields in the surroundings.

2.1.1 Source and moderator (1)

Positron emission or beta plus decay (β^+ decay) is a particular type of radioactive decay, in which a radionuclide nucleus is converted into another nucleus while releasing a positron and an electron neutrino (ν_e).
Positron emission (β^+ decay) in AEgIS is achieved with sodium-22 decaying into neon-22:

$$^{22}Na \longrightarrow ^{22} Ne + e^+ + \nu_e + \gamma \tag{2.1}$$

Its half-life period is 2.6 yr, which is sufficient for carrying out long-term experiments. The source in AEgIS originally had an activity of 18 mCi when it was commissioned in 2011. During the Ps excitation experiment an activity of ~ 8 mCi was estimated.

Commissioning

The source assembly used here, including all of the coils, pumps and components except for the sodium isotope itself, is provided by `First Point Scientific Inc.`, a

company specialised in supplying commercially available positron systems. The RGM, Rare Gas Moderator, is the commercial name of the positron source and moderator system developed by `First Point Scientific Inc.` Not only the hardware but also the software controlling the system was provided. A scheme of the positron source and source holder is shown in Fig.2.4. The sodium source is installed on a tantalum-coated

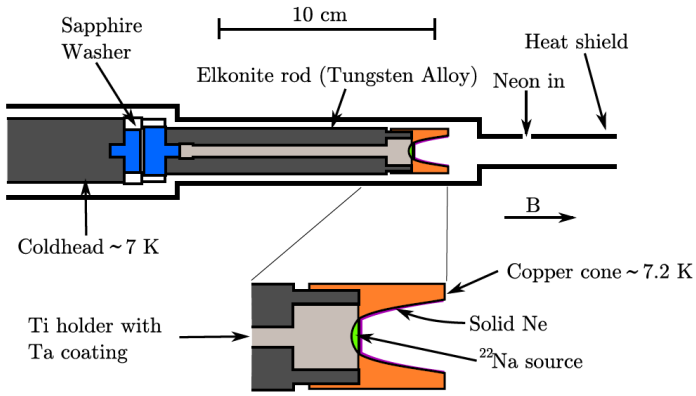

Figure 2.4: Positron source and source holder used at AEGIS. The ^{22}Na source is mounted on a titanium holder coated with tantalum, which is situated inside an elkonite rod. A sapphire washer divides the elkonite rod into two electrically isolated parts, and the rod can be cooled down to 7 K via a cold head [78].

titanium head, and is enclosed by titanium walls. Tantalum is a high-Z material and is used to reflect positrons, as it has a very high probability of positron back-scattering at $\sim 25\%$. The beam is therefore made of those positrons that are emitted towards the moderator, as well as some of those that are backscattered by the tantalum.
The source holder itself is a rod made of elkonite, which is a tungsten-copper alloy. Elkonite has good thermal conduction properties, and is also a good shield for gamma radiation emitted from the source due to its high density. The elkonite rod is split into two parts that are kept electrically insulated through the use of a sapphire (Al_2O_3) disc. Sapphire has good thermal properties while being a poor electrical conductor, which means that a bias voltage can be applied on the source. A copper cone is mounted on the rod so that it surrounds the positron source. This conical geometry has been established before as the best structure for growing RGS moderators and obtaining efficient positron moderation [79]. The operational pressure for the source is of around 10^{-9} mBar. At this pressure, neon solidifies between 10 K and 13 K. Therefore, the cold head on the source has to go down to 7 K.

Moderation

Since positron emission process is a three body decay, the positron is not emitted with a fixed energy, but it has a spectrum with a maximum at about 511 keV with end point energy at 543 keV (see Fig.2.5). Because of this high energy, positron accumulation is impossible. It is therefore necessary to convert the positron energy distribution from a beta plus spectrum to a monoenergetic one (Gaussian with a much lower average energy, in our case we have 2 eV with a spread of ~ 1 eV). This process is named "moderation".

Moderation is achieved by making positron interact with materials. Positrons slow down in a solid body initially through ionization losses (electron - hole pair generation)

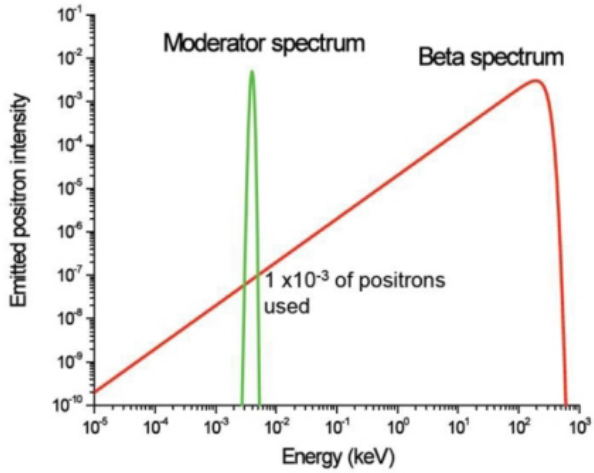

Figure 2.5: Positron emission energy spectrum before (red) and after (green) moderation.

and, below the ionization threshold, through excitation of excitons and phonons. Once it has been slowed down, a positron can either diffuse to the surface and escape from the substance or be trapped in the substance and annihilate with an electron directly or via formation of Positronium. A solid is characterized by a work function for positron ϕ_+, which is equal to the difference of the particle's potential energy outside the solid and inside it. For $\phi_+ > 0$, a potential barrier is formed at the surface - vacuum border, which forbids the escape of positrons.
Neon has a small but positive work function, which means that positrons can only be emitted from the surface if their kinetic energy is larger than the work function. As positrons thermalize relatively slowly in rare gas solids due to the band gap, a large fraction of positrons will therefore have enough energy to overcome the surface barrier despite the work function being positive. To maximize the yield of positrons slowed down by the potential barrier, the thickness of the solid Neon layer (deposited in the inner surface of the copper cone shown in fig. 2.4) must be carefully selected (usually few microns).

Due to impurities, gases coming from the trap and moderator heating caused by gamma rays, moderator loses efficiency at a logarithmic rate (see Fig.2.6). This means that the moderator needs "growing" again, i.e. a new Neon layer must be deposited.

A potential of 18 V is applied over the source to help positrons reach the trap section of the apparatus and accelerate a fraction of thermal positrons outside the moderator. There are also a pair Helmholtz coils situated around the source to guide the moderated positrons to form a beam towards the trap. The efficiency of the emission + moderation + transport to the Surko trap is around 0.1%.

2.1.2 The Surko trap (2)

In order to select only moderated positrons, a tungsten block and two coils with opposite polarities (saddle coil) are installed in the transfer line between the source and the trap. This setup acts as an energy filter. The saddle coil gives rise to a certain magnetic field and as a result, only positrons with certain energy may pass. This results in a more monoenergetic beam of positrons.

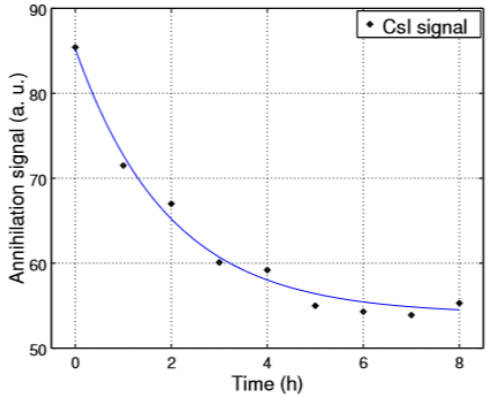

Figure 2.6: Positron counts since a new moderator is grown. The fit shows that efficiency drops at a rate of 7%/h for the first few hours, while it can be considered stabilized after 5 hours.

Fig.2.7 shows schematically how positrons coming from the moderation step are captured, stored and dumped. The confining magnetic field in the trap is 0.07 T.

The inner part of the trap is divided into three regions with decreasing pressure of cooling gas and decreasing electric potential, to store positrons in a well-like potential. Positron cooling is achieved via energy loss due to random collisions with small amounts of gas molecules (N_2 and CO_2). The high pressure allows a high probability of collision between positrons and gas molecules in a single pass, with therefore a high trapping efficiency. The pressure decreases all along the trap while the radius increases. Positrons bounce at the Gate electrode and those with lower energy are kept into the trap by the electrode 2. In Fig.2.7 the filling step is enlarged. The shaded region, i.e. electrode 3 region, hosts cooled positrons. At the bottom of the figure the trap electrodes behaviour is depicted. In the storage step, positrons are stored by increasing the potential of electrode 2. Note that in the picture potential values are not to scale. Positrons are released after trapping every 0.15 s with an energy of 17 eV. The number of positrons in each bunch has been measured to be between 5 and 6×10^4. The trapping/dumping efficiency is 0.14, calculated as the ratio between positrons injected in the trap and positrons dumped from the trap. During filling and storage positrons are radially compressed with a Rotating Wall technique (RW) [80] with a frequency of 6 MHz.

Positron beam diagnostics in the trap

Before installing the accumulator, the positron beam characteristics at the end of the trap were measured by means of a Caesium Iodide (CsI) scintillator coupled with a photomultiplier (PMT), and of a phosphor screen coupled with a CCD camera. The phosphor screen was placed on the positron's way in order to annihilate positrons on it and study the beam shape. While, in order to estimate the positron number, the CsI scintillator, previously calibrated, was set at known distance from the point of annihilation, outside the trap.

Firstly, the number of positrons at the end of the trap was estimated in continuous mode without the buffer and cooling gases: the positrons were only accelerated with a constant voltage difference towards the phosphor screen. In this way the trap doesn't affect the positron characteristics. A 2.5×10^{-3} efficiency was measured for the moderation step.

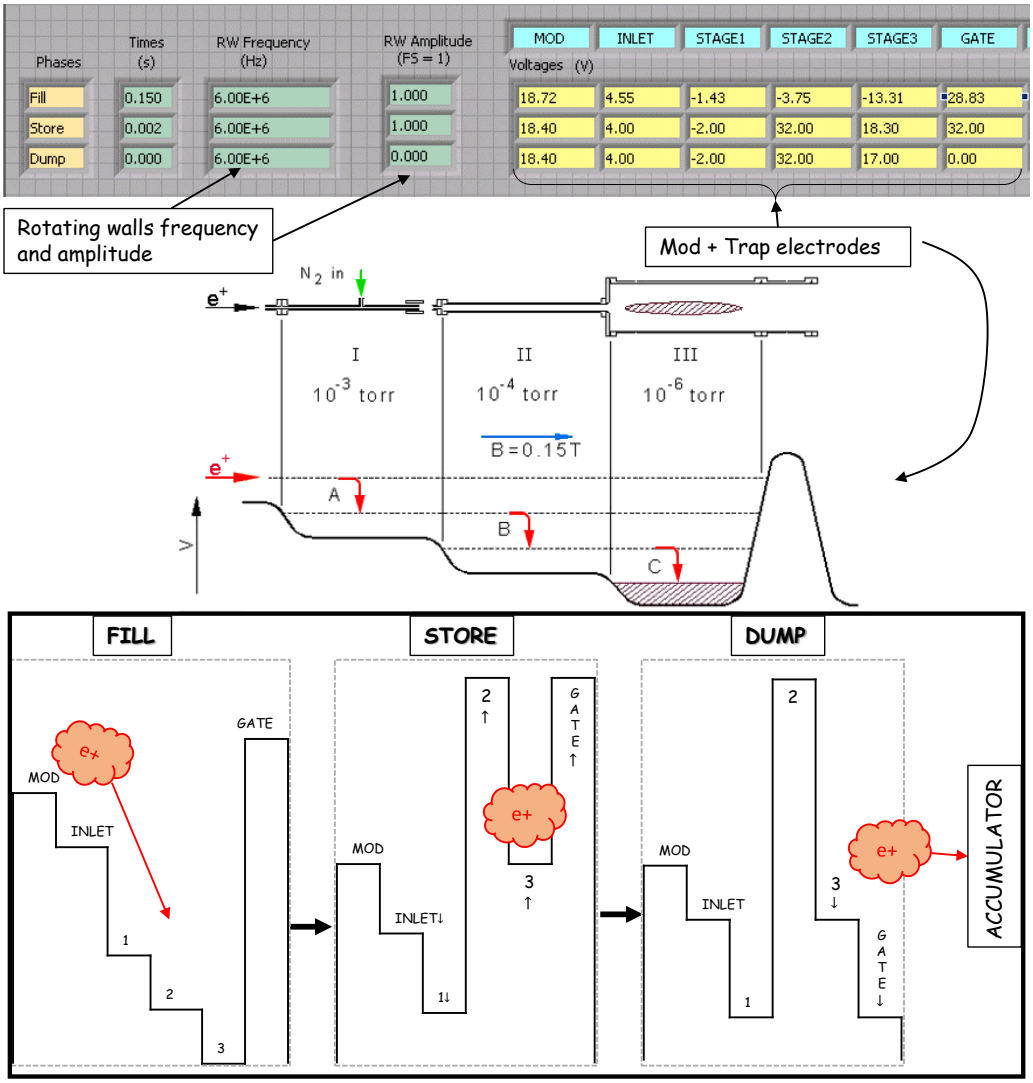

Figure 2.7: Positron trapping phases in pulse mode. On the top you see the labview interface for potential manipulation. In the middle, the "FILL" phase: trap configuration when positrons arrive from the moderator. Notice the decreasing pressure wile going further into the trap. On the bottom, the three different configurations of the trap electrodes are shown: filling, storage phase and dumping towards the accumulator.

In the upper part of Fig.2.8 the image of the beam in continuous mode taken with the CCD camera is shown, with the related intensity profile.
The phosphor screen, charged at -6 kV, shows a bright ring, with a diameter of $4-5$ mm, due to implanted positrons. The ring shape is reminiscent of the geometry of the moderator (see Fig.2.4): the design of the trap makes us lose the fastest positrons portion, that is the one emitted from the center of the moderator region, because the transport efficiency decreases with the positron's speed.
Later, the positron beam in pulsed mode (as described in the previous paragraph) was

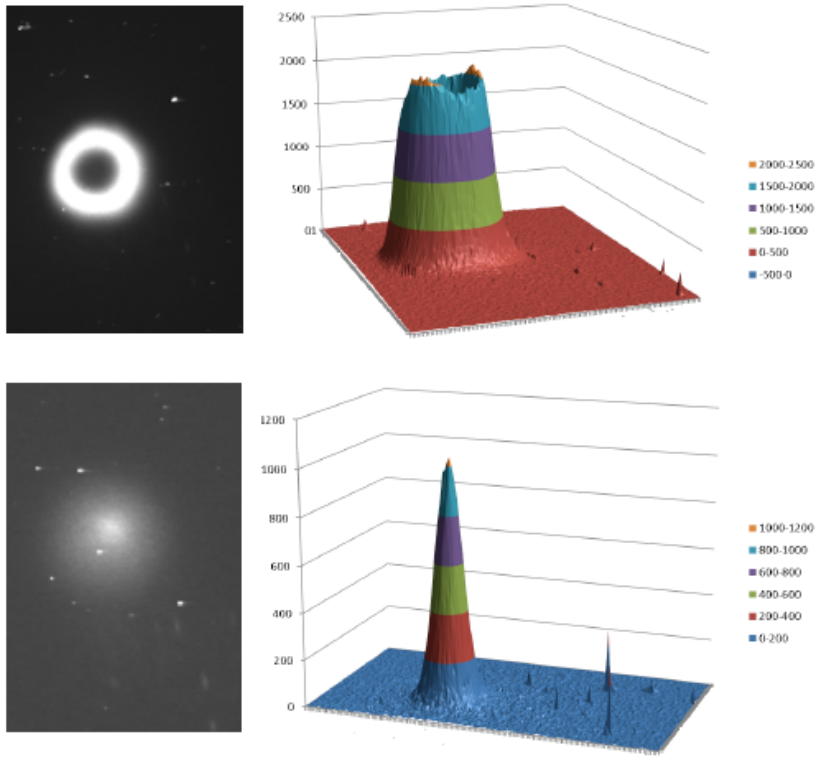

Figure 2.8: On the top the positron beam spatial shape as it is before trapping. On the bottom the positron beam spatial shape after trapping. Histograms represents different zoom and perspective of the CCD images.

characterized. The spot dimension turned out to be of about 2 mm, with a FWHM about 1 mm. With the CsI detector it has been possible to estimate the number of positrons for each pulse, $5 - 6 \times 10^4$ positrons for dump, and also the trap efficiency of 14% (the trap efficiency declared by the First Point is 17%).

2.1.3 The accumulator (3)

After the cool-down positrons are magnetically guided towards the accumulator at a rate of 6 Hz.
The accumulator is a Penning-Malmberg trap [81] with a magnetic field of 0.1 T for radial confinement. Apart from the main coil, there are two other coils installed inside the accumulator. These are used to improve the homogeneity of the field.
Inside the accumulator there is a low pressure environment. In stand-by mode 10^{-9} mbar are measured, while in run mode the pressure has to reach 6×10^{-8} mbar. This is a lower bound, because a buffer gas for positron cooling is needed (CO_2). Traces of N_2 could also be present: when the valve between the accumulator and the trap is opened to let positrons pass, the higher pressure of the trap pollutes the accumulator environment.

Accumulation process

A digital delayer receives the signal from the GATE in the trap dump process and reduces ($\sim$ 1 V) the INLET potential of the accumulator with a certain delay ($\sim$ 430 ns), in order to let e^+ enter the accumulator. After that, all other electrodes in the trap keep their potentials (see Fig.2.9). The accumulator can collect several hundred pulses from the trap, forming a positron plasma with a large number of positrons. The 21 electrodes

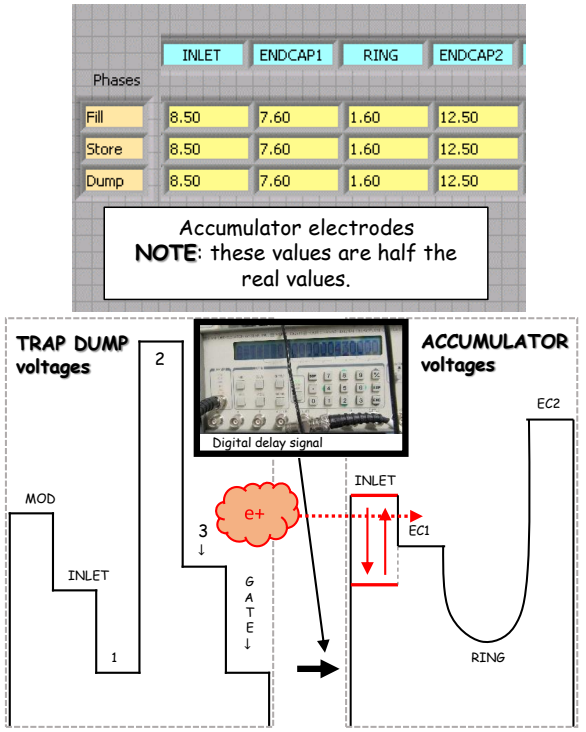

Figure 2.9: Transfer step: when positrons are dumped from the trap, the INLET potential of the accumulator goes down and let positrons enter. Timing is managed with the digital delayer in the picture. The accumulator potentials form a harmonic well instead of a step-wise

in the accumulator form a harmonic potential well rather than a step function potential. The harmonic potential well is illustrated in Fig.2.9. The electrodes are designed so that only the two boundary electrodes (endcap 1 EC1 and endcap 2 EC2) and the central electrode (Ring) are connected directly to power supplies (some typical values are given in the table of the picture). All other electrodes are connected to the boundary potentials with resistors: setting a voltage over one electrode will by default set the other electrodes as well, giving the harmonic shape as a result.
The central electrode is segmented into four sections in order to apply a rotating electric field for radial compression of the positron plasma. Therefore lifetime of the positron plasma is improved by the application of this rotating wall technique, which is kept working during the entire accumulation process [82]. The optimum RW parameters are strongly dependent on external fields. A potential of 360 mV and a frequency of 5.3 MHz was used in the apparatus tests presented in [85].

Dumping process

When the desired number of pulses is reached, a signal is sent to dump the positron plasma from the accumulator and into the transfer line. A trigger generates a TTL signal that lasts more than 0.5 ms. The square wave goes down when the number of e^+ pulses reaches the needed value. This makes accumulator potentials configuration change (depicted in Fig.2.10). Positrons are emitted towards the transfer line with a raising potential with its maximum amplitude tunable from a few tens of eV up to around 400 eV.

When the square wave goes down, a diagnostic apparatus is activated: at the accumulator exit, a calibrated CsI detector is placed, in proximity of a stopper in the positron's trajectory towards the Bread Box. The stopper acts as an annihilation point

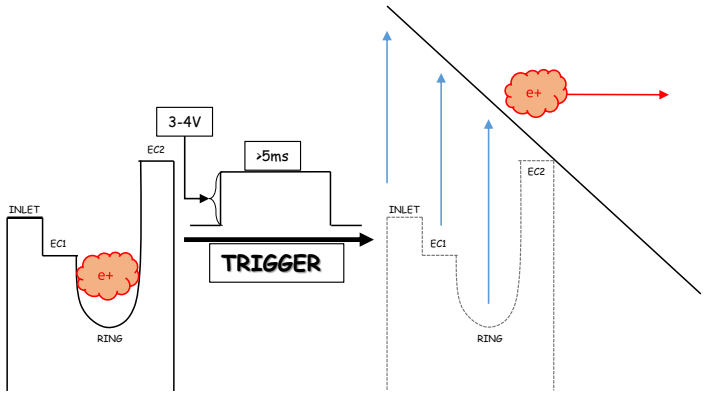

Figure 2.10: Dumping process. On the falling edge of the TTL signal, potential configuration changes to build a ramp.

and the CsI scintillator coupled with a photodiode determines the positron number by counting the annihilation gamma rays. This diagnostic system allowed us to optimize several parameters of the accumulation process such as the Ring potential, vertical/horizontal corrections of the confining magnetic fields, RW parameters and accumulation time. In Fig.2.11 optimization measurements for the ring potential and the accumulation time are reported. The latter also gives informations about the positron lifetime inside the accumulator. On the bottom you can find a spot dimension measurement, achieved via the "knife edge" method (see [83]). In the caption I explain the graphs. The optimum value for the ring potential turned out to be 3.2 V. Depending on the activity of the 4.5 T magnet, vertical and horizontal optimum correction were different: a 15 A as horizontal correction is used when the main magnet is off, and a 15 A for the vertical + 40 A for the horizontal correction are used with the main magnet on. We obtained these values optimizing the lifetime curves on the upper left of Fig.2.11. We also measure the spot dimension, that with the optimum setting is of 2.2 mm. In Fig.2.11 you read 2.8 mm of FWHM only because it is not taken into account yet the beam expansion due to the magnetic gradient between the accumulator and the not activated transfer line.
With these measurements we found that up to 8×10^7 positrons can be stored in around 450 s (corresponding to roughly 3000 pulses from the trap) with the 4.5 T off. However, accumulating for such a long time leads to a longitudinal expansion of the plasma, and

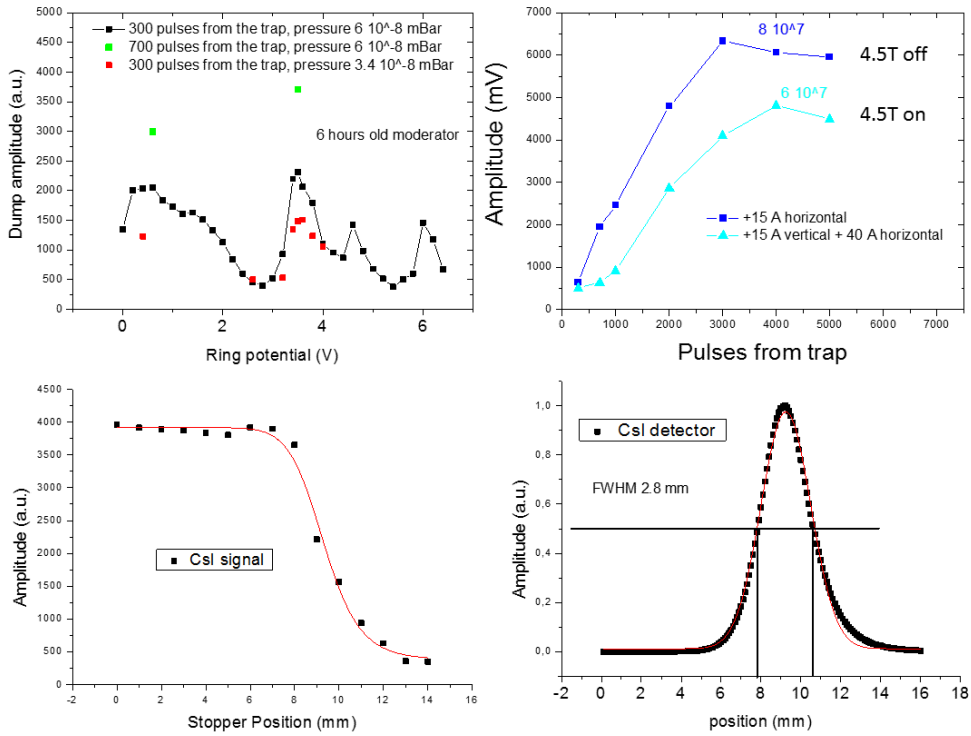

Figure 2.11: At the upper left the number of positrons dumped outside the accumulator as a function of the ring potential. At the upper right the number of positrons dumped outside the accumulator as a function of the number of stored pulses. The optimal magnetic corrections are reported in the graph for both 4.5 T on and off. When the main cryostat is off, it is possible to store a higher number of positrons inside the accumulator. At the bottom of the figure an example of positron beam dimension measurement. On the left you see experimental data (error function), while on the right the related derivative, giving the beam spatial parameters on the horizontal transversal axis.

results in time consuming measurements. For these reasons, the positron beam is usually comprised of 1000 pulses for the Ps excitation measurement.
The bunching system described in the following has been designed to work with positrons dumped from the accumulator with an energy of around 100 eV. The positron bunch at the exit of the accumulator has a typical temporal FWHM of about $15 - 20$ ns.

2.2 The transfer line

The transfer line has the task to deliver positrons previously dumped by the accumulator to the desired recipient. The transport towards the breadbox switches from magnetic to electrostatic in proximity of the buncher entrance.

2.2.1 The magnetic transfer (4)

In Fig.2.12 a picture of the transfer line is reported with an inset view of the latest configuration of the first four magnets. Positrons dumped from the accumulator are trans-

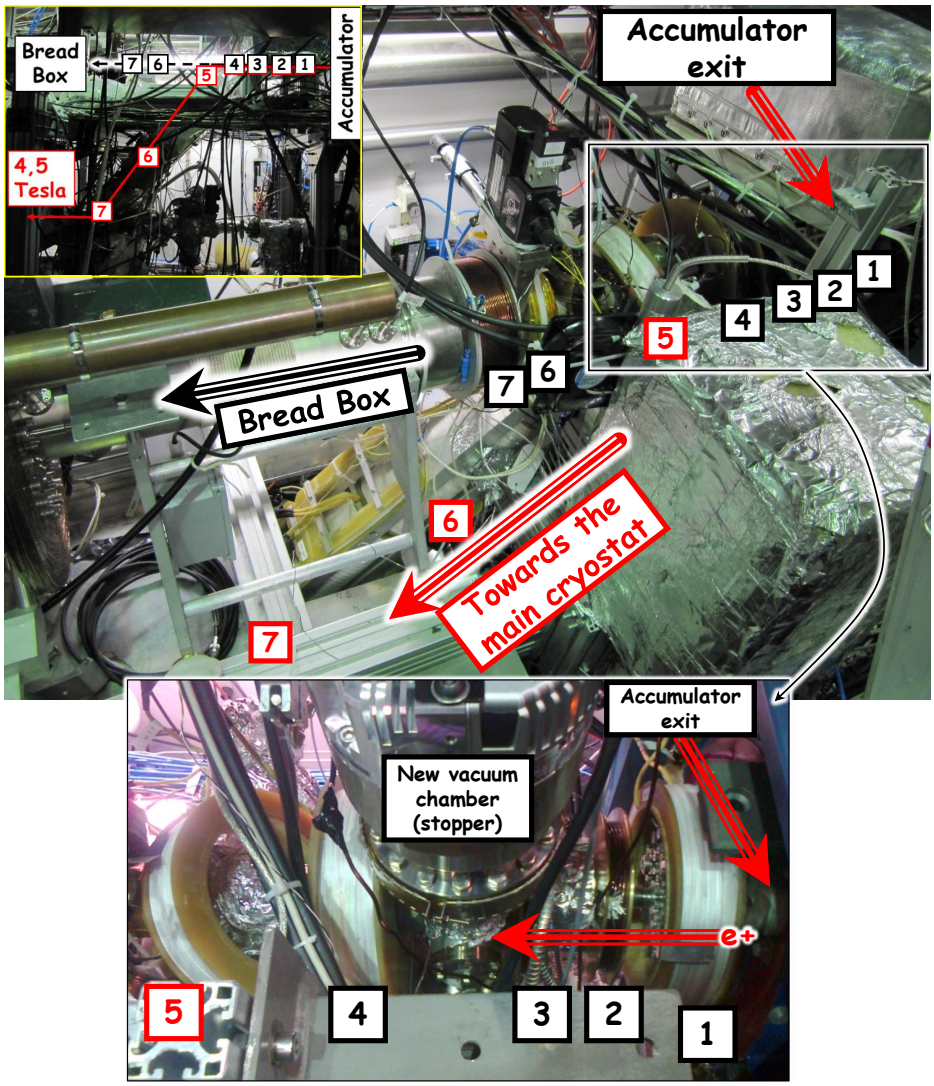

Figure 2.12: A picture of the transfer line. In black the Bread Box line, in red the main cryostat line. The upper left inset shows the side total view of the two transfer lines with their vertical displacement. On the bottom you see the latest configuration of the first 4 magnets, including the new vacuum chamber where the stopper of the previous paragraph is placed.

ported magnetically for a length of $\sim$ 60 cm when they are transferred to the Bread Box . The radial confinement in this first part of the transport is controlled by six main solenoids around the transfer line (black numbers in Fig.2.12), generating a maximum magnetic field of 0.14 T, in addition to some smaller correction coils. There is no longitudinal confinement, as the transport is dynamic and ends with the positron implantation in the Bread Box.

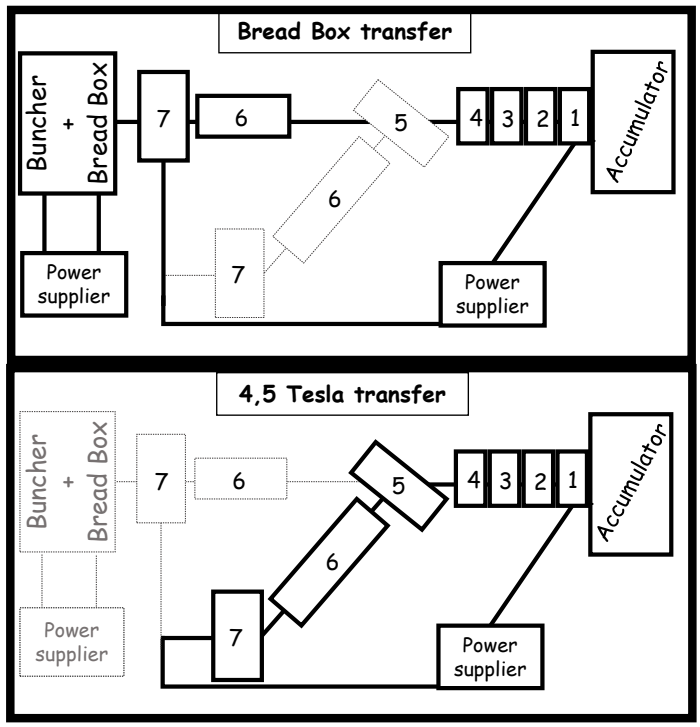

Figure 2.13: For transport to the test chamber, coils 1-6 (without 5) are connected in series and are supplied with 100 A raising a magnetic field between 800 Gauss and 1400 Gauss each. Coil number 7 is supplied by a separated power supply with a current of 35 A resulting in a field of approximately 600 Gauss

The positron beam can be steered into either the Bread Box or the main region using a remote-controlled beam switch (see 2.13). This switch is managed by the tilted solenoid, number 5 Fig.2.12 and 2.13. When this solenoid is active, the positron beam is directed towards the main apparatus. When the tilted solenoid is not switched on, the positron beam is steered towards the region with electrostatic transport ("Buncher + Bread Box" in the figure).

Note In all the following optimization tests, to measure annihilations on the target region we used an aluminum target instead of a positronium converter. The reason is that positronium generation affects the direct connection between annihilations due to positrons arriving at the target region and the signal amplitude. More on this in subsection 3.2.1.

2.2.2 The electric transfer: lens voltages optimization (6)

One of the main tasks of the Bread Box is to perform measurements on o-Ps in a magnetic field ranging from 0 to 300 Gauss. Thus, terminating the magnetic field away from the Bread Box is necessary. The switch from magnetic to electrostatic transport takes place where the buncher begins, just after the coil number 7. The shielding of magnetic fields is done by having the first electrode supported with a mu-metal flange blocking the field on the boundary. This field terminator reduces the field from 0.085 T (the transport magnetic field immediately before the injection in the electrostatic system) to 0.02 T within 5 mm. A large fraction of positrons is lost in this boundary due to divergence of the magnetic field. The electrostatic transport is carried out by the electrodes shown in Fig.2.14: V1, V2, Vfoc and buncher electrodes (initially held at a Vb voltage). V1 and V2

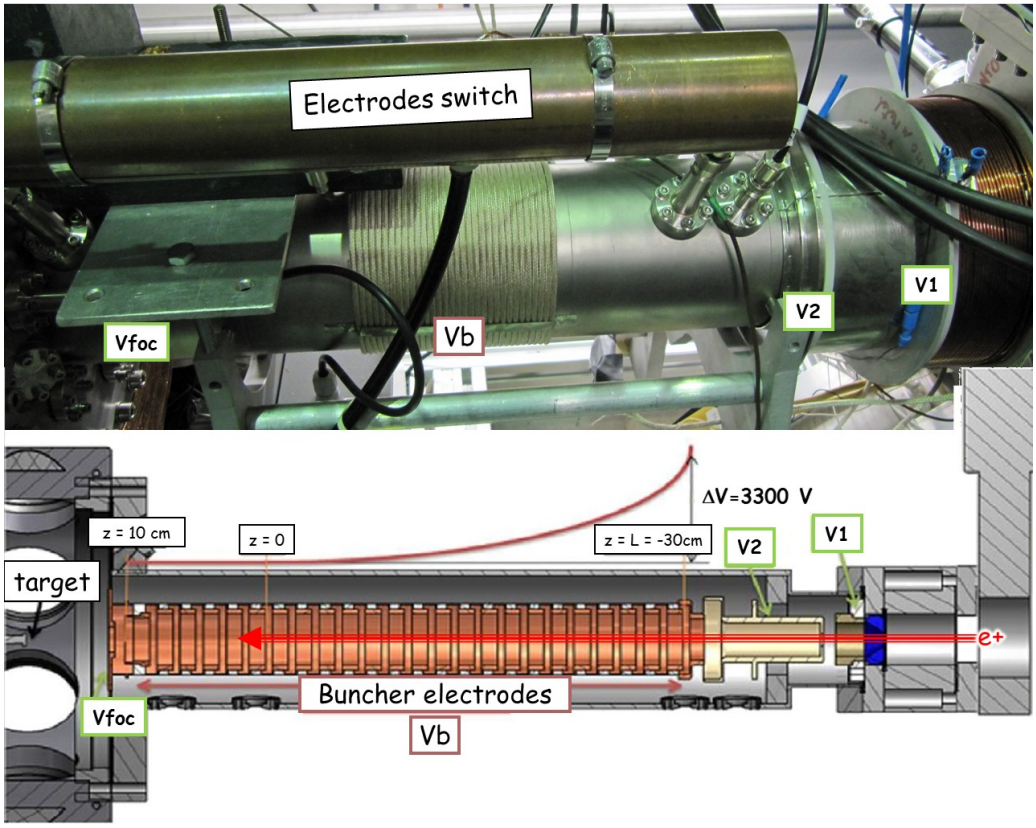

Figure 2.14: Picture and schematic view of the electrostatic transport section of the transfer line. From right to left, positrons are guided with lenses (V1 + V2 + Vb + Vfoc) kept on during the transfer, together with the buncher pulsed action, giving a kick to the positron bunch. Vfoc focuses positrons on the target for their last ~ 10 cm of path.

are necessary to extract positron from the magnetic transport and guide them towards the buncher electrodes, while Vfoc focuses the positron cloud on the target. Optimal values for V1, V2 and Vfoc were really robust. We always use V1 $= -800$ V, V2 $= -2100$ V and Vfoc $= -3000$ V, and these values are optimum in a wide voltage range. On the contrary, Vb is a more delicate issue. We performed a first rough optimization of Vb by

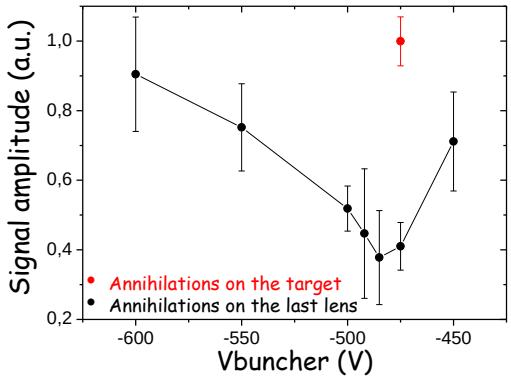

Figure 2.15: Annihilations acquired with a plastic scintillator. Where annihilations on the last lens are minimized, annihilations on the target are maximized (see text).

minimizing positron annihilations on the last lens (the one generating Vfoc). In Fig.2.15 there is also a red point. It is an annihilation test, showing that the obtained minimum was due to annihilations reduction on the last lens, and not to a bad transport towards the target (a detailed description of the Bread Box setup will be given in the following). Here the annihilation rate is equal to the annihilation rate on the last lens when Vb is not optimized (meaning that almost all positrons are annihilating there). However in this way we had just an optimum "region" for Vb, as the error bars with this method are too big. The definitive test to optimize Vb voltages was made with a phosphor screen + MCP (Multi-channel plate) on the target place. According to this method we decided to use Vb $= -535$.

All these electrodes work together with the buncher, and we optimized their value making always use also of the buncher for the positron transfer towards the Bread Box.

2.2.3 The positron buncher (5)

The buncher[1] is composed of 25 electrodes of 1.6 cm and has a total length of 40 cm: in this way, according to the simulations (SIMION® 8 code), it is able to contain the entire positron pulse ($\sim$ 20 at the entrance). When the positron bunch enters the buncher, between the first and the last electrode a parabolic potential is raised (see Fig.2.14). As a consequence, the positron pulse gets compressed both in time and space [84]. This parabolic function has a variable amplitude and is superimposed to a tunable bias. This accelerates positrons towards the target. The total voltage (parabolic amplitude + bias) is generated by a customized $4 - 10$ kV HV power supply (`FID GmbH technology`, model FPG 10–003NM30) with a pulse duration of 30 ns and a rise time of $2 - 3$ ns (Fig.2.16).

Buncher timing

To synchronize the buncher's electric pulse with positrons dumped from the accumulator, we used a digital delay generator (`Stanford Research Systems DG 645`). In order to be more sensitive to the time parameters of the positron pulses at the target position, we used a fast detector with a PbF_2 crystal (diameter 20 mm, length 60 mm)

[1]Some of the figures and the descriptions in this subsection follow the work published in [85].

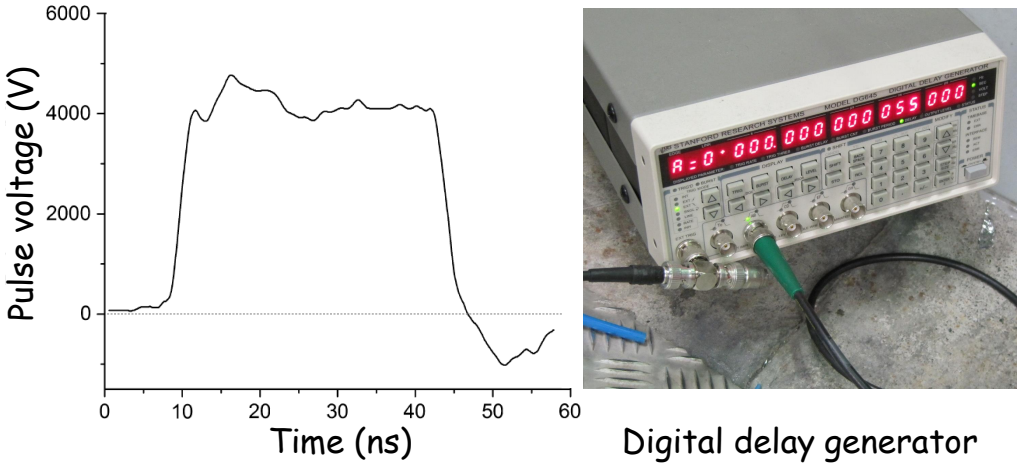

Figure 2.16: On the left: shape of the high voltage pulse as a function of time acquired at the input of the buncher, measured with a Magnelab CT-C1.0 current transformer (plot from [85]). On the right: `Stanford Research Systems DG 645` digital delayer

coupled to a `Hamamatsu R11265-100` PMT. We placed it 4 cm far from the target region, to detect gamma rays generated by the annihilation of the transported positrons onto the aluminum target. The measured FWHM of the single photon signal was < 3 ns. We optimized the buncher timing against both amplitude and FWHM of the annihilation signal on the aluminum target. In Fig.2.17(a) there is a plot of the signal amplitude of the PbF_2 + PMT detector as a function of the time delay between the positron dump of the accumulator and the switching-on of the pulser. The time reported on the x-axis of the figure is referred to a time-zero that takes into account all the delays due to the trigger of the digital delayer, the pulser, the electronics of the accumulator and the cables. In order to carry out this measurement, 1000 pulses from the trap were stored in the accumulator before dumping. When we switched on too early the parabolic potential in the buncher

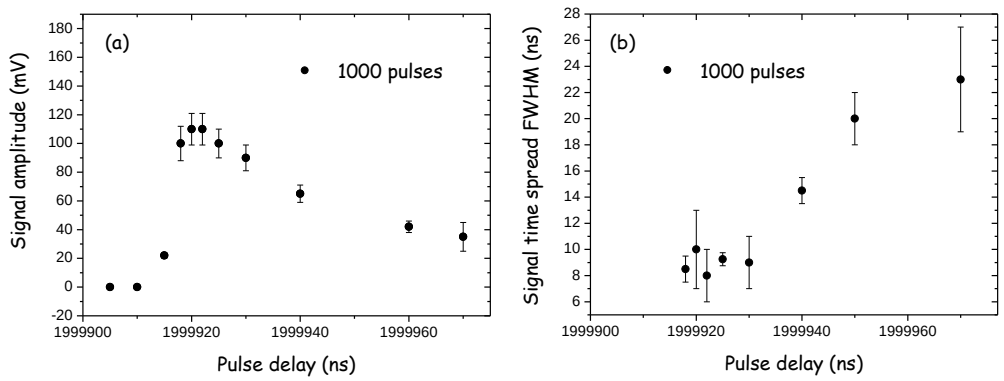

Figure 2.17: In (a) annihilations in the target region versus the buncher pulse delay are measured. When positron annihilations have their maximum, meaning that a more efficient transport has occured, we see in plot (b) that the FWHM of the positron bunch reaches its minimum value (plots from [85]).

(time delay < 15 ns), positrons bounce back on the potential wall raised at the entrance of the buncher. Therefore, we measure a ~ 0 mV signal with the PMT. As opposed to this, when we switch on too late the pulser (time delay > 60 ns), positrons transit through the buncher without being affected (so-called *pass-through* configuration), and the amplitude of the signal stays around 40 mV. While approaching the right timing, the amplitude increases: with a delay time of about 20 ns, the signal amplitude is almost three times higher, reaching a value of around 110 mV. The increase of the amplitude with respect to the pass-through configuration is consistent with the compression in time of the positron bunch. In Fig.2.17(b) there is the plot of the FWHM of the positron annihilation signal as a function of the delay. For a delay longer than 40 ns, the FWHM ranges between 15 and 23 ns, meaning that positrons flying through the buncher are not, or only partially, compressed. The more the synchronization is adjusted, the narrower signal gets and, between 18 and 25 ns delay, the FWHM reaches a minimum value of around $7 - 9$ ns. In Fig.2.18 you can find an example of compressed signal (buncher on) with respect to a normal one (buncher off). Here the total applied voltage is 4200 V. With the buncher

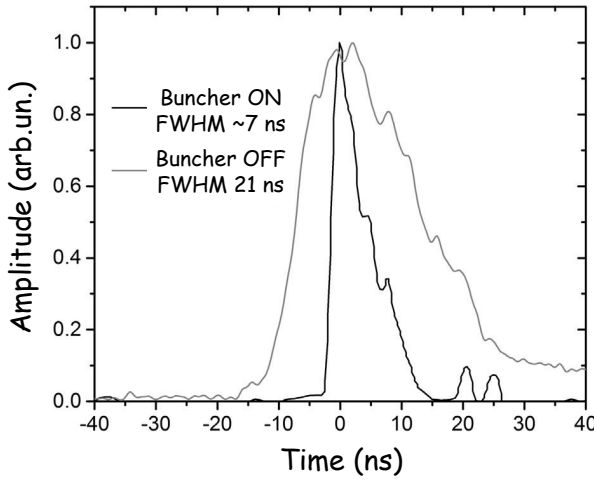

Figure 2.18: Comparison of the positron annihilation time distribution on an Al target with the buncher off and buncher on (high voltage pulse of 4200 V). Both signals are normalized to the same amplitude. The FWHM is reduced from 21 ns to ~ 7 ns (figure from [85]).

off the FWHM of the positron annihilation time distribution is around 21 ns, while it decreases to ~ 7 ns when the buncher is on.

2.3 The Bread Box chamber (7)

The Bread Box is a chamber dedicated to positronium spectroscopy studies as, for example, positronium excitation tests. In this section I describe the geometry of the chamber. Fig. 2.19 shows where the chamber is placed with respect to the transfer line as well as what it has inside.
The chamber is kept in a vacuum of $\sim 5 \times 10^{-8}$ mbar by a turbo pump.
The middle of the chamber is the "target region" because it is where positrons are delivered at the end of their path through the transfer line. The chamber contains a sample holder which is connected to an actuator installed at one of the flanges perpendicular to the beam line (the one behind the Macor® screen in the picture). The sample holder

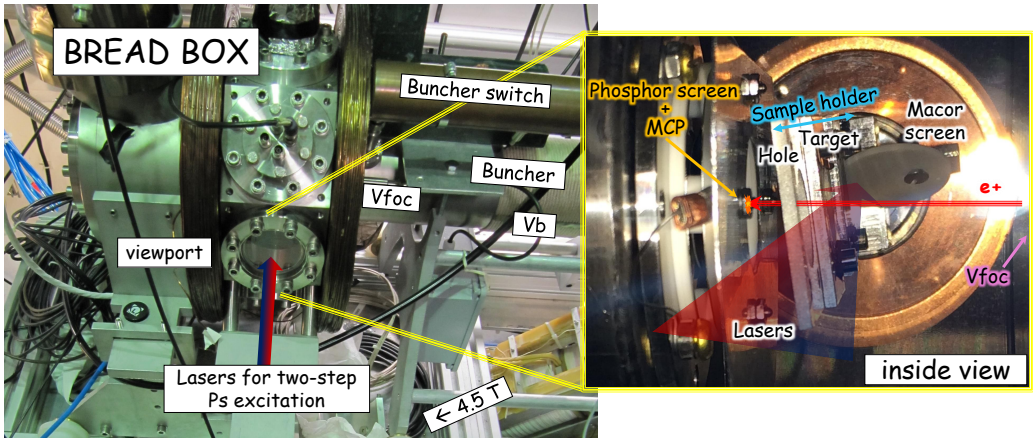

Figure 2.19: On the left a picture of the Bread Box, showing the relative position with the transfer line and the laser injection direction. On the right a picture of the inside of the chamber, as it is seen from the viewport.

is elongated, and up to three different samples can be installed at the same time. The actuator is used to move the sample holder back and forward along the laser axis: in this way several samples can be investigated shot by shot, without the need to open the chamber and break the vacuum. The positron beam can also be implanted into the sample holder itself, which is made from aluminium (configuration used for the transfer line parameter optimization), meaning that no Ps will be formed.

The target holder has also several 5 mm diameter holes. These holes can be used to let the positrons pass through and have a fast diagnostic of the positron beam spatial properties.

For experiments requiring a specific magnetic field in the target region [86], two coils, generating a field up to 300 Gauss in the direction parallel to the beam, are powered. Easily visible in Fig. 2.19, they are the two brown rings placed around the Bread Box, symmetrically with respect to the plane of the target. A flange on the top of the Bread Box hosts a detector holder. The bottom face of the detector holder is 4.5 cm far from the center of the chamber, allowing detectors to get closer when we measure positron annihilation on the target region. Note that the inside view of Fig. 2.19 has a real height of ~ 8 cm, for this reason we cannot see the detector holder surface.

2.3.1 Positron beam imaging

An MCP coupled to a phosphor screen and a CCD camera is installed on the backside of the holder. When the holder is removed or we let positrons pass through a hole of the sample holder, positrons annihilate on the MCP assembly, where no positronium is formed. The MCP assembly is a diagnostic tool used for a dedicated imaging camera. The positron signal is thus amplified by the emission of secondary electrons. The electrons generated by the MCP are accelerated towards the phosphor screen, which is therefore excited by the incoming particles. The phosphor screen is thin, therefore light is emitted from both sides. It can be imaged by a camera (`Hamamatsu ORCA-R2` digital CCD camera, model C10600-10B) installed outside the test chamber and viewing the back of the phosphor screen.

Fig. 2.20 reports an example of positron beam imaging together with the effect of the

magnetic field induced by the two surrounding coils. The two lines show an image of the bunched positron beam on the MCP on the left ((a) and (c)) and, on the right, the corresponding intensity distribution ((b) and (d) respectively). Without current in the

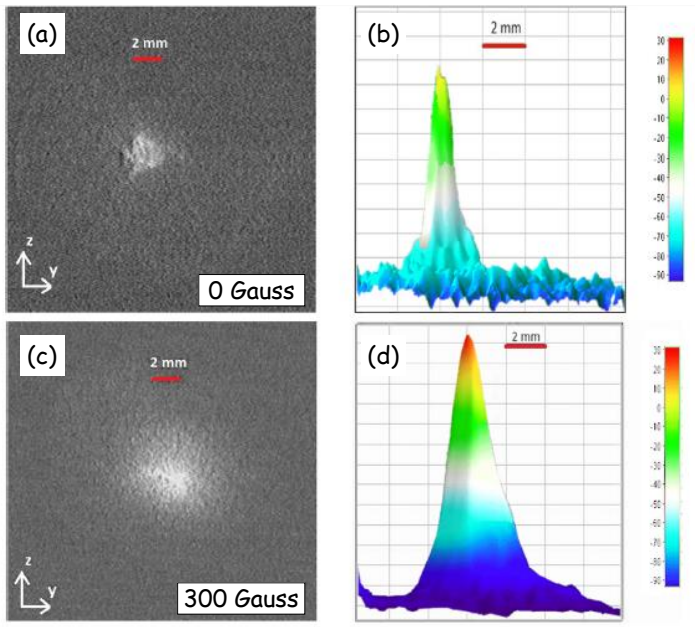

Figure 2.20: Positron beam spot acquired with an MCP assembly (left) and corresponding radial intensity distribution (right) when either no field (a,b)or a 250 Gauss field (c,d) is set in the target region. The FWTM of the positron distribution is less than 4 mm without magnetic field and around 5 mm with the magnetic field. Here positrons are accelerated to an energy of 3.3 keV by the buncher (figure from [85]).

Bread Box coils, we measured a magnetic field in the chamber below 1.8 Gauss in the direction parallel to the positron beam and below 0.5 Gauss in the perpendicular plane. In this low magnetic field configuration, we measured a spot with a FWTM of less than 4 mm. The efficiency of positron extraction from the magnetic field of the transfer line and transport along the buncher has been estimated to be around 30%, using a calibrated CsI detector coupled to a photomultiplier (PMT). Thus, the spot of Fig. 2.20(a) corresponds to an annihilation of around 10^7 positrons when 3×10^7 positrons are dumped from the accumulator. When we set a field higher than 150 Gauss, we positively affect the extraction of positrons from the buncher, increasing the fraction of positrons reaching the target up to around 40%. The missing positron fraction is expected to mainly annihilate at the transitions between magnetic and electrostatic transport. In this configuration with 250 Gauss in the target regionwe measured a FWTM of the spot of around 5 mm (Fig. 2.20(c)). Taking into account the estimated transport efficiency, the image corresponds to about 1.2×10^7 positrons reaching the target when 3×10^7 positrons are dumped from the accumulator.

2.3.2 SSPALS spectra

For Ps excitation detection we used a $PbWO_4$ scintillator ($25 \times 25 \times 20$ mm^3) coupled to a *Hamamatsu R11265-100* PMT, placed above the sample holder at a distance of 4 cm from the target center. This configuration was also used for many of the optimization measurements explained above. This set-up combines a good detection efficiency with a relatively fast time response (FWHM single photon signal around 4 ns). Therefore we used it in order to detect the annihilation radiation produced by the intense positron burst and to perform Single-Shot Positron Annihilation Lifetime Spectroscopy (SSPALS) [87]. This is an important tool, because it is the one we used to detect Ps excitation. The working principle is very simple. When an intense positron pulse impinges upon a target, a pulse of γ-rays is created which can yield information concerning electron–positron pairs just prior to annihilation. This fast detection scheme allows us to measure the timing of these gamma rays, obtaining a the so-called *positron annihilation lifetime*. As shown in Fig. 2.21,

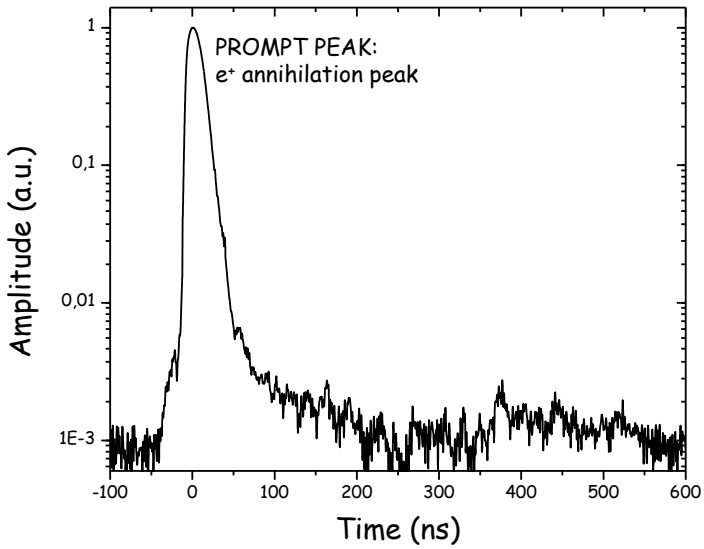

Figure 2.21: A typical SSPALS spectrum measured delivering positrons on the MCP surface. The curve is an average of 10 single shots. Positrons were implanted with an energy of 3.3 keV and no Ps is therefore generated.

a typical SSPALS obtained by implantation of positrons in the MCP shows a sharp peak, the "prompt peak", corresponding to the fast two-gamma annihilations of implanted e^+. On the right side of the peak, the signal quickly decreases and reaches the noise level in about 100 ns.

Positronium generation in the converter induces changes in the measured lifetime spectrum, that will be described in the next chapter. We detect positronium excitation using this method because the excitation process generates discrepancies in the SSPALS spectra related to either a laser ON or a laser OFF configuration.

CHAPTER 3

Positronium

In this chapter we will see how positronium is formed inside the converter that we used for Ps excitation measurements, and what are the characteristics of the emitted Ps cloud. For the Ps excitation measurements, Ps was generated inside a porous silica target with ordered channels, henceforth called *nanochanneled (Si) target* [88].

3.1 Positronium formation

In general, the Ps generation process occurs when a positron captures an electron of a given material (gases, powders, solids) [89]. Concerning solids, in insulating materials positronium formation is allowed also in the target bulk. On the contrary, in metals conduction electrons act like a screen on the surface and prevent Ps production in the bulk. Ps generation in the bulk of materials allows Ps cooling, via the use of porous structures [88, 90].
The Ps system is unstable: the two particles annihilate to predominantly produce two or three gamma-rays, depending on the relative spin states. The ground state of positronium, like that of hydrogen, has two possible configurations depending on the relative orientations of the spins of the electron and the positron. The *singlet state*, with antiparallel spins ($S = 0$, $Ms = 0$), is known as *para-positronium* (p-Ps), while the *triplet state*, with parallel spins ($S = 1$, $Ms = -1, 0, 1$) is known as *ortho-positronium* (o-Ps)

$$\begin{array}{cc} \text{p-Ps} & \text{o-Ps} \\ & |1,1\rangle = |\uparrow\uparrow\rangle \\ |0,0\rangle = \frac{1}{\sqrt{2}}(|\downarrow\uparrow\rangle - |\uparrow\downarrow\rangle) & |1,0\rangle = \frac{1}{\sqrt{2}}(|\downarrow\uparrow\rangle + |\uparrow\downarrow\rangle) \\ & |1,-1\rangle = |\downarrow\downarrow\rangle \end{array}$$

Ps generated inside the bulk of a porous Si target can diffuse into the pores with a kinetic energy spectrum centered around 1 and 3 eV [30], corresponding to a temperature of ~ 10000 K and ~ 20000 K respectively[1]. If these pores are connected to the converter surface (as in our nanochanneled targets), Ps atoms can be emitted in vacuum. In their way towards the target surface, Ps atoms lose energy through collisions with the pores' walls. O-Ps longer mean life (~ 142 ns in vacuum) gives the atom the possibility to escape from the converter bulk, enter the pores and reach the target surface. This is not possible for p-Ps atoms, whose mean life of ~ 125 ps (in vacuum) is not long enough

[1]This energy can be converted in temperature via the thermal energy formula $E_k = \frac{3}{2}k_BT$. In all our experiments, we use this "convention", in order to associate a temperature to the Ps cloud, even if the cloud is not at equilibrium.

to give it the time to complete the process. In addition, in each collision with the pores' walls, there is a probability for the Ps positron to annihilate with an electron of the material (known as a pick-off process), therefore the cooling process is affected by losses due to the short Ps mean life and pick-off annihilations. At the end, the only Ps fraction emitted in vacuum from the converter is made of o-Ps with lower energy than the one it had at the time of emission into the pores.

3.2 Detection of positronium emission in vacuum

In fig. 3.1, a scheme of Ps generation, cooling and emission in vacuum is represented. The positron bunch coming from the buncher is implanted inside the converter, placed

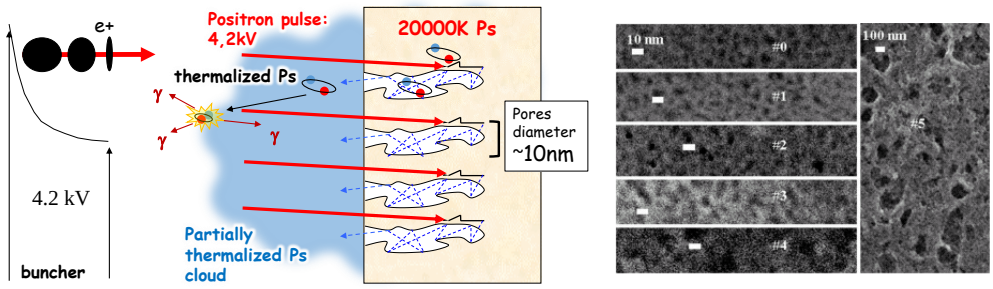

Figure 3.1: On the left, implantation of accelerated positron inside the converter. Some Ps atoms are able to escape into the pores where a fraction of them is thermalized and then emitted into vacuum. On the right, high resolution SEM images of different nanopore size converters.

in the middle of the Bread Box. Ps atoms are generated in the bulk of the material, and some of them are able to escape into the pores, where they have an initial temperature of around 20000 K. A fraction of them is emitted into vacuum after being cooled via collisions with the pores' walls. This is because collisions are inelastic, therefore a fraction of the Ps kinetic energy is given to the wall. Thermalization of Ps atoms can be thus translated into a reduction of the mean velocity of Ps atoms. Outside the converter we have then a Ps cloud, with a fraction of cooled (and hopefully thermalized) atoms. In each direction the cooling process could have different results, but we will talk about the thermalization issue in the following of the chapter.

3.2.1 Positronium formation detection by using SSPALS

The SSPALS technique is a useful tool to detect Ps generation and emission in vacuum. In fig. 2.21 we saw the footprint of positron annihilation on the MCP, were no Ps is generated. When o-Ps is generated and emitted in vacuum, a fraction of gamma rays will be emitted with a certain delay, related to the o-Ps lifetime. The detection of these gamma rays will populate the section of the SSPALS spectra with higher time and will generate a spectrum "tail", as shown in fig. 3.2. The spectrum has a logarithmic scale on the y axis. The light grey spectrum is the one shown in fig. 2.21, it is called background, and it is our reference spectrum. The black spectrum represents the Ps generation signal, normalized at the maximum value. The tail of the spectrum is clearly populated, meaning that a fraction of gamma rays is emitted in vacuum with a certain delay with respect to the prompt peak.

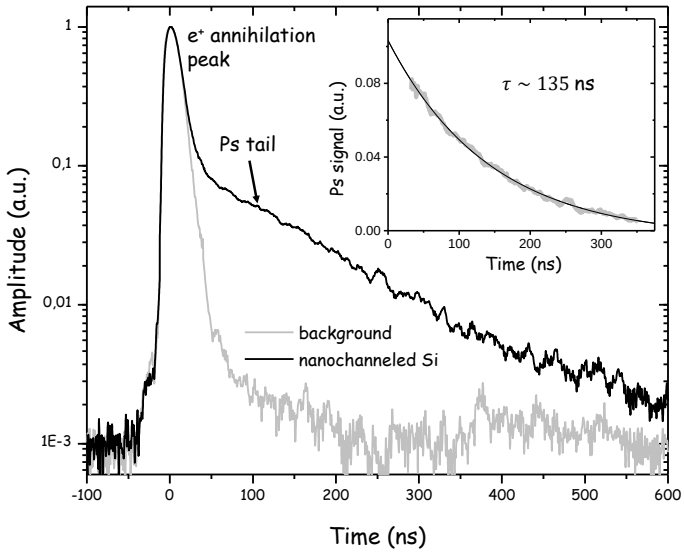

Figure 3.2: Positronium production: typical SSPALS spectrum (Spectrum from [85]).

The inset of the plot shows an exponential fit of the tail, for the first 300 ns time window. The fit gives a decay time slightly lower than the theoretical lifetime of o-Ps, due to distortions of the spectrum caused by random annihilations of Ps atoms either on the Bread Box walls or on the detector surface.
The choice of that specific time windows is due to geometrical issues. As it will be better described in chapter 6, the proximity of the detectors to the Ps generation point and the presence of the Bread Box walls make Ps annihilate on these starting from ~ 400 ns after the prompt peak. Gamma rays emitted in these annihilations add distortion the lifetime tail and, as a consequence, the exponential fit is much less reliable.

3.3 Positronium velocity distribution

Positronium that will be generated in the 1 T production chamber in AEgIS should have certain characteristics with the main goal of producing as much antihydrogen as possible. From the temperature point of view, and therefore from the velocity distribution point of view, longitudinal and transverse distributions affect the antihydrogen process in two different ways. The *longitudinal*[2] *average velocity* affects the antihydrogen formation cross section, mainly because slower Ps atoms have a longer temporal overlap with the antiproton cloud. The *width* of this *longitudinal velocity distribution* affects negatively the temporal overlap with the exciting laser beam. As concerns the transverse direction, the main issue is the spectral overlap between the exciting laser and the Ps cloud (a deep treatment of this will be given in next chapters). This means that, while the average velocity could (ideally) assume any value, the transversal velocity distribution width affects negatively both the laser excitation process and the geometrical overlap between the Ps cloud and the antiproton cloud. The width of the velocity distribution is strictly connected to the Ps cloud temperature: the larger the width, the hotter the Ps cloud in that specific direction.

It is worth noting that a high "monochromatic" Ps cloud on the transverse direction,

[2]direction perpendicular to the converter surface

meaning that we have a Dirac delta velocity distribution, wouldn't affect negatively the excitation process, as it would be enough to *detune*[3] the exciting laser. Therefore, concerning the excitation process, only the width of the velocity distribution has negative effects. On the contrary, on the longitudinal direction both average velocity and width are important parameters because of the limited duration of the laser pulse, that limits its temporal overlap with the Ps cloud.
In the following, I will describe two different methods for measuring the Ps cloud temperature, related to the two different components of the velocity.

3.3.1 Positronium longitudinal velocity distribution

In [31], an AEgIS research group reported results of their measurement of the Ps longitudinal velocity distribution exiting their nanochanneled Si converter. They showed to which extent it depends on several parameters. In their experiment, they realized nanochannels perpendicular to the surface by electrochemically etching Si in a HF solution. Moreover, they oxidized the inner surface of the nanochannels, in order to obtain Ps formation and emission into the vacuum. In their work, they presented yield and longitudinal velocity measurements of Ps on a target for which the synthesis parameters were optimized to obtain nanochannels with a diameter between 5–8 nm and a length of $\sim 2.0\ \mu$m. They measured Ps yield and Time Of Flight (TOF), as a function of

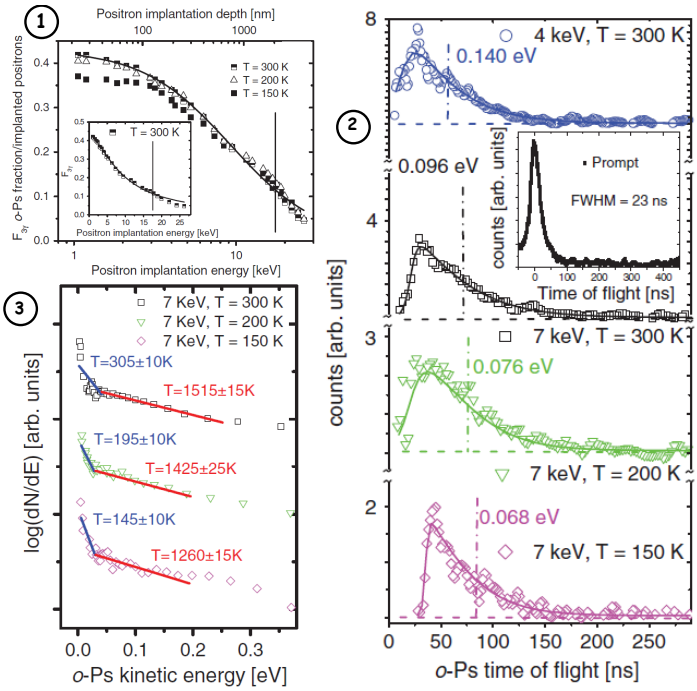

Figure 3.3: Positronium yield and longitudinal velocity measurements for nanochanneled targets [31].

the positron implantation energy and the converter temperature. The TOF measurement was performed by determining the time between positron implantation in the target and

[3] change the laser central wavelength in order to reach the resonance

o-Ps annihilation in flight. Here, I am just going to report their results (see fig. 3.3) and the related descriptions.
Panel 1 shows o-Ps fraction vs positron implantation energy (lower scale) and mean positron implantation depth $\bar{z}$ (upper scale). They marked with a vertical lines the border between the Si layer with channels and the Si bulk. The plot shows how the Ps yield decreases as function of the positron implantation energy (and therefore the implantation depth). **Panel 2** shows the TOF spectra as a function of the implantation energy and the converter temperature. They marked with vertical dash-dotted lines the average time t_a of the o-Ps TOF distribution and report the o-Ps energy, $E_\perp$, corresponding to t_a. They found that, by increasing the positron implantation energy from 4 to 7 keV, the escaping o-Ps fraction (panel 1) and the average o-Ps emission energy decrease from 30% to 25% and from 140 to 96 meV, respectively. We also see that the width of the distribution increases with implantation energy and the converter temperature. In **panel 3** o-Ps energy spectra in a semilog scale obtained by multiplying by t^3 the data of panel 2 was reported. By fitting the data with two-exponential fits they found out that two different Maxwellian beam distributions are present, at the indicated temperatures[4].

3.3.2 Positronium transversal velocity distribution

The measurement of Ps transversal velocity distribution coincides with the Ps $n = 3$ excitation measurement we performed in the AEgIS Bread Box. Here I will only explain the idea of the measurement.
If we shine the excitation laser on the transverse direction (parallel to the target surface), there will be a Doppler shift of the wavelength in the Ps atom frame of reference, related to the Ps velocity in the laser propagation direction. This means that each atom will "see" a different wavelength depending on its velocity. We are able to extrapolate information about the Ps velocity distribution along the laser propagation direction by measuring the Ps excitation efficiency at different laser wavelengths. Theoretical elements about this method will be given in chapter 7, while our measurement results will be shown in chapter 8.

[4]The description of the results follows the source [31]

CHAPTER 4

Lasers, nonlinear optics and frequency generation

As already mentioned before, in order to excite positronium atoms to Rydberg levels one needs specific wavelengths and proper beam characteristics. In AEgIS, the pulsed nature of the experiment leads to the use of a laser which is also pulsed and, for the two-step photoexcitation strategy, a 205 nm radiation for the $n = 1 \rightarrow n = 3$ transition and a $1675 - 1720$ nm radiation for the $n = 3 \rightarrow n > 14 (< 21)$ transition are required.
The requirement of a pulsed laser is fulfilled by employing a laser system based on a Q-switched pump laser. A Nd:YAG 1064 nm laser is used to produce all other required wavelengths by means of nonlinear crystals, capable of generating new frequencies from others (see next section). The AEgIS laser system makes use of different nonlinear processes for the generation of the desired wavelengths .
In this chapter, after an introduction to lasers physics and a theoretical treatment of the Q-switching process (see sec. 4.2), all needed nonlinear processes will be described. An electromagnetic formulation of nonlinear interactions is given in sec. 4.3, with applications to second harmonic generation, optical parametric generation, optical parametric amplification and sum frequency generation.

The introductory section will be developed in the following way. In the first part, basic notions of lasers in continuous mode (in a stationary state) will be described. Then, the behaviour of the laser fluctuations around the stationary state is introduced by explaining the general concept of "relaxation oscillations". Finally, Q-switching equations will be dealt with in order to know more details about the pulse generation process in AEgIS. As we will see later, Q-switching is indeed a way to take oscillation relaxations to extremes.

4.1 What is a laser? [92]

The word LASER is the acronym of *Light Amplification by Stimulated Emission of Radiation*. The "lasing" is the process where light passing through a medium is coherently amplified. But, usually, light is depleted by the passage through normal passive media, and not amplified. What happens then? The definition of LASER itself explains clearly the process behind the generation of laser radiation: an active medium (whose atoms have been previously excited) emits light when de-excited in a process of stimulated emission by some seed light that passes through it. Here, another question arises spontaneously: how can we obtain a certain amount of excited atoms in a medium? With proper words, how can we obtain the so-called *population inversion*? A population inversion regime can be achieved when excitation processes of the active medium are not related to the lasing radiation. A typical scheme of a laser involves three or four level systems to work with, and requires an external energy source as a "pump".

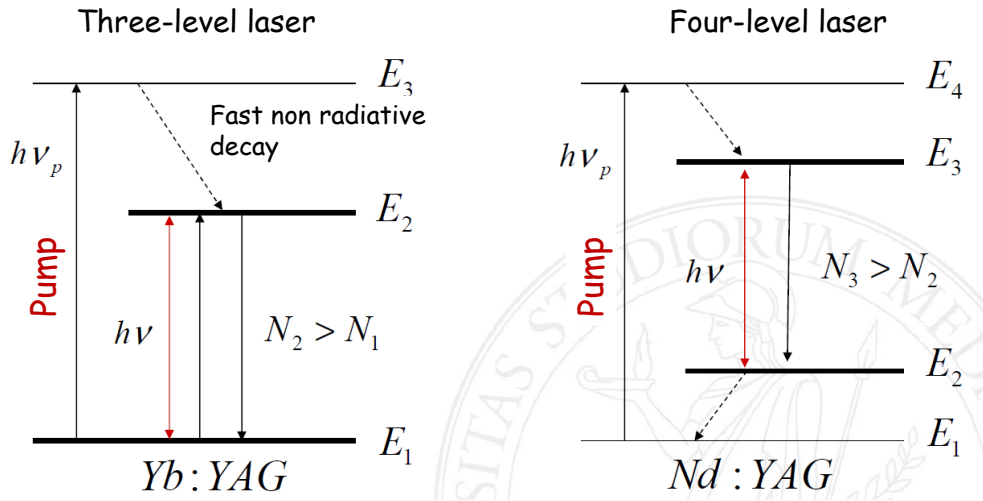

Figure 4.1: A sketch of a three-level laser (Ytterbium doped Yttrium Aluminium Garnet laser, Yb-Yag laser) and a four-level laser (Neodymium-doped Yttrium Aluminium Garnet laser, Nd-Yag laser). Dashed arrows represent fast (usually non radiative) decays, orders of magnitude faster than the laser level decay time. Level 3 (for a three level system) and 4 (for a four level system) can be considered empty (no stimulated emission occurs). In the case of four-level system, the level 2 can be considered empty as well. In this case, the population inversion is achieved with any pump power. In the three-level case, one needs to exceed a power threshold. Lasing is obtained by using the two innermost levels for the four-level system, and between the two lower levels for the three level system.

Referring to fig. 4.1, we consider an *atomic medium* and a *radiation pump*. To begin with, the highest of these levels is externally excited (using flash lamps, diodes or another laser light). Then an intermediate level is reached via *fast*[1] decay. This intermediate level can now radiatively decay, with both stimulated and spontaneous processes, either directly to the ground state (three-level system) or first to another intermediate level and then to the ground state, again via a fast decay.
In this preliminary description of the working principles of lasers, we suppose to be in a regime where laser light is continuously generated by supplying a constant pumping rate. Here the laser is said to work in *continuous mode*. This allows the concept of *stationary state*, crucial for a first comprehension of the lasing process.

Usually, in order to generate "enough" laser light with specific qualities, a so-called resonant cavity is used (henceforth only cavity). The most simple cavity one can use is made of two mirrors facing each other, with the active medium between them. The light emitted via stimulated decay will have the same direction and phase of the incoming light. When this light happens to be directed towards the mirrors, it can be reflected and pass several times inside the active medium. One of the two mirrors (output coupler) lets a few percentage of the light pass through it, while the other one is supposed to be totally reflective. In each passage through the active medium the light is amplified, but

[1]The decay time has to be short enough in order to be negligible with respect to the lasing transition decay time. Usually these happens with non radiative decays.

a certain amount of power be lost inside the cavity and through the output coupler, the latter constituting the desired *laser light*.
An important aspect of laser emission from the cavity is the following one: laser light will be emitted outside the cavity only when the gain inside the active medium balances the total losses of the cavity. When this happens, the number of photons in the cavity is approximatively a linear function of the *pump rate*[2], while the population inversion and the gain saturate (more details in the following).

In a four-level system, for example, the laser behaviour is usually described by the so-called *rate equations*, given by:

$$\begin{cases} \dfrac{dN}{dt} = R_p - B_0\phi N - \dfrac{1}{\tau}N \\ \\ \dfrac{d\phi}{dt} = V_a B_0 \phi N - \dfrac{1}{\tau_c}\phi \end{cases} \tag{4.1}$$

where N is the population inversion density (for example $N = N_3 - N_2$ in Nd-Yag) and ϕ is the number of photons in the laser cavity, R_p is the number of atoms per unit volume sent to the N_2 level per unit time, B_0 is the Einstein coefficient for the stimulated emission and $B_0\phi N$ is called *gain rate* and finally τ is the atomic spontaneous decay time. V_a is the active medium volume invested by the laser radiation and τ_c is the decay time of the cavity ($1/\tau_c$ is the loss rate).
At the stationary state ($\frac{dN}{dt} = 0 = \frac{d\phi}{dt}$), assuming a very low R_p so as to have no photon inside the cavity, from the first equation in (4.1), we obtain

$$N = \tau R_p \tag{4.2}$$

meaning that the population inversion grows linearly with R_p. The condition $\frac{d\phi}{dt} = 0$, in the second equation of (4.1), represents the condition *gain = losses*. Therefore, when the laser is about to turn on, N must saturate to the value

$$N_0 = \frac{1}{\tau_c V_a B_0} \tag{4.3}$$

and, once it is on, from the first equation we find that the number of photons grows linearly with the pump rate

$$\phi = \frac{1}{B_0 N}(R_p - \frac{1}{\tau}N) \tag{4.4}$$

In order to reach this stationary state, a cavity has to fulfil several stability requirements. Mirrors' convexity, cavity length and other parameters are dictated by the aim to have laser beam propagation stability inside the cavity. I will not go deeper in this topic in this thesis, as it is far from the goals of this work, but we need to introduce another fundamental notion in order to understand future discussions: the *Free Spectral Range* (FSR). The FSR is the inverse of the round trip time (T_{RT}) of photons inside the cavity and coincides with the frequency difference between longitudinal radiation modes of the cavity, which compose the stationary laser mode:

$$\nu_{FSR} = \frac{1}{T_{RT}} = \frac{c}{2L_{\text{eff}}}, \tag{4.5}$$

[2]The *pump rate* is related to the amount of energy delivered for population inversion purposes. It is given by $R_p = B_p \rho_p N_1$ - where B_p is the Einstein coefficient for the stimulated absorption of the pump from the ground level to the highest level (E_4 in fig. 4.1, ρ_p is the energy density of the pump) and N_1 is the ground level population.

where L_{eff} is the effective length of the cavity (the optics and the active medium refractive indexes cause a change in the effective length covered by photons).

In AEgIS, we have a Q-switched laser whose cavity is unstable. Here I will describe how Q-switch lasers work theoretically, while the AEgIS pump laser will be described in next chapter, where I will also describe the model we used to simulate the laser pulse produced by the AEgIS pump laser.

4.2 Q-switched lasers

In the previous subsection, in order to understand the behaviour of N and ϕ, we referred to a stationary state where gain balances losses. But, for example, when we want to turn on the laser or move it out of its stationary state, it passes through a transient in which gain doesn't equal losses any more. Q-switching is a technique taking to extremes this behaviour.

4.2.1 Relaxation oscillation

We want to deal, now, with a non-stationary state, i.e. we want $\frac{dN}{dt}$ and $\frac{d\phi}{dt}$ to be non zero. We can reach this result, for example, by introducing more losses inside the cavity for a time longer than τ_c and much shorter than τ: in this case the active medium is not able to depopulate the excited level, the initial power is lower with respect to the one related to the new stationary state, and the inversion population can reach higher values than before. At the beginning, the laser has a typical pulsed behaviour (it produces the so-called *relaxation oscillations*), dumped to the stationary state value in a time scale similar to the spontaneous decay time.

Another example is the switching-on phase of a laser. During the switching-on, the

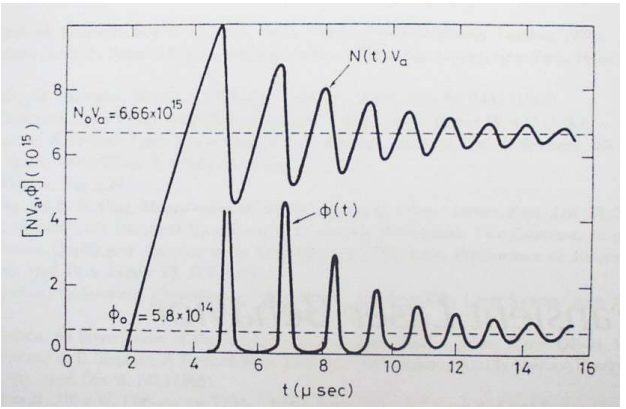

Figure 4.2: Relaxation oscillations for a Ruby laser in the switching-on phase [92].

emitted radiation doesn't follow exactly the population inversion, but oscillates about the stationary state value for a time comparable to the spontaneous decay time of the active medium. Here, the initial population inversion is zero and the initial condition is non stationary. In fig. 4.2, we see what happens when a Ruby laser has to be turned on. At the time $t = 0$ the laser is off, there are no photons in the cavity. When we turn on the pump, the population inversion keeps growing until the production of the first photon. At this point, the photon number in the cavity grows rapidly, being the

population inversion really high. As a consequence, the population inversion drops off rapidly because of the high number of photons produced via stimulated emission. Also the gain decreases following the population inversion decrease, hence reducing the photon production rate in the cavity. After this point, the dynamic is similar as the one described so far but less accentuated, and the laser reaches asymptotically the stationary value.
It is worth noting that we have the photon number peak where the gain equals losses, i.e. where $N = N_0$ in every oscillation.
The equation describing this process is a damped oscillator equation [92] for the photon number variation with respect to the stationary value $\delta\phi := \phi - \phi_0$:

$$\frac{d^2\delta\phi}{dt^2} + \frac{2}{t_0}\frac{d\delta\phi}{dt} + \omega^2\delta\phi = 0 \tag{4.6}$$

where $t_0 := \frac{2\tau}{x}$ and $\omega := \sqrt{\frac{x-1}{\tau_c\tau}}$, with $x := \frac{P_p}{P_{p_{th}}}$, being P_p the pumping power and $P_{p_{th}}$ the threshold pumping power. This equation is obtained by substituting $N(t) = N_0+\delta N(t)$ and $\phi(t) = \phi_0+\delta\phi(t)$ in rate equations (4.1) and neglecting all nonlinear terms. The relationship between ω and t_0 determines whether or not we have oscillations. In the oscillating case ($\omega > \frac{1}{t_0}$), we have, after few simple calculations, that the following relation holds:

$$\frac{x^2}{x-1} < \frac{4\tau}{\tau_c} \tag{4.7}$$

This means that, by keeping constant x and τ_c, the shorter the spontaneous emission time of the active medium, the more oscillations are damped. Therefore, we can go from oscillating behaviours to strongly damped ones, depending on the active medium we work with.

4.2.2 Q-switching

Q-Switched laser modality is one of the most common techniques to operate a laser in pulsed regime, widely used when an intense laser pulses are needed. In Q-switched lasers, the oscillating behaviour of a laser brought out of its stationary state is exploited. Here, in particular, we work in a regime were only the first relaxation oscillation pulse constitutes the laser output.

Even under the pulsed operating conditions considered in the previous subsection, the population inversion is seen to exceed the threshold value by only a relatively small amount (see Fig. 4.2), due to the onset of stimulated emission. Suppose now that a shutter[3] is introduced into the laser cavity. If the shutter is closed, laser action is prevented, so the value of the population inversion may far exceed the stationary threshold population inversion, holding when the shutter is absent. If the shutter is now opened suddenly, the laser will exhibit a gain that greatly exceeds losses: stored energy may then be released in the form of a short and intense light pulse. This first pulse empties the active medium and it is normally followed by a train of pulses like in fig. 4.2. However, Q-switching foresees the closure of the shutter between the first two pulses, preventing the formation of relaxation oscillations. This is the reason why I stated above that only one big pulse constitutes the laser output in each cycle. By actively manipulating this "shutter", one can generate high energy and low duration pulses in a controlled way. In the following, simple equations will be used to describe the process of pulse formation.

[3]Whatever method to achieve 100% losses inside the cavity.

By introducing 100% losses in the cavity the photon number in the cavity will be negligible and we will no more saturate the population inversion with stimulated emission. The first one of rate equations (4.1) becomes

$$\frac{dN}{dt} = R_p - \frac{1}{\tau}N \Rightarrow N(t) = \tau R_p \left(1 - e^{-\frac{t}{\tau}}\right) \tag{4.8}$$

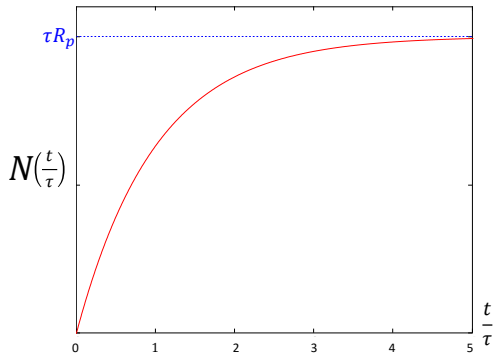

Figure 4.3: Population inversion versus the ratio t/τ.

As we can see from fig. 4.3, R_p being constant, the higher is τ, the higher is the population inversion one can reach. Moreover, it is clear from the plot that it is not worth applying the pump for a time much longer than the spontaneous emission time. When losses are removed, the pulse generated via stimulated emission has so many photons that rapidly empties the active medium, thus bringing the population inversion under the lasing threshold. In this extreme situation we have that:

1. the pulse energy is the one initially present in the active medium, usually of the order of hundreds of mJ, and the dynamic is much faster than that of spontaneous emission

2. being the active medium emptied, the pulse temporal length will be of the same order of the decay time of the cavity τ_c (usually nanoseconds).

This is why we can obtain high energy pulse with a Q-switched laser: one can easily reach hundreds of Megawatts with few hundreds of mJ energy packed up in a nanosecond pulse. In the next subsection, the topic of the pulse generation will be addressed.

Pulse generation

In order to describe the pulse creation in a Q-switched laser, we can divide the process into two parts: the *raising* part and *falling* part. Let's assume the population inversion to be much higher than the population inversion at the stationary state.

Pulse rise When the 100% losses are removed, the raising time of the pulse is shorter than τ_c because of the very high gain induced by the large population inversion, and therefore usually the dynamic is much faster than the spontaneous emission's one, related to τ. In the rate equations the pump ratio can be neglected, because the time scale of the pulse production is orders of magnitude lower than the scale of the pumping process. For the same reason, also the spontaneous emission term and the cavity decay

term do not play a relevant role (as explained above). Therefore rate equations become approximatively:

$$\begin{cases} \dfrac{dN}{dt} = -B_0 \phi N \\ \\ \dfrac{d\phi}{dt} = V_a B_0 \phi N \end{cases} \tag{4.9}$$

This leads to

$$\frac{d\phi}{dt} = -V_a \frac{dN}{dt} \Rightarrow \phi(t) = V_a(N_i - N(t)) \Rightarrow \phi_{\text{pulse}} = V_a N_i \tag{4.10}$$

where N_i is the initial population inversion (and we can assume $N_i = \tau R_p$ from eq. (4.8)). We found analytically that the total number ϕ_{pulse} of photons emitted when losses are drastically reduced is equal to the number of excited atoms in the active medium. This holds only when N_i is much higher than the population inversion at the stationary state.

Pulse fall We can consider that, after the pulse rise, the active medium has no more excited atoms. This means $N = 0$ and, therefore, the only condition left from rate equations is

$$\frac{d\phi}{dt} = -\frac{1}{\tau_c}\phi \Rightarrow \phi = \phi_{pulse} e^{-\frac{t}{\tau_c}} \tag{4.11}$$

This means that the pulse length exiting the cavity is of the order of magnitude of the cavity loss time.
The generated power is

$$P(t) = \frac{h\nu}{\tau_c}\phi_{pulse} e^{-\frac{t}{\tau_c}} \tag{4.12}$$

If we assume that losses are due only to the output coupler, we have that the energy of the pulse is given by

$$E(t) = \int P(t)dt = h\nu\phi_{pulse} = h\nu V_a N_i \tag{4.13}$$

This means that the pulse energy is the energy initially stored in the active medium.
In fig. 4.4 an example of Q-switched laser pulse is reported. It is worth noting the rate differences between the rising and falling part of the optical pulse. This simplified treatment holds when $N_i \gg N_0$ and the losses are due only to the output coupler. When these conditions are not fulfilled, dynamics get more complicated and rising and falling part of the pulse mix, usually leading to a more symmetric pulse.

4.3 Nonlinear optics

Nonlinear optics[4] is the area of optics that studies the interaction of light with matter in the regime where the response of the material system to the applied electromagnetic field is nonlinear. At low light intensities, typical of non-laser sources, the properties of

[4]Reference book [94]

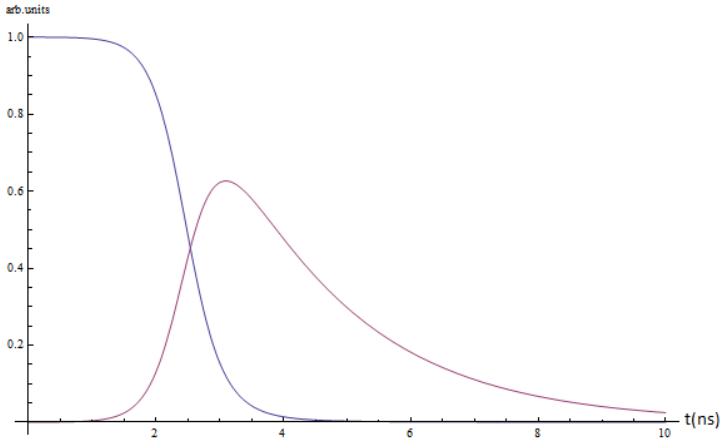

Figure 4.4: Qualitative behaviour of population inversion (blue) and number of photons (red) when the 100% losses are quickly reduced and the laser pulse is created [93].

materials remain independent of the intensity of illumination. The superposition principle [5] holds true in this regime, and light waves can pass through materials or be reflected from boundaries and interfaces without interacting with each other. Laser sources, on the other hand, can provide sufficiently high light intensities to modify the optical properties of materials. Light waves can then interact with each other, exchanging momentum and energy, and the superposition principle is no longer valid. This interaction of light waves can result in the generation of optical fields at new frequencies, including optical harmonics of incident radiation or sum- or difference-frequency signals.

4.3.1 Electromagnetic field and Maxwell's equations

The ideal laser emits coherent electromagnetic radiation which can be described by its electric and magnetic field vectors. The propagation of this radiation field is governed by Maxwell's equations. Nonlinear-optical effects belong to the broader class of electromagnetic phenomena described within the general framework of macroscopic Maxwell equations. These, together with the use of a nonlinear polarization model, are able to explain the nonlinear-optical propagation effects.
We write the set of Maxwell equations for the electric, **E**, and magnetic, **H**, field vectors. To include the effect of the field on matter, it is necessary to introduce a second set of vectors, **D** and **B**, called the electric displacement and the magnetic induction, respectively. In SI units, Maxwell equations have the form

$$\nabla \times \mathbf{E} = -\frac{\partial \mathbf{B}}{\partial t} \tag{4.14}$$

$$\nabla \times \mathbf{H} = \frac{\partial \mathbf{D}}{\partial t} + \mathbf{J} \tag{4.15}$$

$$\nabla \cdot \mathbf{D} = \rho \tag{4.16}$$

$$\nabla \cdot \mathbf{B} = 0 \tag{4.17}$$

[5] In physics and systems theory, the superposition principle states that, for all linear systems, the net response at a given place and time caused by two or more stimuli is the sum of the responses which would have been caused by each stimulus individually

where **J** is the electric current density (amperes per square meters) and ρ is the electric charge density (coulombs per cubic meters). As we are inside an insulating material, we can set both ρ and **J** equal to zero. We therefore have equation (4.16) implying $\nabla \cdot \mathbf{D} = 0$. Furthermore, in this discussion, we specialize the problem to a plane wave-like formulation, by taking $\partial/\partial y = \partial/\partial x = 0$ and assuming propagation along z. Taking into account electric and magnetic polarizations **P** and **M** respectively, for **D** and **B** the following relations, called *constitutive equations*, hold:

$$\mathbf{B} = \mu_0(\mathbf{H} + \mathbf{M}), \qquad \text{where} \quad \mathbf{M} := \chi_m \mathbf{H} \tag{4.18}$$

and

$$\mathbf{D} = \varepsilon_0 \mathbf{E} + \mathbf{P} \tag{4.19}$$

In optics, we deal usually with non-magnetic materials and with high frequency fields, that prevent magnetic dipoles to change with them. Therefore we can assume $\chi_m = 0$ and $\mathbf{M} = 0$.
The electric polarization can be considered as the sum of linear and nonlinear terms in the field E:

$$\mathbf{P} = \mathbf{P}_L + \mathbf{P}_{NL} \tag{4.20}$$

Taking into account the delayed answer of the medium, we can write

$$\mathbf{P}_L(z,t) = \varepsilon_0 \int \chi(t-t')\mathbf{E}(z,t')dt' \tag{4.21}$$

where χ is the linear susceptibility tensor of the medium (assumed to be homogeneous), written in the crystal frame of reference.
While for the linear polarization a delayed answer of the medium is necessary (for fulfilling requirements of the causality principle and the Kramers-Kronig relations), for nonlinear terms we can assume for simplicity an instantaneous response of the medium, meaning that the nonlinear susceptibility is a Dirac delta in the time domain. This cancels the effect of the convolution operator.
In this thesis we are interested in the second-order term of the Taylor series expansion of the polarization vector, hence we can neglect all higher orders. So we write the i-th component of $\mathbf{P}_{NL}$ in the usual form [94]

$$P_{NL}(z,t)_i = 2d_{ilm}E_l E_m \tag{4.22}$$

where d_{ilm} is the second-order nonlinear optical susceptibility of the medium (frequency independent), and i, l and m are the Cartesian directions (for example of the laboratory), that are not necessary the same as the crystal x, y and z axes, in which case d_{ilm} is the transformed d'_{ilm}.

A first step to derive the electromagnetic formulation of nonlinear interaction is to write wave equations taking into account nonlinear polarization. We thus rewrite (4.14) and (4.15) as:

$$\nabla \times \mathbf{E} = -\frac{\partial(\mu_0 \mathbf{H})}{\partial t} = -\mu_0 \frac{\partial \mathbf{H}}{\partial t} \tag{4.23}$$

$$\nabla \times \mathbf{H} = \frac{\partial(\varepsilon_0 \mathbf{E} + \mathbf{P}_L + \mathbf{P}_{NL})}{\partial t} = \varepsilon_0 \frac{\partial \mathbf{E}}{\partial t} + \frac{\partial(\mathbf{P}_L + \mathbf{P}_{NL})}{\partial t} \tag{4.24}$$

By using the relation $\nabla \times \nabla \times \mathbf{E} = -\nabla^2 \mathbf{E} + \nabla \cdot (\nabla \cdot \mathbf{E})$ and, having assumed $\nabla \cdot \mathbf{E} = 0$, we obtain

$$-\nabla^2 \mathbf{E} = -\mu_0 \frac{\partial}{\partial t}(\nabla \times \mathbf{H}) \tag{4.25}$$

Therefore we have

$$\frac{\partial^2 \mathbf{E}}{\partial z^2} = \mu_0 \frac{\partial}{\partial t}\left(\varepsilon_0 \frac{\partial \mathbf{E}}{\partial t} + \frac{\partial(\mathbf{P}_L + \mathbf{P}_{NL})}{\partial t}\right) = \mu_0 \varepsilon_0 \frac{\partial^2 \mathbf{E}}{\partial t^2} + \frac{\partial^2(\mathbf{P}_L + \mathbf{P}_{NL})}{\partial t^2} \tag{4.26}$$

leading to the wave equation

$$\frac{\partial^2 \mathbf{E}}{\partial z^2} = \frac{1}{c^2}\frac{\partial^2 \mathbf{E}}{\partial t^2} + \mu_0 \frac{\partial^2(\mathbf{P}_L + \mathbf{P}_{NL})}{\partial t^2} \tag{4.27}$$

From now on, we will always deal with the specific case of three main frequencies ω_1, ω_2 and ω_3, linked by the relation

$$\omega_3 = \omega_1 + \omega_2 \tag{4.28}$$

We will use the index $j = 1, 2, 3$ for them. Given the *dispersion relation*

$$k_j = \frac{\omega_j}{c} n(\omega_j) \tag{4.29}$$

where $n(\omega_j)$ is the refractive index, the i-th component of the electric field vector can be written as

$$E_i(z,t) = \sum_{j=1}^{3} \frac{1}{2}\left(A_{ji}(z,t)\mathrm{e}^{-\mathrm{i}\omega_j t + \mathrm{i}k_j z} + c.c.\right) \tag{4.30}$$

where j is related to the mode ω_j.
It is clear that the presence of $\mathbf{P}_{NL}$ in equation (4.27) couples the equations for the different spatial components of the electric field (see eq. (4.22)).

We write $P_{NL}(z,t)_i$ for each frequency ω_j in terms of the electric field of eq. (4.30). We start, for example, with ω_1:

$$\begin{aligned} P_{NL}(z,t)_{1i} = (2d_{ilm}E_l E_m)_1 = \\ \left[2d_{ilm}\left\{\sum_{j=1}^{3}\frac{1}{2}\left(A_{jl}(z,t)\mathrm{e}^{-\mathrm{i}\omega_j t + \mathrm{i}k_j z} + c.c.\right)\right\} \times \right. \\ \left. \times \left\{\sum_{j'=1}^{3}\frac{1}{2}\left(A_{j'm}(z,t)\mathrm{e}^{-\mathrm{i}\omega_{j'} t + \mathrm{i}k_{j'} z} + c.c.\right)\right\}\right]_1 \end{aligned} \tag{4.31}$$

As we are investigating the nonlinear polarization related to ω_1, we keep the relative terms satisfying relation (4.28). At the end we come out with

$$P_{NL_{1i}} = d_{ilm}\left(A_{3l}A^*_{2m}\mathrm{e}^{-\mathrm{i}(\omega_3-\omega_2)t + \mathrm{i}(k_3-k_2)z} + c.c.\right) \tag{4.32}$$

We consider also P_L in terms of the frequency ω_j and along i

$$P_{L_{ji}}(z,t) = \varepsilon_0 \int \chi(t-t')E_{ji}(z,t')dt' \tag{4.33}$$

We write now eq. (4.27) for a frequency j and along i:

$$\boxed{\frac{\partial^2 E_{ji}}{\partial z^2} = \frac{1}{c^2}\frac{\partial^2 E_{ji}}{\partial t^2} + \mu_0 \frac{\partial^2 P_{L_{ji}}}{\partial t^2} + \mu_0 \frac{\partial^2 P_{NL_{ji}}}{\partial t^2}} \tag{4.34}$$

We now define

$$E_{ji}(z,t) = \frac{1}{2}\left(E_{ji}(z,t)^{(+)} + E_{ji}(z,t)^{(-)}\right) \tag{4.35}$$

$$P_{L_{ji}}(z,t) = \frac{1}{2}\left(P_{L_{ji}}(z,t)^{(+)} + P_{L_{ji}}(z,t)^{(-)}\right) \tag{4.36}$$

$$P_{NL_{ji}}(z,t) = P_{NL_{ji}}(z,t)^{(+)} + P_{NL_{ji}}(z,t)^{(-)} \tag{4.37}$$

where the quantity $E^{(+)}$ ($E^{(-)}$) corresponds to the positive frequency part, proportional to $\mathrm{e}^{-i\omega t}$ (negative frequency part, proportional to $\mathrm{e}^{+i\omega t}$) of the expansion in eq.(4.30). The same expansion holds for P_L and P_{NL}.
We move to the frequency domain with the Fourier transform of the i-th component of the field **E** related to the frequency j. The Fourier transform of $E_{ji}(z,t)$ is

$$\begin{aligned}
\widetilde{E}_{ji}(z,\omega) &:= \int E_{ji}(z,t)\mathrm{e}^{\mathrm{i}\omega t}dt = \\
&= \frac{1}{2}\left(\int E_{ji}(z,t)^{(+)}\mathrm{e}^{\mathrm{i}\omega t}dt + \int E_{ji}(z,t)^{(-)}\mathrm{e}^{\mathrm{i}\omega t}dt\right) = \\
&= \frac{1}{2}\left(\int A_{ji}(z,t)\mathrm{e}^{-\mathrm{i}\omega_j t + \mathrm{i}k_j z}\mathrm{e}^{\mathrm{i}\omega t}dt + c.c.\right) = \\
&:= \frac{1}{2}\left(\widetilde{E}_{ji}(z,\omega-\omega_j)^{(+)} + \widetilde{E}_{ji}(z,\omega+\omega_j)^{(-)}\right)
\end{aligned} \tag{4.38}$$

Eq. (4.34) becomes, by using the convolution theorem for the linear polarization[6] and by considering only the $(+)$ part of $\widetilde{E}_{ji}(z,\omega)$ and by using the linearity property:

$$\frac{\partial^2}{\partial z^2}\widetilde{E}_{ji}^{(+)} = -\frac{\omega^2}{c^2}\widetilde{E}_{ji}^{(+)} - \frac{\omega^2}{c^2}\widetilde{\chi}(\omega)\widetilde{E}_{ji}^{(+)} + 2\mu_0\widetilde{\mathcal{F}}\left(\frac{\partial^2 P_{NL_{ji}}^{(+)}}{\partial t^2}\right) \tag{4.39}$$

Now, eq. (4.39) becomes:

$$\frac{\partial^2}{\partial z^2}\widetilde{E}_{ji}^{(+)} + \frac{\omega^2}{c^2}(1+\widetilde{\chi}(\omega))\widetilde{E}_{ji}^{(+)} = 2\mu_0\widetilde{\mathcal{F}}\left(\frac{\partial^2 P_{NL_{ji}}^{(+)}}{\partial t^2}\right) \tag{4.40}$$

By defining $\sqrt{n} = \varepsilon(\omega) = 1 + \widetilde{\chi}(\omega)$ (in the usual assumption of negligible absorption in the useful range, where $\chi(\omega)$ is real[7]) and considering the relation (4.29), previous equation simplifies as:

$$\boxed{\frac{\partial^2}{\partial z^2}\widetilde{E}_{ji}^{(+)} + k^2(\omega)\widetilde{E}_{ji}^{(+)} = 2\mu_0\widetilde{\mathcal{F}}\left(\frac{\partial^2 P_{NL_{ji}}^{(+)}}{\partial t^2}\right)} \tag{4.41}$$

with

$$\widetilde{E}_{ji}(z,\omega-\omega_j)^{(+)} = \widetilde{A}_{ji}(z,\omega-\omega_j)\mathrm{e}^{\mathrm{i}k_j z} \tag{4.42}$$

[6] $\widetilde{P}_{L_{ji}} = \widetilde{\chi}(\omega)\widetilde{E}_{ji}(z,\omega-\omega_j)$, where $\widetilde{\chi}(\omega)$ is the Fourier transform of the linear susceptibility

[7] From Kramers-Kronig relations, $\chi(\omega)$ is complex. The imaginary part embodies the absorption process. In nonlinear optics, however, are employed frequencies such that $\Im(\chi(\omega))$ becomes negligible, and therefore $\chi(\omega)$ can be assumed to be real ($\chi(\omega) \approx \Re(\chi(\omega))$).

In this equation, $\widetilde{A}_{ji}(z,\omega-\omega_j)$ varies much slower along z than the carrier. This allows us to make use of the *Slowly Varying Envelope Approximation* (SVEA) as follows:

$$\begin{aligned}
\frac{\partial}{\partial z}\left(\frac{\partial}{\partial z}\widetilde{E}^{(+)}_{ji}\right) &= \frac{\partial}{\partial z}\left[\frac{\partial}{\partial z}\left(\widetilde{A}_{ji}(z,\omega-\omega_j)\mathrm{e}^{\mathrm{i}k_j z}\right)\right] \\
&= \frac{\partial}{\partial z}\left(\frac{\partial}{\partial z}\widetilde{A}_{ji}(z,\omega-\omega_j)\mathrm{e}^{\mathrm{i}k_j z} + \widetilde{A}_{ji}(z,\omega-\omega_j)\mathrm{i}k_j\mathrm{e}^{\mathrm{i}k_j z}\right) = \\
&= \frac{\partial^2}{\partial z^2}\widetilde{A}_{ji}(z,\omega-\omega_j)\mathrm{e}^{\mathrm{i}k_j z} + \frac{\partial}{\partial z}\widetilde{A}_{ji}(z,\omega-\omega_j)\mathrm{i}k_j\mathrm{e}^{\mathrm{i}k_j z} + \\
&\quad + \frac{\partial}{\partial z}\widetilde{A}_{ji}(z,\omega-\omega_j)\mathrm{i}k_j\mathrm{e}^{\mathrm{i}k_j z} + \widetilde{A}_{ji}(z,\omega-\omega_j)\cdot(-k_j^2)\mathrm{e}^{\mathrm{i}k_j z} = \\
&= 2\mathrm{i}k_j\frac{\partial}{\partial z}\widetilde{A}_{ji}(z,\omega-\omega_j)\mathrm{e}^{\mathrm{i}k_j z} - k_j^2\widetilde{A}_{ji}(z,\omega-\omega_j)\mathrm{e}^{\mathrm{i}k_j z} \qquad (4.43)
\end{aligned}$$

where we neglected $\dfrac{\partial^2}{\partial z^2}\widetilde{A}_{ji}(z,\omega-\omega_j)$ because of the SVEA.
We can now substitute the result (4.43) in eq. (4.41) and obtain

$$\boxed{2\mathrm{i}k_j\frac{\partial}{\partial z}\widetilde{A}_{ji}(z,\omega-\omega_j)\mathrm{e}^{\mathrm{i}k_j z} + \left(k^2(\omega)-k_j^2\right)\widetilde{A}_{ji}(z,\omega-\omega_j)\mathrm{e}^{\mathrm{i}k_j z} = 2\mu_0\widetilde{\mathcal{F}}\left(\frac{\partial^2 P^{(+)}_{NL_{ji}}}{\partial t^2}\right)} \qquad (4.44)$$

If we expand $k(\omega)$ in Taylor series and keep only the linear terms we obtain:

$$k(\omega) = k(\omega_j) + \left.\frac{\partial k}{\partial\omega}\right|_j(\omega-\omega_j) + \ldots \approx k_j + \frac{1}{v_{g_j}}(\omega-\omega_j) \qquad (4.45)$$

In this way, the coefficient $\left(k^2(\omega)-k_j^2\right)$ becomes:

$$\begin{aligned}
\left(k^2(\omega)-k_j^2\right) &= \left(k(\omega)+k_j\right)\left(k(\omega)-k_j\right) = \\
&= \left(2k_j + \frac{1}{v_{g_j}}(\omega-\omega_j)\right)\left(\frac{1}{v_{g_j}}(\omega-\omega_j)\right) = \qquad (4.46) \\
&= \frac{2k_j}{v_{g_j}}(\omega-\omega_j) + \frac{1}{v_{g_j}^2}(\omega-\omega_j)^2 \qquad (4.47)
\end{aligned}$$

and we can neglect the second order term of the result[8]. We can continue from eq. 4.44 using the latter result:

$$2\mathrm{i}k_j\frac{\partial}{\partial z}\widetilde{A}_{ji}(z,\omega-\omega_j)\mathrm{e}^{\mathrm{i}k_j z} + \frac{2k_j}{v_{g_j}}(\omega-\omega_j)\widetilde{A}_{ji}(z,\omega-\omega_j)\mathrm{e}^{\mathrm{i}k_j z} = 2\mu_0\widetilde{\mathcal{F}}\left(\frac{\partial^2 P^{(+)}_{NL_{ji}}}{\partial t^2}\right)$$

$$\Downarrow$$

$$\boxed{\frac{\partial}{\partial z}\widetilde{A}_{ji}(z,\omega-\omega_j)\mathrm{e}^{\mathrm{i}k_j z} - \frac{\mathrm{i}}{v_{g_j}}(\omega-\omega_j)\widetilde{A}_{ji}(z,\omega-\omega_j)\mathrm{e}^{\mathrm{i}k_j z} = -\frac{\mathrm{i}\mu_0}{k_j}\widetilde{\mathcal{F}}\left(\frac{\partial^2 P^{(+)}_{NL_{ji}}}{\partial t^2}\right)} \qquad (4.48)$$

[8]More rigorously speaking, by keeping second-order terms in eq. (4.45), the second-order term in eq.(4.47) is almost compensated and only the first-order term survives.

For the latest steps towards the formulation we need, we go back to the time domain

$$\boxed{\left(\frac{\partial}{\partial z}A_{ji}(z,t)\right)\mathrm{e}^{-\mathrm{i}\omega_j t+\mathrm{i}k_j z}+\frac{1}{v_{g_j}}\left(\frac{\partial}{\partial t}A_{ji}(z,t)\right)\mathrm{e}^{-\mathrm{i}\omega_j t+\mathrm{i}k_j z}=-\frac{\mathrm{i}\mu_0}{k_j}\frac{\partial^2 P^{(+)}_{NL_{ji}}}{\partial t^2}} \tag{4.49}$$

$$\begin{aligned}\left(\frac{\partial}{\partial z}A_{1i}(z,t)\right)\mathrm{e}^{-\mathrm{i}\omega_1 t+\mathrm{i}k_1 z}+\frac{1}{v_{g_1}}\left(\frac{\partial}{\partial t}A_{1i}(z,t)\right)\mathrm{e}^{-\mathrm{i}\omega_1 t+\mathrm{i}k_1 z}=\\ =-\frac{\mathrm{i}\mu_0}{k_1}\frac{\partial^2}{\partial t^2}\left(d_{ilm}A_{3l}(z,t)A^*_{2m}(z,t)\mathrm{e}^{-\mathrm{i}(\omega_3-\omega_2)t+\mathrm{i}(k_3-k_2)z}\right)\\ =\frac{\mathrm{i}\mu_0}{k_1}d_{ilm}A_{3l}(z,t)A^*_{2m}(z,t)\left[(\omega_3-\omega_2)^2\mathrm{e}^{-\mathrm{i}(\omega_3-\omega_2)t+\mathrm{i}(k_3-k_2)z}\right]\end{aligned} \tag{4.50}$$

where, for the SVEA, we considered not zero only the time derivative of the fast varying part. We can now divide by $\mathrm{e}^{-\mathrm{i}\omega_1 t+\mathrm{i}k_1 z}$ and use the energy conservation law (4.28):

$$\boxed{\frac{\partial}{\partial z}A_{1i}(z,t)+\frac{1}{v_{g_1}}\frac{\partial}{\partial t}A_{1i}(z,t)=\frac{\mathrm{i}\mu_0\omega_1^2}{k_1}d_{ilm}A_{3l}(z,t)A^*_{2m}(z,t)\mathrm{e}^{\mathrm{i}(k_3-k_2-k_1)z}} \tag{4.51}$$

We define, for each frequency j, the coefficient

$$\gamma_j := \frac{\mu_0\omega_j^2}{k_j} \tag{4.52}$$

and also the *phase matching* term

$$\Delta k := k_3 - k_2 - k_1 \tag{4.53}$$

The procedure can obviously be repeated for all the relevant fields and we can finally write the following three equations for the electromagnetic formulation of nonlinear interactions:

$$\frac{\partial}{\partial z}A_{1i}(z,t)+\frac{1}{v_{g_1}}\frac{\partial}{\partial t}A_{1i}(z,t)=\mathrm{i}\gamma_1 d_{ilm}A_{3l}(z,t)A^*_{2m}(z,t)\mathrm{e}^{\mathrm{i}\Delta kz} \tag{4.54}$$

$$\frac{\partial}{\partial z}A_{2i}(z,t)+\frac{1}{v_{g_2}}\frac{\partial}{\partial t}A_{2i}(z,t)=\mathrm{i}\gamma_2 d_{ilm}A_{3l}(z,t)A^*_{1m}(z,t)\mathrm{e}^{\mathrm{i}\Delta kz} \tag{4.55}$$

$$\frac{\partial}{\partial z}A_{3i}(z,t)+\frac{1}{v_{g_3}}\frac{\partial}{\partial t}A_{3i}(z,t)=\mathrm{i}\gamma_3 d_{ilm}A_{1l}(z,t)A_{2m}(z,t)\mathrm{e}^{-\mathrm{i}\Delta kz} \tag{4.56}$$

A part of the presented calculations can also be performed in the time domain instead of the spectral domain, leading to the same results.
These nonlinear interaction equations (4.54), (4.55) and (4.56) will be used to describe different nonlinear process: *Second Harmonic Generation* (SHG) in 4.4, *Optical Parametric Generation* (OPG) in 4.5, that is part of the more general process of *Optical Parametric Amplification* (OPA), and *Sum Frequency Generation* (SFG) in 4.6.

4.4 Second harmonic generation and the phase-matching condition

In second-harmonic generation, a pump wave with a frequency ω generates a signal at the frequency 2ω as it propagates through a medium characterized by a quadratic nonlinearity. With a conversion efficiency of $\sim 10^{-8}$, the first second harmonic generation experiment was performed by Franken, Hill, Peters and Weinreich [95] in 1961. The utilization of more efficient materials, higher intensity lasers and phase matching techniques has resulted, in the last years, in conversion efficiencies approaching unity.
The first step will be to explain in the specific frame of second harmonic generation the meaning of the "phase matching" condition[9] $\Delta k = 0$ and how one can achieve it. Results, then, can easily be applied to all other kinds of frequency generation.
After this, the second harmonic generation phenomenon will be investigated through the use of equations (4.54)-(4.56).

4.4.1 Phase matching (PM)

A pulse of frequency ω propagating inside a suitable nonlinear crystal leads the polarization to oscillate at frequency 2ω. In order to generate a high energy second harmonic pulse, all the irradiated 2ω fields coming from different points of the crystal have to sum in a constructive way. This means that, in order to obtain a continuous energy exchange between first and second harmonic, they need to "travel together", or, in more specific words, they need to have the same phase velocity: this is the reason why we use the words *phase matching* for the condition $\Delta k = 0$.
To achieve this condition, the two refractive indexes must be the same. But the refractive index decreases with the wavelength and having the same refractive index for two different wavelengths is impossible in an isotropic crystal[10]. However, one can obtain the phase-matching condition with one of the following techniques:

1. *noncritical phase-matching*, with birefringent crystals (depending on the temperature)
2. *critical phase-matching* , with birefringent crystals (depending on the beam orientation)
3. *quasi-phase-matching* (**QPM**), with *periodically-poled* crystals

In noncritical and critical phase-matching, first and second harmonic must travel through the crystal with different polarization directions. This could allow to find a geometrical configuration of the birefringent crystal for which, at a given temperature, the phase-matching condition can be fulfilled. It is worth noting that, as different polarizations are needed, the birefringent crystal must allow a second harmonic oscillation along a polarization axis that differs from the forcer's one.

Noncritical phase-matching

We take as an example the *lithium niobate* crystal. It is a nonlinear and birefringent crystal. It is uniaxial, meaning that it has three reference axes x, y and z where two of them have a refractive index named n_o (ordinary refractive index), while the third one has a different refractive index named n_e (extraordinary refractive index). When, for example, taking

[9] Generally speaking, we say to be in a *phase matching* condition when the phase matching term defined in (4.53) is null. In this case $k_3 = k_1 + k_2$

[10] Isotropic means that it has the same refractive index in every direction

z as as the propagation direction, the first harmonic's polarization lies on the x axis (the ordinary axis) and the second harmonic's one lies on the y axis (the extraordinary axis), it is possible to find a temperature where $n_o(\omega) = n_e(2\omega)$. Note that, being the polarization

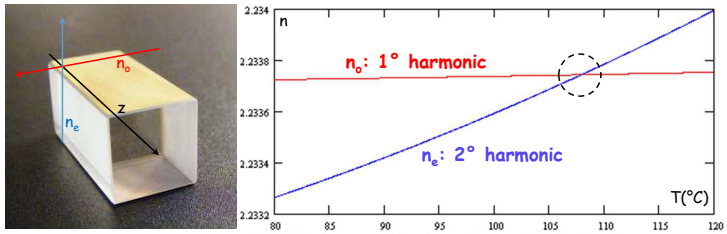

Figure 4.5: Lithium niobate crystal: ordinary and extraordinary axes drawn on the crystal on the left, with the beam direction z. On the right, ordinary and extraordinary refractive indexes as a function of the temperature. The intersection gives the phase-matching condition.

directions coincident with the crystal axes, no walk-off [11] occurs. In these case we say that a beam is *ordinary*.

Critical phase-matching

We take as an example the *barium borate* crystal (β-BBO). It is again a uniaxial nonlinear birefringent crystal. At room temperature no noncritical phase-matching occurs. However, we can obtain the phase-matching condition in a different way, by using the first harmonic as an *ordinary beam* and the second harmonic as an *extraordinary beam*. This means that the second harmonic polarization direction has two components: one of them lies on the y axis of the crystal (ordinary axis with n_o), and the other one on the z axis (ex-

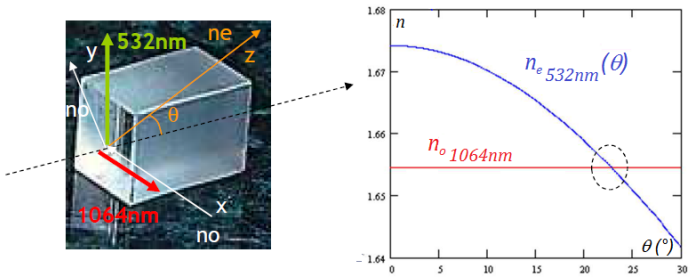

Figure 4.6: An example of second harmonic generation (532 nm from 1064 nm). On the left a Barium borate crystal: ordinary and extraordinary crystal axes and beam polarizations are drawn, with the beam direction z. On the right, ordinary and extraordinary refractive indexes as a function of the angle θ between the propagation direction and the z axis. The intersection abscissa is called "phase-matching angle".

traordinary axis with n_e), that in this case is not coincident with the beam propagation direction. Therefore we call the second harmonic an *extraordinary beam* and the refractive index depends on the θ angle between the propagation direction and the z axis (see Fig.

[11] The phenomenon that the intensity distribution of a beam in an anisotropic crystal drifts away from the direction of the wave vector (for more details see Appendix B.2)

4.6) under the relation:

$$\frac{1}{n_{2\omega}^2(\theta)} = \frac{\sin(\theta)^2}{n_{e,2\omega}^2} + \frac{\cos(\theta)^2}{n_{o,2\omega}^2} \tag{4.57}$$

In this configuration the phase-matching condition is fulfilled by tuning the θ angle.
As first and second harmonic tend to get separated while propagating through the crystal, walk-off occurs.

Quasi phase-matching

In both previous cases, in order to fulfil the phase-matching condition, we need the crystal to generate a beam with a polarization different from the forcer field's one. In many cases, mostly when high second harmonic conversion efficiencies are required, one would like to exploit large elements of the nonlinear tensor.

Intuitively, the forcer induces a stronger displacement along its own direction. Thus, it could happen that a crystal has a huge tensor element related to the generation, for example, of a second harmonic with the same polarization as the forcer's one. In this case, neither a noncritical nor a critical phase-matching can be achieved. In fact, the second harmonic intensity oscillates because the phase matching factor $e^{i\Delta kz}$ induces alternate sign changes in the P_{NL}, and the process passes from gain to absorption and viceversa.
How can we circumvent this problem and generate anyway a second harmonic beam?

The first step will be to explain with more details the phase velocity issue. I recall here the formula for the nonlinear polarization in a schematic form for the second harmonic generation (now ω and 2ω have the same polarization):

$$P_{NL_i} = 2d_{ijj}E_jE_j \tag{4.58}$$

were **d** is the nonlinear tensor and **E** the electric field. When **d** changes sign (i.e. the crystal axis z is inverted), the polarization phase shifts by π. This implies that, even though no phase-matching condition can be achieved, one can avoid the gain-absorption alternance in the the second harmonic generation process by inverting the z axis of the crystal "in time".
In order to describe this technique, we first make a simple example. Suppose we have two harmonic nonlinear oscillators at a distance h, invested from the first harmonic beam in sequence: Both oscillators generate the frequency 2ω, but, in order to know the total

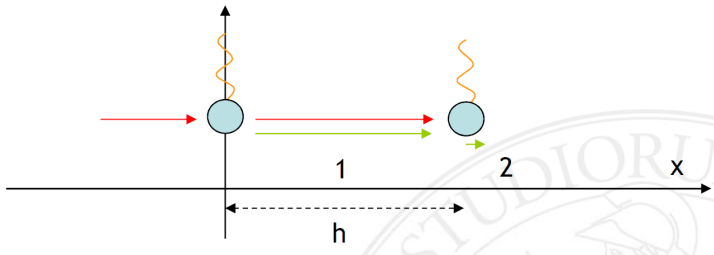

Figure 4.7: Two nonlinear oscillators generating a second harmonic beam.

second harmonic field generated by the system, we must take into account several terms: the field generated by the first oscillator until position h and, concerning the second

oscillator, we need to consider the forcer propagation until h and the fact that the second harmonic goes as the square of the first harmonic (from (4.58) and better described in the next subsection). Thus in h we have:

$$E_{2\omega} \propto e^{ik_2 h} + e^{i2k_1 h} = e^{ik_2 h}(1 + e^{i\Delta k \cdot h}) \tag{4.59}$$

When h is such that $\Delta k \cdot h = \pi$, the total generated field is zero.
But if we invert the second oscillator axis, we obtain a constructive action:

$$E_{2\omega} \propto e^{ik_2 h} - e^{i2k_1 h} = e^{ik_2 h}(1 - e^{i\Delta k \cdot h}) = 2e^{ik_2 h} \tag{4.60}$$

If instead of two oscillators we have a continuum (like a crystal), then we need to take into account second harmonic fields generated in each point between 0 and h. In this case, h is no more the zero field position, but it is the point where the total second harmonic field starts to decrease. Again, if we invert the oscillators (z axis of the crystal) after a step h, the second harmonic keeps growing.
This is the **Quasi Phase-Matching** (QPM) technique that requires the use of the so called "periodically poled" crystals (a sketch in Fig. 4.8). In the figure, Δ is named the *period* of

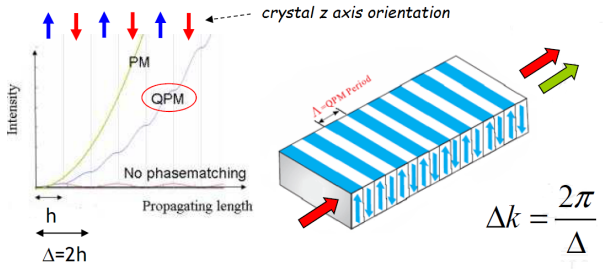

Figure 4.8: The plot shows three intensity functions for the field generated in three different cases: perfect phase-matching in the bulk crystal(PM), QPM in a periodically poled crystal, no PM in a bulk crystal.

the crystal. The inversion of the z axis is achieved in the constructive phase by applying a strong electric field with opposite orientation in each section of the crystal (two adjacent sections being a period).
A real example of periodically poled crystal will be done in the next chapter, as in AEgIS periodically poled crystals are used to generate some frequencies from vacuum.

The condition

$$\Delta k = \frac{2\pi}{\Delta} \tag{4.61}$$

is the QPM rule (and $\frac{2\pi}{\Delta}$ is called the QPM term), meaning that, while in bulk crystal the PM condition is $\Delta k = 0$, in periodically poled crystals (of length l) the best achievable PM factor is not equal to 1 but equal to $e^{i\frac{2\pi}{\Delta}l}$. In subsection 4.5 we will obtain the same result via more detailed calculations.

4.4.2 Second harmonic generation equations

The aim of this subsection is to adapt equations (4.54), (4.55) and (4.56) to the SHG process. We have a three-frequency interaction where two of the frequencies are equal

($\omega_1 = \omega_2$) and $\omega_3 := 2\omega_1$. We therefore need only two equations. This interaction can be described by the coupled differential equations:

$$\frac{\partial}{\partial z}A_1 + \frac{1}{v_{g_1}}\frac{\partial}{\partial t}A_1 = \mathrm{i}\gamma_1 A_3 A_1^* \mathrm{e}^{\mathrm{i}\Delta k z} \tag{4.62}$$

$$\frac{\partial}{\partial z}A_3 + \frac{1}{v_{g_3}}\frac{\partial}{\partial t}A_3 = \mathrm{i}\gamma_3 A_1^2 \mathrm{e}^{-\mathrm{i}\Delta k z} \tag{4.63}$$

where, now, the phase mismatch is $\Delta k = k_3 - 2k_1$.
One of the most common approximations [96] in order to analytically solve equations (4.62) and (4.63) is to assume that the pump is not depleted during the conversion process. As we can see from fig. 4.9, the undepleted pump approximation is not far from the exact behaviour until quite high up-conversion efficiencies ($50 - 60\%$). In fact, the efficiency in real cases saturates, while the undepleted pump curve ideally can reach unlimited high values. In this scenario, we neglect the right hand side in (4.62) so that the

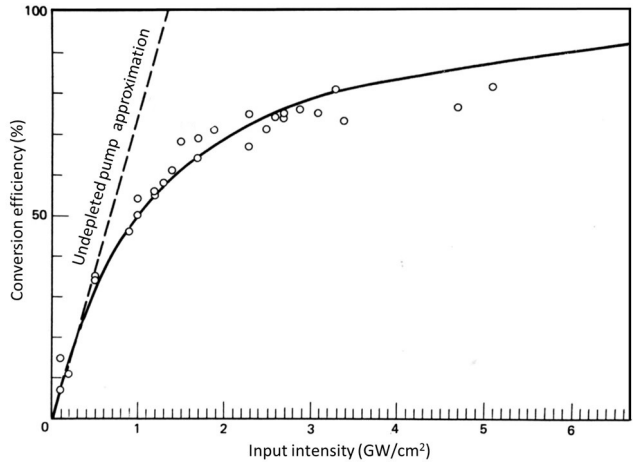

Figure 4.9: Study of the up-conversion efficiency of a KDP crystal in SHG depending on the pump intensity [94, 97].

slowly varying part of the input pulse A_1 propagates along the crystal keeping all the initial energy. We have therefore

$$\frac{\partial}{\partial z}A_1 + \frac{1}{v_{g_1}}\frac{\partial}{\partial t}A_1 = 0 \tag{4.62*}$$

and the solution will be of the type:

$$A_1(z,t) = A_1(0, t - z/v_{g_1}) \tag{4.64}$$

We can then write eq. (4.63) as follows:

$$\frac{\partial}{\partial z}A_3 + \frac{1}{v_{g_3}}\frac{\partial}{\partial t}A_3 = \mathrm{i}\gamma_3 A_1(0, t - z/v_{g_1})^2 \mathrm{e}^{-\mathrm{i}\Delta k z} \tag{4.63*}$$

A more useful equation is obtained by changing the time frame of reference by $t' = t - z/v_{g_3}$. This implies the following relations:

$$\begin{aligned} z &= z' \\ t &= t' + z/v_{g_3} \\ \frac{\partial}{\partial z} &= \frac{\partial}{\partial z'} - \frac{1}{v_{g_3}}\frac{\partial}{\partial t'} \\ \frac{\partial}{\partial t} &= \frac{\partial}{\partial t'} \end{aligned} \tag{4.65}$$

Substituting them in eq. (4.63) we have:

$$\frac{\partial}{\partial z'}A_3 - \frac{1}{v_{g_3}}\frac{\partial}{\partial t'}A_3 + \frac{1}{v_{g_3}}\frac{\partial}{\partial t'}A_3 = \mathrm{i}\gamma_3 \left[A_1(0, t' + z'/v_{g_3} - z'/v_{g_1})\right]^2 \mathrm{e}^{-\mathrm{i}\Delta k z} \tag{4.66}$$

thus obtaining

$$\frac{\partial}{\partial z}A_3 = \mathrm{i}\gamma_3 \left[A_1(0, t + \beta z)\right]^2 \mathrm{e}^{-\mathrm{i}\Delta k z} \tag{4.67}$$

where $\beta = 1/v_{g_3} - 1/v_{g_1}$ and we removed the primed designation on variables z' and t' for a simpler readability. β represents the *group velocity mismatch parameter*. When the delay between the components along the crystal is lower than the time coherence, we can approximate $\beta \approx 0$. In this simple case, the solution at the exit of the crystal is well known and is:

$$A_3(L, t) = \mathrm{i}\gamma_3 \left(\frac{\mathrm{e}^{-i\Delta k L} - 1}{-i\Delta k}\right) A_1^2(0, t), \tag{4.68}$$

asserting that $A_3(t) \propto A_1(t)^2$ and the maximum output intensity is obtained in the phase matching condition $\Delta k = 0$.
When $\beta \neq 0$, we can work into the spectral domain in order to find a more general solution. By assuming to be in phase matching condition for all the spectral components of $\widetilde{A}_3(z, \omega)$, we may perform the transformation of eq. (4.67) into the frequency domain obtaining:

$$\frac{\partial}{\partial z}\widetilde{A}_3 = \mathrm{i}\gamma_3 \mathrm{e}^{-\mathrm{i}\beta z\omega}\widetilde{A}_1(\omega) \otimes \widetilde{A}_1(\omega) \tag{4.69}$$

Where $\mathrm{e}^{-\mathrm{i}\beta z\omega}\widetilde{A}_1(\omega) = \mathcal{F}(A_1(0, t - z/v_{g_1}))$ for the Fourier transform properties, and the symbol $\otimes$ represents the convolution operator. Solving eq. (4.69) with zero initial conditions, we obtain

$$\widetilde{A}_3(z, \omega) = \mathrm{i}\gamma_3 \left(\frac{\mathrm{e}^{-\mathrm{i}\beta z\omega} - 1}{-\mathrm{i}\beta z\omega}\right) \widetilde{A}_1(\omega) \otimes \widetilde{A}_1(\omega) \tag{4.70}$$

This equation says that the resulting pulse of a SHG process has a spectrum that is given by the convolution of the input pulse with itself. As a consequence, the spectrum results wider than the input pulses' one. But the solution has also a modulation coefficient, of the type $\mathrm{sinc}^2(x)$ with $x = \beta z\omega/2$, that defines how the frequency bandwidth of the resulting pulse depends on the crystal length L. It can be readily noted how the spectrum shrinks with the crystal length.

Second harmonic of a comb-shaped spectrum light

It is worth dedicating few words about what happens when our input pulse spectrum is comb-shaped. A Labview simulation of this effect is shown in Fig. 4.10.

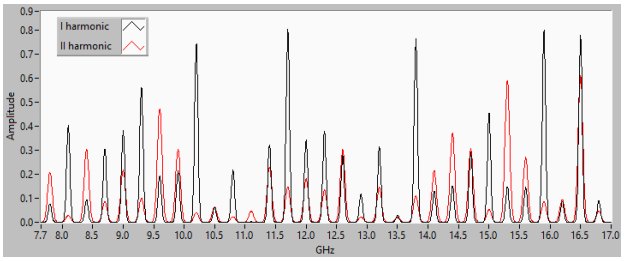

Figure 4.10: An example of peak broadening of a comb-shaped spectrum second harmonic

When we deal with a comb-shaped spectrum, like the one of the AEgIS laser pump (see next chapter), the up converted pulse spectrum will keep the comb-shaped structure. In fact, the peak distance will still be equal to the FSR of the pump laser cavity[12], while the convolution operator will broaden the individual peaks as well as the spectral envelope profile of the pulse.

4.5 Optical Parametric Generation and Amplification

Before dealing with the parametric down conversion process, as already mentioned at the beginning of subsection 4.4.2, it is helpful to see more in detail what happens when up-conversion occurs in periodically poled crystals. In this case, we consider a process of sum frequency generation: to a certain extent, the process of *Sum Frequency Generation* (SFG) is opposite to the down conversion process. In SFG, two laser fields with frequencies ω_1 and ω_2 generate a nonlinear signal at the frequency $\omega_3 = \omega_1 + \omega_2$.

4.5.1 Sum frequency in periodically poled crystals

Here we are going to use equations (4.54) - (4.56) specialized to the case of periodically poled crystals by letting γ_3 depend on the propagation axis z, in order to find the QPM term (eq. (4.61)). Moreover, we look for an effective constant coefficient that can substitute the spatially modulated $\gamma_3(z)$ coefficient.

We assume to be in an undepleted regime, that means that A_1 and A_2 keep their energy along the crystal. Therefore, (4.54) and (4.55) are ineffective and we can get rid of them in this treatment. Only eq. (4.56) is left over, that, in case of periodically poled crystals, appears like:

$$\frac{\partial}{\partial z} A_3(z) = \mathrm{i}\gamma_3(z) A_1 A_2 \mathrm{e}^{-\mathrm{i}\Delta k z} \tag{4.71}$$

where, in order to simplify calculations in this auxiliary paragraph, we neglected the time derivative of the field (I will come back to this point in the following). In eq. (4.71), all the amplitudes are along the z axis, the laboratory axes coincide with the crystal ones and we use the d_{zzz} element of the electrical susceptibility tensor of the crystal, that now is embedded in $\gamma_3(z)$. The dependence on z of γ_3 comes from the fact that d_{zzz} changes

[12] There are cases in which the peak distance is a submultiple of the FSR when several pulses travel simultaneously inside the cavity (i.e. combs in fibers), but this is not our case.

sign in each domain. But we would like to write eq. (4.71) as if we had a bulk crystal and a simple PM condition, i.e.

$$\frac{\partial}{\partial z}A_3(z) = \mathrm{i}\widetilde{\gamma}_3 A_1 A_2. \tag{4.72}$$

Let's start with the definition of $\gamma_3(z) := \gamma_3 f_\Delta(z)$ as a square function (fig. 4.11) with

$$f_\Delta(z) := \begin{cases} -1 & -\dfrac{\Delta}{2} \le z < 0 \\ \\ 1 & 0 \le z \le \dfrac{\Delta}{2} \end{cases} \tag{4.73}$$

for each period Δ of the crystal. Thus, from eq. (4.71), we have

$$A_3(L) = \mathrm{i}\gamma_3 A_1 A_2 \int_0^L f_\Delta(z)\mathrm{e}^{-\mathrm{i}\Delta k z}dz \tag{4.74}$$

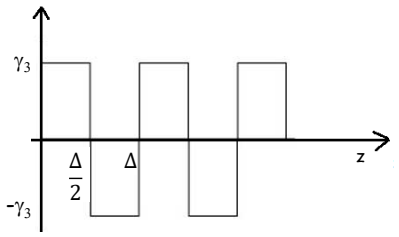

Figure 4.11: The $\gamma_3(z)$square function.

and the aim is to maximize the integral with a suitable Δk value.
To begin with, we approximate $f_\Delta(z)$ with the first term of its Fourier expansion:

$$f_\Delta(z) \approx \frac{4}{\pi}\sin\left(\frac{2\pi}{\Delta}z\right) \tag{4.75}$$

thus obtaining

$$\begin{aligned} A_3(L) &\approx \mathrm{i}\gamma_3 A_1 A_2 \frac{4}{\pi}\int_0^L \sin\left(\frac{2\pi}{\Delta}z\right)\mathrm{e}^{-\mathrm{i}\Delta k z}dz = \\ &= \mathrm{i}\gamma_3 A_1 A_2 \frac{4}{\pi}\int_0^L \left(\frac{\mathrm{e}^{\mathrm{i}\frac{2\pi}{\Delta}z} - \mathrm{e}^{-\mathrm{i}\frac{2\pi}{\Delta}z}}{2\mathrm{i}}\right)\mathrm{e}^{-\mathrm{i}\Delta k z}dz = \\ &= \gamma_3 A_1 A_2 \frac{2}{\pi}\left[\frac{1}{\mathrm{i}\left(\frac{2\pi}{\Delta}-\Delta k\right)}\left(\mathrm{e}^{\mathrm{i}\left(\frac{2\pi}{\Delta}-\Delta k\right)L}-1\right) + \frac{1}{\mathrm{i}\left(\frac{2\pi}{\Delta}+\Delta k\right)}\left(\mathrm{e}^{-\mathrm{i}\left(\frac{2\pi}{\Delta}+\Delta k\right)L}-1\right)\right] = \\ &= \gamma_3 A_1 A_2 \frac{2}{\pi}L\left\{\mathrm{sinc}\left[\left(\frac{2\pi}{\Delta}-\Delta k\right)L\right]\mathrm{e}^{-\mathrm{i}\left(\frac{2\pi}{\Delta}-\Delta k\right)L}\right. \\ &\qquad \left. -\mathrm{sinc}\left[-\left(\frac{2\pi}{\Delta}+\Delta k\right)L\right]\mathrm{e}^{\mathrm{i}\left(\frac{2\pi}{\Delta}+\Delta k\right)L}\right\} \end{aligned} \tag{4.76}$$

We immediately note that, by letting $\Delta k = \frac{2\pi}{\Delta}$, the minuend inside the braces is maximum and equal to 1, while the subtrahend contains

$$\mathrm{sinc}\left(-\frac{4\pi}{\Delta}L\right) = 0$$

because $L/\Delta \in \mathbb{N}$. This is the same QPM condition stated in eq. (4.61), that leads to

$$A_3(L) \approx \gamma_3 A_1 A_2 \frac{2}{\pi}L \tag{4.77}$$

Therefore we can set

$$\widetilde{\gamma}_3 = \gamma_3 \frac{2}{\pi} \tag{4.78}$$

and make calculation as if we were in PM with a bulk crystal.

This information is really useful while dealing with a down conversion process.

4.5.2 Down conversion in periodically poled crystals

A *down conversion* process occurs when in nonlinear crystals a photon is split into two photons, in accordance with the laws of conservation of energy and momentum. As far as the energy is concerned, in our notation we have the so-called *pump*, of frequency ω_3, split into two photons, called *signal* and *idler*, with frequencies ω_1 and ω_2 respectively, such that $\omega_1 + \omega_2 = \omega_3$. This process is stimulated by quantum vacuum fluctuations, giving an initial seed for signal and idler, necessary for producing two beams of down-converted photons. In fact, when we adapt equations (4.54)-(4.56) to this process, by considering an undepleted pump and a periodically poled crystal, we have:

$$\frac{\partial}{\partial z}A_1(z,t) + \frac{1}{v_{g_1}}\frac{\partial}{\partial t}A_1(z,t) = \mathrm{i}\gamma_1(z)A_3(z,t)A_2^*(z,t)\mathrm{e}^{\mathrm{i}\Delta kz} \tag{4.79}$$

$$\frac{\partial}{\partial z}A_2(z,t) + \frac{1}{v_{g_2}}\frac{\partial}{\partial t}A_2(z,t) = \mathrm{i}\gamma_2(z)A_3(z,t)A_1^*(z,t)\mathrm{e}^{\mathrm{i}\Delta kz} \tag{4.80}$$

The equation are coupled, meaning that an analytical solution is hard to achieve (if not impossible). In the next chapter, results of a numerical simulation (with the SNLO[13] program) on equations (4.79) and (4.80) will be shown, related to the AEgIS case in order to have global informations about the generated spectrum. Here, instead, the aim is to understand qualitatively the internal structure of the generated spectrum. We can consider a regime where the delay due to the velocity mismatching between the three frequencies is lower than the coherence time, that is practically equivalent to a quasi-stationary situation, and therefore it is possible to neglect the term with the time derivative. We obtain

$$\frac{\partial}{\partial z}A_1(z) = \mathrm{i}\gamma_1(z)A_3A_2^*(z)\mathrm{e}^{\mathrm{i}\Delta kz} \tag{4.81}$$

$$\frac{\partial}{\partial z}A_2(z) = \mathrm{i}\gamma_2(z)A_3A_1^*(z)\mathrm{e}^{\mathrm{i}\Delta kz} \tag{4.82}$$

When we are in QPM we know that we can write:

$$\frac{\partial}{\partial z}A_1(z) = \mathrm{i}\widetilde{\gamma}_1A_3A_2^*(z) \tag{4.83}$$

$$\frac{\partial}{\partial z}A_2(z) = \mathrm{i}\widetilde{\gamma}_2A_3A_1^*(z) \tag{4.84}$$

which is equivalent to an equation for A_1 to solve

$$\frac{\partial^2}{\partial z^2}A_1(z) = \widetilde{\gamma}_1\widetilde{\gamma}_2|A_3|^2A_1 \tag{4.85}$$

The general solution of this differential equation is:

$$A_1(z) = a\mathrm{e}^{\lambda z} + b\mathrm{e}^{-\lambda z}, \qquad \text{with} \quad \lambda := \sqrt{\widetilde{\gamma}_1\widetilde{\gamma}_2|A_3|^2} \tag{4.86}$$

We assume the following initial conditions:

$$\begin{cases} A_1(0) = A_{1_{\mathrm{in}}} \\ \left.\dfrac{\partial A}{\partial z}\right|_0 = \mathrm{i}\widetilde{\gamma}_1A_3(0)A_2^*(0) = \mathrm{i}\widetilde{\gamma}_1A_{3_{\mathrm{in}}}A_{2_{\mathrm{in}}}^* \end{cases} \tag{4.87}$$

[13] http://www.as-photonics.com/snlo

where $A_{i_{\text{in}}}$ are the amplitudes related to the frequency ω_i entering the crystal.
The special solution for this Cauchy problem is given by

$$A_1(z,t) = A_{1_{\text{in}}}(t)\cosh\left(\sqrt{\widetilde{\gamma}_1\widetilde{\gamma}_2|A_3(t)|^2}z\right) + \mathrm{i}\sqrt{\frac{\widetilde{\gamma}_1}{\widetilde{\gamma}_2}}\mathrm{e}^{\mathrm{i}\phi_3(t)}A^*_{2_{\text{in}}}(t)\sinh\left(\sqrt{\widetilde{\gamma}_1\widetilde{\gamma}_2|A_3(t)|^2}z\right) \tag{4.88}$$

where we showed again the time dependence of each term and we considered

$$A_3(t) = |A_3(t)|\,\mathrm{e}^{\mathrm{i}\phi_3(t)}. \tag{4.89}$$

Depending on the initial conditions, we distinguish two different, although similar, processes: the *Optical Parametric Generation*, that occurs when nothing but the pump beam enters the crystal (in this case $A_{1_{\text{in}}}$ and $A_{2_{\text{in}}}$ denotes instantaneous quantum fluctuating amplitudes), and the *Optical Parametric Amplification*, that occurs when a "seed" of signal and/or idler enters the crystal together with the pump. This is a crucial element in analysing the generated spectra.

4.5.3 Spectral analysis of a down converted light

In order to look at the internal structure of the generated spectrum in a down conversion process, we go into the spectral domain via the Fourier transform of $A_1(t)$ as follows:

$$\begin{aligned}\widetilde{A}_1(z,\omega) = \widetilde{A}_{1_{\text{in}}}(\omega) \otimes \mathcal{F}\left(\cosh\left(\sqrt{\widetilde{\gamma}_1\widetilde{\gamma}_2|A_3(t)|^2}z\right)\right) + \\ +\mathrm{i}\sqrt{\frac{\widetilde{\gamma}_1}{\widetilde{\gamma}_2}}\widetilde{A}^*_{2_{\text{in}}}(\omega) \otimes \mathcal{F}\left(\mathrm{e}^{\mathrm{i}\phi_3(t)}\sinh\left(\sqrt{\widetilde{\gamma}_1\widetilde{\gamma}_2|A_3(t)|^2}z\right)\right)\end{aligned} \tag{4.90}$$

If we consider a comb-shaped spectrum, the presence of the Fourier transform of a $\cosh$ and a $\sinh$ contributes in broadening the total spectrum width. In fact, in the time domain, these hyperbolic functions accentuate the spectrum peaks, thus reducing the total width. Therefore they don't affect the internal structure of involved spectra.

Optical Parametric Generation

When nothing but the pump beam enters the crystal, $\widetilde{A}_{i_{\text{in}}}(\omega)$ represents the complex amplitude for the vacuum state related to the frequency ω_i ($i = 1, 2$). It is worth noting that eq.(4.90) reports convolution operations between the pump and the signal/idler spectra (usually described as white noise spectra). Therefore, in presence of a comb-shaped pump like in the AEgIS laser, generating radiation from vacuum erases the peak structure of the pump (shown in the next chapter) and the output of the nonlinear process results in a spectrum that is not linked to the FSR of the laser pump cavity.

Optical Parametric Amplification

Still in case of a comb-shaped pump, when a seed of signal/idler enters the crystal, the convolution products in eq. (4.90) return a spectrum that follows the signal/idler structure: a comb-shaped spectrum will have its peaks broadened by the pump peaks and the original peak structure will be preserved. A continuum spectrum, instead, will kill the peak structure of the pump.

4.6 Sum Frequency Generation

Now, we apply equations (4.54)-(4.56) to the SFG process, assuming a nondepletion regime for the pump beams:

$$\frac{\partial}{\partial z}A_3(z,t) + \frac{1}{v_{g_3}}\frac{\partial}{\partial t}A_3(z,t) = \mathrm{i}\gamma_3 d A_1(z,t)A_2(z,t)\mathrm{e}^{-\mathrm{i}\Delta k z} \tag{4.91}$$

Here we are able to keep the time derivative of $A_3(z,t)$ in speculating about the generated spectrum [98]. Only at the end we will make again some assumption in order to obtain our information about the local structure of the generated spectrum.
Since we are in a nondepletion regime, pulses A_1 and A_2 are not appreciably modified while propagating along the crystal. They propagate with velocities v_{g_1} and v_{g_2} respectively; therefore $A_1 = A_1(0, t - \frac{z}{v_{g_1}}) = A_1(t - \frac{z}{v_{g_1}})$ and $A_2 = A_2(0, t - \frac{z}{v_{g_2}}) = A_2(t - \frac{z}{v_{g_2}})$ as in subsection 4.4.2. By substituting these expressions in eq. (4.91), applying the time transformation $t_1 = t - \frac{z}{v_{g_3}}$ and making a Fourier transform, we obtain

$$\begin{gathered}\frac{\partial}{\partial z}\widetilde{A}_3 = \mathrm{i}\gamma_3 d\left(\widetilde{A}_1\mathrm{e}^{-\mathrm{i}\beta_{31}z\omega}\right) \otimes \left(\widetilde{A}_2\mathrm{e}^{-\mathrm{i}\beta_{32}z\omega}\right)\mathrm{e}^{-i\Delta k z} \\ \text{with} \quad \beta_{ij} := \frac{1}{v_{g_i}} - \frac{1}{v_{g_j}}\end{gathered} \tag{4.92}$$

It is clear that a trivial solution for this differential equation doesn't exist because of the presence of the exponentials inside the convolution product terms. Once again, their presence is responsible of the global spectrum width generated in the process. The general equation (4.92) has been used in a `Labview` simulation whose results will be shown in the following chapter. As here we just need to know something about the internal structure, we assume to have $\beta_{31} = \beta_{32} =: \beta$ (and therefore we can neglect the A_3 time derivative term) and to be in perfect phase matching ($\Delta k = 0$). Thus we obtain

$$\frac{\partial}{\partial z}\widetilde{A}_3 = \mathrm{i}\gamma_3 d\mathrm{e}^{-\mathrm{i}\beta z\omega}\widetilde{A}_1(\omega) \otimes \widetilde{A}_2(\omega) \tag{4.93}$$

whose solution is

$$\widetilde{A}_3(\omega, z) = \mathrm{i}\gamma_3 dz\left(\frac{\mathrm{e}^{-\mathrm{i}\beta z\omega} - 1}{-\mathrm{i}\beta z\omega}\right)\widetilde{A}_1(\omega) \otimes \widetilde{A}_2(\omega) \tag{4.94}$$

We conclude by noting that, when we neglect the velocity mismatch between the three beams, the analysis of the resulting spectrum becomes immediate. We have a modulation factor (almost with the same meaning of the one in eq. (4.70)) and the convolution product between the two amplitudes, indicating that the presence of a continuous spectrum among the summed pulses makes the up-converted spectrum continuous.

CHAPTER 5

The AEgIS laser system: a spectral analysis

The AEgIS laser system has been shaped on the fundamental goal of efficiently exciting positronium atoms to Rydberg states in the general framework of a pulsed regime experiment.
The need for an efficient laser excitation of the positronium cloud having a given Doppler width leads to the requirement of a spectrum broad enough and an energy high enough to approach the saturation of the transition. Moreover, the pulsed nature of the AEgIS experiment, in addition to the above mentioned requirements, spontaneously translates itself into the use of a properly designed pulsed laser system.
In this chapter, the AEgIS laser system will be presented. Since several nonlinear crystal are used with different tasks, a spectral analysis of the output of each nonlinear process will be reported. Such analysis have been carried out via numerical approach (by using `SNLO` and `Labview` programs) to equations (4.54)-(4.56), representing the electromagnetic formulation of nonlinear interactions.

5.0.1 AEgIS laser general scheme

In subsection 1.2.4 I stated that, in order to bring positronium on a Rydberg state, we need two simultaneous beams. In this way we perform a two step excitation with a 205 nm beam for the $n = 1 \rightarrow n = 3$ transition and a $1600 \div 1700$ nm beam for the $n = 3 \rightarrow$high-n transition (reasons for choosing these strategy will be explained in the next chapter). The whole process of generation of these two wavelengths begins with a pump laser, providing a 1064 nm pulsed beam. Then, the light is split and manipulated via nonlinear processes in order to generate the desired exciting wavelengths.

In fig. 5.1 the general scheme of the AEgIS laser is depicted. Each sector has a specific goal. We have an `EKSPLA` Nd:Yag Q-switched laser[1] providing a ~ 4 ns pulse at[2] 1064 nm (10 Hz, 800 mJ). Part of the energy of this pulse is sent through a set of nonlinear crystals in order to convert it into a ~ 1680 nm pulse. The remainder of the energy of the 1064 nm pulse undergoes a second harmonic generation process that generates a 532 nm pulse. A percentage of this second harmonic pulse is again frequency doubled to obtain a 266 nm pulse. Both second and fourth harmonic are then sent through a set of nonlinear crystals to obtain the 205 nm pulse. At this point, these two exciting pulses need spatial and temporal overlapping, important to efficiently excite positronium to Rydberg states. Finally, an optical line transfers the pulse pair towards the breadbox, where positronium excitation tests can be performed. In the following, all these steps will be described in details, especially for the 205 nm pulse generation part. I will also describe laser performances during the excitation tests that will be reported in the last

[1] Model `EKSPLA NL303-10`, website `http://ekspla.com`.
[2] Sometimes I will use the symbol @ to mean "*at*"

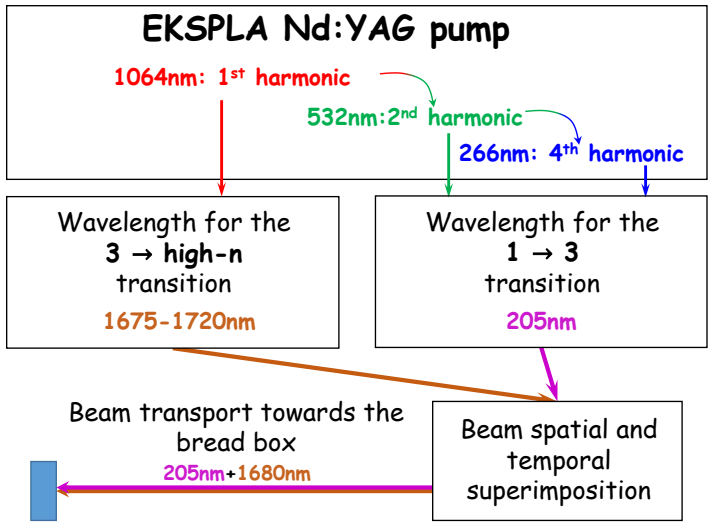

Figure 5.1: From the top, the steps to get the desired wavelengths. A Q-switched laser provides a 1064 nm pulse. Part of the beam is sent directly to the section dedicated to the production of the $\sim$ 1680 nm radiation. From the remainder, second and fourth harmonic are generated and then sent to the section dedicated to the production of the 205 nm radiation. The following step is the spatial and temporal overlap between the two beams, which finally are delivered to the positronium cloud.

part of this thesis.
I will complete the description of each part of the laser with the spectral analysis of the output of the related nonlinear processes.

5.1 The pump system

In fig. 5.2, an overview of the pump laser and the associated "harmonic generator" is given. We call *pump system* the ensemble of these two devices.

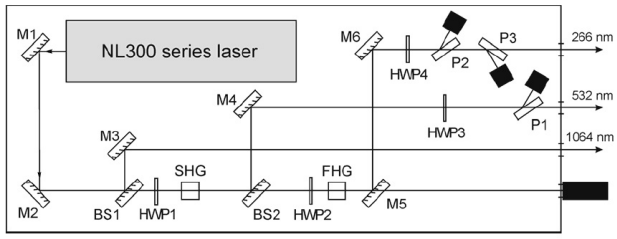

Figure 5.2: Pump system general optical scheme: the shaded box represents the EKSPLA Nd:YAG laser.The emitted pulse is manipulated to produce the needed harmonics. Legend: SHG=second harmonic generation; FHG=fourth harmonic generation (actually another SHG); M=mirror; BS=beam splitter; HWP=half wave plate; P=polarizer (Brewster plate). Source:EKSPLA NL300 series laser manual

5.1.1 The pump laser: the Q-switching strategy

The pump laser is based on a cavity where a Nd:YAG rod is allocated. Here the population inversion occurs, induced by the energy delivered by a flash lamp with a rate of 10 Hz. The Q-switching, and therefore the pulse generation process, is controlled with a Pockels Cell[3] (PC) and a Brewster plate. By holding the polarizer axis steady and by changing the applied voltage to the PC, one is able to regulate the transmitted energy.

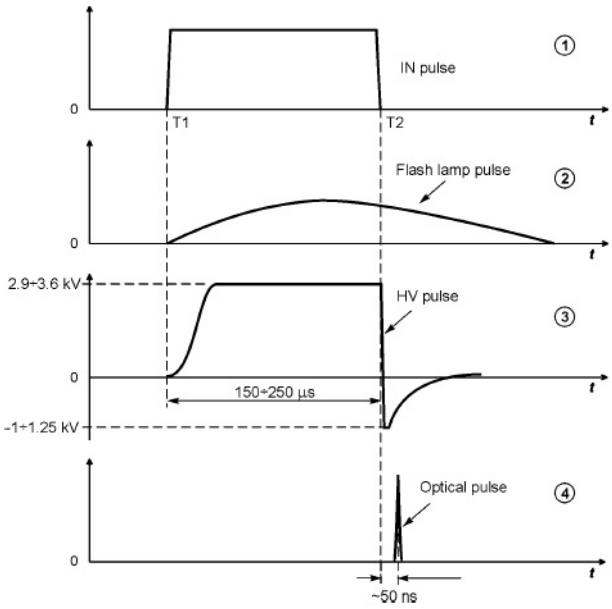

Figure 5.3: Pulse generation timing scheme (source: EKSPLA NL300 Series Laser manual). (1) trigger signal pulse; (2) flash lamp intensity (to which the population inversion is proportional); (3) PC applied potential; (4) generated laser pulse.

By looking at fig. 5.3, the process of pulse generation is defined by the following steps: the population inversion occurs in the active medium through the flash lamp. While the potential applied to the PC is high, the cavity has high losses and no emission occurs, because of the combined action of the PC and the Brewster plate action. When the PC potential drops, in response to a trigger signal, the combined action of the PC and the Brewster plate reduces drastically these losses. As the gain of the cavity is well above the losses, the pulse is generated (*Q-switching*): the intensity of the emitted radiation depends on the quantity of excited atoms in the active medium. The pulse duration is strictly linked to the decay time τ_c of the cavity (see subsec. 4.2.2).
In the AEgIS system, the trigger pulse is activated when the desired number of positrons is stored inside the accumulator. The rising edge activates the flash lamp and, at the same time, the PC potential is increased. The falling edge governs the pulse generation as well as the positron dump from the accumulator. The flash lamp pulse lasts longer than the PC potential falling edge time, therefore, by optimizing the Q-switching phase

[3]The **Pockels effect** (after Friedrich Carl Alwin Pockels who studied the effect in 1893), or Pockels electro-optic effect, is the generation of birefringence in an optical medium linearly dependent on the electric field applied on it. Pockels cells are voltage-controlled wave plates and may be used to rotate the polarization of a beam that passes through.

delay with respect to the maximum population inversion, the emitted energy can be maximized.

The results of the optimization process of the PC delay time will be reported later. Before, we need to model the Q-switched pulse on the basis of the informations we have about the AEgIS pump laser. In fig. C.1 in appendix C, the principal characteristics of the EKSPLA pump cavity are listed.

Q-switch pulse properties and modelling

The EKSPLA pump cavity is an unstable passive optical resonator. This implies the presence of many longitudinal modes spaced by a FSR (chapter 5 of [92]). The evidence of the presence of these modes in the EKSPLA pump laser comes out from the Fourier analysis of the temporal profile of the Q-switched pulse. In practice, this measurement was performed with the use of a fast photodiode by delivering on it just a portion of diffused 1064 nm radiation. The generated signal was analysed with an oscilloscope, displaying the temporal profile and the related FWHM. The temporal profile of each pulse shows a main maximum and the presence of secondary maxima is linked with the presence of longitudinal modes with different and irregulare relative phases: by Fourier transforming the temporal profile of the pulse, a frequency decomposition is obtained, where the components have the same mutual distance, exactly the FSR of the laser. The values of the time width, the spectral and the FSR of the EKSPLA laser, related to the period of the positronium excitation measurements, are:

Wavelength (nm)	**Temporal FWHM** (ns)	**FSR** (MHz)	**Spectral FWHM** (GHz)
1064	5.0 ± 0.5	300 ± 10	30

Table 5.1: EKSPLA laser pulse main specifications.

The presence of 5 ns in the temporal FWHM field is not in contrast with the 4 ns mentioned before. On the contrary, this is an important detail about the behaviour of a Q-switched laser. The reason why we had a 5 ns 1064 nm pulse during the Ps excitation measurements is that the flash lamp was working at the 97% of its maximum power. This is a general law: the lower the working pump power, the longer the generated pulse.

The presence of many longitudinal modes implies a comb-shaped spectrum (like the one in Fig. 4.10). Specifications in table 5.1 provides the necessary elements to make a model of the generated pulse spectrum. By calling ν the frequency shift from the central frequency ν_0 and $\Delta\tau_p$ the pulse duration FWHM, the spectral amplitude $A(\nu, dt)$ of the Q-switched multimode pulse can be modelled (in the Gaussian approximation) as:

$$A(\nu, \Delta\tau_p) = \sum_{n=-\frac{N}{2}}^{\frac{N}{2}} \mathrm{e}^{-\frac{(\nu-\nu_n)^2}{\mathrm{w}^2_{\nu_n}(\Delta\tau_p)}} \mathrm{e}^{\mathrm{i}\phi_{\mathrm{rnd}}(n)} f(\nu), \qquad f(\nu) = \mathrm{e}^{-\frac{\nu^2}{\mathrm{w}^2_{\nu_{laser}}}} \tag{5.1}$$

where $\mathrm{w}_{\nu_n}(\Delta\tau_p)$ and $\mathrm{w}_{\nu_{laser}}$ are the waist of each single peak of the comb-shaped spectrum and the total waist of the laser spectrum respectively, and $\phi_{\mathrm{rnd}}(n)$ is a random phase in $[-\pi, \pi]$. The width of the single peak is a function of the measured pulsed duration: in this gaussian approximation, by making the Fourier transform of a pulse with

a time FWHM of $\Delta\tau_p$, we have longitudinal modes ν_n with a waist :

$$w_{\nu_n}(\Delta\tau_p) = \frac{\sqrt{2\ln(2)}}{\pi\Delta\tau_p} \tag{5.2}$$

that, in our case, is $w_{\nu_n} = 75$ MHz, corresponding to a FWHM of ~ 88 MHz.
By using the `Labview` software to implement these calculations, and setting a random phase between 0 and 2π for each longitudinal mode ν_n, the simulation gives the spectrum in fig. 5.4 This spectrum will be our starting point for the spectral analysis per-

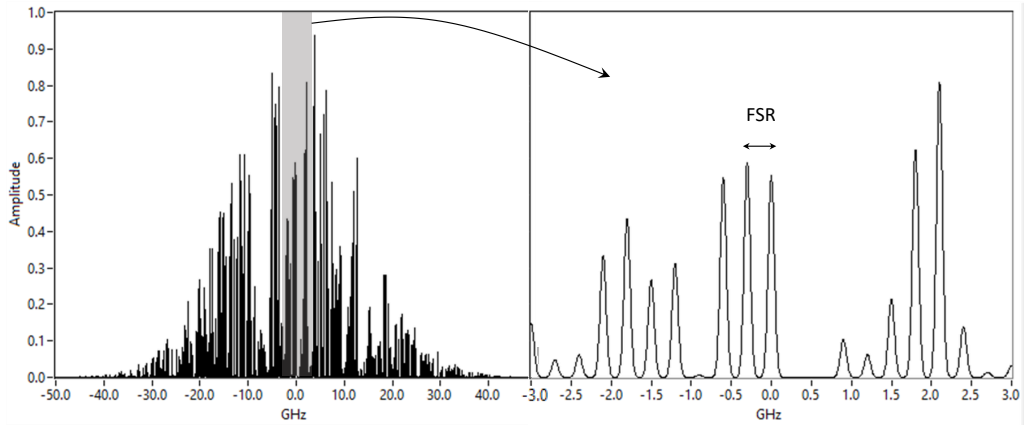

Figure 5.4: On the left, the total spectrum of the Q-switched pulse simulated with `Labview`. On the right, a zoom over few peaks, where the Free Spectral Range can be clearly be identified.

formed in the following of this chapter.

It is worth noting that, from the spatial point of view, the use of an unstable cavity, as the one of the EKSPLA pump laser, has big advantages on its own. As better described in [92], this "positive branch" unstable cavity allows the emission of a large (~ 2 cm of FWHM) single spatial mode beam. It is not a TEM_{00} (the fundamental spatial mode, that is a Gaussian transversal mode), but it is the *fundamental mode of the unstable cavity*, and its spatial coherence is crucial for focusing the beam, necessary for dimension and divergence manipulation.

5.1.2 The harmonic generator

Harmonic generator is a name that has been given to the outermost box in fig. 5.2, containing the set of optics dedicated to the generation of second and fourth harmonics. Fig. 5.2 represents schematically the configuration of all these optics, while in fig. 5.5 a picture of the harmonic generator is shown, together with all the light paths and two zoomed pictures of inner part of the pump laser and the second *second harmonic* crystal's equipment.
The generated 1064 nm pulse is divided with a beam splitter: the first portion forms the first harmonic output (on the left) and can reach a maximum energy of 120 mJ/pulse; the second portion passes through a KDP (potassium dihydrogen phosphate) crystal, and is frequency doubled. The process occurs in critical phase matching conditions. With the crystal kept at constant temperature $\sim 40°$C (KDP is an hygroscopic crystal. By keeping

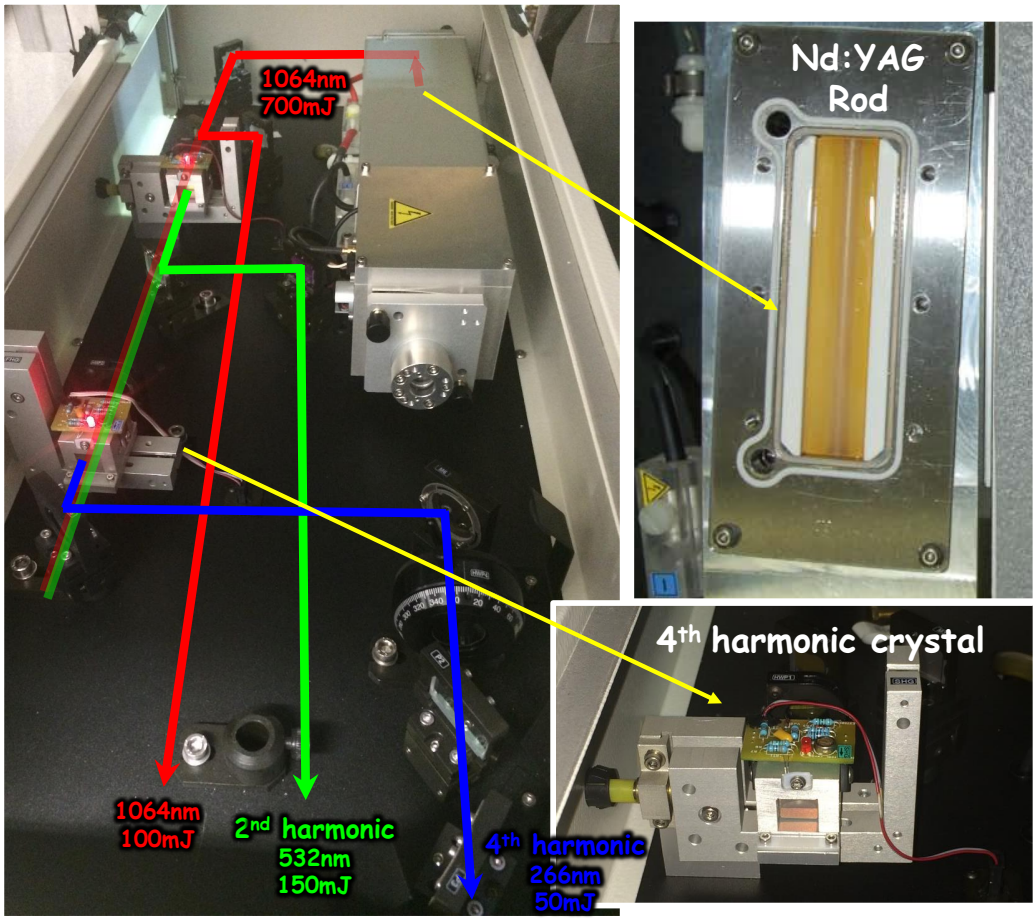

Figure 5.5: On the left, a picture of the laser pump, comprehensive of the pump laser and the harmonic generator. Beam splitting and harmonic generation are shown with the related coloured path. In the top right picture, a capture of the Nd:YAG rod: the flash lamp is visible, together with some cooling water. In the bottom picture, a zoom on the 4th harmonic KDP crystal: the electronics are responsible of keeping the crystal temperature constant. Energies specified in the picture correspond to a typical operating situation.

it at a constant temperature slightly higher than the room temperature, the absorption of humidity is prevented), the specifications of the process are:

$1064\text{nm}_{(o)} + 1064\text{nm}_{(o)} \rightarrow 532\text{nm}_{(e)}$	
$d_{\mathbf{eff}}$	2.65×10^{-1} pm/V
$\theta_{\mathbf{PM}}$	$41.1°$

where $d_{\mathbf{eff}}$ is the nonlinear coefficient related to the directions of the fields, their polarizations and the considered optical axis[4]; $\theta_{\mathbf{PM}}$ is the phase matching angle at the given temperature; letters o and e subscripted to the interacting wavelengths indicate whether

[4] d_{eff} is obtained by transforming the related d_{ijk} element of the susceptibility tensor (given in the crystal coordinates) into the laboratory coordinates.

they are ordinary or extraordinary beams. Keeping the temperature constant is necessary because temperature shifts cause different phase matching conditions, and stability is crucial for long-lasting measurements.
The 1064 nm beam leaves the harmonic generator with vertical polarization (with respect to the optic table), therefore the 532 nm radiation is generated with horizontal polarization.
Again with the use of a beam splitter, a fraction of the 532 nm energy (~ 150 mJ/pulse at the maximum energy) is delivered outside the harmonic generator, while the remaining fraction undergoes a frequency doubling through a second KDP crystal kept again at constant temperature:

$532\text{nm}_{(o)} + 532\text{nm}_{(o)} \rightarrow 266\text{nm}_{(e)}$	
$d_{\mathbf{eff}}$	4.64×10^{-1} pm/V
$\theta_{\mathbf{PM}}$	77°

By following the same reasoning as above, the fourth harmonic travels with a vertical polarization. The maximum measured energy @ 266 nm exiting the harmonic generator is around 60 mJ/pulse.
We observe that the transverse profile of each harmonic in the near field is made of concentric circles. In the far field (for example on the focal plane of a convergent lens) it is observed to be, with good approximation, gaussian.

Pulse energy as a function of the PC delay [99]

It is clear from the description above, that when the Q-switching starts at the time of maximum population inversion, the maximum energy is delivered outside the cavity. In the AEgIS laser system, it is important to consider that we have the the possibility to tune the emitted radiation energy by changing the PC delay time value. A direct measurement of the energy of the three harmonics has been performed, as a function of the PC delay time. This parameter can be set with the laser control system; the single pulse energy was measured with an energy meter. This device is able to provide both the energy of a single pulse and the average of the energies of a given number of pulses with the related standard deviation. This gives informations about the stability of the laser pump energy. The results of the measurements are shown in fig. 5.6: the optimum delay time of the PC turns out to be equal to 225 μs.

From eq. (4.68) we know that, if W_ω and $W_{2\omega}$ are the power of the first and second harmonic respectively, then

$$W_{2\omega} \propto W_\omega^2 \tag{5.3}$$

By normalizing the plot on the maximum value

$$\frac{W_{2\omega}}{W_{2\omega}^{\mathbf{max}}} = \left(\frac{W_\omega}{W_\omega^{\mathbf{max}}}\right)^2 \tag{5.4}$$

and applying a square root to the second harmonic and a fourth root to the fourth harmonic, we obtain the plot in fig. 5.7 Now the curves are almost superimposed, with the exception of the tail of the 266 nm curve, due probably[5] to the fact that we have very low energy values and huge fluctuations (scaling as the fourth power of the fluctuations of the pump).

[5]There could have been some error bar estimation issue. For example a bad calibration of the power meter behaviour at low energies, a neglected systematic error, an error in the propagation or a bad statistics.

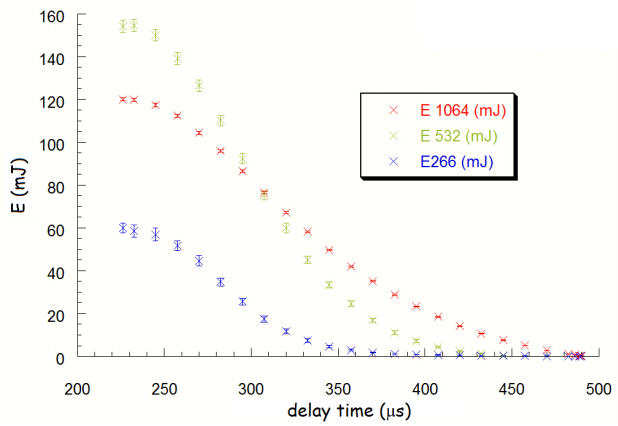

Figure 5.6: Pulse energy as a function of the PC delay [99]

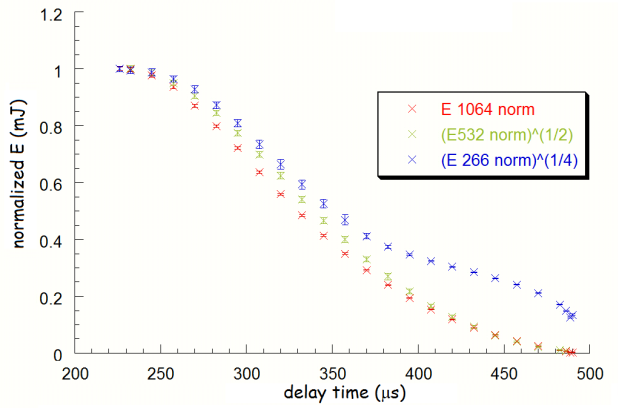

Figure 5.7: Pulse energy as a function of the PC delay, rescaled [99].

5.1.3 Simulated spectra for the first, second and fourth harmonics: a comparison

I used `Labview` in order to simulate second and fourth harmonic spectra, starting from the Q-switched pulse spectrum model in fig. 5.4. By iterating twice equation (4.70), an example of resulting spectra for the three harmonics is depicted in fig. 5.8:
It is clear how the FSR is preserved for each harmonic, as in the right panel of fig. 5.8 peaks keep their mutual distance. On the other hand, the FWHM of each peak and of the envelope of each harmonic increases at each iteration (by a factor $\sim \sqrt{2}$).

5.2 Laser system for the n=1 → n=3 Positronium excitation

In this section, the AEgIS strategy to produce the 205 nm radiation will be explained. In fig. 5.9 all the optics dedicated to the 205 nm radiation are sketched and, some of them, pictured. Fig. 5.9 is connected to fig. 5.1; it gives a more detailed view about this part of the apparatus and it shows approximatively the real arrangement of the optics.

Second and fourth harmonics are needed for the 205 nm radiation generation. The

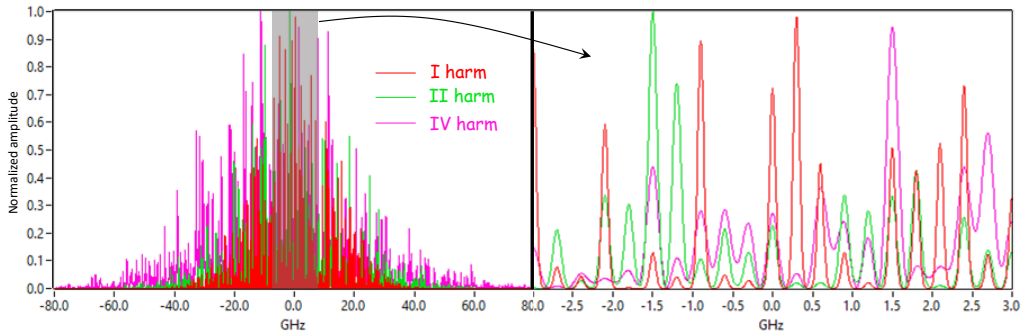

Figure 5.8: On the left: normalized spectra of I, II and IV harmonics, centered on their nominal central wavelength. On the right: a zoom on the shaded region shows individual peaks of the spectra. While the mutual distance is preserved, the FWHM of each longitudinal mode increases with the harmonic order. For the fourth harmonic we can also find some peak overlap.

final step to produce 205 nm radiation is due to the sum crystal where the process of sum frequency generation occurs.

NOTE: Henceforth, I will omit the word "radiation" when referring to a propagating beam, and I will just use its wavelength to identify it.

By looking at fig. 5.9 one immediately understand that, while the 266 nm is an ingredient for the final sum by itself , the 532 nm is not. It needs manipulating in order to obtain the second ingredient of the sum process: a 894 nm radiation. It is worth, here, starting from the laser pump and following each path until the generation of the 205 nm.

Just outside the laser pump, each harmonic's beam height from the optical table is lowered with a periscope[6] (each periscope is identified by a circled P in the figure). The 266 nm is reduced in size via a telescope, and delivered into the sum crystal with a prism. The frequency sum is achieved in non collinear configuration (later this will be better explained). The way to produce the other ingredient of the sum, the 894 nm radiation, is less straightforward. The main idea is the following one: we have to produce 894 nm from vacuum. Thus, in order to achieve the right amount of 894 nm energy, we make use of two consecutive steps:

- **High gain** but **low energy**: the **generation step**. We generate 894 nm from vacuum, this means that we need a crystal with a high nonlinear coefficient for the desired nonlinear process. This can be achieved with Periodically Poled crystals in QPM conditions, but usually they are too small and fragile for us to be able to enter with high energy pump beams. This is the reason why, usually, a low energy output is expected, that will be the seed for the following step.

- **High energy** with **low gain**: the **amplification step**. The presence of a seed at 894 nm makes the use of bulk crystals in critical PM convenient. In fact, even if the nonlinear coefficient is lower, input faces can be larger. Together with the higher damage thresholds of these crystals, all these features make the crystal able to stand high input energies, necessary to efficiently amplify the existent seed.

[6] A *periscope* is a system made of a couple of mirrors, the first of which points down/up and the second one points in the desired direction of the horizontal plane. After a periscope, the polarization of the beam gets changed when the final direction is not coincident with the original one.

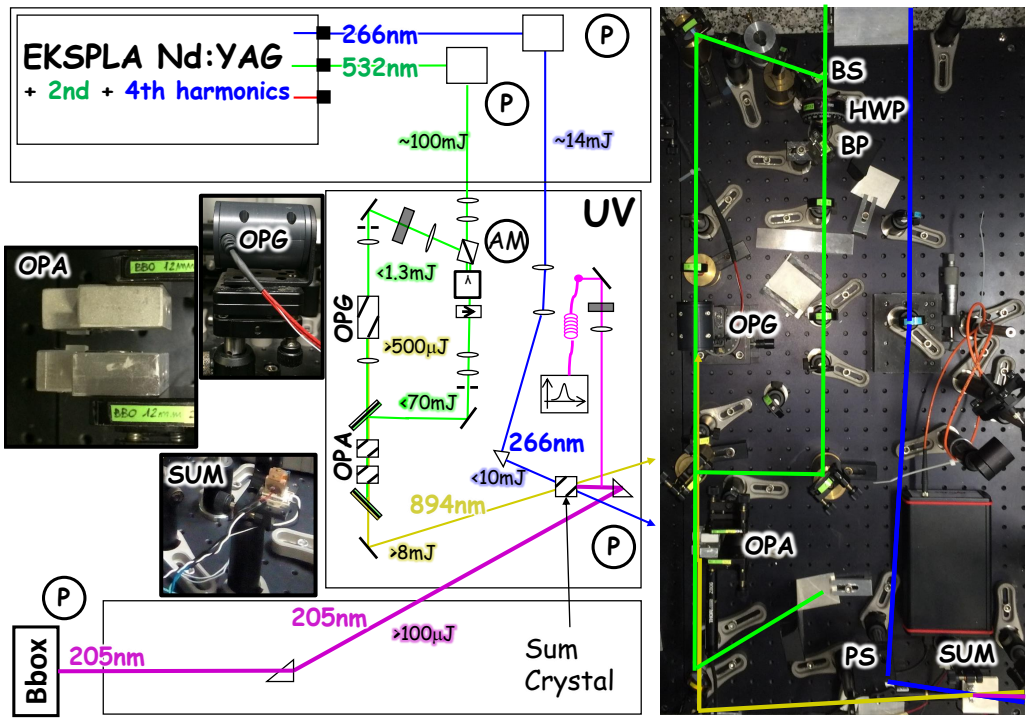

Figure 5.9: On the left: sketch of the laser system part dedicated to the 205 nm radiation generation. Small pictures of the nonlinear crystals' arrangement are reported. On the right: a picture of this part of the system as it was at CERN in the AEgIS laser hut at the moment of the Ps excitation measurements. Radiation paths are drawn, in order to facilitate the comprehension of the picture. On the picture: BS = beam splitter; HWP = half wave plate; BP = brewster plate; PS = prism. On the sketch: P = periscope; AM = HWP + BP (Attenuation Module); triangles = prisms. In each important part, values of the needed/suggested energy are reported, each one shaded according to the associated wavelength.

In order to implement this strategy, after the periscope, there is a beam splitter that divides the second harmonic into two beams: the lower energy beam passes through the Optical Parametric Generator to form a seed of 894 nm radiation, while the higher energy beam is first attenuated in amplitude with a half wave plate + brewster plate system (called *Attenuation Module*, a circled AM in the figure) and then sent into the Optical Parametric Amplification system together with the 894 nm seed. Here the 894 nm is amplified and then "purified" from the 532 nm with a dichroic mirror.
At this point, the beam is sent to the sum crystal for the final step to obtain the 205 nm beam. In the following subsection, each nonlinear process will be explained, and the relative spectral analysis will be shown.

5.2.1 Optical Parametric Generation of the 894 nm pulse.

The generation of the 894 nm radiation takes place inside a PPKTP crystal (Periodically Poled *Potassium Titanyl Phosphate* crystal). The choice of a periodically poled crystal reflects the fact that we want to generate 894 nm radiation from vacuum, therefore we need really high gain, possible if we exploit the d_{zzz} element of the susceptibility tensor

of the crystal[7]. In the previous chapter I explained why this choice is strictly related to the necessity of working in a QPM condition.
Important parameters related to the crystal setup are shown in tab. 5.2. Periodically

$532\text{nm}_{(o)} \rightarrow 894\text{nm}_{(o)} + 1313\text{nm}_{(o)}$	
d_{eff}	9.8 pm/V
period	9.05 μm
crystal length	30 mm
crystal input face	2×1 mm^2
critical intensity	200 MW/cm^2

Table 5.2: PPKTP crystal main specifications: UV line. The period is the one decided by the manufacturer, given the desired output parameters.

poled crystals have transverse dimensions hardly larger than the ones specified in the table. The reason is that the applied voltage required in order to invert the crystal domain increases with the crystal width. Therefore, over a certain width, it breaks the crystal. This implies the need of a small crystal, forcing us to enter the crystal with a small transverse beam dimension ($\sim 600 \times 600$ μm^2 of FWHM). As a consequence, in fig. 5.9 an energy less than 1.3 mJ is reported at the entrance of the OPG (safe value). In fig.5.10, the input face of the OPG crystal is shown: such a small beam waist carries a really high intensity, able to scrape the material of the oven face. In fig. 5.9, the oven containing the PPKTP crystal is fully shown. We need the oven in order to keep the crystal at a constant temperature of 152.6°C, that is the QPM temperature for the desired wavelength around 894 nm (the one necessary to generate the precise 205.05 nm in the sum crystal). The picture on the right of fig. 5.10 shows the damage of the crystal that occurred when

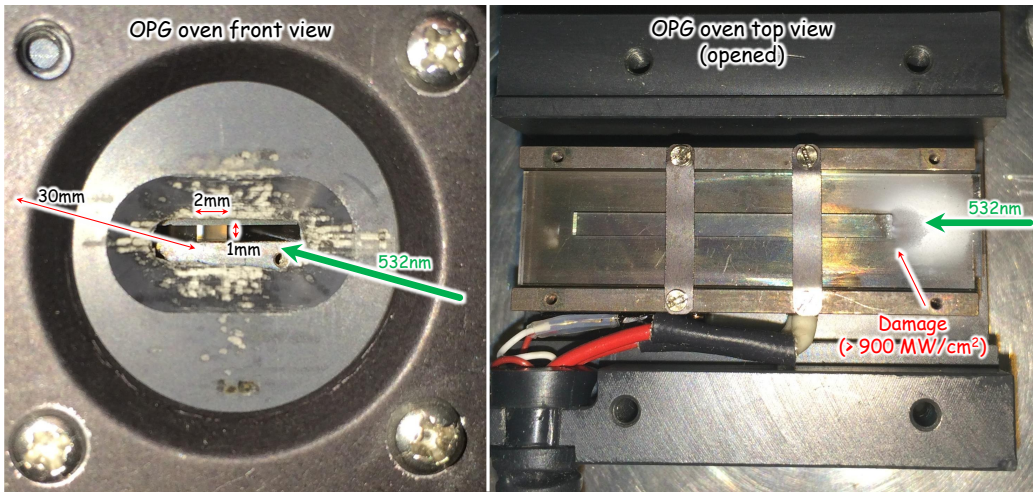

Figure 5.10: PPKTP crystal damage.

[7]The KTP susceptibility tensor is (pm/V): $d = \begin{pmatrix} 0 & 0 & 0 & 0 & 1.95 & 0 \\ 0 & 0 & 0 & 3.9 & 0 & 0 \\ 1.95 & 3.9 & 15.3 & 0 & 0 & 0 \end{pmatrix}$

the cooling system of the laser wasn't working properly. The flux instabilities changed periodically the active medium thermal focal length, leading to quick variations of the spot dimensions at the entrance of the OPG crystal: from 650μm to 200μ every 30 s. Fortunately, this happened right after the excitation measurement period. The crystal face was completely crumbled as an intensity of more than 900 MW/cm^2 was periodically delivered for hours.

Spectral analysis

Inside the crystal, the down conversion process specified in the first line of tab. 5.2 occurs. The use of a periodically poled crystal means that we produce signal and idler

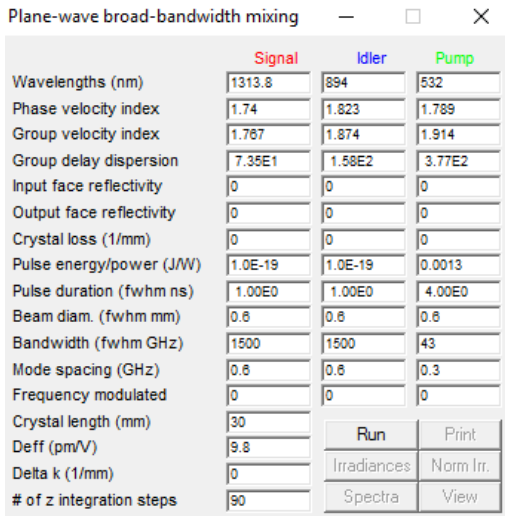

Figure 5.11: Parameters for the SNLO simulation of the OPG pulse.

radiation in Quasi Phase Matching conditions. We have therefore three ordinary rays and the strongest element of the nonlinear susceptibility tensor is exploited: $d_{zzz} = 15.3$ pm/V, that becomes $\widetilde{d}_z = 9.75$ pm/V because of the QPM factor $\frac{2}{\pi}$. The oven is used to keep the crystal at a temperature of around $152°$C. In fact, given the period of the periodically poled crystal, there is an optimal temperature at which the desired wavelength is generated with maximum efficiency. By changing the temperature, it is possible to tune the wavelength.
Coupled equations (4.79) and (4.80) describe the process, giving all the spectral informations on the output beam. In the previous chapter, I made few theoretical considerations about the inner structure of the spectrum by making several assumption, in order to obtain an analytical solution. Here, I report the results of a simulation performed with the SNLO software, where a numerical solution of the set of complete equations is provided. In fig. 5.11, the parameters used to perform the simulation are shown. We start from the vacuum for signal and idler, and the related bandwidth is the maximum possible for the numerical simulation in this part of the SNLO program. Mode spacings related to signal and idler were forced by the SNLO program to be grater than 600 MHz. Vacuum should have a continuous spectrum with no gap. Despite this, the 600 MHz mode spacing condition is still good to simulate a continuous spectrum (were gaps don't drop to zero) as the width of the modes is comparable with the spacing value.

An example of resulting optical parametric generated 894 nm spectrum is reported in fig. 5.12. Here we can see that the 894 nm doesn't follow any more the comb-shaped

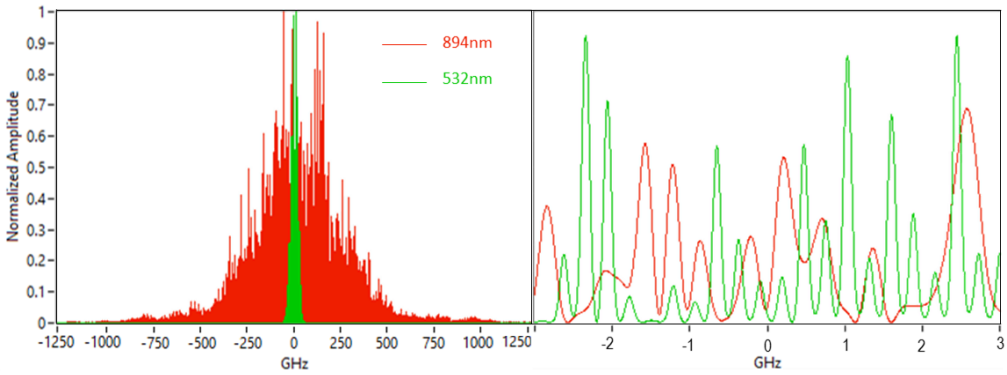

Figure 5.12: On the left, the spectrum of the 894 nm pulse simulated with SNLO, compared with the II harmonic spectrum (the OPG pump). On the right, a zoom over few peaks: while in the II harmonic profile the Free Spectral Range can be clearly identified, for the OPG output no regular structure can be found.

profile of the OPG pump. The resulting spectrum is much broader than the 532 nm one and it is evident that between the apparently randomly distributed peaks the field is not zero. therefore it is immediately evident the fact that the OPG spectrum doesn't follow any comb-shaped structure. Peaks don't have a constant mutual distance and therefore the FSR of the pump laser is lost.

During the Ps excitation tests we performed the measurement of the 894 nm spectrum

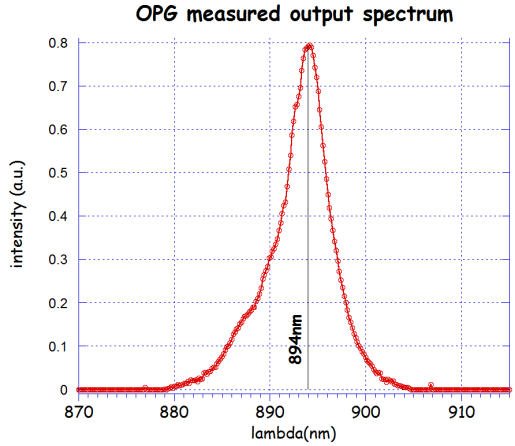

Figure 5.13: Measured OPG output spectrum, after calibration with mercury lines.

with a commercial Thorlabs CCS175 spectrometer (old model). The wavelength range is[8] between 500 and 1100 nm, the FWHM resolution in the 894 nm region was ~ 0.95 nm

[8] I established the resolution by comparing the FWHM of the measured 1064 and 532 nm spectra with the 30 GHz of the laser pump specifications and the related second harmonic width respectively.

(∼ 350 GHz) and the wavelength shift is 1.14 nm[9]. In fig. 5.13 the measured spectrum is reported.
The measured FWHM of 5.16 nm has to be deconvolved with the spectrometer resolution, thus obtaining 5.07 nm, meaning that we had at the OPG output a spectrum of 1.9 THz, much more than the simulated one. In fact, while with a 9.4 μm crystal period the

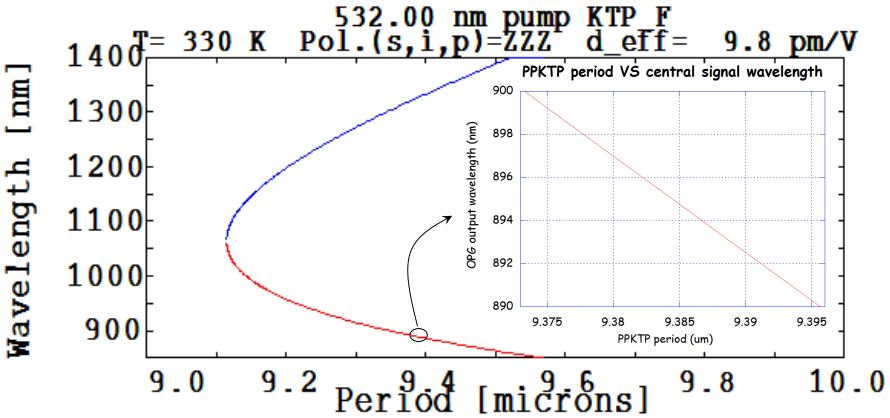

Figure 5.14: SNLO simulation: generated wavelength as a function of the period. A zoom on the required period in the inset.

SNLO simulations give an output of around 600 GHz, we measure 1.9 THz. This could be explained with a manufacturer error on the period dimensioning. In fig. 5.14 the SNLO curve obtained with the QPM panel is reported. It shows how the signal and idler wavelengths change as a function of the crystal period. A zoom around 894 nm is shown in the inset. Here we see how an error of ∼ 2‰ itself (∼ 20 nm) could contribute to this broadening of the 894 nm pulse total spectral width. But there is another element that might confirm this hypothesis. When a new PPKTP crystal was bought from the same company in order to substitute the damaged one (fortunately after the Ps excitation measurements), a new temperature had to be set (176°C). The phase matched wavelength at the old temperature (152°C) was 910 nm, 16 nm more than the desired 894 nm. This shift corresponds to a systematic error in the crystal's period of 50 nm, probably meaning that the company doesn't build these crystals with a sub-50 nm precision on the period width. Therefore, the measured total spectral width seems to be compatible with the one obtained with SNLO.

The width of the OPG spectrum and the lack of a comb-shaped inner structure will be two crucial elements in our spectral analysis of the 205 nm excitation efficiency. One could experimentally check the absence of FSR comb-structure by using a photodiode coupled with an oscilloscope. By performing the Fourier transform of the time dependent trace it is possible to check the absence of the FSR peak at 300 MHz[10].

[9] established via a calibration with a Mercury lamp

[10] Peaks in the Fourier transform are due to frequency differences in the laser pulse. Being the FSR the mutual frequency difference between all the pulse spectral modes, the absence of a peak at 300 MHz would be an experimental confirm of the loss of the FSR-induced comb-structure.

5.2.2 Optical Parametric Amplification of the 894 nm pulse

The high gain of the previous OPG process allows us to generate ~ 600 μJ of 894 nm from vacuum. This is due to the small dimensions of the crystal and the small amount of input energy. In order to obtain a 205 nm pulse energy higher than the saturation energy of the excitation process (described in the following chapter), we need to amplify the 894 nm beam. We do this with an Optical Parametric Amplification (OPA) step after the OPG. In this case, we have an 894 nm input seed, that makes the down conversion of the 532 nm efficient in a bulk crystal. We decided to use the BBO crystal[11] (already described in section 4.4.1). Essential parameters of this crystal are reported in table 5.3.
While reading all the specifications, one can wonder why *that* crystal length. The choice

$532\text{nm}_{(e)} \rightarrow 894\text{nm}_{(o)} + 1313\text{nm}_{(o)}$	
d_{eff}	2.02 pm/V
crystal length	12 mm
crystal input face	5×5 mm^2
critical intensity	500 MW/cm^2
angular acceptance	0.58 mrad·cm
bandwidth acceptance	1.45 THz·cm
temperature range	21.02 K·cm
PM angle	22.6°
walk-off angle	55.38 mrad

Table 5.3: OPA crystals main specifications: UV line.

of the length for a nonlinear crystal has several consequences, that affect the efficiency of the nonlinear process as well as the output beam spectral characteristics (for example the maximum bandwidth). When walk-off occurs in a crystal (in this case for the extraordinary 532 nm beam, called also pump beam here), the 894 nm and the 532 nm overlap over a finite length, called *interaction length*. This makes useless a crystal longer than the interaction length. This can be a tiresome issue when high output energies are required. In the following, two important issues will be addressed: what beam properties are required? How can we address the walk-off issue?

Input beam configuration

Here we are dealing with a critical phase matching. The pump beam (532 nm) is extraordinary while signal and idler (894 nm and 1312 nm respectively) are ordinary. The 532 nm radiation is the output of the amplitude modulator (fig. 5.9) and it has horizontal polarization. Being the 532 nm extraordinary, we need a crystal configuration such that the optic axis lays on the horizontal plane. The AM is necessary in order to keep under control the pump input energy. A critical intensity of 500 MW/cm^2 means that, if we have a ~ 2.5 mm FWHM (achieved with a telescopic system), its energy must be lower than 70 mJ. When the AEgIS laser system is well aligned, much lower energies are

[11] The BBO susceptibility tensor (from `SNLO`) is (pm/V): $d = \begin{pmatrix} 0 & 0 & 0 & 0 & 0.08 & 2.2 \\ 2.2 & -2.2 & 0 & 0.08 & 0 & 0 \\ 0.08 & 0.08 & ? & 0 & 0 & 0 \end{pmatrix}$
SNLO program doesn't give this value (you really find a question mark in the matrix). I tried to email the owner of the program and ask for the meaning of the exclamation mark, but I had no answer.

required, therefore the AM allows us to manipulate the pump energy as needed. The pump beam divergence was about 0.2 mrad, while the seed had a FWHM of ~ 2.1 mm and a convergence lower than 0.4 mrad. Therefore these parameters were well under the specified acceptances of the crystal.

The walk-off issue

Spatial walk-off is encountered in nonlinear frequency conversion schemes based on critical phase matching in nonlinear crystals. Its consequence is that the waves interacting within a focused beam lose their spatial overlap during propagation, because those waves with extraordinary polarization experience the walk-off, whereas this is not the case for those with ordinary polarization. (Note that birefringent phase matching necessarily involves beams with both polarization states.) In effect, the useful interaction length and thus the conversion efficiency can be limited, and the spatial profile of product beams may be broadened and the beam quality reduced. Unfortunately, it is not a solution to work with more strongly focused beams, requiring a shorter interaction length, because the spatial walk-off becomes more important for smaller beam radii. The problem is reduced, however, for high optical intensities, which allow for good conversion within a short length.

The phenomenon of spatial walk-off is directly related to that of a finite angular phase-matching bandwidth. Equation (B.1) in the Appendix shows that a large walk-off angle occurs in situations with a strong angular dependence of the extraordinary refractive index. In such cases, the phase-matching conditions also depend strongly on the propagation angle, and phase matching becomes incomplete when using tightly focused beams, having a large beam divergence.

Spatial walk-off can be avoided altogether by using a noncritical phase matching scheme. This, however, generally requires operation of the crystal at a temperature either far from the room temperature or even that doesn't exist.

It is however possible to achieve a kind of walk-off compensation by using a pair of aligned nonlinear crystals oriented such that the walk-off directions are opposite to each other. There is then still a residual walk-off within these crystals, but its overall effect can be strongly reduced.
Therefore, in the AEgIS OPA system, two crystals are used, (both with specifications of table 5.3). Moreover, in each single BBO crystal, we reduce the impact of the walk-off by slightly shifting one of the input beams (the one having walk-off) in the opposite direction. More precisely, we send the pump and the seed at a distance of $\frac{1}{2} l \theta_{wo} = 300$ μm on the horizontal direction (see fig. 5.15).

Considerations about the output 894 nm spectrum

The 894 nm spectrum at the exit of the second OPA crystal is strictly dependent on how much we exceed the bandwidth acceptance of each crystal and on the mutual alignment of the beams. While, on one hand, each crystal tends to reduce a bit the 894 nm spectrum (we enter with 1.9 THz while the acceptance is about 1.2 THz), on the other hand each small misalignment of the two crystals will amplify different spectral portions of the signal, thus broadening the resulting spectrum. In the following simulations about the generation of the 205 nm, I will use simulated OPG spectra like the one in fig. 5.12. As that spectra are well below the 1.2 THz bandwidth acceptance, they will still generate an under-estimated 205 nm spectrum width, and therefore an under-estimated excitation efficiency (referred to in the following chapter).

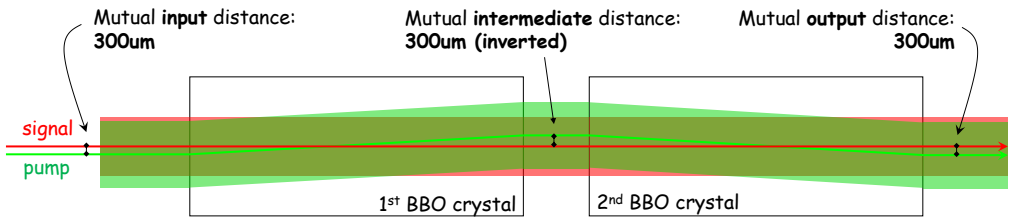

Figure 5.15: OPA crystals: positioning scheme. The pump beam undergoes walk-off. If the two crystals have their axes inverted, the overlap between signal and pump is maximized in the middle of the crystal. **Dimensions in this figure are to scale**, in particular: the two FWHM (2.1 mm for the 894 nm and 2.4 mm for the 532 nm), the distance between the axes of the two beams (300 μm) and crystals' dimensions ($5 \times 5 \times 12$ mm^3).

5.2.3 205 nm generation: sum of the 894 nm and 266 nm pulses.

The 894 nm and the 266 nm allow the generation of the 205 nm radiation, necessary for the $n = 1 \rightarrow n = 3$ Ps excitation. The involved nonlinear process is the sum frequency generation (SFG), already described in section 4.6. We use a BBO crystal, and both beams

$894\text{nm}_{(o)} + 266\text{nm}_{(o)} \rightarrow 205\text{nm}_{(e)}$	
d_{eff}	1.68 pm/V
crystal length	5 mm
crystal input face	4×4 mm^2
critical intensity	500 MW/cm^2 (IR) - 185 MW/cm^2 (UV)
angular acceptance	0.61 mrad·cm (IR) - 0.2 mrad·cm (UV)
bandwidth acceptance	51 GHz·cm (IR) - 128 GHz·cm (UV)
temperature range	3.59 K·cm
PM angle	59.6°
incidence angle	6.5° (IR) - 1.8° (UV)
walk-off angle	88.53 mrad

Table 5.4: Sum crystal main specifications

enter with a vertical polarization and non-collinear configuration (the scheme is in fig. 5.17). We have a critical PM and the generated 205 nm is extraordinary and therefore it has horizontal polarization (this implies that the crystal principal axis lies on the horizontal plane). In table 5.4 the main specifications of the crystal are listed.
As the OPA crystals don't introduce significant divergence to the 894 nm (the seed determines the spatial characteristic of the output), the beam keeps its spatial FWHM of $\sim$ 2.1 mm. But the infrared radiation includes both signal and idler radiations. Their total fluence is $\sim$ 60 MW/cm^2, well below the damage threshold. For this reason, the beam is purified only from the pump radiation, while signal and idler keep going together towards the sum crystal, where only the 894 nm will contribute to the sum.
The 266 nm beam transverse dimension after the telescope is $\sim$ 2.4 mm and its divergence is less than 0.25 mrad. The damage threshold energy for this radiation should be therefore 27 mJ/pulse. Unfortunately, we discovered, at our own expenses, that the real

threshold is far below this value. In fig. 5.16 there is a picture of the sum crystal at the end of the Ps excitation measurement, where a constant 266 nm energy of $\sim 10mJ$ was used. We have no explanation for this. It might be linked with some sporadic pulse

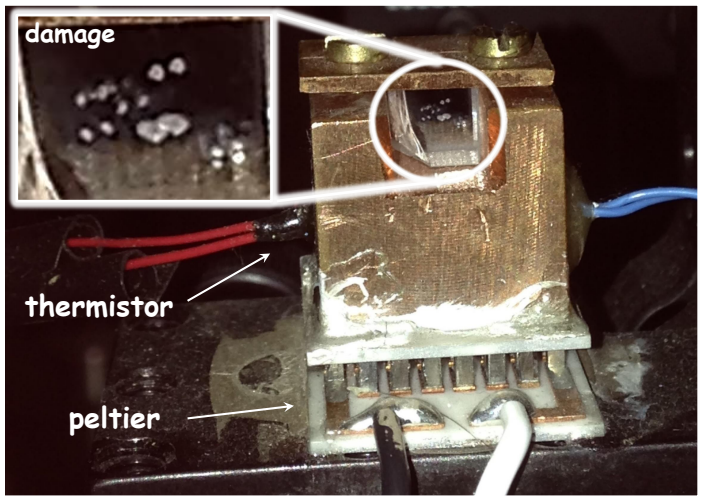

Figure 5.16: SUM crystal: the temperature control system and a zoom on the damage due to high intensity pulses entering the crystal.

energy fluctuation, but we haven't a fast control to check this hypothesis.
The 266 nm divergence is below the angular acceptance value of the crystal (the crystal is 0.5 cm long, meaning that the angular acceptance written in table 5.4 should be doubled) as well as the 894 nm divergence.

The reason for the non-collinear configuration choice is the need to separate the 205 nm radiation from the two mixing radiations. This is important in AEgIS because the Ps

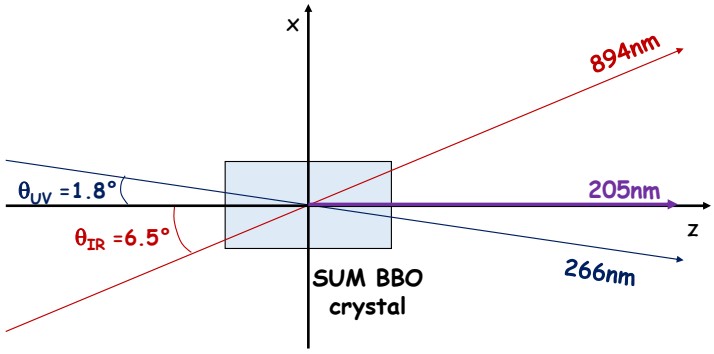

Figure 5.17: SUM crystal: non-collinear configuration. Dimensions are not to scale.

excitation process takes place inside a cryogenic environment: any superfluous radiation warms up the environment. In this way we easily get rid of the 894 nm and 266 nm thanks to the extraordinary nature of the 205 nm polarization.
By calculating the PM angles in non collinear configuration, the required setup turns out to be the one in fig. 5.17. Obviously, in order to keep a good overlap between the 894 nm

and the 266 nm inside the crystal, one should prefer small incidence angles.

The sum crystal is placed inside a thermoregulator support, that makes use of a peltier and a temperature controller connected with a thermistor. Being the BBO crystal hygroscopic, a temperature of $40°$ is kept, also in order to stabilize the PM condition and to produce a stable wavelength all along the Ps excitation measurements. In fact, the fine adjustment of the generated wavelength can be done by varying the PM angle of the crystal. As the 894 nm spectrum is much broader than the bandwidth acceptance of the crystal, a small shift from the PM angle doesn't induce an immediate energy decrease of the generated 205 nm radiation. More precisely, different angles lead to PM for slightly different wavelengths (few tenths of nanometer). By detecting in real time the generated wavelength, it is possible to set PM angles that give a wavelength of around 205.05 nm. The need for a precise control of the wavelength is due to the presence of electric and magnetic fields inside the Bread Box , that can induce a shift of Ps levels ([123]).

5.2.4 Considerations about the 205 nm pulse spectral properties

Our analysis of the 205 nm spectrum is based on equations of section 4.6. We start from the main equation (4.91) describing the sum process, with $\Delta k = 0$ assuming prefect phase matching conditions (I write it here for convenience):

$$\frac{\partial}{\partial z}A_3(z,t) + \frac{1}{v_{g_3}}\frac{\partial}{\partial t}A_3(z,t) = \mathrm{i}\gamma_3 d A_1(z,t)A_2(z,t) \tag{4.91}$$

where $\omega_1 = 894nm$, $\omega_2 = 266nm$ and $\omega_3 = 205nm$. Then, we directly wrote the Fourier transform (4.92) in order to have a first clue about the difficulties of looking for an analytical solution of eq. (4.91). Here, we want to show a numerical solution of (4.91). In this case, it is computationally advantageous to make calculations in the time domain, therefore we used the following equation (that is the equation the Fourier transform (4.92) comes from):

$$\begin{gathered}\frac{\partial}{\partial z}A_3 = \mathrm{i}\gamma_3 d A_1\left(t+\beta_{31}z\right)A_2\left(t+\beta_{32}z\right) \\ \text{with} \quad \beta_{3j} := \frac{1}{v_{g_3}} - \frac{1}{v_{g_j}}\end{gathered} \tag{5.5}$$

The result is given by the integral over the crystal length l:

$$A_3(l) = \mathrm{i}\gamma_3 d\int_0^l dz A_1\left(t+\beta_{31}z\right)A_2\left(t+\beta_{32}z\right) \tag{5.6}$$

By numerically solving integral 5.6 with `Labview` and subsequently performing the Fourier transform of the result, one attains a 205 nm spectrum like the one in fig. 5.18. Even if an analytical solution with a sinc modulation factor is not trivial to find (in the case of non-negligible velocity mismatching between the three components), it is clear that a sort of "sinc-wise" trend is hidden inside the integral.

205 nm spectrum measurement

The resulting spectra of my simulations (see fig. 5.18) reveal a FWHM of about 120 GHz. I measured the spectrum in three different ways: with a commercial spectrometer collecting diffused 205 nm light, with the same spectrometer by scanning directly the beam spot transversally, and finally by measuring divergences and spectra of the input beams and applying an acceptance cut for Fourier transform limited pulses (giving a lower

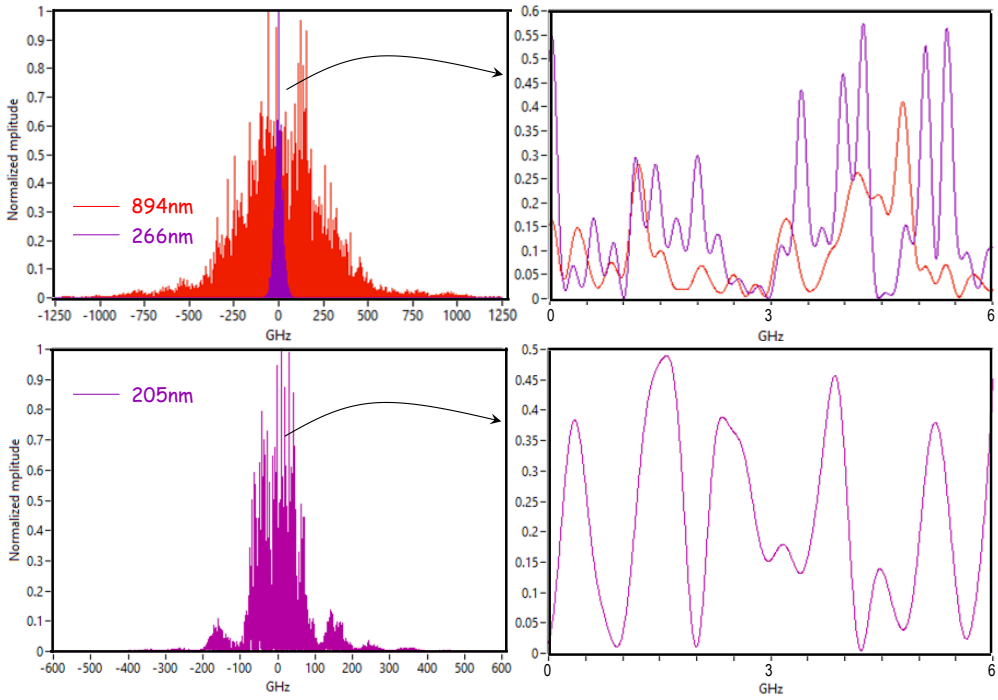

Figure 5.18: On the top, spectra of the 894 nm and the 266 nm are compared. On the bottom, the resulting 205 nm spectrum. In is worth noting two important aspects of the risult: the sinc-wise oscillations of the 205 nm spectrum tails (lower left panel) and the broader and disordered nature of the peaks (lower right panel).

bound to the generated spectrum, although it can be considered reliable in more general cases).
We used an `Avantes AvaSpec-3648-USB2` wavemeter to measure in real time the 205 nm diffused light spectrum. Despite the high precision on the peak wavelength, the resolution of the spectrometer was not suitable to perform an accurate measurement of the generated spectrum width. In fact, a resolution > 400 GHz cannot be used to measure a spectrum narrower than the resolution itself. The only way to use the spectrometer was to exploit the spatial shift of the wavelength along the spot transversal profile. Therefore I first report the results of the "divergence method", then I report the results of this measurement with the spectrometer.
Divergence method means that I tried to extrapolate the generated 205 nm spectrum by measuring the divergence of the input beams and by considering the related spectra. With these data, a good approximation of the output spectrum is then given by

$$\Delta\nu = \sqrt{\Delta\nu_{\mathrm{IR}}^2 \mathrm{div}_{\mathrm{IR}} + \Delta\nu_{\mathrm{UV}}^2 \mathrm{div}_{\mathrm{UV}}} \tag{5.7}$$

where $\mathrm{div}_{\mathrm{IR}}$ and $\mathrm{div}_{\mathrm{UV}}$ are equal to 1 when the input beam divergence is within the crystal angular acceptance, while they are

$$\mathrm{div}_{\mathrm{x}} := \frac{\text{measured divergence of } x}{\text{angular acceptance for} x} \tag{5.8}$$

when it exceeds the crystal angular acceptance. By averaging several measurements, the resulting spectrum was 127 ± 10 GHz (where the broadening is mainly due to the UV divergence slightly exceeding the crystal acceptance).
To check the reliability of this result, a fiber connected to the commercial spectrometer was placed in a mount whose knobs allow a transverse translation of the fiber head. I numbered each position of the knob and I scanned the spatial profile of the 205 nm beam. In fig. 5.19 an example of measurement is reported. In each position I reported the am-

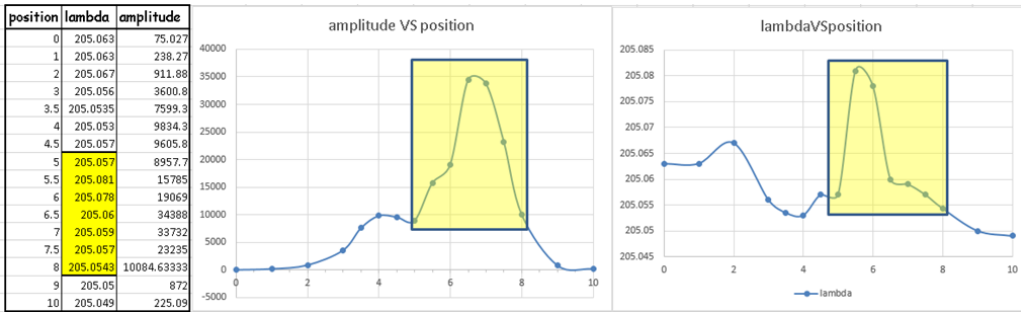

position	lambda	amplitude
0	205.063	75.027
1	205.063	238.27
2	205.067	911.88
3	205.056	3600.8
3.5	205.0535	7599.3
4	205.053	9834.3
4.5	205.057	9605.8
5	205.057	8957.7
5.5	205.081	15785
6	205.078	19069
6.5	205.06	34388
7	205.059	33732
7.5	205.057	23235
8	205.0543	10084.63333
9	205.05	872
10	205.049	225.09

Figure 5.19: Example of a measurement concerning the wavelength shift of the 205 nm along the beam transversal section. For each position of the mount knob (numbers are only indicative), the amplitude and the central wavelength were measured with the commercial spectrometer. Then, the FWHM was associated to the related band shift. In this example, a bandwidth of 0.027 nm was measured.

plitude and the central wavelength acquired with the AvaSPEC spectrometer. The measured bandwidth $\Delta\lambda_{\text{meas}}$, had to be convolved with the band acceptance of the crystal $\Delta\lambda_{\text{BBO}}$ and deconvolved with the spectrometer central wavelength resolution res $= 0.01$ nm (half the pixel width of the spectrometer):

$$\Delta\lambda_{\text{fin}} = \sqrt{\Delta\lambda_{\text{meas}}{}^2 + \Delta\lambda_{\text{BBO}}{}^2 - \text{res}^2} \tag{5.9}$$

The $\Delta\lambda_{\text{meas}}$ had a big instrumental error of about 95 GHz, hence this result is meant to be just a check of the input beam divergence measurement. By making the average of the measurements and considering the big error, the resulting spectrum was 208 ± 95 GHz with an horizontal scan, and 122 ± 95 GHz with a vertical scan. It is worth noting that both measurements give a result compatible with the divergence method ones, while it is incompatible with the direct measurement with the spectrometer: even if we deconvolve the measured spectrum with the spectrometer resolution, we find a FWHM higher than 400 GHz. At the same time, the difference between the horizontal and vertical measurements is compatible with the phase matching configuration of the sum process. This non-collinear process lies on the horizontal plane, and, therefore, exceeding the acceptances widens the spectrum on that plane more than in the vertical plane.
A weighted average of these two kind of measurements gives a spectrum of 128 ± 10 GHz. Therefore, the small divergence of the 266 nm during the Ps excitation experiment didn't affect too much the spectrum width. The simulated spectrum in fig. 5.18, therefore, is suitable to perform reliable Ps excitation simulations.

In the following, I will describe the Rydberg part of the AEgIS laser system and how we deliver the laser beams inside the Bread Box.

5.3 Laser system for the n=3 → Rydberg Positronium excitation

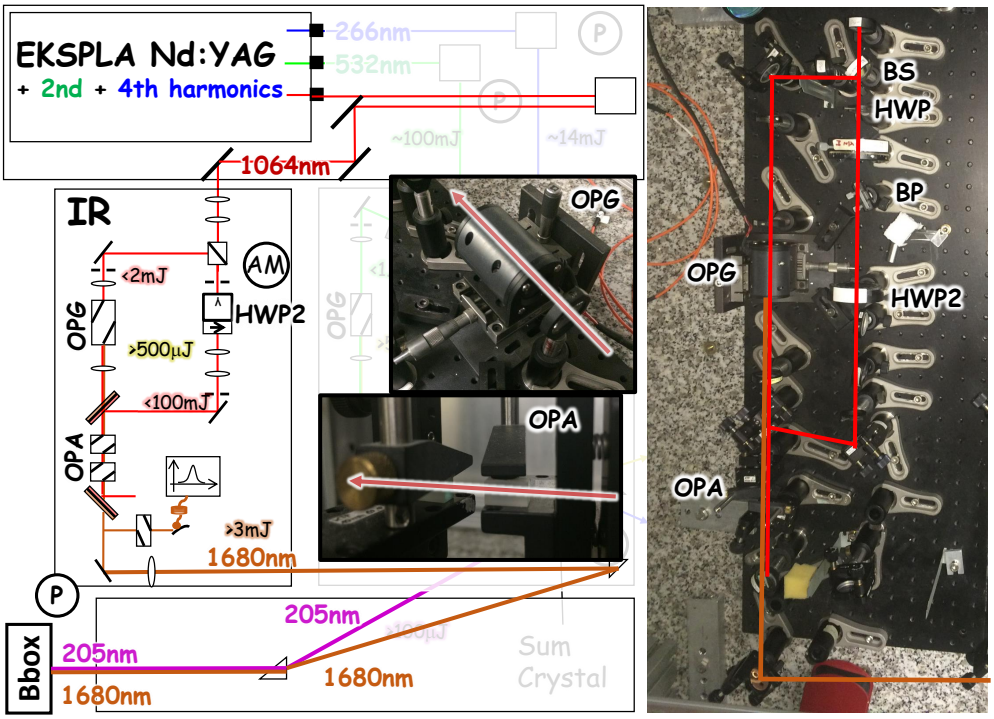

Figure 5.20: On the left: sketch of the laser system part dedicated to the $1670-1720$ nm generation. Small pictures of the nonlinear crystals' arrangement are reported. On the right: a picture of this system section as it was at CERN in the AEgIS laser hut at the moment of the Ps excitation measurements. Radiation paths are drawn, in order to facilitate the comprehension of the picture. On the picture: BS = beam splitter; HWP = half wave plate; BP = brewster plate; On the sketch: P = periscope; AM = HWP + BP (Amplitude modulator); triangles = prisms. In each important part, values of the needed/suggested energy are reported, each one shaded according to the associated wavelength.

In this section, the AEgIS strategy to produce the $1670-1720$ nm radiation will be explained. In fig. 5.20 all the optics dedicated to the $1670-1720$ nm radiation are sketched. Differently from the $n = 3$ excitation case, for the Ps Rydberg excitation the opportunity of choosing the output wavelength is a fundamental prerequisite. The choice of the wavelength, in fact, is connected to the Rydberg level to excite. Being Rydberg levels very close, with a range of $1670 - 1720$ nm we are able to excite Ps levels from $n = 15$ to $n = 21$. The saturation fluence for this transition is equal to of 0.98 mJ/cm^2 [35], corresponding to ~ 140 μJ for a 3 mm FWHM spot. The generation scheme of the desired wavelength is the same of the 894 nm case, but with a PPKTP crystal (see table 5.5 for specifications) with a different period with respect to the UV line one, and the working temperature that covers the $1675 \div 1720$ nm band is $30 \div 180$°C. Again here, a beam splitter splits the 1064 nm beam into two parts: less than 1.5 mJ reaches the OPG (for crystal safety reasons), after reducing the spot to ~ 600 μm of FWHM with a telescopic system, to generate the $1675 \div 1720$ nm radiation; the reminder will be the OPA pump for the OPG seed amplification step. From the OPG ~ 500 μJ of $1675 \div 1720$ nm are obtained. This seed will enter the OPA system with vertical polarization. In this case,

$1064\text{nm}_{(o)} \rightarrow 1675 \div 1720\text{nm}_{(o)} + 2920 \div 2790\text{nm}_{(o)}$	
d_{eff}	9.4 pm/V
period	37.4 μm
crystal length	30 mm
crystal input face	2×1 mm^2
critical intensity	200 MW/cm^2

Table 5.5: PPKTP crystal main specifications: IR line. The period is the one decided by the manufacturer, given the desired output parameters.

$1064\text{nm}_{(o)} \rightarrow 1675 \div 1720\text{nm}_{(o)} + 2920 \div 2790\text{nm}_{(e)}$	
d_{eff}	-3.10 pm/V
crystal length	10 mm
crystal input face	5×5 mm^2
critical intensity	2.4 GW/cm^2
bandwidth acceptance	2.12 THz·cm
temperature range	$33.84 \div 34.22$ K·cm
PM angle	$67.6 \div 64.2°$
walk-off angle	$32.6 \div 36.45$ mrad

Table 5.6: OPA crystals main specifications: IR line.

KTP crystals are used, and the phase matching is achieved by using ordinary signal and pump, while the idler is extraordinary.
In order to have an ordinary 1064 nm, a Half Wave Plate (HWP) is placed just after the AM that makes the polarization vertical. Both OPA crystals have their axes on the horizontal plane, but with symmetric configuration (to compensate the walk-off effect). After the OPA system the spectrum of the generated radiation is measured with the same `Thorlabs` spectrometer used for the 894 nm line. Being the wavelength out of its range, we first double the frequency of the beam with a LNB crystal (*Lithium niobate*[12]). The second harmonic $837.5 \div 860$ nm is then detectable and gives immediately the value of the first harmonic's wavelength.
From this point, the goal is to superimpose this beam to the UV one and deliver them into the Bread Box to excite Ps atoms.

5.4 Laser transfer line for Positronium photoionization

In both UV and IR lines, one can use lenses or telescopic systems after the last nonlinear step in order to adjust the spot dimension to the value required inside the breadbox. I will not consider these optics part of the transfer line. In this section, I will describe the transfer line configuration for two Ps excitation measurements: Ps $n = 3$ excitation (detected via photoionization of the *n=3* level with the 1064 nm) and Ps Rydberg excitation (detected without auxiliary processes). In both cases, all the involved pulses have to

[12]The LNB susceptibility tensor (from `SNLO`) is: $d = \begin{pmatrix} 0 & 0 & 0 & 0 & -4.6 & -2.6 \\ -2.6 & 2.6 & 0 & -4.6 & 0 & 0 \\ -4.6 & -4.6 & -25.0 & 0 & 0 & 0 \end{pmatrix}$ (pm/V)
.

reach the Bread Box plane: while the AEgIS production trap is at the same level as the laser board, the breadbox is located at the accumulator height (see fig. 1.2). In fig. 5.21 a scheme of the top view of both configurations is shown. On the "ground floor" table all the required wavelength for Ps excitation are generated, while a sort of "first floor" table hosts both a 243 nm dye laser (of the Orsay research group) and all the transfer line optics.

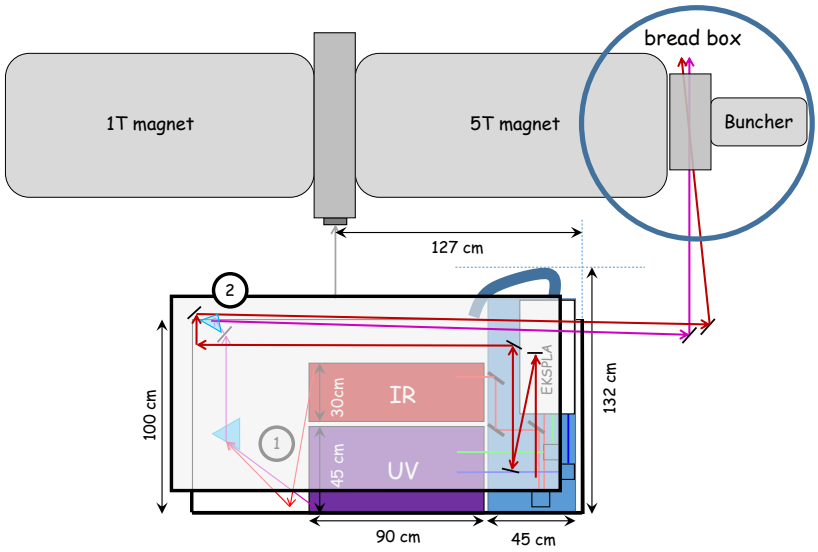

Figure 5.21: Laser transfer line towards the Bread Box. Circled 1 and 2 represent the ground floor and the first floor ($\sim$ 2 m above ground) respectively.

5.4.1 Rydberg excitation transfer line

In order to perform a Ps Rydberg excitation measurement, we need to deliver both the 205 nm and the $1675 \div 1720$ nm inside the Bread Box. There are two main steps:

1. Superimpose UV and IR beams
2. Bring them towards the breadbox

The superposition of the two beams is achieved with a fused silica prism immediately after the respective generation, on the ground floor table (circled 1 in fig. 5.21). By sending the two beams at the right respective angles toward the prism, it superimposes them and diverts the couple toward an aluminum ultra wide-band mirror facing upwards. This mirror sends the beams to the first floor table, where a prism deviates them outside the laser hut. Placed in line with the converter, another aluminum ultra wide-band mirror delivers the Rydberg excitation pulses through the Ps cloud exiting the converter.

5.4.2 Ps photoionization transfer line

For the photoionization experiment, with which we detect the $n = 3$ Ps excitation, we need to invest the Ps cloud with both 205 nm and the ionizing 1064 nm pulses simultaneously.

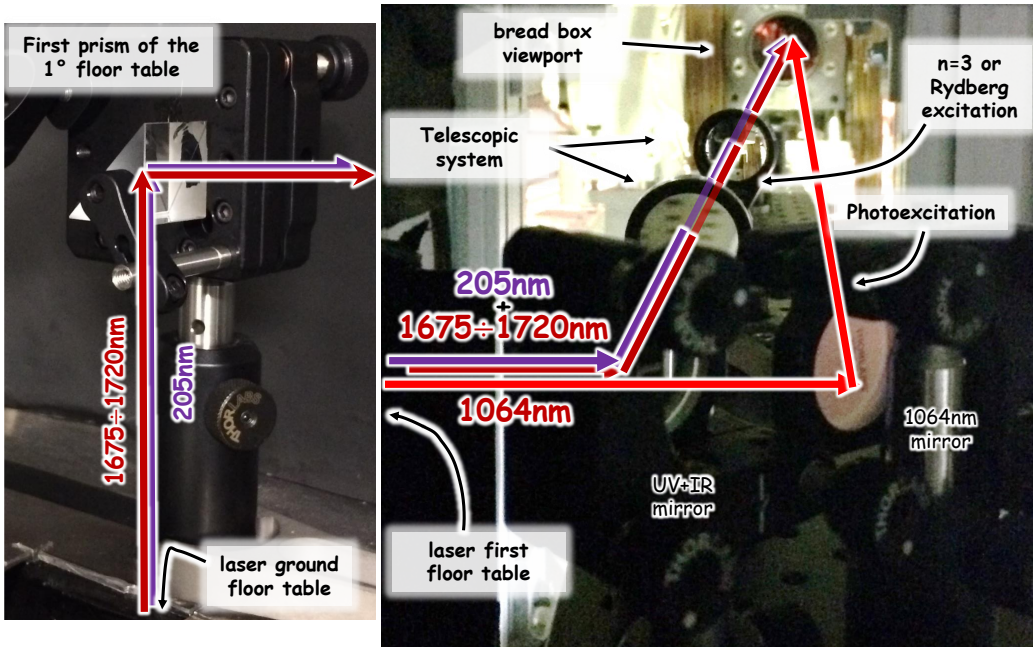

Figure 5.22: On the left, the first prism met by the two excitation beams, on the first floor table. They are sent, then, outside the laser hut, towards the same aluminum ultra wide-band mirror. On the right, the last part of the transfer line: another aluminum ultra wide-band mirror delivers the 205 nm (or the $205\text{nm} + 1675 \div 1720$ nm) in front of the Ps converter, inside the Bread Box , whose viewport is visible in the picture. Another mirror is needed for the photoionization experiment, in order to send the ionizing 1064 nm in front of the converter together with the 205 nm.

While the 205 nm path is exaclty the same as that of the Rydberg excitation measurement, for the 1064 nm we had to make a new line, by taking care also of the temporal overlap of the two pulses.
In this case, the spatial overlap between the two beams is only temporary and occurs only in front of the Ps converter.
In fig. 5.21, the configuration of the optics (on the first floor table) dedicated to the 1064 nm transfer towards the Bread Box is visible. Another hole in the first floor table allows us to send upstairs the 1064 nm directly from the harmonic generator output. After that, it passes through a set of optics, needed for setting up a suitable delay line. The 1064 nm is then sent outside the laser hut, alongside the 205 nm. In fig. 5.22 the last mirror sending the 1064 nm towards the target region is shown, and it will overlap the 205 nm just in front of the Ps converter.

Detection of the laser alignment in the Bread Box

We checked the alignment of the beams inside the breadbox by using the macor screen attached to the converter attenuator (see fig. 2.19). It emits light when invested by the UV light and the 1064 nm radiation, while it doesn't when invested with the $1675 \div 1720$ nm. In this case, we used the LNB crystal on the $205 + 1675 \div 1720$ nm path in order to double the IR frequency: in this $837.5 \div 860$ nm range the macor is able to re-emit the light. Therefore, with a CCD camera we can capture the macor screen luminescence. At

this point, once we had our reference position (the one that optimizes the excitation efficiency), it was trivial afterwards to set up every day the pulse position with the optimal configuration. The CCD was placed in front of a small viewport underneath the laser's one, at a $45°$ angle. An example of alignment reference is depicted in fig. 5.23.

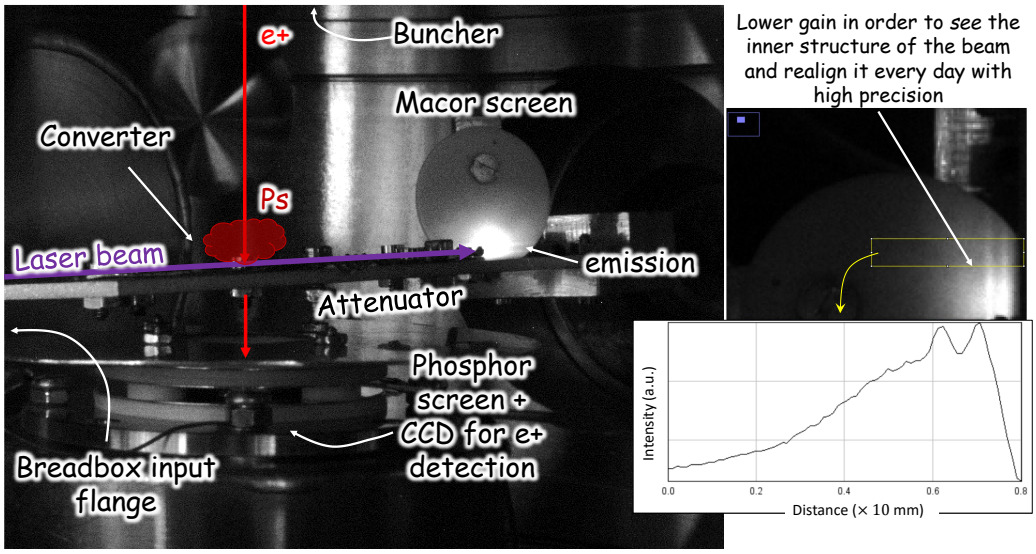

Figure 5.23: On the left, how the CCD *sees* inside the Bread Box. Indications of the mutual position of the objects inside the Bread Box are given. On the right, a low gain picture of the Macor emission, giving a high precision reference for the every day laser setting up. Kind of reflections are visible in this picture, allegedly due to the attenuator aluminum surface.

205 nm transport efficiency

The UV light is absorbed by air (as a matter of fact from oxygen and water vapour). Therefore, the further away one wants to deliver it, the more energy one loses. Therefore, in addition to the reflectivity of optics, the covered distance is an important parameter to take into account.

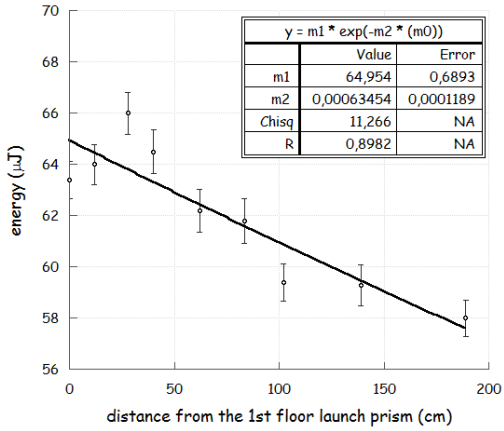

Figure 5.24: UV energy measured with the energy meter as a function of the position. Exponential fit data in the inset.

In the AEgIS laser transfer line, in order to measure the percent loss I measured the

UV energy with the energy meter all along a 2 m path free of optics. I estimated losses of $(6 \pm 1)\%/\text{m}$ (see data plot in fig. 5.24).

The UV light travels for ~ 4.5 m before entering the Bread Box (kept in vacuum). Therefore a $\sim 25\%$ loss in the AEgIS transfer line is due to air absorption of the 205 nm light. Another 25% is due to the optics' reflectivity. The power reaching the Ps target in typical excitation measurement conditions is 54 μJ.

CHAPTER 6

A geometrical simulation of Ps excitation

In this chapter I show results of my `c++` code where the breadbox geometry and the spatial properties of the exciting beam are modelled and SSPALS spectra are simulated. This simulation was very useful in order to have broad indications about the most convenient spatial configuration for the Ps excitation measurement. We can have, for example, a rough estimation of the temporal and spatial overlap between lasers and the Ps cloud by varying a large number of parameters. Simulating SSPALS spectra is crucial for our understanding and prediction of the effects of Ps excitation/ionization on the real Ps lifetime curve.
In this simulation, lasers spectral and spatial properties are input parameters. In the first period of my work, the spectral properties and the excitation efficiency parameters for the simulation came from calculations related to the work in [35]. In the last period I worked on a `Labview` simulation, where the excitation efficiency of a laser pulse is estimated in relation to the spectral profile. The simulation results concerning the generated laser spectra have been shown in chapters 4 and 5, while results of the attainable excitation efficiency depending on these spectra will be explained and reported in chapter 7.
These two simulations could potentially provide the ingredients to make an estimation of the global excitation efficiency we can achieve in AEgIS. On the other hand, an effort could be done to merge them into a global simulation.

6.1 The general idea of the Montecarlo simulation

My code is a Montecarlo simulation, where I simulate the whole Ps formation + Ps excitation + gamma ray emission and detection process *atom by atom*. At the end, I sum up all the results for a number N_{tot} of Ps atoms (equal to the real number of Ps atoms generated per positron bunch). For each atom the following stages are simulated:

- Ps emission from the target (parameters from [31], [88] and all related works)
- random velocity assignment to the atom.
- Ps propagation in the vacuum chamber.
- Ps excitation
- Ps gamma ray emission, due either to annihilation in flight or to collisions with the Bread Box surfaces (including the detector surface)
- gamma ray detection

Finally, data about detected gamma rays are collected in a histogram and annihilation points of all positronium atoms are plotted in a three-dimensional graph.

6.2 Simulation description

In this section I am going to describe the stages of the simulation. In particular I will describe the idea and the tools I used.

6.2.1 Positronium emission simulation

As already said before, Ps emission from the target in the simulation follows the literature information. All the parameters can be changed at will.
I take into account the positron beam spatial and temporal profile. The spatial profile determines the spatial distribution of Ps emission point from the converter, while the temporal profile determines the emission time distribution of Ps atoms. For the latter issue, I can control the time spent by Ps inside the converter (higher values are linked to higher positron implantation energies, [31, 100]).
At this point, each atom needs a velocity and a direction, in order to propagate with *uniform linear motion*[1] inside the chamber. For the longitudinal direction, the random velocity is taken by the velocity distribution measured in [31] (I used a 10% of 305 K Ps and a 90% of 1515 K Ps). For the transverse direction, it is taken from a bidimensional Maxwellian distribution (the temperature is a tunable parameter). This stage ends up with a Ps atom whose direction and velocity are given. Taking into account the atom lifetime, each Ps atom will be given a certain "death" time. When the laser excitation is simulated, it depends also on whether it is excited or not.
Once the atom dies, it emits two or three gamma rays (depending on the annihilation process). If the above stage makes the atom live long enough to reach the walls, it will annihilate into two gamma rays[2], otherwise it will annihilate in flight into three gamma rays, because it is assumed that the Ps atom exits the converter in the long-living triplet state [31].
I assumed a null Ps atom velocity with respect to the speed of light: in this way I simulated an isotropic gamma ray emission for Ps annihilating in flight (despite the energy and momentum conservation, the overall gamma ray distribution at the end can be assumed uniform[3]) and, for Ps annihilation on the walls, I randomly chose an angle (isotropically in space) and I made both photons lie on the same straight line but propagate in opposite directions.
At this point, gamma rays could intersect the detector and generate a signal.
All the stages of this geometrical part of the simulation can be monitored by plotting Ps positions at each step. In fig. 6.1, we see on the left the schematic chamber geometry, where real distance values are used. In order to check the position of the surfaces where Ps atom could annihilate, one can give Ps a very long life. In fig. 6.1, only half chamber is represented, that means the half space delimited by the positron entrance face and the converter plane. Green points represent Ps annihilations on the walls. The Bread Box geometry is observed and also annihilations on the detector surface facing the converter can be seen (simulation test 1). In the test 2 image, Ps annihilation (real) point are shown. A big fraction of Ps atoms annihilates close to the converter. By plotting the intersections between emitted gamma-rays and the detector, the detector geometry is checked. Test 3 is dedicated to the laser excitation. Pink dots represent Ps atom position when (if) they are excited by the laser.

[1] Assuming negligible the very small deviations due to presence of magnetic field or electric field gradients, as in the real experiment (see for example [101]).

[2] A 100 % annihilation probability is assumed as walls are made of aluminum. But in other material this assumption could not be realistic [102]

[3] I made this assumption mainly for computing time issues

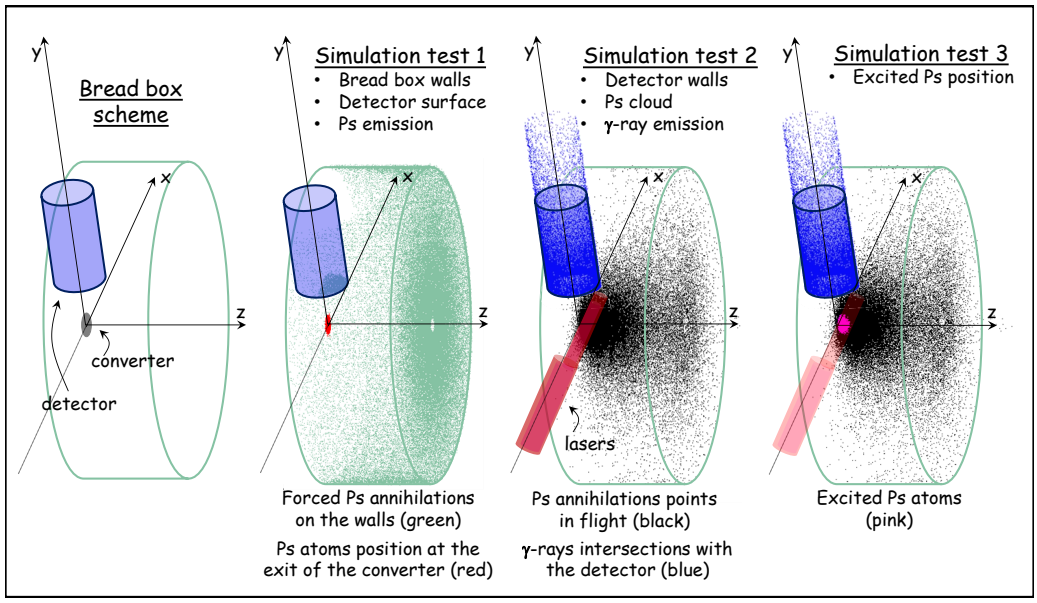

Figure 6.1: Geometrical tests on the simulation.

6.2.2 Laser parameters simulation (spatial and spectral)

With the software `mathcad`, I simulate the transverse shape of the laser pulse. Then I simulate the excitation probability of the laser depending on the Ps distance from the laser propagation axis. A saturation behaviour is embedded in this software simulation, together with a spectral efficiency (that is not connected to the simulation presented in the next chapter). These two informations came from the same calculation procedure leading to the publication of [35]. At the time of the c++ simulation implementation, spectral considerations about the AEgIS laser shown in the following chapter had not been done yet. From this `mathcad` simulation, all the parameters concerning the laser

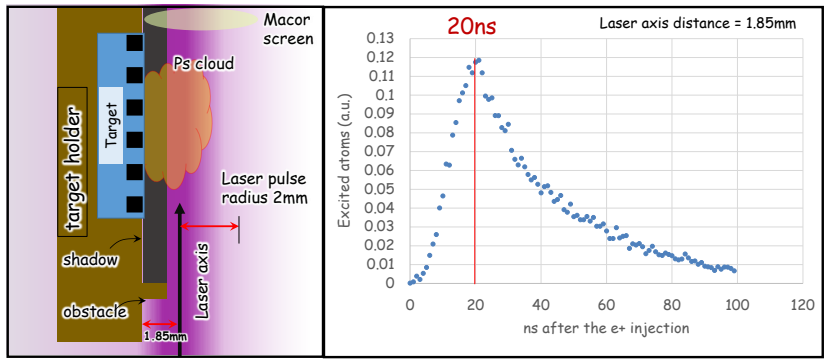

Figure 6.2: On the left, the optimal spatial configuration for the 4×6 mm$\times$mm UV laser. We use an obstacle to prevent the laser hit the converter. On the right, the delay time optimization curve. With our parameters, the optimum delay time given by the simulation between the positron implantation and the laser pulse is 20 ns.

excitation were obtained and included inside the c++ code. This part of the simulation was crucial for finding out that the laser had to be shined with the propagation axis as close as possible to the converter. This is the reason why the laser depicted in fig. 6.1 has that shape, and almost half of the beam is lost. In fact, the simulation shows that it is worth loosing almost half the beam, in order to get closer to the target with the laser axis. If not, the laser axis would be far from the converter, meaning that the laser should be shined later. In this way a huge fraction of Ps atoms would die before reaching the maximum intensity region, and therefore excitation for all these atoms would occur with smaller probability. In fig. 6.2 the laser position with respect to the converter is sketched (left panel). Few hundreds of μm of shadow were made in order to prevent damages of the converter due to the UV light. It is worth comparing this image to fig. 5.23, where the configuration used for the Ps excitation measurement is reported. Indeed, the macor screen shows the proximity of the laser to the converter. In fig. 6.2, right panel, for a 1.85 mm distance of the laser from the converter, we see a delay time optimization plot. By shining the laser 1.85 mm away from the converter, the plot indicates that the optimum laser delay time after the positron injection into the converter is 20 ns. I made several of these plots, depending on the laser distance from the converter. What happened was that the further the distance of the laser, the broader the optimization curve, the more the peak is delayed but the lower the related Ps excited fraction obtained. During the Ps excitation experiment, a delay time of 16 ns was used, because of trigger timing discretization issues[4].

6.2.3 Gamma rays detection simulation and SSPALS generation

In the code, scintillator + photomultiplier (PMT) gamma ray detection is simulated. The

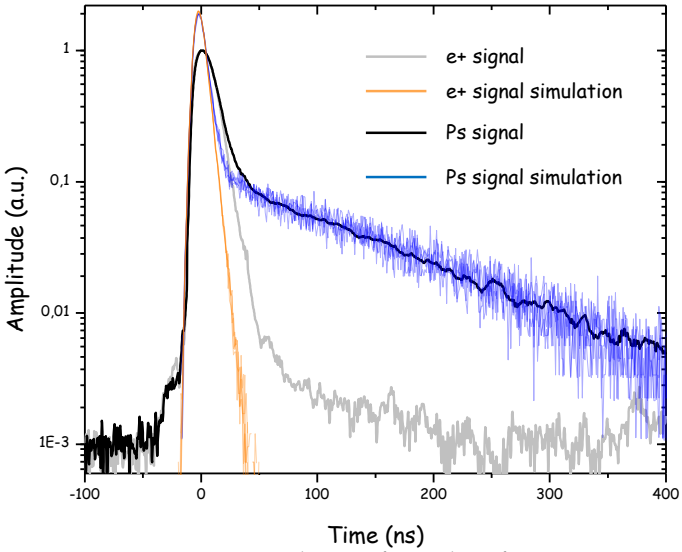

Figure 6.3: Simulation of signals in fig. 3.2

code checks if the gamma ray intersects the detector, then the detector efficiency parameter is used to decide if the photon has to be detected or not. When the photon is detected, then the decay time of the scintillator is taken into account in order to give the detection the proper resolution. By making an histogram with the gamma detection time of all the

[4]It was possible to set a delay time with steps of 8 ns starting from 0

atoms, I obtain the SSPALS spectrum. In fig. 6.3 I superimpose the simulation results to the spectra in fig. 3.2. This superimposition triggers several remarks. First of all, Ps lifetime curve is well simulated. The orange curve is the simulation of the background present in fig. 6.3, and we see that a small tail is missing. It could be explained with the presence of electrical noise in the real measurement, but also with a very small fraction of Ps generated inside the MCP and suddenly annihilating. But the only "big" discrepancy with the data concerns the prompt peak width, for both signals. The explanation is very likely related to a detector saturation process when a high number of gamma rays is detected[5]. Then, the normalization to 1 makes the rest: the peak after the normalization gets broader than it actually is. This feature should be added to the simulation code in the future, by, for example, simulating the dead time of the detector or simulating the phenomenon of back scattered positrons.

6.2.4 Photoionization signal simulation

Here I will briefly explain the AEgIS photoionization strategy in order to understand how SSPALS spectra are affected from the photoionization process and show how simulation behaves when this process is added to the code.
The idea is to excite Ps to the $n = 3$ level with the 205 nm pulse and to photoionize only excited atoms with a 1064 nm pulse. These two pulses are sent simultaneously, in order to be able to have a three-state dynamics (see section 7.4). Photoionization immediately depopulates uniformly the SSPALS spectrum tail, as it "kills" almost all Ps atoms excited by the UV laser. This means that the spectrum tail should go down rigidly. In fig. 6.4 I report the result of my simulation.

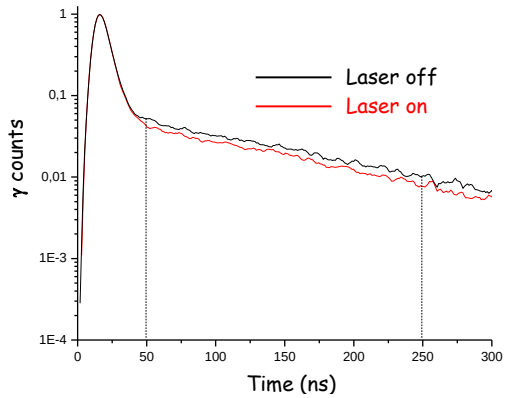

Figure 6.4: Simulation of Ps photoionization effect on SSPALS spectra.

Simulated SSPALS spectra behave as expected[6]. The estimation of the photoionized Ps fraction is given by the formula:

$$\text{eff}_{\text{PI}} \approx \frac{A_{\text{ON}} - A_{\text{OFF}}}{A_{\text{OFF}}} \tag{6.1}$$

where A_{ON} and A_{OFF} are the area delimited by the dashed lines in fig. 6.4 for (UV + ionizing) laser ON and (UV + ionizing) laser OFF simulation respectively.

[5]Check measurements were done to confirm this feature.

[6]Note that, being the number of Ps atoms in the simulation equal to the real one, a comparison is possible between simulations and measurements.

I will explain better in chapter 8 the AEgIS strategy for detecting Ps $n = 3$ excitation, wheresimulation and measurement will be compared.

CHAPTER 7

Positronium n=3 excitation spectral simulation

In this chapter I will show results of my simulation about the Ps $n = 3$ excitation efficiency from the *spectral* point of view. The simulation shows how both global and internal structures of the exciting radiation spectrum can affect the efficiency of the process. In this respect, a comparison between the excitation efficiency simulated for our 205 nm spectrum and for another kind of spectrum is proposed.

7.1 Simulation of Ps excitation efficiency: the influence of the spectrum shape

My analysis concerns the dynamics of a two level system. Here, following [35], we consider the most probable transition of a Ps atom that is laser-excited from ground towards an excited level. The aim is to understand how the spectral profile of the exciting radiation can affect the efficiency of the process. In this section, a rate equation model will be presented and applied to two real cases:

1. Ps excitation from ground state to the $n = 2$ level with a comb-shaped spectrum at 243 nm: this radiation is obtained via second harmonic generation from a dye pump laser, whose spectrum is comb-shaped and peaks are spaced a FSR apart.
2. Ps excitation from ground state to the $n = 3$ level with a spectrum that is not comb-shaped at 205 nm: this radiation comes from an OPG plus a SFG process (where one input spectrum exceeds the crystal spectral acceptance), thus the comb-structure gets lost and the output spectrum is shaped by the crystal.

The main goal is to demonstrate how the AEgIS strategy of generating radiation from vacuum introduces the opportunity to improve the Ps excitation efficiency (with respect to the use of a comb-shaped spectrum with a Gaussian envelope).

7.1.1 Rate equations

Consider a two level system and an exciting radiation. This radiation can either excite or de-excite the atom, in a stimulated way. The higher level can also spontaneously decay. In fig. 7.1 a sketch of the system is depicted. Suppose to have a near monochromatic laser pulse of spectral energy E, with a transverse area S and a time duration Δt. We call $\rho = \frac{I}{c}$, with $I \approx \frac{E}{S\Delta t}$, the *energy (spectral) density* of the exciting radiation, $\tau_s = \frac{h\nu}{\sigma I}$ the *stimulated decay time* and τ the *spontaneous decay time*. This formula for τ_s comes from:

$$\tau_s = \frac{1}{\sigma c X} = \frac{h\nu}{\sigma c \rho} = \frac{h\nu}{\sigma I} \tag{7.1}$$

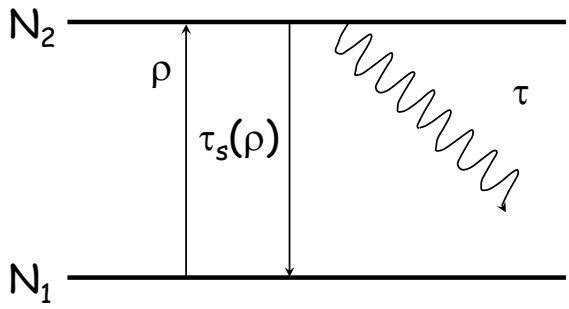

Figure 7.1: Scheme of a two level excitation process. The pump energy density ρ affects stimulated absorption and emission processes (straight arrows), whose characteristic time is $\tau_s(\rho)$. In addition, we have spontaneous emission (undulated arrow), with a characteristic time τ independent on the radiation.

Where X is the number of photons per unit volume, h is the Planck constant, ν is the frequency of the exciting radiation and σ is the cross section of the considered interaction. We already know that radiation induces both stimulated emission and absorption, therefore τ_s must have a dependence on the radiation properties. On the contrary, the spontaneous emission is not linked to the incoming radiation and, therefore, there is no dependence on its properties.
Now, if N_2 is the population on the higher level, that is the excited level, and N_1 is the population of the lower level, that we consider from now on to be the ground state, we have:

$$\begin{cases} \dfrac{dN_2}{dt} = \dfrac{1}{\tau_s}N_1 - \dfrac{1}{\tau_s}N_2 - \dfrac{1}{\tau}N_2 \\ \\ \dfrac{dN_1}{dt} = -\dfrac{1}{\tau_s}N_1 + \dfrac{1}{\tau_s}N_2 + \dfrac{1}{\tau}N_2 \end{cases} \tag{7.2}$$

By defining $N := N_1 + N_2$ and considering the excited level, we find

$$\begin{aligned} \frac{dN_2}{dt} &= \frac{1}{\tau_s}(N - N_2) - \frac{1}{\tau_s}N_2 - \frac{1}{\tau}N_2 = \\ &= \frac{N}{\tau_s} - \frac{2}{\tau_s}N_2 - \frac{1}{\tau}N_2 \Rightarrow \\ \Rightarrow \frac{dN_2}{dt} &= \frac{N}{\tau_s} - \left(\frac{2}{\tau_s} + \frac{1}{\tau}\right)N_2 \end{aligned} \tag{7.3}$$

When the system reaches the stationary state, that means $\dfrac{dN_2}{dt} = 0$, we have a population

$$\begin{aligned} N_2^0 = \frac{N}{\tau_s\left(\dfrac{2}{\tau_s} + \dfrac{1}{\tau}\right)} = \frac{N}{2 + \dfrac{\tau_s}{\tau}} = \frac{N}{2 + \dfrac{h\nu}{\sigma\tau I}} \Rightarrow \\ \Rightarrow N_2^0 = \frac{\dfrac{N}{2}}{1 + \dfrac{h\nu}{2\sigma\tau I}} \end{aligned} \tag{7.4}$$

We define $\frac{1}{\tau^*} := \frac{2}{\tau_s} + \frac{1}{\tau}$ so to write the solution of eq. (7.3) as follows:

$$N_2(t) = N_2^0 \left(1 - \mathrm{e}^{-\frac{t}{\tau^*}} \right) \tag{7.5}$$

As we want to know the population at the end of the laser pulse, we consider $t = \Delta t$. For the following, we expand the $\frac{t}{\tau^*}$ exponent:

$$\frac{t}{\tau^*} = \Delta t \left(\frac{2}{\tau_s} + \frac{1}{\tau} \right) = \frac{2\Delta t \sigma I}{h\nu} + \frac{\Delta t}{\tau} = \frac{2\sigma E}{h\nu S} + \frac{\Delta t}{\tau} \tag{7.6}$$

When considering constant all other physical quantities in this equation, we immediately see that the population N_2 exhibits a saturating trend as a function of the laser pulse energy E.

Positronium Doppler bandwidth

The positronium cloud emitted from the converter is not monochromatic, this means that atoms do not have the same velocity, with the consequence of different excitation frequencies. The cloud has therefore a Doppler bandwidth, that depends on several parameters (see chapter 3). The most important are the pore dimension, the positron implantation energy and the converter temperature. When the laser pulse arrives, each atom has a different velocity along the pulse propagation direction. If we send a *monochromatic* exciting laser at the resonance frequency ν_0 towards the cloud, each atom "sees" a different frequency, ν_0', depending on its velocity. When ν_0' is out of the natural linewidth of the level we want to excite, the atom is no more resonant with the radiation and no excitation can occur. For this reason, a *broadband* laser pulse gives the opportunity to excite atoms that are not resonant with the central frequency of the laser pulse due to their velocity. As a disadvantage, in this way we spread the pulse energy over a wider range of frequencies, thus reducing $E(\nu)$.
The AEgIS exciting laser has a large bandwidth, therefore it fulfils the requirement of high excitation efficiency for a broadband cloud of Ps atoms emitted in vacuum from the converter.
Here, we are interested in studying the Ps Doppler spectrum along the laser beam direction z. The Doppler width is then related to the temperature of the Ps cloud via the Maxwell -Boltzmann unidimensional normalized distribution

$$P_{\mathrm{MB}}(v_z) = \sqrt{\frac{m_{\mathrm{Ps}}}{2\pi K_B T}} \mathrm{e}^{-\frac{m_{\mathrm{Ps}} v_z^2}{2k_B T}} \tag{7.7}$$

where m_{Ps} is the Ps mass, K_B is the Boltzmann constant, T the Ps cloud temperature and v_z is the Ps velocity along the z axis.
This can be translated directly into a Doppler distribution Ps(ν), depending on the frequency ν:

$$\nu_0 = \nu \left(1 - \frac{v_z}{c} \right) \Rightarrow \nu = \frac{\nu_0}{1 - \frac{v_z}{c}} \approx \nu_0 \left(1 + \frac{v_z}{c} \right) \Rightarrow v_\nu \approx c \left(\frac{\nu}{\nu_0} - 1 \right) \tag{7.8}$$

where I called v_ν the Ps velocity along the z axis giving a frequency shift of $\nu - \nu_0$. By substituting v_ν in eq (7.7), we obtain a Ps Doppler profile[1]

$$\mathrm{Ps}(\nu) = A\mathrm{e}^{-2\frac{(\nu-\nu_0)^2}{\left(\frac{\Delta\nu_{\mathrm{Ps}}}{\sqrt{2\ln(2)}}\right)^2}} \tag{7.9}$$

where A is a suitable normalization coefficient such that

$$\int \mathrm{Ps}(\nu)d\nu = 1 \tag{7.10}$$

and the FWHM $\Delta\nu_{\mathrm{Ps}}$ is

$$\Delta\nu_{\mathrm{Ps}} = 2\sqrt{2\ln 2}\sqrt{\frac{\nu_0^2 K_B T}{mc^2}} \tag{7.11}$$

In the Ps excitation measurements where Ps was only partially cooled in the converter at room temperature, it is $\Delta\nu_{\mathrm{Ps}} \approx 1000$ THz (see chapter 8).
It is clear that eq. (7.5) holds for a monochromatic Ps cloud in resonance with ν_0, while, in the case of AEgIS, we have a large Doppler bandwidth for the Ps cloud (that takes each atom out of resonance with the central frequency of our pulse) and a broadband laser is essential to keep $N(t) \neq 0$ for a certain range of frequencies. In the following I will describe the model I used in Labview in order to translate this concept into a simulation that calculates the excitation efficiency of a not monochromatic Ps cloud with a broadband laser.

7.2 The importance of the exciting spectrum properties in Ps excitation

Wavelengths required for Ps excitation are not typical lasing wavelengths. Therefore, until now they have been generated by using nonlinear crystals. The output spectrum of such crystals strictly depends on the crystal properties and the involved nonlinear process. The crystal spectral acceptance affects the total width of the output pulse, while the chosen nonlinear process and the nature of the input spectra affect the inner structure of the spectrum.
Consider the case of a SFG process (including also SHG). Each input beam can have either a comb-shaped or a continuous[2] spectrum, and a spectrum envelope width either lower or higher than the crystal acceptance. In the following, we will call the envelope width simply *spectrum width*. When the input spectrum width exceeds the crystal acceptance, the output spectrum is reduced with a sinc-wise envelope by the crystal, therefore in this case the original spectrum envelope is no longer present in the crystal output beam. On the other hand, when at least one of the input spectra is continuous, the output beam will be continuous, provided that the other beam (even if is not continuous) has a comb-structure with a typical width smaller than the continuous one. All these effects have been fully explained already in chapter 4 and 5. At the end, we have four possible scenarios:

(a) *input comb-shaped spectra*:

[1] Thanks to approximation (7.8), we don't have ν as a denominator of the exponent.
[2] "Holes" in the spectrum, if present, don't drop all to zero.

1 *within the crystal acceptance* ⇒ comb-shape is preserved and the output spectral envelope only depends on the input beam spectral envelopes

2 *exceeding the crystal acceptance* ⇒ comb-shape is preserved and the output spectral envelope depends on the crystal properties

(b) *at least one continuous input spectrum*:

3 *within the crystal acceptance* ⇒ comb-shape is lost but the output spectral envelope still depends on the input beam spectral envelopes

4 *exceeding the crystal acceptance* ⇒ comb-shape is lost and the output spectral envelope depends on the crystal properties

The aim is to demonstrate that the choice of one of these scenarios heavily affects the excitation efficiency.
In order to do this, I make a comparison between the excitation efficiencies of two different lasers and transitions: Ps $n = 2$ excitation with a laser pulse @ 243 nm and comb-shaped spectrum, Ps $n = 3$ excitation with a the AEgIS laser pulse at 205 nm. The choice to study these two transitions is not random: in literature we read that Rydberg Ps excitation is usually achieved via a two-step excitation, passing through the $n = 2$ level. The usual way to generate the 243 nm radiation is via SHG of a dye laser output [103] at 486 nm. This gives to the 243 nm pulse a comb-shaped spectrum and, as in general the input spectral widths are far below the crystal acceptances, a Gaussian envelope (determined by the dye laser): we are in ***case 1***. On the contrary, as I explained in the previous chapter, in AEgIS we have an OPG step where a continuous broad spectrum is generated. The 894 nm large spectrum far exceeds the BBO spectral acceptance: we are in ***case 4***.
I will demonstrate that being in ***case 4*** affects positively the excitation efficiency and that, even if the cross section of the $n = 3$ transition is lower than the $n = 2$ one, we may offset, or indeed outweigh, this disadvantage.
It would be essential, at this point, a comparison with experimental data.

7.2.1 @243nm generation simulation

In order to simulate the spectrum of the 243 nm laser used by *Cassidy et al.* in [103], I used specifications of their laser, given both in [103] and [104]. They generate the 243 nm radiation starting from a `Spectra-Physics PDL-1` dye laser, with the grating in Littrow configuration set at first order, using LD 489 dye (Exciton) to produce broadband 486 nm pulses. The 486 nm output is then frequency doubled in a critical phase-matched BBO crystal to produce 4 ns duration pulses at 243 nm. The dye laser is pumped with the third harmonic (355 nm, 7 ns) of a Nd:YAG Q-switched laser, the `Continuum Surelite I-20`.
In order to generate the 243 nm spectrum with my `Labview` simulation, I needed to know the dye laser FSR. The dye laser output @ 486 nm forgets the Nd:YAG FSR (it has a $2 - 5$ ns spontaneous decay time). For this reason the dye laser cavity itself determines the FSR for the 486 nm output pulse. I needed to know the dye laser FSR, which is determined by the dye cavity itself. In [103] they declare a FSR of 500 MHz and a final 243 nm spectrum of 85 GHz. By assuming a Gaussian envelope for the 486 nm spectrum, the simulated 243 nm spectrum looks like in fig. 7.2 It is worth noting that the FSR of this laser is higher than the AEgIS laser one (see fig. 5.8).

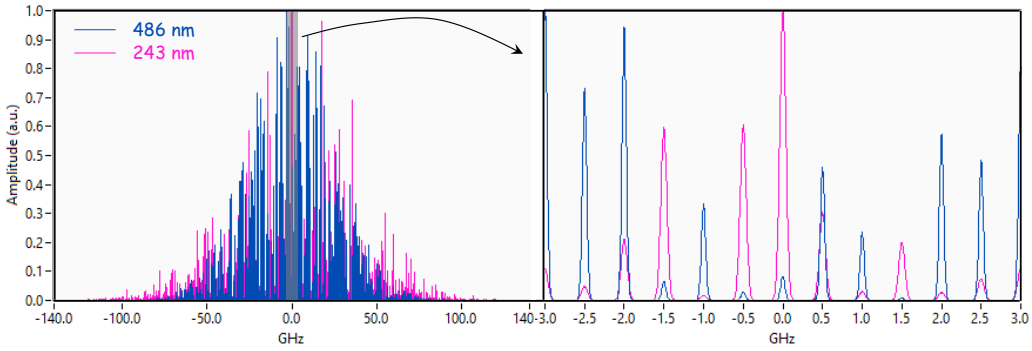

Figure 7.2: 486 nm and the second harmonic @ 243 nm simulated spectra.

Why a comb-shaped spectrum is problematic?

In the study of transitions in atomic spectra, and indeed in any type of spectroscopy, one must be aware that those transitions are not precisely "sharp". There is always a finite width to the observed spectral lines, called the *natural linewidth*. This is because of the uncertainty principle[3]: energy levels above the ground state with energy E and lifetime τ has uncertainty in energy ΔE such that $\Delta E\tau \sim \hbar$, i.e. short-lived states have large uncertainties in the energy. This means that a photon emitted/absorbed in a transition from this level to the ground state (and vice versa) will have a range of possible frequencies

$$\Delta\nu_{\mathbf{nat}} \sim \frac{\Delta E}{h} \sim \frac{1}{2\pi\tau} \tag{7.12}$$

The $n = 2$ level has a spontaneous decay time of ~ 3.2 ns, and therefore a linewidth of ~ 50 MHz. The $n = 3$ level has a spontaneous decay time of ~ 10 ns, corresponding to a linewidth of ~ 16 MHz.
In both cases, a comb-shaped spectrum with a FSR larger than the natural linewidth $\Delta\nu_{\mathbf{nat}}$ is not able to excite a huge class of atoms (the ones whose velocities fall inside this spectral holes). In the case of the Ps atom, $n = 2$ and $n = 3$ levels are very close under this point of view, therefore one should find the way to avoid this problem by using a continuous spectrum.

7.3 Excitation simulation of two real cases

Here I report simulation results of the two cases listed at the beginning of the chapter. Spectra involved in the respective transitions come from the `Labview` simulations, already described and shown in fig. 7.2 and 5.18. These spectra are inputs of the final `Labview` simulation vi[4], where I calculate results of the rate equations. I describe here the calculation idea, that is the same for both transitions. The only difference is in the parameters characterizing each transition.

[3] Actually, a classical description is possible: one can consider a classical dumped oscillator with an exponential decay time, where the Fourier Transform gives a finite Lorentzian linewidth.

[4] Labview projects have the extention .vi. Therefore usually a Labview file is called directly "vi".

Parameters

In order to perform the calculation, I need to give in input the following parameters for each transition:

1. *Resonance wavelengths*: $\lambda_{1\to2} = 243.005$ nm and $\lambda_{1\to3} = 205.035$ nm.
2. Transition *cross section*: the cross section was calculated [105] in a regime of monochromatic radiation. We have $\sigma_{1\to2} = 2.758 \times 10^{-10}$ cm^2 and $\sigma_{1\to3} = 1.65 \times 10^{-10}$ cm^2.
3. *Spontaneous emission time*: necessary to calculate the natural linewidth. We have $\tau_{n=2} = 3.2$ ns and $\tau_{n=3} = 10$ ns.
4. *Pulse duration*: $\Delta t_{1\to2} = 5$ ns and $\Delta t_{1\to3} = 1.5$ ns. Here, important for the spectra normalization and the calculation of $N(\Delta t)$.
5. Transverse spot *dimension*: I used the same dimension for both cases, that is the AEḡIS experimental spot dimension $S = 4 \times 6$ mm^2.

Calculations

There are two main blocks: the part I where I calculate $N(\Delta t)$ and the part II where the Ps Doppler spectrum is considered. The final excitation efficiency is given by

$$\int Ps(\nu)N(\nu)d\nu \tag{7.13}$$

where $N(\nu)$ is normalized to 1. In the following it will be explained why N appears as a function of ν.
The input of the `Labview` simulation is the power spectrum[5] of the radiation we want to analyze, called $D_{\text{in}}(\nu)$. We suppose to be in a simplified situation where the energy of the laser pulse is

$$E_{\text{tot}} = S\Delta t \int D(\nu)d\nu \tag{7.14}$$

where S is the spot dimension and Δt the pulse duration and $D(\nu)$ is the power spectrum of the radiation. Therefore our $D_{\text{in}}(\nu)$ must be such that

$$\int D_{\text{in}}(\nu)d\nu = \frac{E_{\text{tot}}}{S\Delta t} \tag{7.15}$$

The first step in the program is to normalize the $D_{in}(\nu)$ to this value. I will call $D(\nu)$ the normalized power spectrum.
Therefore, starting from part I, we want to calculate two quantities: N_2^0 and $\frac{t}{\tau^*}$. Now, for each ν, the intensity I in N_2^0 (eq. 7.4) is determined by the input spectrum as follows:

$$I(\nu) = D(\nu)\Delta\nu_{\text{nat}} \tag{7.16}$$

Therefore the program calculates N_2^0. On the other hand, from eq. (7.6), we obtain

$$\frac{t}{\tau^*} = \Delta t\left(\frac{2\sigma I(\nu)}{h\nu_0} + \frac{1}{\tau}\right) = \Delta t\left(\frac{2\sigma D(\nu)\Delta\nu_{\text{nat}}}{h\nu_0} + \frac{1}{\tau}\right) \tag{7.17}$$

With these ingredients we can calculate $N(\nu)$.
Finally, in the part II, we generate a Gaussian representing the Ps Doppler profile, characterized by a FWHM $\Delta\nu_{\text{Ps}}$ (given in eq. (7.11)).

[5]Per unit surface, but for simplicity I will omit this in the text.

Results

Consider two cases: a Ps cloud 1 THz large, corresponding to a temperature of $\sim$ 1000 K, and a Ps cloud 100 GHz large, corresponding to a temperature of $\sim$ 10 K.
With these two scenarios, I want to study separately the effects of the inner structure of the spectrum and the spectral envelope on the excitation efficiency.
With the simulation, by increasing the pulse energy, we can study the saturation process. In the case of 100 GHz Ps cloud, the spectral envelope doesn't affect any more the efficiency, as both lasers are broad enough to cover the Doppler width. Therefore, this scenario is suitable to study how the inner structure of the exciting spectrum affects the excitation efficiency. On the contrary, in the case of a 1 THz Ps cloud, we add the necessity to cover a Doppler spectrum broader than the laser one's. Therefore, this scenario is suitable to study the effects of the spectral envelope of the exciting pulse (and therefore of the whole generation process of the exciting radiation) on the excitation efficiency.

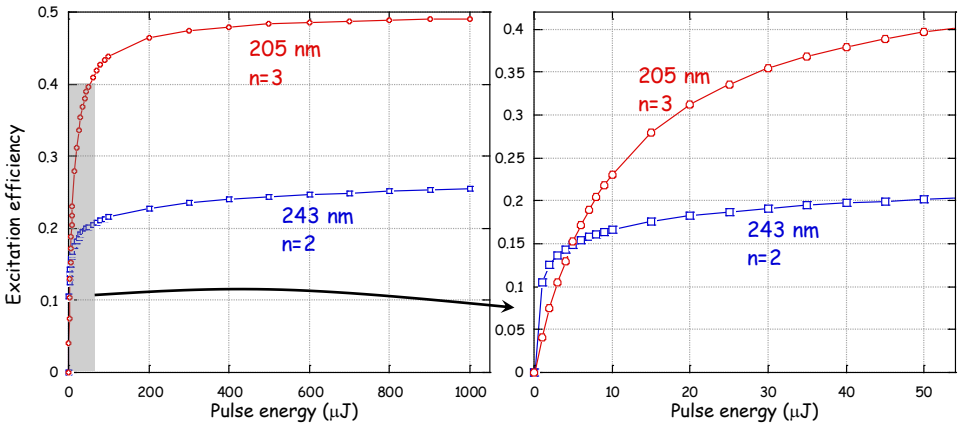

Figure 7.3: Excitation efficiency saturation curves for a Ps cloud 100 GHz large: on the right, a zoom at lower energies (shaded region), where an overlap between the two curves occurs.

In relation to the 100 GHz Ps cloud case, in fig. 7.3, we see how the excitation efficiency saturates as a function of the exciting pulse energy. At low energies (< 5 μJ), the $n = 2$ excitation with the simulated 243 nm spectrum is more efficient. Then, while approaching the saturation, the fact that the 205 nm has a continuous spectrum becomes crucial: we have a higher saturation energy[6] (a factor 2), therefore the continuous 205 nm spectrum becomes more efficient than the 243 nm spectrum, and we achieve a higher excitation efficiency despite the negative gap in the transition cross section with respect to the $n = 2$ case. In relation to the 1 THz Ps cloud case, in fig. 7.4, we see again the two saturation curves. At much lower energies than the previous case (< 10 μJ) the $n = 2$ excitation is more efficient. Then the spectral envelope becomes the crucial parameter: immediately the $n = 3$ excitation efficiency increases much more than the $n = 2$ excitation efficiency and its saturation energy reaches a value more than three times higher[7].

For cold positronium clouds, spectra wings are not used for excitation purposes. For this reason the inner structure of the spectrum is the main parameter affecting the pro-

[6] With "saturation efficiency" here I mean the asymptote the curve seems to tend to.

[7] The energy range in the x-axis in not large enough to see from the picture that the it actually is more than six times higher (found by running the simulation for very high energies)

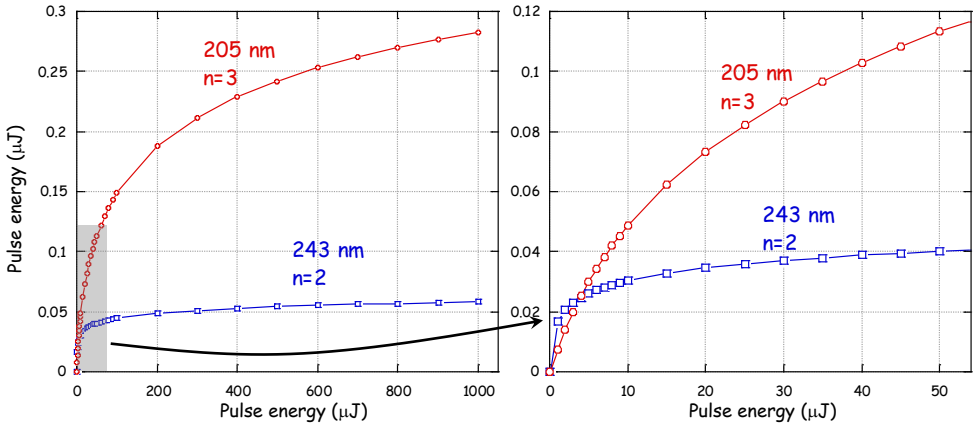

Figure 7.4: Excitation efficiency saturation curves for a Ps cloud 1 THz large: on the right, a zoom at lower energies (shaded region), where an overlap between the two curves occurs.

cess. For hot positronium clouds, the tails of exciting spectra are necessary to excite fast atoms, therefore the characteristics of the spectral envelope of the exciting radiation are decisive. In fig. 7.5, four cases are simulated: 100 GHz (top half) and 1 THz Ps (bottom half) cloud, with a pulse energy giving the same excitation efficiency for the two transitions ($\text{Eff}_{205} = \text{Eff}_{243}$) and the pulse energy used in the AE$\bar{\text{g}}$IS Ps $n = 3$ excitation measurement. It is worth noting that when we reach the same efficiency, in both cases (for both Ps temperatures) 243 nm spectrum peaks are already in saturation, while this doesn't happen for the 205 nm spectrum peaks. At 54 μJ, the 205 nm spectrum saturates and almost all spectral holes are filled in. At this energy this filling doesn't occur for the 243 nm spectrum, because saturation only causes peaks broadening. As regards the spectrum wings, we can see the huge *spectral broadening* effect occurring for the sinc-wise envelope of the 205 nm spectrum. We will use this data for considerations about the Ps temperature measurement in the dedicated chapter.

7.4 Simulating the photoionization process

In order to simulate the photoionization process and analyse the measurements, we need another set of rate equations. The exciting 205 nm and the ionizing 1064 nm pulses are shined simultaneously through the Ps cloud, therefore we have a three-level dynamics. We have the Ps ground state with population $N_1(t)$, the Ps $n = 3$ level with population $N_2(t)$ and the continuum (ionized Ps), with population $N_3(t)$. Rate equations for the photoionization process can be written as follows:

$$\begin{cases} \dfrac{dN_3}{dt} = \Gamma_{\text{ion}} N_2 \\ \dfrac{dN_2}{dt} = \dfrac{1}{\tau_s} N_1 - \dfrac{1}{\tau_s} N_2 - \dfrac{1}{\tau} N_2 - \Gamma_{\text{ion}} N_2 \\ \dfrac{dN_1}{dt} = -\dfrac{1}{\tau_s} N_1 + \dfrac{1}{\tau_s} N_2 + \dfrac{1}{\tau} N_2 \end{cases} \tag{7.18}$$

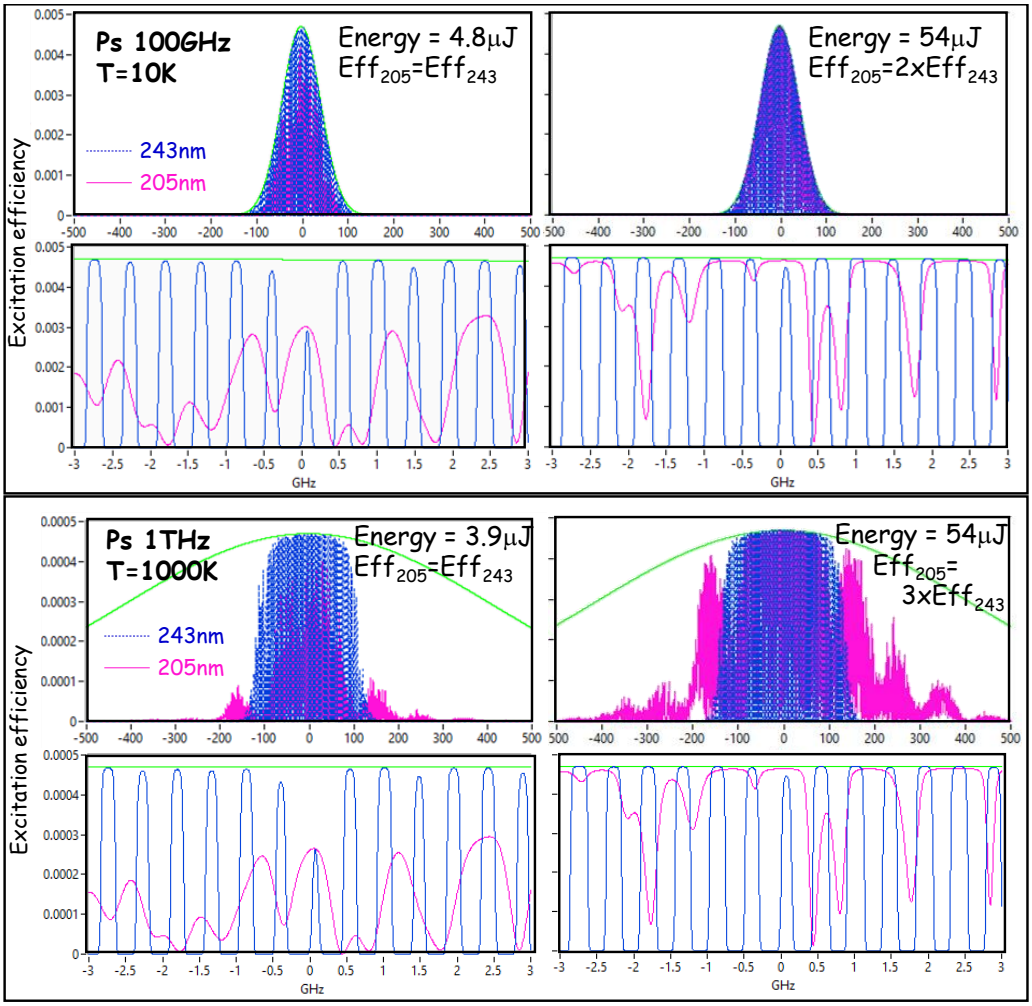

Figure 7.5: Spectral broadening and excitation efficiency saturation in the case of 100 GHz (top half) and 1 THz Ps clouds (bottom half).

The huge ionization cross section suggests that N_2 is always near zero, and implies the negligibility of the terms $-\frac{1}{\tau_s}N_2 - \frac{1}{\tau}N_2$ in the N_2 equation (and, therefore, of terms $+\frac{1}{\tau_s}N_2 + \frac{1}{\tau}N_2$ in the N_1 equation). And in fact, we know from several simulations that the photoionization efficiency is almost 100% [123]. This further simplifies the set of rate equations, leading to the following (two-equation) set:

$$\begin{cases} \dfrac{dN_3}{dt} = -\dfrac{dN_1}{dt} \\ \left(\dfrac{dN_2}{dt} = 0\right) \\ \dfrac{dN_1}{dt} = -\dfrac{1}{\tau_s}N_1 \end{cases} \tag{7.19}$$

with initial conditions $N_1(0) = N_1^0 = 1$ and $N_3(0) = 0$.
We find, then, the following solutions for the system:

$$\begin{cases} N_1(t) = \dfrac{1}{\tau_s} \mathrm{e}^{-\dfrac{t}{\tau_s}} \\ \\ N_3(t) = 1 - \mathrm{e}^{-\dfrac{t}{\tau_s}} \end{cases} \tag{7.20}$$

where $\dfrac{t}{\tau_s}$ is a function of t and ν:

$$\frac{t}{\tau_s} = t\frac{\sigma I}{h\nu_0} = t\frac{\sigma D(\nu)\Delta\nu_{\text{nat}}}{h\nu_0} \tag{7.21}$$

By calculating $N_3(\Delta t)$ (being Δt the laser pulse duration), I obtain $N_3(\nu)$, which corresponds to the fraction of excited atoms $N(\nu)$ in my Labview spectral simulations (see eq. (7.13)).
It is worth noting that a saturation behaviour is still present, despite the "one-way" nature of the process.

7.5 Spectral analysis conclusions

We have seen how, at a pure spectral level, hot Ps excitation to the $n = 3$ level with a continuous and sinc-wise spectrum is far more efficient than hot Ps excitation to the $n = 2$ level with a comb-shaped Gaussian spectrum (by keeping the same laser pulse energy). In [103], it is measured a 25% $n = 2$ photoionization efficiency and it is declared:

"*We attribute this unexpectedly high excitation efficiency to (i) the effectiveness of the contributions in the wings of the laser frequency spectrum and (ii) power broadening, which effectively fills in the* 0.5 *GHz gaps between the individual laser gain modes typical of an unseeded pulsed dye laser. Our data also demonstrate that, even though the excitations are incoherent, the effective removal of 2P states via quenching, photoionization, or further excitation means that the overall fraction of transitions can be close to 100%, rather than the 50% one would obtain for a simple two-level system.*"

My analysis might be able to give indications about this. We start from their statement that their way to detect $n = 2$ excitation could take their excitation efficiency to the 100% level instead of 50%. This is true, we would only make a 10 % error in stating this (I made a comparison between the excitation and photoionization simulations). But, by assuming they had a geometrical efficiency of 100%, the photoionization simulation gives no more than 14% efficiency. The process of "gap filling" is therefore not enough to explain a 25% efficiency.
My simulation seemed to show that a reason why they reach a 25% efficiency could be the use of a pulse whose spectral wings are higher than the ones typical of a Gaussian spectral envelope (the one I used to simulate the dye laser output spectrum @ 486 nm). This topic should be given deep investigation, as in literature it is not easy to find information about the spectral envelope of the output of a dye laser pumped with a Q-switched laser.

Also the presence of a strong (1 T) magnetic field, affecting the fine structure of the Ps atomic levels, might be a reasonable cause for this enhanced photoionization efficiency.

As far as our measurements are concerned, simulated values for the efficiency are very close to the experimental ones, but this will be addressed in chapter 8.

7.5.1 Advantages for Rydberg excitation

In addition to the fact that we found a way to make $n = 3$ excitation itself as efficient as (if not more than) the $n = 2$ excitation, $n = 3$ excitation is also more suitable for Rydberg excitation purposes. The longer lifetime of the $n = 3$ state allows a more efficient depopulation of the level by means of a Rydberg excitation pulse [35, 36].

CHAPTER 8

Positronium excitation measurements

In previous chapters the experimental apparatus configuration for this measurement was described. In this last chapter I am going to report Ps excitation measurement results. I will describe two separated measurements and results: *magnetic quenching* and *photoionization* methods to detect $n = 3$ Ps excitation (the latter also provided information about the Ps cloud Doppler broadening on the transverse direction) and the *Rydberg Ps excitation* (performed as a check of our ability to excite Ps to the $n = 3$ level).
Concerning the photoionization, a test on $n = 3$ transition saturation as a function of the UV energy was performed[1]. The measurement result will be shown and compared with my spectral simulation.

8.1 n = 3 excitation detection

As already mentioned at the end of chapter 6, the fraction of $n = 3$ excited o-Ps was measured by analyzing the decrease in the annihilation rate in the SSPALS spectra.
Two methods can be used for this purpose:

(i) quenching in a magnetic field

(ii) photoionization with the IR @ 1064 nm laser pulse

When no magnetic field is present inside the Bread Box, 3^3P states decay radiatively to the 1^3S state in 10.5 ns (up to the 88%, the remainder decays on a 2S state). The presence of a superimposed magnetic field (i) mixes the two sub-states of Ps with $m = 0$, the levels with $m = 1$ remaining unaltered, due to Zeeman effect [126]. This leads to annihilation in two gamma rays of the $m = 0$ o-Ps state; the effect is normally called o-Ps *magnetic quenching*, since the lifetime of $m = 0$ o-Ps is decreased (quenched) by the magnetic field [127] from 142 ns to 125 ps (after decaying to the ground state).
Otherwise (ii), photoionization of the 3^3P state splits Ps atoms into an electron and a positron, and all the free positrons are quickly accelerated toward the last negative electrode of our set-up, where they annihilate.
Whichever technique is chosen, both of them induce a decrease of the o-Ps population decaying into three gamma rays (like in the simulated SSPLAS spectrum in fig. 6.4) and the fraction of quanched/photoionized o-Ps can be evaluated by eq. (6.1) in the range between 50 and 250 ns from the prompt peak. I will refer to this SSPALS signal with S.

[1] Mostly in the Rydberg excitation section, some descriptions of measurement details and results follows reference [123].

8.1.1 Magnetic quenching method

To predict the value of the external field required to get the maximum magnetic quenching efficiency, it was used a simulation code which performs the numerical diagonalization of the full interaction Hamiltonian in arbitrary electric and magnetic fields and calculates the generalized Einstein coefficients and sub-level lifetimes. These coefficients were fed into a rate equation solver [36] to study the complex excitation dynamics of Ps considered as an incoherent process induced by the UV laser pulse at resonance, assuming ideal conditions (exact superposition of the UV laser bandwidth on Ps Doppler linewidth, perfect temporal and geometrical overlap). According to simulation results, a 0.025 T magnetic field gives the maximum quenching efficiency (17 %) on the $n = 3$ state (fig. 8.1). The results were largely independent on the Ps velocity. For this reason, we set

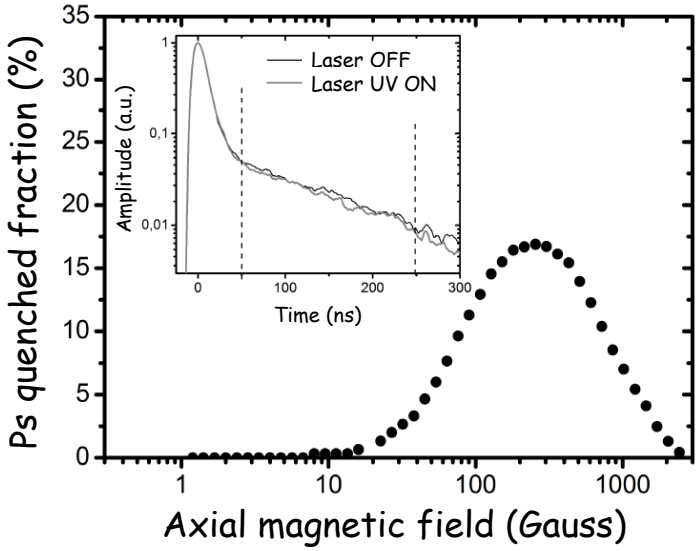

Figure 8.1: $n = 3$ magnetic quenching. In the main plot we have the quenching efficiency as a function of the magnetic field. In the inset we have the SSPALS spectrum (comparison between UV laser ON and OFF) related to the magnetic quenching measurement. Picture from [123].

a 0.025 T magnetic field in the sample region and measured the quenching efficiency due the $n = 3$ excitation. The SSPALS spectra obtained in this experiment are reported in the inset of fig. 8.1, showing a small reduction of o-Ps annihilations in the selected window when the UV laser is on. The maximum observed reduction through quenching was $S = (3.6 \pm 1.2)\%$.

8.1.2 Photoionization method

When applying the 50 mJ IR pulse for photoionization, the decrease in o-Ps annihilations becomes clearly visible in the SSPALS spectrum of fig. 8.2, corresponding to $S = (15.5 \pm 1.1)\%$.
This makes this method more suitable for Ps Doppler linewidth measurement. In order to measure the Ps Doppler linewidth along the laser axis (see eq. (7.7)), we exploit eq. (7.9). The idea is to tune UV laser wavelength and measure the photoionization efficiency: the more we move away from $\lambda = 205.0474nm$[2], the faster is our excitation

[2]predicted value in [36] for exciting Ps "at rest", in presence of our magnetic and electric fields

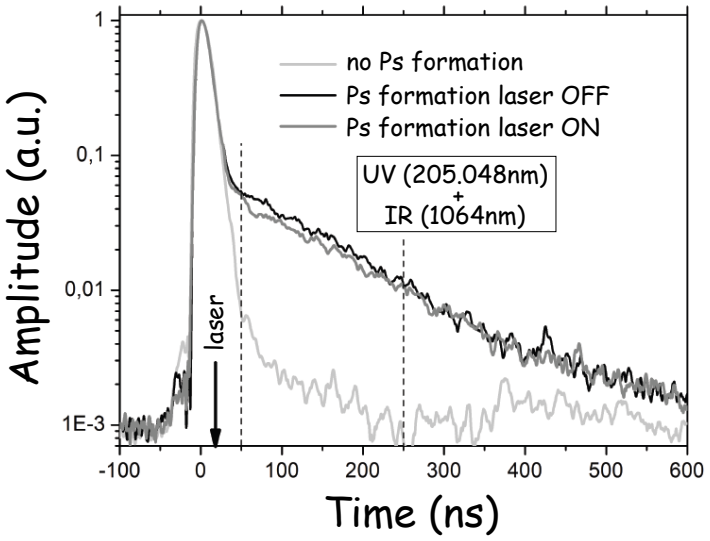

Figure 8.2: $n = 3$ photoionization SSPALS spectra. The positron background is also plotted. Picture from [123].

target (meaning that we address a faster fraction of the Ps cloud). Therefore, at each wavelength, the mean S value and its standard deviation were calculated for a sample of 15 shots (fig. 8.3). Fitting a Gaussian to the resulting points gives the central value of

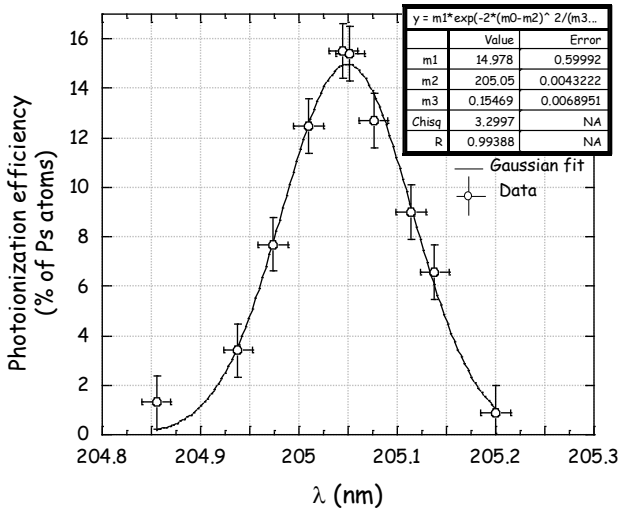

Figure 8.3: Photoionization resonance curve with a simple Gaussian fit.

the 3P excitation line at (205.05 ± 0.02) nm. The saturation behaviour of both 1S$\rightarrow$ 3P and 3P$\rightarrow$ionization transitions has been studied (see fig. 8.4). Ps photoionization efficiency as a function of the UV laser energy was measured, while keeping the IR laser at 50 mJ energy (left panel in fig. 8.4). We did the same for Ps photoionization efficiency as a function of the IR laser energy, while keeping the UV laser at 54 μJ energy (right panel in fig. 8.4). The 1S$\rightarrow$ 3P transition appears only slightly saturated, while the 3P$\rightarrow$continuum is strongly saturated, meaning that almost all of $n = 3$ atoms are photoionized as soon

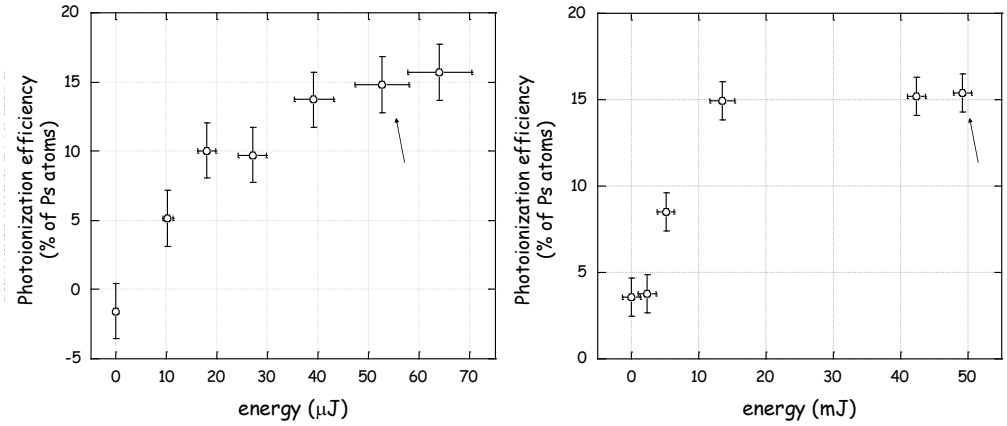

Figure 8.4: $n = 3$ photoionization saturation measurement. On the left, $n = 3$ transition (UV) saturation measurement. On the right, Ps photoionization (IR) from $n = 3$ transition measurement. Arrows indicate the energy used during the resonance measurements.

as they are excited. Thus, the S value found when photoionizing can directly be seen as the excitation efficiency in the photoionization process. From our data we conclude that $\sim 15\%$ of the overall positronium emitted in vacuum has been excited into the $n = 3$ state, and subsequently photoionized.

8.1.3 Photoionization data analysis

With the model proposed in [123], the data are fitted as shown in fig. 8.5. Ps temperature

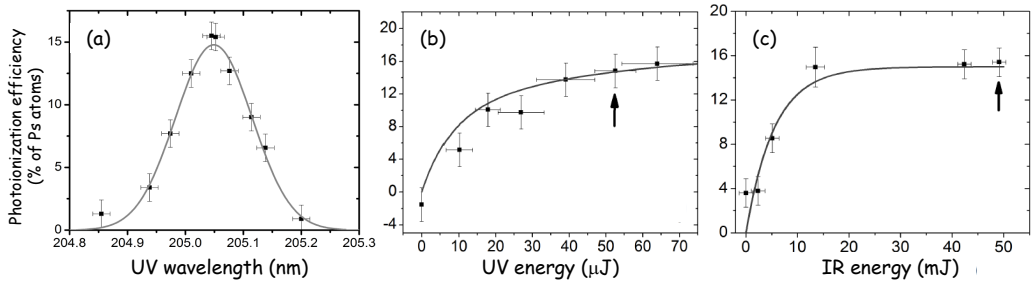

Figure 8.5: Fits of the model in [123] for (a) photoionization resonance curve (b) $n = 3$ excitation saturation curve (c) photoionization saturation curve. Pictures from [123].

and geometrical efficiency of our laser are estimated to be ~ 1300 K and 80% respectively.

New analysis

I can use my numerical `Labview` simulation, properly adapted to the photoionization process as described in section 7.4, to fit the resonance measurement and the UV saturation data. With respect to the analysis in [123], a new element is taken into account: the spectral properties of our UV pulse. The temperature T of the Ps cloud is a fit parameter, together with the geometrical efficiency η of our experimental setup. The resonance fit is plotted together with the data in fig. 8.6, while the saturation data fit is in fig. 8.7.

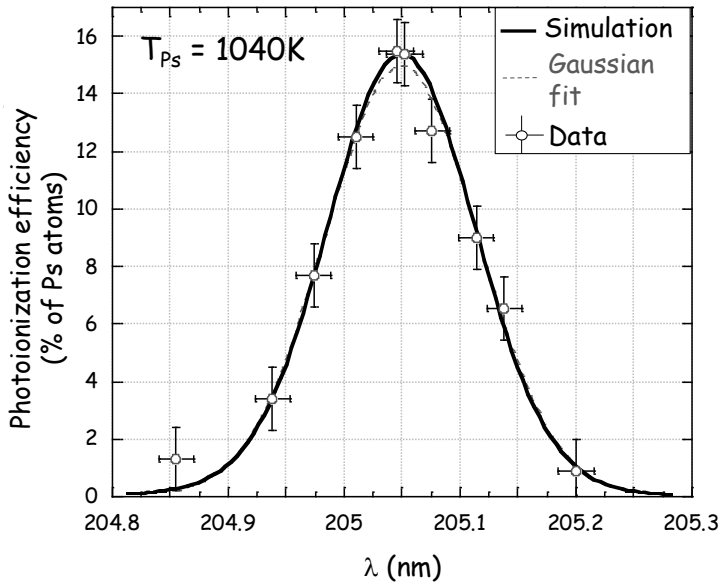

Figure 8.6: UV resonance curve. The solid black line represents the theoretical prevision that best fits the data, the dashed line represents the Gaussian fit of fig.8.3.

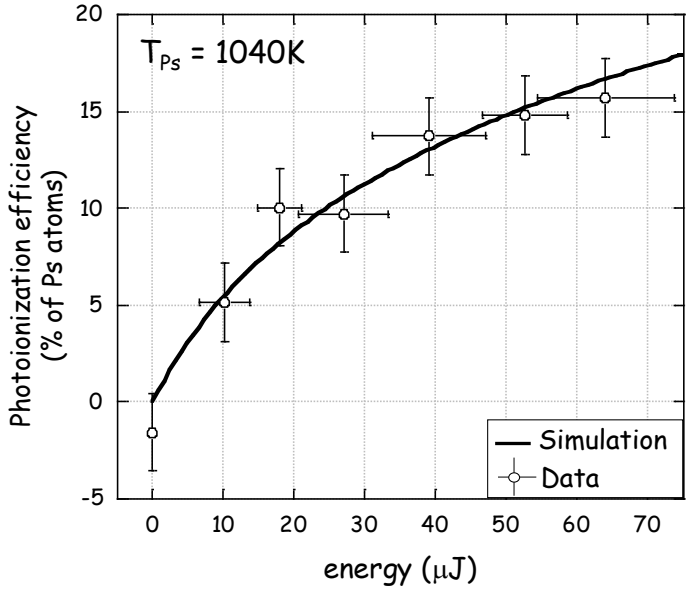

Figure 8.7: $n = 3$ photoionization efficiency saturation curve. The solid black line represents the theoretical prevision made with the couple of parameters that best fits the data in the resonance curve (fig. 8.7).

The couple of fitting parameters T and η were determined by fitting the resonance curve (fig. 8.6). Then, the same couple of parameters were used to fit the saturation data, and the result is shown in fig. 8.7. This could be read as a consistency test of the model and the reliability of the related fitting parameters.
The Ps cloud temperature and the geometrical efficiency estimated with this model are

$$T = (1040 \pm 100)\,\mathrm{K} \qquad \eta = (87 \pm 10)\,\% \tag{8.1}$$

Errors are estimated starting from those of the Gaussian fit in fig. 8.3, to which the simulated curve is almost perfectly superimposed. The fit was, in fact, a hand-made optimization of the simulation parameters T and η: the superposition of the simulation curve to the Gaussian fit gave the optimum couple of parameters above. Both simulation prevision and Gaussian fit are plotted in fig. 8.6.
Taking into account the error, the geometrical parameter $\eta = 87\%$ is not far from the one estimated by my c++ simulation, that is equal to $\eta_{\text{sim}} = (73 \pm 3)\%$. On the contrary, it seems that the temperature estimated with this model differs a lot (almost three sigma) from the one estimated in [123].
The fact that the model takes into account the inner structure of the exciting spectrum could have led to the better fit performance in the low energy section of the saturation data set (fig. 8.7). Probably, the presence of gaps inside the spectrum could be the reason why, at low energies, the expected photoionization efficiency with my model is lower than the one expected in [123].

8.2 Rydberg excitation tests

An independent test to demonstrate the excitation of the 3^3P level was performed with an IR laser pulse suitable for exciting Ps to Rydberg levels (see chapter 5). A first demonstration of Rydberg excitation using 3^3P as the intermediate level was carried out by simply varying the wavelength of the IR pulse and keeping the UV pulse at the resonant wavelength.

The effects of Rydberg excitation on SSPALS spectra

Rydberg excitation increases the excited o-Ps lifetime. This allows a large number of o-Ps to reach the walls of the Bread Box. As a consequence, the SSPALS spectra show a

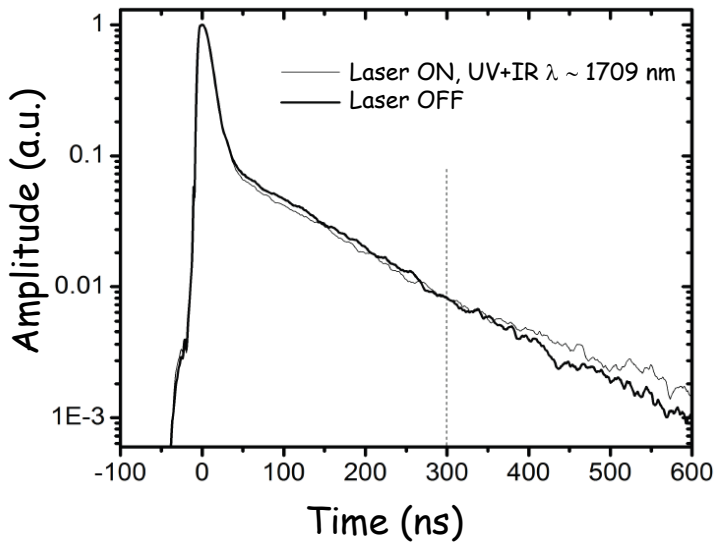

Figure 8.8: SSPALS spectra of Ps into vacuum with UV+IR lasers OFF in black, and laser UV+IR ON (205.05 nm $+1709$ nm) in dark gray. Shown spectra are composed by averaging 40 single shots. Area between 300 ns (vertical dashed line) and 600 ns from the prompt peak has been considered for evaluation of S for Rydberg levels (see text). Picture from [123].

decrease of annihilations immediately after the laser shot and an increase at later times (fig. 8.8). The structure of the SSPALS spectrum after 300 ns from the prompt peak depends on the Bread Box walls geometry and this is confirmed by the geometrical c++ simulation.

The Rydberg resonance curve

As we did for the photoionization experiment, a scan of the IR laser wavelength was carried out in order to excite Ps from $n = 3$ to levels between $n = 15$ and $n = 18$, while keeping the UV laser on the resonance with the $n = 1 \rightarrow n = 3$ transition ($\lambda = 204.05$ nm, $E = 54$ μJ). The IR pulse energy was kept constant during the scan at $E = 1.1 \pm 0.1$ mJ. The Rydberg excitation signal was extracted from the SSPALS spectra by calculating the S parameter in the time window between 300 ns and 600 ns after the prompt positron annihilation peak[3]. We expect the $n = 15$ level to be even more broadened than the $n = 3$ one, due to the added contribution from the motional Stark effect [**?**], almost negligible for low excited states. Fig. 8.9 reports experimental data together with a Gaussian fit

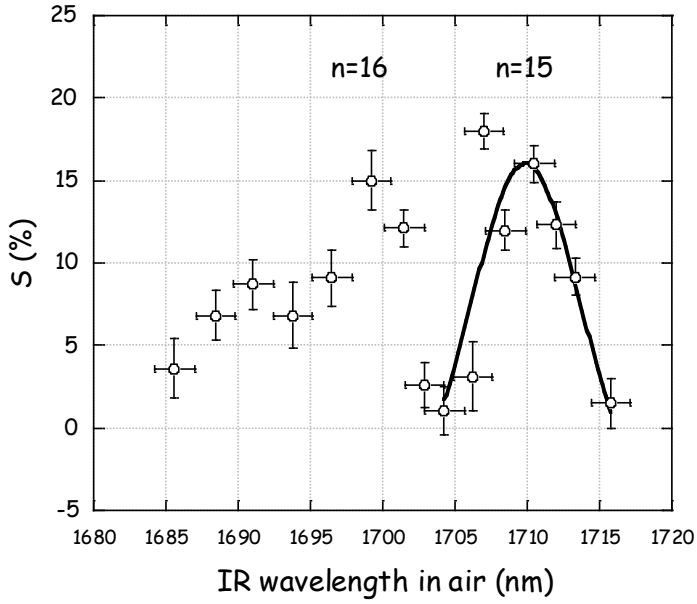

Figure 8.9: Scan of the S parameter as defined in eq. (6.1) versus the IR wavelength in air in the range $n = 15..18$. The clearly identifiable peak, associated to the transitions to $n = 15$, has been fitted with a Gaussian. For $n > 16$, lines are no more clearly separated due to the excessive broadening.

of the Rydberg $n = 15$ line. The resulting peak wavelength has been determined to be 1710.0 ± 0.6 nm.
The zero field excitation line central value for $n = 15$ is expected to be 1708.63 nm[4]. In order to state whether we have a line shift in the resonance curve or not, a more precise

[3]The S parameter here could not exactly be equal the Rydberg excitation efficiency, as the integral of the difference in the selected region is due to annihilations of Ps on the walls and not only to Ps annihilating in flight

[4]hence our experimental data shows a line shift of around 1.4 nm towards higher wavelengths

measurement ought to be performed. This will be the topic of a future dedicated study [129].
Despite this significant broadening of the Rydberg lines, we observed the $n = 15$ transition clearly isolated; for higher states, different n-manifolds start to overlap in a continuum of energy levels [**?**].

8.3 Final considerations on Ps excitation measurements

With these measurements we have demonstrated the first laser excitation of Ps to the $n = 3$ state. The total excitation+photoionization efficiency of $\sim 15\%$ is mainly limited by the ratio of the laser linewidth to the Doppler broadening of the Ps line. Reduction of the o-Ps emission velocity from the target is thus an obvious way to enhance the excitation efficiency. The simulation and the new fit of the data show that the strategy chosen in AEgIS to produce the exciting 205 nm pulse allows to cover a wider portion of the Doppler spectrum of the Ps cloud than the mere spectral width of our laser, because of the huge power broadening effect.

An excitation to Rydberg levels using 3^3P as the intermediate state has also been shown, opening the possibility for further studies involving $n = 3 \rightarrow$ Rydberg transitions [**?**]. Hence, the production of Ps in the $n = 3$ level paves the way to many intriguing research subjects, ranging from the study and manipulation of long-lived exotic atoms to the production of ultracold antimatter.

CHAPTER 9

Conclusions

In this work, I studied the impact of involved nonlinear processes on the excitation efficiency of a Doppler broadened atomic cloud. Presented simulation results show that, by exploiting properly nonlinear processes, we are able to improve the excitation efficiency of a laser pulse. It is crucial, in AEgIS, the use of a periodically poled crystal in quasi phase matching regime. This gives us a broadband continuous output spectrum whose wings survive to the spectral cutting of the last nonlinear crystal of the chain (which has insufficient spectral acceptance). This means that, at high laser energies, these wings can be amplified and the spectrum gaps can be filled in, leading to high reachable saturation efficiencies. On the contrary, in a laser pulse with a comb-shaped spectrum with a Gaussian envelope both wings and gaps drop rapidly to zero, and amplification hardly occurs at usually employed energy regimes.

9.1 AEgIS photoionization data fitting

By fitting the AEgIS photoionization measurement data with the new simulation, I estimate a Ps temperature of 1040 K. Best fit performances than in the past were attained at low laser energy data points (fig. 8.7), due to the presence of a more realistic exciting spectrum in the simulation. We could ideally[1] cover a 4000 K (2 THz) Ps cloud by "simply" increasing the laser energy, in order to exploit all the 894 nm pulse spectrum in the SFG process and populate all the 205 nm spectral wings in the excitation saturation process.
A 1040 K temperature estimation for our Ps cloud is reasonable, due to the fact that in our case we use a nanochanneled target, where pores are ordered and at $45°$ with respect to the target surface. In [31], Ps longitudinal velocity distribution was measured, with a nanochanneled target whose pores were *perpendicular* to the target surface. This means that the cooling process mainly affects the transversal direction, and not the longitudinal one (indeed they measured higher temperatures). *Disordered* pores affect the whole tridimensional velocity distribution. In our case, with $45°$ pores, we didn't have the possibility to predict the cooling effect of collisions with the pore walls both on the transverse direction (parallel to the target surface) and the longitudinal direction (e^+ direction, perpendicular to the target), because no measurement was performed before with this kind of nanochanneled target.
But still, the result of better (even if non complete yet) cooling performances on the transverse direction is not incompatible with the cooling results obtained in [31]: as we are dealing with the transverse direction, better cooling performances than in [31] can be expected, and the incomplete cooling might be due to the tilted pores and a non sufficient implantation energy of positrons.

[1] We would need hundreds of mJ

9.1.1 Future improvements

In the future, the same kind of experiments could be carried out in order to confirm and link the analyses listed above. It could be useful a new measurement campaign with different working conditions:

- Make a new UV resonance scan in a non saturation regime, where the power broadening issue is not present.
- Make a new UV resonance scan with the same nanochanneled target used in [31].
- Make UV resonance scans with the laser shined in different direction so as to study the tridimensional Doppler distribution of the emitted Ps in vacuum.

and to keep testing and making further improvements to the spectral simulation. For example, the whole project would be more consistent and complete if the OPG output spectrum were simulated in `Labview` as it is for all the others, instead of using `SNLO`. This would allow the use of a mode spacing much smaller than the laser modes' width.

Appendices

APPENDIX A

High-order dispersion effects in two-photon interference

In this appendix I report about my contribution to a quantum mechanics experiment, in collaboration with the AQM (Applied Quantum Mechanics) group of the Physics Department of the University of Milano. We studied the effects of second and third order dispersions on the two-photon interference process.
For convenience, it is reported here the arxiv preprint of the published paper, while the related reference is given in the main bibliography ([130]).

Two-photon interference and Hong-Ou-Mandel (HOM) effect are relevant tools for quantum metrology and quantum information processing. In optical coherence tomography, HOM effect is exploited to achieve high-resolution measurements with the width of the HOM dip being the main parameter. On the other hand, applications like dense coding require high-visibility performances. Here we address high-order dispersion effects in two-photon interference and study, theoretically and experimentally, the dependence of the visibility and the width of the HOM dip on *both* the pump spectrum and the down-converted photon spectrum. In particular, a spatial light modulator is exploited to experimentally introduce and manipulate a custom phase function to simulate the high-order dispersion effects. Overall, we show that it is possible to effectively introduce high-order dispersion effects on the propagation of photons and also to compensate such effect. Our results clarify the role of the different dispersion phenomena and pave the way for optimization procedures in quantum technological applications involving PDC photons and optical fibers.

A.1 Introduction

Two-photon interference (TPI) and in particular the the Hong-Ou-Mandel (HOM) [131] effect are relevant tools in photonic quantum technology. The HOM dip plays a central role in dense and superdense coding, since it allows to identify two of the four Bell states [132, 133]. Here the crucial parameter is the visibility of the HOM dip: the higher the visibility, the higher the mutual information [134, 135]. TPI have found applications also in quantum metrology, where frequency entangled states of photons produced by down-conversion (PDC) represent a resource for clock synchronization [136] and optical coherence tomography [137]. However, the need to improve the resolution performances while using low-coherence interference leads to a halt: if one increases resolution widening the spectrum, the effect of dispersive media all along the path gets larger, thus preventing any further improvement [138]. Nevertheless, since the width of the HOM dip is not affected by dispersive media [139], TPI represents a promising candidate to face

the resolution puzzle [146, 147]: the so-called Quantum Optical Coherence Tomography [140, 141] represents an interferometric technique for axial imaging offering several advantages over conventional methods.

This feature of the HOM effect, i.e. the independence of the dip width on dispersion, however, holds only if the pump laser is nearly monochromatic. When a broadband source is used to produce frequency entangled photons, the HOM dip becomes sensitive to even order dispersions [142], and both width and visibility are degraded.

In view of its relevance for quantum technology [139, 134], theoretical [143, 144, 145] and experimental [146, 147, 148, 149] studies have been performed to characterize TPI and the HOM dip. However, a full analysis of both the visibility and the width of the HOM dip as a function of the pump spectrum and of the PDC spectrum is still missing. We also mention that HOM interference experiments has been carried out between one photon from a SPDC source and a coherent field, i.e. a laser, with the aim to infer the degree of purity of the interfering single photon [150, 151] However, externally added dispersion does not play any role in these experiments.

The dispersive effects on the propagating photons can be described by a suitable phase function: this is the main topic of the present work. In particular, we develop an experimental apparatus to introduce and manipulate a custom phase function with a spatial light modulator, as well as to work with different pump and PDC spectrum. As a matter of fact, we can simulate high-order dispersive effects of different transmission channels by exploiting the same setup. Indeed, we have performed a complete theoretical and experimental study of how the HOM effect is affected by the presence of second and third order dispersions, together with a direct comparison between theoretical and experimental results. The same setup can be used to compensate this kind of effect, paving the way for optimization in quantum technological applications involving PDC photons and optical fibers.

The chapter is structured as follows. In Section A.2 I review the description of frequency entangled photons obtained by PDC and provide the basic principles of two-photon interference in dispersive media. In Section A.3 I describe in some details our experimental apparatus, whereas Section A.4 is devoted to the experimental results. I discuss our findings in Section A.5 and close the chapter with some concluding remarks in Section A.6.

A.2 Two-photon interference

The HOM effect occurs in TPI when two frequency-entangled photons generated by PDC interfere at a beam splitter (BS). In order to describe the TPI process after the propagation in dispersive media, we need to introduce the two-photon state produced via PDC and traveling from the source to the BS. In the presence of a broadband source laser the quantum state of the two photons, i.e. the signal "s" and the idler "i" photons, which interfere at the BS, is given by (see, e.g., [152]):

$$|\Phi\rangle = \iint d\omega_p \, d\omega \, A(\omega_p) \, F(\omega_p, \omega) \, \mathrm{e}^{\mathrm{i}\phi_s(\omega_p,\omega)+\mathrm{i}\phi_i(\omega_p,-\omega)} |\omega_p, \omega\rangle_s |\omega_p, -\omega\rangle_i, \tag{A.1}$$

where ω_p and ω are the frequency shifts from the central pump and the central PDC frequencies, respectively, whereas $A(\omega_p)$ and $F(\omega_p, \omega)$ are the pump and the PDC spectral amplitudes, respectively. The explicit form of $F(\omega_p, \omega)$ may be found in [153]. It accounts for the finiteness of the PDC generating crystal and the pump beam waist. On the other hand, in our case $\omega_p \ll \omega$, i.e. the pump spectral width is negligible compared to that

of the PDC, and thus the effects of the broadband pump on $F(\omega_p, \omega)$ are negligible. As a consequence, we may safely replace F in the Eq. (A.1) by the function $f(\omega) = F(0, \omega)$. Furthermore, we emphasize that Eq. (A.1) is written as a coherent superposition because we are interested in analyzing the interference of two photons well within the pump coherence time. Conversely, when the temporal width of the HOM dip and the generating crystal propagation length are of the order of the pump coherent length, the coherent sum should be replaced with an incoherent one as in [148].

In Eq. (A.1) we introduced the two phase functions $\phi_s(\omega_p, \omega) \equiv \phi_s(\omega_s)$ and $\phi_i(\omega_p, \omega) \equiv \phi_i(\omega_i)$ denoting the phase functions induced by the propagation of the signal and the idler photon with frequencies

$$\omega_s = \left(\frac{\omega_p}{2} + \omega\right), \qquad \omega_i = \left(\frac{\omega_p}{2} - \omega\right)$$

respectively. The phase functions are responsible for high-order effects on the propagation of state. In order to enlighten the different contributions, we expand $\phi_x(\omega_x)$ up to the third order in ω_x, $x = s, i$, namely:

$$\phi_x(\omega_x) \simeq \sum_{k=0}^{3} \frac{1}{k!} \frac{\partial^n}{\partial \omega_x^n} \phi_x(0)\, \omega_x^n \tag{A.2}$$

$$\simeq \beta_x^{(0)} + \beta_x^{(1)} \omega_x + \frac{\beta_x^{(2)}}{2!} \omega_x^2 + \frac{\beta_x^{(3)}}{3!} \omega_x^3, \tag{A.3}$$

where $\beta_x^{(k)} = \partial_{\omega_x}^n \phi_x(0)$. Each coefficient $\beta_x^{(k)}$ of the expansion plays a well defined role in the photon propagation (in our analysis we do not consider the constant phase $\beta_x^{(0)}$ since, as we will see, it will not contribute to the quantities of interest considered throughout the rest of the chapter). The first order coefficient $\beta_x^{(1)}$ represents the "time" spent by the photons to reach the BS and is related to the group velocity. The second order coefficient $\beta_x^{(2)}$ refers to the group velocity dispersion experienced by both photons and it is due to the presence of dispersive media. Finally, the third order dispersion coefficient $\beta_x^{(3)}$, though it has usually a small impact in common materials, may have a huge effect when using very long optical fibers.

In each path, then, the two photons can experience a different dispersion, which may largely affect the TPI process and the occurrence of the HOM effect. More in details, if we introduce the "delay time"

$$\tau = \beta_s^{(1)} - \beta_i^{(1)},$$

the probability of having coincident counts after the BS as a function τ reads:

$$P(\tau) = \iint d\omega_p\, d\omega\, |A(\omega_p)|^2 \left| T f(\omega) \mathrm{e}^{\mathrm{i}[\phi_s(\omega_p,\omega)+\phi_i(\omega_p,-\omega)]} - R f(-\omega) \mathrm{e}^{\mathrm{i}[\phi_s(\omega_p,-\omega)+\phi_i(\omega_p,\omega)]} \right|^2, \tag{A.4}$$

where T and R are the transmission and reflection coefficients of the beam splitter.

In the following we will show how we can experimentally manipulate and control the different contributions described above and, in particular, we will investigate their effects on the HOM dip and visibility.

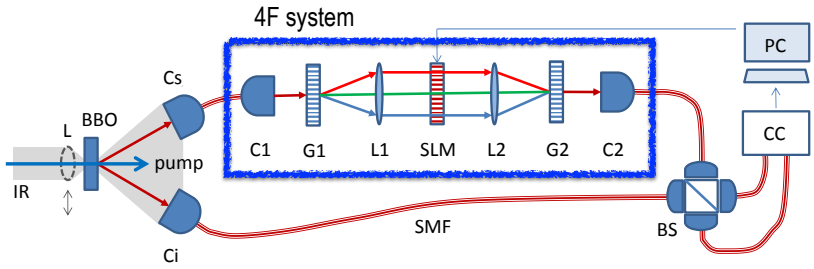

Figure A.1: Schematic diagram of our the two-photon interference apparatus. From left to right, the pump laser @ 405.5 nm (blue arrow) enters the BBO crystal and is downconverted. PDC photons are collected with couplers (Cs, Ci). The idler photon travels until the BS entirely through the fiber (SMF). The signal photon travels also through the 4F optical system before entering again the fiber and reaching the BS. Two single photon detectors, with a Time-to-Amplitude Converter/Single-Channel Analyzer (TAC/SCA) system, detect the coincident counts (CC) at the two BS outputs. The shadowed region on the left, represents an IR laser beam that a lens (L) focalizes in the BBO position in order to perform an interference test. The See the text for details.

A.3 Experimental apparatus

In Fig. A.1 we show a schematic diagram of the experimental apparatus. The two frequency-entangled photon state is generated with a diode pump laser @ 405.5 nm by using a BBO crystal (1 mm thick). The signal and idler photons are then collected by two fiber couplers and sent into single spatial mode and polarization preserving fibers (SMF). A 1 mm thick crystal is enough to couple the maximum amounts of PDC radiation with our fiber couplers (Cs and Ci), as the interaction length inside the crystal between the pump and the fiber mode is slightly lower than 1 mm [154]. The residual of the pump reaches a homemade high-resolution spectrometer (not shown in the figure). The possibility to stabilize the laser to different temperatures allows to keep the same central wavelength while changing the current (and, thus, the laser power) and to perform two-photon interference measurements with different pump laser spectral widths (70 mA and 150 mA to have a narrower and broader pump respectively). We note that the radiation generated by a broadband laser diode is made by a comb of spectral modes without phase relationship. However, as we wrote in the previous section, in our case $\omega_p \ll \omega$, thus the temporal width of the HOM dip is well within the pump coherence time. For this reason, in order to perform the theoretical prediction about the HOM dip, we can use the Eq. (A.1) where we have a coherent superposition of all pump modes. When the idler photon enters the coupler Ci, it travels entirely through the fiber towards the BS. Conversely, the signal photon, after a short fiber, enters a 4F system [155], i.e. propagates in the air, through few optical devices (the couplers C1 and C2, the gratings G1 and G2 and lens L1 and L2) and a spatial light modulator (SLM). At the end of the 4F system the signal photon is again coupled to a fiber and finally reaches the BS, where it interferes with the idler.

The SLM is a 1D liquid crystal mask (640 pixels, 100 μm/pixel) and is placed on the Fourier plane between the two lenses L1 and L2 of the 4F system (see Fig. A.1). The SLM can be used to introduce and control a phase function $\phi_{\mathrm{M}}(\omega_p, \omega)$ on the signal photon. The possibility to choose at will $\phi_{\mathrm{M}}(\omega_p, \omega)$ allows us to achieve several goals (even at the same time): 1) to introduce from second to high-order dispersion effects on the HOM dip; 2) to perform a delay-time scan of the coincidence counts rate, avoiding any mechanical

stress on the apparatus (this method to perform a delay scan is crucial for the stability of the 4F coupling efficiency); 3) to compensate any dispersion effects introduced by the fibers and the 4F system.

As a matter of fact, also the presence of the 4F optical system on the signal path introduces a phase function $\phi_{4F}(\omega_p, \omega)$ and, in particular, due to small shifts of the grating positions with respect to the optimal ones, it introduces second [156] and third order dispersions on its own.

Finally, the signal and idler optical fibers lead to the further phase functions $\phi_{f,s}(\omega_p, \omega)$ and $\phi_{f,i}(\omega_p, \omega)$, respectively.

Taking into account all the mentioned contributions, we have:

$$\phi_s(\omega_p, \omega) = \phi_{f,s}(\omega_p, \omega) + \phi_{4F}(\omega_p, \omega) + \phi_M(\omega_p, \omega), \tag{A.1a}$$

$$\phi_i(\omega_p, \omega) = \phi_{f,i}(\omega_p, \omega), \tag{A.1b}$$

and we can rewrite Eq. (A.4) as:

$$\begin{aligned} P(\tau) = \iint d\omega_p\, d\omega\, |A(\omega_p)|^2 \Big\{ & T^2 f(\omega)^2 + R^2 f(-\omega)^2 \\ & - 2\,R\,T\,\Re\mathrm{e}\Big[f(\omega)\overline{f(-\omega)}\, \mathrm{e}^{\mathrm{i}\phi_{\mathrm{tot}}(\omega_p,\omega)} \Big] \Big\}, \end{aligned} \tag{A.2}$$

$$\begin{aligned} \simeq \iint d\omega_p\, d\omega\, |A(\omega_p)|^2 \Big\{ & T^2 f(\omega)^2 + R^2 f(-\omega)^2 \\ & - 2\,R\,T\,\Re\mathrm{e}\Big[f(\omega)\overline{f(-\omega)} \times \mathrm{e}^{\mathrm{i}2\omega\tau + i\phi^{(2)}_{\mathrm{tot}}(\omega_p,\omega) + i\phi^{(3)}_{\mathrm{tot}}(\omega_p,\omega)} \Big] \Big\}, \end{aligned} \tag{A.3}$$

where $\phi_{\mathrm{tot}}(\omega_p, \omega) = \phi_s(\omega_p, \omega) - \phi_s(\omega_p, -\omega) + \phi_i(\omega_p, -\omega) - \phi_i(\omega_p, \omega)$, and the total second and third order dispersion terms are (note that, as mentioned, the zero order terms cancel out):

$$\phi^{(2)}_{\mathrm{tot}}(\omega_p, \omega) = \beta^{(2)}_{\mathrm{tot}}\, \omega_p\, \omega, \tag{A.4}$$

$$\phi^{(3)}_{\mathrm{tot}}(\omega_p, \omega) = \frac{1}{4}\, \beta^{(3)}_{\mathrm{tot}}\, {\omega_p}^2\, \omega + \frac{1}{3}\, \beta^{(3)}_{\mathrm{tot}}\, \omega^3, \tag{A.5}$$

respectively, with:

$$\beta^{(k)}_{\mathrm{tot}} = \beta^{(k)}_{\mathrm{f}} + \beta^{(k)}_{\mathrm{4F}} + \beta^{(k)}_{\mathrm{M}} \qquad (k = 2, 3). \tag{A.6}$$

According to our formalism, the quantities appearing at the RHS of the last equation refer to the k-th order dispersion coefficients due to the fibers (f), to the 4F system (4F) and to the SLM (M). It is worth noting that $\beta^{(k)}_{\mathrm{f}} = d^{(k)}_{\mathrm{f}} \Delta L$, where $d^{(k)}_{\mathrm{f}}$ is the k-th order dispersion of the fiber and ΔL is the length difference between the signal and idler optical fiber. We want to emphasize that while the 4f system and the SLM are only along the path of the signal photon, both photons pass through different thicknesses of optical fibers, such that Eq. (A.6) describe the dispersions on both photons.

It is straightforward to see that in the presence of an almost monochromatic pump, i.e., $\omega_p \simeq 0$, the only relevant dispersion effect comes from the second term of the RHS in Eq. (A.5), that is the second order dispersion does not affect the HOM dip shape, in other words, in the case of monochromatic pump our model reduces to the well know second order dispersion cancellation effect [139]. Moreover, we note that when the two optical fibers have the same length, the high order dispersion effect due to the fibers vanishes. For the same reason, the high orders dispersion due to the generating crystal does not affect the HOM dip profile.

The presence of several optical components in the apparatus leads to an overall loss in purity of the polarization quantum state of the photons. In order to assess the purity, we performed an interferometric measurement: after a strong filtering with neutral density filters, we focus a 811 nm laser in the BBO position and couple the radiation of the resulting divergent beam with the fibers. Then we obtain a Mach-Zehnder interferometer where the action of focusing plays the role of the first BS. Counts are then balanced by carefully positioning the focusing lens: this is crucial in order to have the same amount of direct counts on both paths, thus maximizing the interferogram visibility.

If θ is the polarization mismatching between the two beams reaching the BS, the visibility of the interferogram is given by $V_{\mathrm{I}} = |\cos\theta|$. It is now straightforward to show that the visibility of the HOM dip V_{H} is directly linked to the interferogram visibility by

$$V_{\mathrm{H}} = \frac{R\,T\,V_{\mathrm{I}}^2}{1 - 2\,R\,T - R\,T\,V_{\mathrm{I}}^2}. \tag{A.7}$$

In our experiment the measured visibility is $(95.6 \pm 0.5)\%$, corresponding to a mismatching angle of $\theta = (17.2 \pm 0.9)^\circ$ and a purity factor $p = \cos^2\theta \approx 91\%$. Since, given p, the coincidence counts probability becomes:

$$P_{\mathrm{tot}}(\tau) = P(\tau)\,p + \frac{1}{2}(1-p), \tag{A.8}$$

then the maximum dip visibility we can achieve with the measured $T = 0.467$, $R = 0.533$ and a symmetric PDC spectrum, i.e. $f(\omega) = f(-\omega)$, turns out to be $(82 \pm 2)\%$.

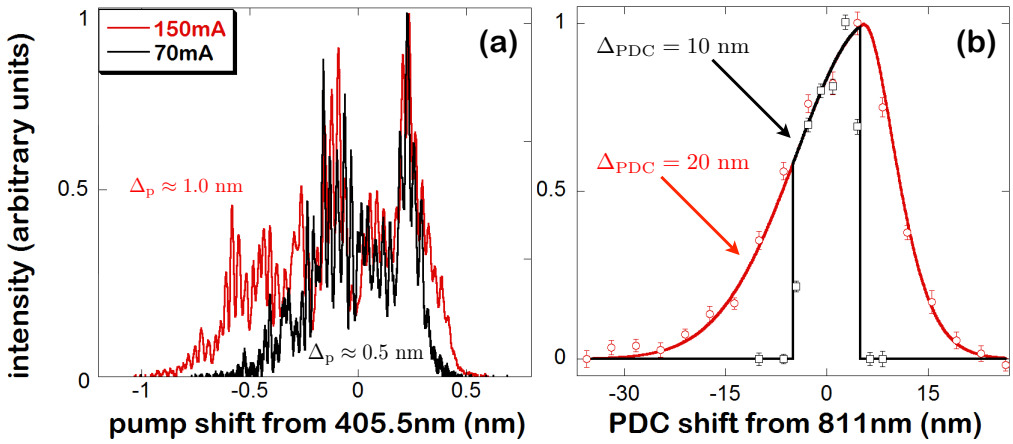

Figure A.2: Pump and PDC spectra. Panel (a): measured pump spectrum shift about the central wavelength of 405.5 nm, with 70 mA (spectrum width $\Delta_{\mathrm{p}} \approx 1.0$ nm) and 150 mA (spectrum width $\Delta_{\mathrm{p}} \approx 0.5$ nm) current. Panel (b): PDC spectrum data points and curve fit, with a slit on the Fourier plane (spectrum width $\Delta_{\mathrm{PDC}} = 10$ nm) and without it (spectrum width $\Delta_{\mathrm{PDC}} = 20$ nm).

In Fig. A.2 we show the pump and PDC spectra we used during our measurements. On the pump side, in Fig. A.2(a) one can see the difference in the pump spectrum width between two different current settings: the narrower spectrum ($\Delta_{\mathrm{p}} \approx 0.5$ nm) corresponds to a current of 70 mA, while a current of 150 mA leads to a broader spectrum ($\Delta_{\mathrm{p}} \approx 1$ nm). We measured the pump spectrum with a homemade spectrometer as follows. We collected the residual of the pump light with a fiber and delivered it towards a

collimating lens. Then, a grating (3600 l/mm) divides the collimated beam into its spectral components. These are then focused with a 300 mm lens onto the sensor of a CMOS camera placed on the Fourier plane.

Figure A.2(b) shows the PDC spectrum. We can choose the nominal spectrum ($\Delta_{\mathrm{PDC}} = 20$ nm) or the "cut" spectrum ($\Delta_{\mathrm{PDC}} = 10$ nm) with a slit placed on the Fourier plane of the 4F system. We measured PDC spectra with a 2 mm slit on the Fourier plane of the 4F system. We calibrated the slit using a graduated reference on the Fourier plane: we found the 811 nm component position for the slit, we measured a dispersion coefficient of 3.62 nm for a 2 mm slit displacement and finally, in order to measure the spectrum, for each slit position (and therefore for each wavelength) we recorded coincidence counts from the detectors.

As mentioned above, one usually desires to have symmetric PDC spectra. However, Fig. A.2(b) shows that we used a non symmetric signal photon spectrum. It is worth noting that our apparatus allows us to center the PDC spectra on 811 nm: this is possible by transversally moving a mirror that delivers the pump inside the BBO crystal. In this way we make the pump axis (that is the PDC cone axis) be at the exactly same distance from both fiber couplers. However, we found that the 4F system introduced an asymmetric cut on the PDC spectrum tails, that is translated in an antisymmetric cut on the idler photon spectrum. This makes the two photons distinguishable and the visibility worsen. The spectrum we report in Fig. A.2(b) correspond to the spectrum giving the highest visibility possible in our configuration: the peaks are not superimposed at 811 nm but the tails are. Overall, this makes the two photons less distinguishable than the situation where the tails are not superimposed.

A.4 Experimental results

A slit placed under one of the fiber couplers is used to match signal and idler paths. The SLM delay-time scan method allows us to match the two paths with an error of less than 1 μm. A range of several picoseconds can be covered with an SLM delay-time scan. Therefore, before measuring, signal and idler paths were always perfectly matched. In Fig. A.3, we report some measured dip profiles (points) together with the corresponding theoretical predictions (lines). It is worth noting that the predictions are obtained from Eq. (A.8) and from the experimental spectra of Fig. A.2 without any fitting parameter. The experimental data are normalized using the mean value at high delay time (i.e., outside the HOM dip). The time windows for the counts acquisition for each point are 2 s and 2.5 s, respectively, for the cases at 150 mA and 70 mA. Each line in Fig. A.3 corresponds to a different configuration. On the left column, we show three different profiles related to three different values of the second order dispersion coefficient; on the right column, we report the profiles for three different values of the third order dispersion coefficient. In the top panels, (a1) and (b1), we have results for the broader pump spectrum (1 nm) and normal PDC spectrum (20 nm) (from now on we refer to these values as to configuration S1). We found a huge dependence on second and third order dispersion: the dip visibility decreases and its width increases, with increasing dispersion. In the panels (a2) and (b2), we show results for the case of the narrower pump spectrum ($\Delta_{\mathrm{p}} \approx 0.5$ nm) and normal PDC spectrum ($\Delta_{\mathrm{PDC}} = 20$ nm, configuration S2). In this case, the dependence of the dip shape on the second order dispersion is significantly weaker, while the dependency on the third order dispersion remains the same of the previous case.

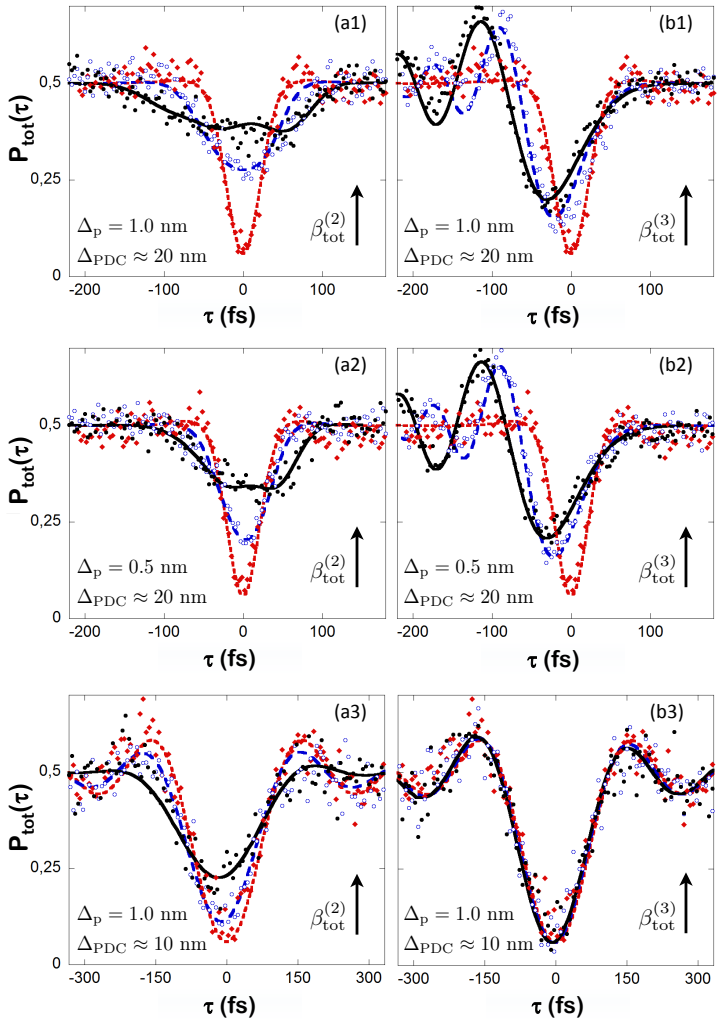

Figure A.3: The HOM dip in the presence of second and third order dispersion. In panels (a1), (a2), and (a3) we show the dip profiles for three different second order dispersion values, from the lower to the higher dip we set $\beta_{tot}^{(2)} = 0$ fs^2 (red dotted line and rhombus for theoretical prevision and data points, respectively), 17.6×10^3 fs^2 (blue dashed line and empty circles), 35.2×10^3 fs^2 (black solid line and filled circles). In panels (b1), (b2), and (b3) we show the dip profiles for three different third order dispersion values, from the lower to the higher dip we set $\beta_{tot}^{(3)} = 0$ fs^3 (red dotted line and rhombus), 17.6×10^4 fs^3 (blue dashed line and empty circles), 35.2×10^4 fs^3 (black solid line and filled circles). The corresponding values of Δ_p and Δ_{PDC} of the pump and PDC spectrum widths are reported in the panels. All solid lines are theoretical predictions obtained from Eq. (A.8).

This is in agreement with the fact that two-photon interference is affected by second order dispersion only if the pump is not monochromatic, while it is always affected by third order dispersion (and all odd orders, including the first order). In the above cases, one may quantify the effects of the third order dispersion on the HOM dip by looking at the visibility. On the bottom line of Fig. A.3, panels (a3) and (b3), we have the

case of the broader pump spectrum ($\Delta_p \approx 1.0$ nm) and the cut PDC spectrum ($\Delta_{PDC} = 10$ nm, configuration S3). While we still have a visible dependence on the second order dispersion, the dependence on the third order dispersion disappears. The width of the compensated dip, here, is much larger than in the cases above. This comes directly from Eq. (A.3). A peculiar behaviour can be seen here: symmetric oscillation appear on the dip, caused by the clean cut of the PDC spectrum.

A.5 Discussion

As we mentioned in the introduction, by a suitable choice of the phase function we can simulate the high order dispersion effects of a particular transmission channel. In particualr, the values of the second and third order contribution we used in our experiment are related to those obtained in current optical fibers. For instance, a dispersion of 30×10^3 fs^2 is induced by a fused silica fiber ≈ 850 mm long ($d_f^{(2)} \approx 35$ fs^2/mm). For a third order dispersion of 300×10^3 fs^3, on the other hand, ≈ 11 m of fiber are needed ($d_f^{(3)} \approx 30$ fs^3/mm) or, for example, 35 cm of ZnSe ($d_f^{(3)} = 870$ fs^3/mm). It is worth noting that these lengths are quite small compared to those to be used in telecommunications. For this reason the full comprehension of these dispersion effects on the HOM dip becomes a fundamental a prerequisite. In Fig. A.4 we summarize our main results:

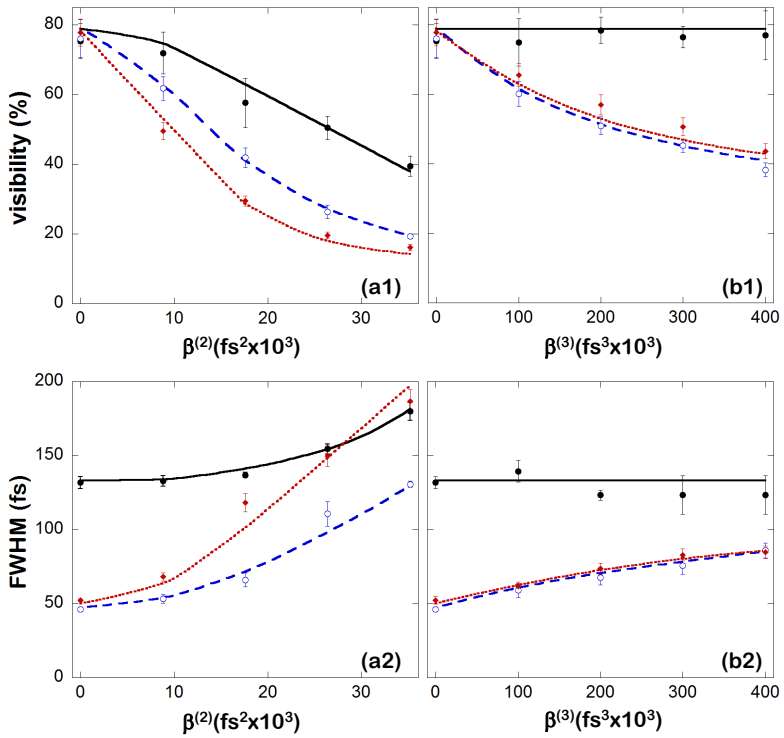

Figure A.4: Visibility and FWHM of the HOM dip as a function of $\beta_{tot}^{(2)}$ and $\beta_{tot}^{(3)}$ for different pump and PDC spectra: PDC $\Delta_{PDC} = 10$ nm and $\Delta_p = 1.0$ nm (solid lines); Dotted line: $\Delta_{PDC} = 20$ nm and $\Delta_p = 1.0$ nm (dotted); $\Delta_{PDC} = 20$ nm and $\Delta_p = 0.5$ nm (dashed lines).

we can see the behaviour of the dip visibility and full width at half maximum (FWHM) as a function of second and third order dispersions. The visibility and the FWHM are defined with respect to the normalized value and are obtained by using suitable fitting functions. Each plot reports the results for the three different experimental configurations introduce above: dotted red line for S1, dashed blue line for S2 and solid black line for S3. In panel (a1), on the upper left, we see how visibility decreases as the the second order dispersion increases. This worsening gets less sharp if we cut down either the PDC spectrum (S3) or the pump spectrum (S2). In panel (a2), on the lower left, we see how the dip FWHM increases (the dip gets broader) when the second order dispersion coefficient increases. As already mentioned above, without dispersion the dip FWHM in S3 is larger than in S1 and S2. In both S2 and S3, the FWHM is much less sensitive to the second order dispersion compared to the case of broad pump and PDC spectra.

In Fig. A.4(b1) and (b2), on the right, we studied again the changes in the dip visibility and FWHM as a function of the third order dispersion. We can see how the cut of the PDC spectrum keeps frozen the dip parameters, making them insensitive to any third order dispersion coefficient. However, we can also clearly see that the visibility and the FWHM do not depend on the pump spectrum.

A.6 Conclusions

In this work we have designed and developed an experimental setup to engineer second and third order dispersion effects on the propagation of PDC photons. By using our innovative apparatus, which is able to introduce and manipulate a custom phase function with a SLM, we have analyzed high-order dispersion effects in two-photon interference. In particular, we have studied theoretically and experimentally, the dependence of both the visibility and the width of the HOM dip on both the pump spectrum and on the downconverted photon spectrum. The motivations behind our work are the characterization and the optimization of quantum resources for protocols based on a non-collinear HOM, e.g. superdense coding or quantum optical coherence tomography. In these examples, the two photons usually propagate with different dispersion before the beam splitter and a precise characterization of this effect is in order.

Our results show that our system may be effectively employed to introduce high-order dispersion effects on the propagation of photons. We emphasize that the same setup may be used to *compensate* such effect. Therefore, on the one hand, our results clarify the role of the different dispersion coefficients and, on the other hand, they pave the way for optimization procedures in communications protocols and other applications in quantum technology involving PDC photons and optical fibers.

APPENDIX B

Theoretical tools

B.1 Comments about the $\nabla \cdot \mathbf{E} = 0$ condition

In chapter 4 I used the condition $\nabla \cdot \mathbf{E} = 0$. Actually, the condition we have when ρ and J are zero is $\nabla \cdot \mathbf{D} = 0$, that automatically implies that $\nabla \cdot \mathbf{E} = 0$ only if $\mathbf{D}$ and $\mathbf{E}$ are proportional. It is immediate when we consider, for simplicity, an instantaneous linear medium response: in this case, we have $\mathbf{D} = \varepsilon_0(1+\chi)\mathbf{E}$. Any nonlinear correction to the polarization would be typically small and can be neglected, therefore we can still assume $\nabla \cdot \mathbf{E} = 0$. For example, in the presence of a second order nonlinearity we can proceed as follows. Thanks to eq. 4.19 we can write

$$\nabla \cdot \mathbf{D} = \nabla \cdot (\varepsilon_0 \mathbf{E} + \mathbf{P}_L + \mathbf{P}_{NL}) = \varepsilon_0 \nabla \cdot \mathbf{E} + \varepsilon_0 \chi \nabla \cdot \mathbf{E} + \varepsilon_0 \chi^{(2)} \nabla \cdot \mathbf{E}^2 = 0, \tag{B.1}$$

where we considered only the presence of a second order nonlinearity and a homogeneous medium. As a consequence we have

$$\varepsilon_0 \nabla \cdot \mathbf{E}(1 + \chi + 2\chi^{(2)}\mathbf{E}) = 0 \Rightarrow \nabla \cdot \mathbf{E} = 0 \tag{B.2}$$

as, for small nonlinear corrections, the term in brackets does not go to zero.

B.2 Walk-off

For a laser beam propagating in an isotropic medium, the transverse intensity distribution propagates along the beam axis as defined by the medium wave vector (**k** vector). In anisotropic (and thus birefringent) crystals, this is not necessarily the case: it can occur that the intensity distribution drifts away from the direction defined by the wave vector, as illustrated in Fig. B.1 where the gray lines indicate wavefronts and the blue color the region with significant optical intensity.

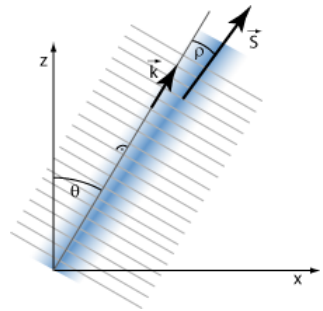

Figure B.1: Spatial walk-off: the intensity distribution of a beam in an anisotropic crystal propagates in a direction which is slightly different to that of the wave vector.

This phenomenon, called *spatial walk-off*, *birefringent walk-off* or *Poynting vector walk-off*, is associated with some finite angle ρ (called walk-off angle) between the Poynting vector and the wave vector. The Poynting vector defines the direction of energy transport, whereas the wave vector is normal to the wavefronts.
Spatial walk-off occurs only for a beam with extraordinary polarization propagating at

some angle θ against the optical axes, so that the refractive index n_e and the phase velocity become dependent on that angle. The walk-off angle can then be calculated from the equation

$$\rho = -\frac{1}{n_e(\bar{\theta})} \left. \frac{\partial n_e}{\partial \theta} \right|_{\bar{\theta}} \tag{B.1}$$

where the minus sign indicates that the walk-off occurs in the direction where the refractive index would decrease. The extraordinary index n_e and its derivative are the values occurring for the specific angle $\bar{\theta}$. A beam with ordinary polarization (where the refractive index is not dependent on the propagation angle) does not experience walk-off.
The magnitude of the walk-off angle is exaggerated in Fig. B.1. In typical cases, it is in the range between a few milliradians and some tens of milliradians. For propagation directions close to one of the axes of the index ellipsoid, the walk-off can even become much smaller.

Thesis tools

EKSPLA NL303-10 characteristics	
Active medium	Nd:YAG
Wavelength	$1064\,nm$
Pulse duration	$4.0 \pm 0.3\,ns$ at 100% pump level
Pulse energy (max)	$800\,mJ$
Pump type	High power halogen gas flash lamp
Pump power	Tunable to more than 200 W
Max. operating frequency	10 Hz
Nd:YAG rod length	$114.4 \pm 3.8\,mm$
Nd:YAG rod radius	$3.35 \pm 0.13\,mm$
Effective cavity length (mirror-mirror)	$500 \pm 15\,mm$
Beam radial diameter	$10.0 \pm 0.5\,mm$
Beam radial profile	Top-hat function
Jitter trigger signal-pulse shot	$< 0.3\ ns$ (instrument limited)
Free spectral range	$300 \pm 10\,MHz$
Spatial structure	single modal (top-hat profile)
Spectral structure	multi modal

Figure C.1: Principal characteristics of the EKSPLA pump cavity

Bibliography

[1] ATLAS collaboration, *Phys. Lett. B* **716**, 1 (2012).

[2] CMS collaboration, *Phys. Lett. B* **716**, 30 (2012).

[3] LIGO and VIRGO collaborations, *Phys. Rev. Lett.* **116**, 061102 (2016).

[4] D. Colladay and V. A. Kostelecky, *Phys. Rev. D* **55**, 6760 (1997).

[5] E. G. Adelberger *et al.*, *Prog. Part. Nucl. Physics* **62**, 102 (2009).

[6] N. Arkani-Hamed, S. Dimopoulos, and G. Dvali, *Phys. Rev. D* **59**, 086004 (1999).

[7] J. Barrow and R. Scherrer, *Phys. Rev. D* **70**, 103515 (2004).

[8] A. H. Chamseddine and A. Connes, *Phys. Rev. Lett.* **77**, 4868 (1996).

[9] G. J. Ni, Nova Science Publications, p. 123 (2004).

[10] M. M. Nieto, T. Goldman, *Physics Reports* **205**, 221 (1991).

[11] M. Villata, *Europhys. Lett.* **94**, 20001 (2011).

[12] A. G. Cohen, A. De Rujula and S. L. Glashow, *The Astrophysical Journal* **495**, 539 (1998).

[13] M. Yu. Khlopov, S. G. Rubin, and A. S. Sakharov, *Phys. Rev. D* **62**, 083505 (2000).

[14] M. Dine and A. Kusenko, *Rev. Mod. Phys.* **76**, 1 (2003).

[15] N. J. Popławski, *Phys. Rev. D* **83**, 084033 (2011).

[16] J. P. Ostriker and P. J. Steinhardt†, *Nature* **377**, 600 (1995).

[17] T.W. Darling *et al.*, *Rev. Mod. Phys.* **64**, 237 (1992).

[18] V. Vanyashin, *Lett. Math. Phys.* **31**, 143 (1994).

[19] H. K. Avetissian, A. K. Avetissian and G. F. Mkrtchian, *Phys. Rev. Lett.* **113**, 023904 (2014).

[20] K. Shu *et al.*, *J. Phys. B: At. Mol. Opt. Phys.* **49**, 104001 (2016).

[21] A. A. Penin, *Int. J. Mod. Phys. A* **19**, 3897 (2004).

[22] L. Badano *et al.*, *Proceedings of DIPAC 2007*, 352 (2007).

[23] D. H. E. Dubin and T. M. O'Neil, *Rev. Mod. Phys.* **71**, 87 (1999).

[24] R. Caravita, WAG conference proceeding under publication.

[25] D. Kranss *et al.*, *AIP Conference Proceedings* **1521**, 144 (2013).

[26] R. G. Greaves and C.M. Surko, *Phys. Plasmas* **4**, 1528 (1997).

[27] J. R. Danielson *et al.*, *Rev. Mod. Phys.* **87**, 247 (2015).

[28] C. Canali *et al.*, *Eur. Phys. J., Sect. D* **65/3**, 499 (2011).

[29] E. M. Hollmann, F. Anderegg, and C. F. Driscoll, *Phys. of Plasm.* **7**, 2776 (2000).

[30] Y. Nagashima et al., *Phys. Rev. B* **58**, 12676 (1998).

[31] S. Mariazzi *et al.*, *Phys. Rev. Lett.* **104**, 243401 (2010).

[32] E. A. Hessels, D. M. Homan, and M. J. Cavagnero, *Phys. Rev. A* **57**, 1668 (1998).

[33] A. Speck, C. H. Storry, E. A. Hessels, and G. Gabrielse, *Phys. Lett. B* **597**, 257 (2004).

[34] J. E. Blackwood, M. T. McAlinden, and H. R. J. Walters, *Phys. Rev. A* **65**, 032517 (2002).

[35] F. Castelli, I. Boscolo, S. Cialdi, M. G. Giammarchi, D. Comparat, *Phys. Rev. A* **78**, 052512 (2008).

[36] F. Villa, *Laser system for positronium excitation to Rydberg levels for Aegis experiment*, PhD thesis, Milano (2011).

[37] G. Consolati *et al.* (AEḡIS collaboration), *EPJ Web of Conferences* **96**, 01007 (2015).

[38] G. Baur *et al.*, *Phys. Lett. B* **368**, 251 (1996).

[39] G. Blanford *et al.*, *Phys. Rev. Lett.* **80**, 3037 (1997).

[40] M. Amoretti *et al.*, *Nature* **419**, 456 (2002).

[41] G. Gabrielse, *et al.*, *Phys. Rev. Lett.* **89**, 213401 (2002).

[42] M. C. Fujiwara *et al.*, *Hyperfine Int.* **172**, 81 (2006).

[43] E. Widmann (ASACUSA collaboration), *Nuclear Physics A* **655**, C353 (1999).

[44] A. Kellerbauer (AEḡIS collaboration), *EPJ Web of Conferences* **126**, 02016 (2016).

[45] G. Gabrielse *et al.*, *Phys. Rev. Lett.* **57**, 2504 (1986).

[46] A. Müller and A. Wolf, *Hyperfine Int.* **109**, 233 (1997).

[47] J. Stevefelt, J. Boulmer and J.F. Delpech, *Phys. Rev. A* **12**, 1246 (1975).

[48] G. B. Andresen *et al.* (ALPHA collaboration), *Nature Physics* **7**, 558 (2011).

[49] C. Amole *et al*., *Nature Commun.* **4**, 1785 (2013).

[50] J. P. Merrison, H. Bluhme, J. Chevallier, B. I. Deutch, P. Hvelplund, L. V. Jorgensen, H. Knudsen, M. R. Poulsen, and M. Charlton, *Phys. Rev. Lett.* **78**, 2728 (1997).

[51] C. Storry *et al*. (ATRAP collaboration), Phys. Rev. Lett. 93, 263401 (2004).

[52] J. Di Sciacca *et al*. (ATRAP collaboration), *Phys. Rev. Lett.* **110**, 130801 (2013).

[53] A. Mooser *et al*., *Nature* **509**, 596 (2014).

[54] H. Häffner *et al*., *Eur. Phys. J. D* **22**, 163 (2003).

[55] J. Di Sciacca and G. Gabrielse, *Phys. Rev. Lett.* **108**, 153001 (2012).

[56] A. Mohri and T. Yamazaki, *Europhys. Lett.* **63**, 207 (2003).

[57] H. Saitoh, A. Mohri, Y. Enomoto, Y. Kanai and Y. Yamazaki, *Phys. Rev. A* **77**, 051403 (2008).

[58] Y. Enomoto *et al*. (ASACUSA collaboration), *Phys. Rev. Lett.* **105**, 243401 (2010).

[59] N. Kuroda *et al*. (ASACUSA collaboration), *Nature Commun.* **5**, 3089 (2014).

[60] M. Hori *et al*. (ASACUSA collaboration), *Nature* **475**, 484 (2011).

[61] Amsler *et al*., *International Journal of Modern Physics A* **29**, 1430035 (2014).

[62] G. Testera *et al*, (AE$\bar{g}$IS Collaboration), *AIP Conf. Proc.*, **1037**, 5 (2008).

[63] E. Vliegen, S. D. Hogan, H. Schmutz, and F. Merkt, *Phys. Rev. A* **76**, 023405 (2007).

[64] P. Crivelli, D. Cooke, M. Heiss, *Phys. Rev. D* **94**, 052008 (2016).

[65] S. Aghion *et al*. (AEGIS collaboration), *Nature Commun.* **5**, 4538 (2014).

[66] C. Amsler *et al*., *Jinst* **8**, P02015 (2013).

[67] E. Vliegen and F. Merkt, *Journ. Phys. B* **39**, L241 (2006).

[68] M. Kimura *et al*. (AEGIS collaboration), *Nuclear Instr. Meth. in Phys Res A* **732**, 325 (2013).

[69] M. Scampoli *et al*. (AEGIS collaboration), *JInst* **9**, C01061 (2014).

[70] M. K. Oberthaler, S. Bernet, E. M. Rasel, J. Schmiedmayer, and A. Zeilinger, *Phys. Rev. A* **54**, 3165 (1996).

[71] M. Fujiwara *et al*., *Phys. Rev. Lett.* **101**, 053401 (2008).

[72] M. Amoretti *et al*., *Phys. Lett. B* **590**, 133 (2004).

[73] P. A. M. Dirac, *Proc. Cambridge Philos. Soc.* **26**, 361 (1930).

[74] C. D. Anderson, *Physical Review* **43**, 491 (1933).

[75] C. D. Anderson, *Science* **76**, 238 (1932).

[76] E. R. Cohen, and B. N. Taylor, *J. Phys. Chem. Ref. Data* **2**, 663 (1973).

[77] E. Bellotti, M. Corti, E. Fiorini, C. Liguori, A. Pullia, A. Sarracino, P. Sverzellati, and L. Zanotti, *Phys. Lett. B* **124**, 435 (1983).

[78] M. J. T. Collier, L. V. Jørgensen, O. I. Meshkov, D. P. van derWerf, and M. Charlton, *AIP Conf. Proc.* **498**, 13 (1999).

[79] R. Khatri, M. Charlton, P. Sferlazzo, K. G. Lynn, A. P. Mills, and L. O. Roellig, *Appl. Pys. Lett.* **57**, 2374 (1990).

[80] T. J. Murphy and C. M. Surko, *Phys. Rev. A* **46**, 5696 (1992).

[81] C. M. Surko and R. G. Greaves, *Physics of Plasmas* **11**, 2333 (2004).

[82] E. M. Hollmann, F. Anderegg, and C. F. Driscoll, *Rhysics of Plasmas* **7**, 2776 (2000).

[83] M. de Araújo, R. Silva, E. de Lima, D. Pereira, and P. de Oliveira, *Appl. Opt.* **48**, 393 (2009).

[84] L. Penasa *et al*, *J. Phys.: Conf. Ser.* **505**, 012031 (2014).

[85] S. Aghion, *et al*, *Nucl. Instrum. Meth.*, **B362**, 86 (2015).

[86] F. Castelli, *Eur. Phys. J. Spec. Top.* **203**, 137 (2012).

[87] D.B. Cassidy, A.P. Mills Jr, *Nucl. Instr. Meth. Phys. Res. Sect. A* **580**, 1338 (2007).

[88] S. Mariazzi *et al*., *Phys. Rev. B*, **81**, 235418 (2010).

[89] P. J. Schultz and K. G. Lynn, *Rev. Mod. Phys.* **60**, 701 (1988).

[90] R. Ferragut *et al.*, Journal of Physics: Conference Series **225**, 012007 (2010).

[91] Y. Nagashima *et al*., *Phys. Rev. B* **58**, 12676 (1998).

[92] O. Svelto, *Principle of Lasers*, 5th edition (2010).

[93] R. Caravita, "Laser apparatus for exciting Positronium in AEGIS Positronium spectroscopy experiment" master thesis, Università Degli Studi Di Milano (2011-2012).

[94] A. Yariv and P. Yeh, *Optical Waves in Crystals*, (1984).

[95] P.A. Franken, A.E. Hill, C.W. Peters and G. Weinreich, *Phys. Rev. Lett.* **7**, 118 (1961).

[96] S. Cialdi, F. Castelli and I. Boscolo, *Appl. Phys. B* **82**, 383 (2006).

[97] W. Seka, S.D. Jacobs, J.E. Rizzo, R. Boni and R.S. Craxton, *Opt. Commun.* **34**, 469 (1980).

[98] S. Cialdi, M. Petrarca and C. Vicario, *Opt. Lett.* **31**, 2885 (2006).

[99] F. Ferri, bachelor degree thesis (in italian), "*Progettazione e realizzazione di un sistema laser per l'eccitazione efficiente del positronio a livelli Rydberg*"

[100] L. Di Noto, PhD thesis "Positronium in the AEg̅IS experiment: study on its emission from nanochanneled samples and design of a new apparatus for Rydberg excitations", Universitá degli Studi di Trento, sec 3.7.1.

[101] D. Krasnický, R. Caravita, C. Canali, and G. Testera, *Phys. Rev. A* **94**, 022714 (2016)

[102] D. Cooke, P. Crivelli, J. Alnis, A. Antognini, B. Brown, S. Friedreich, A. Gabard, T. W. Haensch, K. Kirch, A. Rubbia, V. Vrankovic, *Hyperfine Int.* **233**, 67 (2015).

[103] D. B. Cassidy, T. H. Hisakado, H. W. K. Tom, and A. P. Mills Jr., *Phys. Rev. Lett.* **108**, 043401 (2012).

[104] D. B. Cassidy, T. H. Hisakado, V. E. Meligne, H. W. K. Tom, and A. P. Mills Jr., *Phys. Rev. A* **28**, 052511 (2010).

[105] I. I. Sobelman, "Atomic Spectra and Radiative Transitions", (1979)

[106] M. Amoretti *et al*. *Phys. Lett. B* **583**, 59 (2004).

[107] M. K. Oberthaler *et al*., *Phys. Lett. A*, **54**, 3165 (1996).

[108] S. Aghion *et al*. (AEḡIS Collaboration), *J. Instrum.*, **8**, P08013 (2013).

[109] A. Kellerbauer, J. Waltz, *New J. Phys.*, **8**, 45 (2006).

[110] D. Comparat, M. Doser, S. Gerber, M. Hamamda, P. Yzombard, *Phys. Rev. Lett*, **114**, 213001 (2015).

[111] U. Warring *et al*., *Phys. Rev. Lett.* **102**, 043001 (2009).

[112] A. Fischer *et al*., *Phys.Rev. Lett.* **104**, 073004 (2010).

[113] E. Jordan *et al*., *Phys. Rev. Lett.* **115**, 113001 (2015).

[114] S. Di Domizio *et al*, *JINST* **10**, P01009 (2015).

[115] M. Charlton, *Phys. Lett. A*, **143**, 143,(1990).

[116] J.R. Danielson, D.H.E. Dubin, R.G. Grieves and C. M. Surko, *Rev. Mod. Phys.*, **87**, 247 (2015).

[117] R.G. Greaves, and C. M. Surko, *Phys. Rev. Lett.*, **85**, 1883 (2000).

[118] L. Penasa, L Di Noto, M Bettonte, S Mariazzi, G Nebbia and R S Brusa, *J. Phys.: Conf. Ser.* **505**, 012031, (2014).

[119] D.B. Cassidy, A.P. Mills, *Nucl. Instrum. Meth. A* **580**, 1338 (2007).

[120] S. Cialdi, I. Boscolo, F. Castelli, F. Villa, G. Ferrari , M.G. Giammarchi, *Nucl. Instrum. Meth.B* **269**, 1527 (2011).

[121] R.W. Boyd, *Nonlinear Optics*, third ed., (2008).

[122] F. Castelli, M.G. Giammarchi, in: *Proceedings of the International School of Physics "Enrico Fermi"*, Course CLXXIV: Physics with many Positrons, (2010).

[123] S. Aghion *et al*. (AEgIS Collaboration), *Phys. Rev. A* **94**, 012507 (2016).

[124] S. Mariazzi, L. Di Noto, G. Nebbia and R. S. Brusa, *Journal of Physics: Conference Series* **618**, 012039 (2015).

[125] D. B. Cassidy, T. H. Hisakado, H. W. K. Tom, and A. P.Mills, *Phys. Rev. Lett.* **108**, 043401 (2012).

[126] O. Halpern, *Phys. Rev.* **94**, 904 (1954).

[127] A. Bisi, A. Fiorentini, E. Gatti and L. Zappa, *Phys. Rev.* **128**, 2195 (1962).

[128] T. E. Wall, A. M. Alonso, B. S. Cooper, A. Deller, S. D. Hogan, and D. B. Cassidy, *Phys. Rev. Lett.* **114**, 173001 (2015).

[129] R. Caravita and F. Castelli, in preparation.

[130] Z. Mazzotta, S. Cialdi, D. Cipriani, S. Olivares and M. G. A. Paris, *Phys. Rev. A* **94**, 063842 (2016).

[131] C. K. Hong, Z. Y. Ou, and L. Mandel, *Phys. Rev. Lett.* **59**, 2044 (1987).

[132] H. Weinfurter, *Europhys. Lett.* **25**, 559 (1994).

[133] S. L. Braunstein, and A. Mann, *Phys. Rev. A* **51**, R1727 (1995).

[134] K. Mattle, H. Weinfurter, P. G. Kwiat, and A. Zeilinger, *Phys. Rev. Lett.* **76**, 4656 (1996).

[135] J. T. Barreiro, T.-C. Wei, P. G. Kwiat, *Nature* **4**, 282 (2008).

[136] V. Giovannetti, S. Lloyd, L. Maccone, and F. N. C. Wong *Phys. Rev. Lett.* **87**, 117902 (2001).

[137] D. Huang, E. A. Swanson, C. P. Lin, J. S. Schuman, W. G. Stinson, W. Chang, M. R. Hee, T. Flotte, K. Gregory, C. A. Puliafito, and J. G. Fujimoto, *Science* **254**, 1178 (1991).

[138] A. G. Van Engen, S. A. Diddams, and T. S. Clement, *Appl. Opt.* **37**, 5679 (1998).

[139] A. M. Steinberg, P. G. Kwiat, R. Y. Chiao, *Phys. Rev. Lett.* **68**, 2421 (1992).

[140] A. F. Abouraddy, M. B. Nasr, B. E. A. Saleh, A. V. Sergienko, and M. C. Teich, *Phys. Rev. A* **65**, 053817 (2002).

[141] M. B. Nasr, B. E. A. Saleh, A. V. Sergienko, and M. C. Teich, *Phys. Rev. Lett.* **91**, 083601 (2003).

[142] K. J. Resch, R. Kaltenbaek, R. Lavoie, and D. N. Biggerstaff, *Proc. SPIE* **7465**, 74650N (2009).

[143] B. Dayan, Phys. Rev. A. **76**, 043813 (2007).

[144] J. Peřina, Jr., A. V. Sergienko, B. M. Jost, B. E. A. Saleh, and M. C. Teich, *Phys. Rev. A* **59**, 2359 (1999).

[145] R. Erdmann, D. Branning, W. Grice, and I. A. Walmsley, *Phys. Rev. A* **62**, 053810 (2000).

[146] M. Okano, R. Okamoto, A. Tanaka, S. Ishida, N. Nishizawa, and S. Takeuchi, *Phys. Rev. A* **88**, 043845 (2013).

[147] M. Okano, H. H. Lim, R. Okamoto, N. Nishizawa, S. Kurimura, and S. Takeuchi, *Sc. Rep.* **5**, 18042 (2015).

[148] M. Atatüre, A. V. Sergienko, B. M. Jost, B. E. A. Saleh, and M. C. Teich, *Phys. Rev. Lett.* **83**, 1323 (1999).

[149] R. Okamoto, S. Takeuchi, and K. Sasaki, Phys. Rev. A. **74**, 011801(R) (2006).

[150] K. N. Cassemiro, K. Laiho, Ch. Silberhorn, *New J. Phys.* **12**, 113052 (2010).

[151] K. Laiho, K. N. Cassemiro, Ch. Silberhorn, *Opt. Expr.* **17**, 22823 (2009).

[152] A. Smirne, S. Cialdi, G. Anelli, M. G. A. Paris, and B. Vacchini *Phys. Rev. A* **88**, 012108 (2013).

[153] A. Joobeur, B. E. A. Saleh, T. S. Larchuk, and M. C. Teich *Phys. Rev. A* **53**, 4360 (1996).

[154] L. E. Vicent, A. B. U'Ren, R. Rangarajan, C. I Osorio, J. P Torres, L. Zhang, and I. A Walmsley, *New J. Phys.* **12**, 093027 (2010).

[155] A. M. Weiner, *Rev. Sci. Instrum.* **71**, 1929 (2000).

[156] S. Cialdi, C. Vicario, M. Petrarca, and P. Musumeci, Appl. Opt. **46**, 4959 (2007).

List of Publications

As of year 2014

Publications on peer reviewed journals

- Aghion, S. et al, *Nucl. Instrum. Meth.*, **B362**, 86 (2015): "Positron bunching and electrostatic transport system for the production and emission of dense positronium clouds into vacuum"
- S. Aghion et al. (AEgIS Collaboration), *Phys. Rev. A* **94**, 012507 (2016): "Laser excitation of the n= 3 level of positronium for antihydrogen production"
- Z. Mazzotta, S. Cialdi, D. Cipriani, S. Olivares, M.G.A. Paris, *Phys. Rev. A* **94**, 063842 (2016): "High-order dispersion effects in two-photon interference"

Publications under review

- proceeding of my WAG conference presentation in London (2015)

Publications in conference proceedings

- A. Kellerbauer (AEḡIS collaboration), *EPJ Web of Conferences* **126**, 02016 (2016): "Probing antimatter gravity – The AEGIS experiment at CERN"
- R. Caravita, S. Aghion, C. Amsler et al., *Il nuovo Cimento* **39 C**, 237 (2016): "Towards a gravity measurement on cold antimatter atoms"
- N. Pacifico, S. Aghion, C. Amsler et al., *Nucl. Instrum. Meth.* **A831** proceedings, 12 (2016): "Direct detection of antiprotons with the Timepix3 in a new electrostatic selection beamline"
- G. Testera, S. Aghion, C. Amsler et al., *Hyperfine Interact* **233**, 13 (2015): "The AEgIS experiment"
- C. Pistillo, S. Aghion, C. Amsler et al., *Hyperfine Interact* **233**, 29 (2015): "Emulsion detectors for the antihydrogen detection in AEgIS"
- G. Consolati, S. Aghion, C. Amsler et al. , *EPJ Web of Conferences* **96**, 01007 (2015): "Experiments with low-energy antimatter"

- M. Kimura, S. Aghion, C. Amsler et al., *Journal of Physics: Conference Series* **631**, 012047 (2015): "Testing the Weak Equivalence Principle with an antimatter beam at CERN"
- J. Storey, S. Aghion, C. Amsler et al., *Journal of Instrumentation* **10**, C02023 (2015): "Particle tracking at cryogenic temperatures: the Fast Annihilation Cryogenic Tracking (FACT) detector for the AEgIS antimatter gravity experiment"

Acknowledgments

Dietro le quinte

Non era nei programmi. No... non era nei programmi, e nemmeno nei pensieri più reconditi, che io provassi ad accedere alla scuola di dottorato IN FISICA. Il prof. Franco Gallone (titolare del corso *Metodi Matematici per la Meccanica Quantistica*) insistette molto, l'anno prima, affinché io seguissi qualche corso di fisica, mentre studiavo per i miei ultimi due esami del corso di laurea magistrale in Matematica. Mi aveva percepito molto interessata a quel campo della conoscenza, naturalmente trasportata da quel mondo, come un bimbo che insegue una farfalla.

Ma sarei stata affascinata dalla farfalla anche dopo averla presa e vista bene da vicino? E dopo aver conosciuto il bruco da cui quei colori prendono vita?

Mi consigliò vivamente di scoprirlo. Io fui molto incuriosita e seguii il suo consiglio. Non capivo tantissimo dei corsi che scelsi, ma lo stupore mi colse nel vedere come, da crude formule, i fisici creassero nuovi mondi, con una fantasia da far invidia ai poeti... Sì, proprio questo mi colpì: la capacità di trasformare i "dettagli tecnici del conto" in qualcosa di diverso, posto su un piano più vicino a quello dei cantastorie che della matematica.
In quel periodo conobbi il Dr. Marco Giammarchi, ricercatore INFN, che mi raccontò dell'esperimento AEgIS sull'antimateria. Avevo appena finito di leggere il libro di Klose, "Antimateria", e quindi la realtà di AE$\bar{g}$IS mi rapì all'istante. Gli chiesi informazioni, mi procurò materiale e cercai di capire il più possibile che cosa combinassero in quel laboratorio al CERN di Ginevra. "Ci rendiamo conto?", pensavo, "il CERN di Ginevra! Sarebbe un sogno andarci a lavorare...". Ma arrivò il momento di lavorare alla tesi di laurea e un po' mi allontanai e mi distrassi da questo sogno ad occhi aperti...

Appena conseguita la laurea magistrale in Matematica a Milano, mi buttai a capofitto in numerosi colloqui di lavoro. Il mio scopo era cominciare al più presto, possibilmente con una posizione non troppo precaria... i colloqui mi divertivano, finché non mi ritrovai a farne tre di seguito per un'azienda di consulenza. Passati i primi due, il terzo sarebbe stata una passeggiata: colloquio motivazionale. Parlai della mia passione per la fisica, il manager mi disse che secondo lui, se la mia passione era quella, la mia voglia di lavorare era dettata unicamente dalla ricerca di una maggiore stabilità economica. Ma convinsi a mani basse il mio interlocutore sulla mia risolutezza nel cominciare a lavorare. Esatto, convinsi lui... ma anche lui convinse me. Nei giorni successivi al colloquio, mentre aspettavo il verdetto, le sue parole risuonavano nella mia testa. Era giugno, il mio ragazzo, Alessandro, era nel suo ultimo mese prima della discussione di laurea.

Invece di tranquillizzarlo, mi ritrovai ad aggiungere pensieri e buttare paglia sul fuoco chiedendogli consiglio, un parere, qualsiasi cosa che mi togliesse da quella passeggiata sulle spine: a pochi giorni dall'esito del colloquio, mi ritrovai a non essere più sicura di voler cominciare a lavorare, perché questo mi avrebbe definitivamente allontanato da quel mondo che tanto mi aveva affascinato fino a quel momento. Parlai con Marco, e appresi che un dottorando sarebbe servito al gruppo milanese in AEḡIS... fu così che prima ho affermato che il Project Manager mi ebbe convinto: volevo provare ad entrare alla scuola di dottorato in fisica, costasse quel che costasse, visto che poi l'esame sarebbe stato *solo sei mesi dopo*...

Chiamai mamma Danila e papà Antonio, per informarli ed avere il loro importantissimo parere prima di rendere decisiva questa scelta. Ovviamente essi preferivano che io cominciassi a lavorare...come biasimarli?

"Che cosa fai se poi non ti prendono? Hai un bel lavoro tra le mani, rinunciarci è un suicidio... Ok... Però dai, noi ci fidiamo di te, finora è andata bene quindi fai come ti senti... siamo dalla tua parte."

Avevo deciso.

Quando, con qualche giorno di ritardo rispetto a quello prestabilito, mi chiamarono per informarmi dell'esito positivo e della proposta di contratto per il lavoro, dissi loro che avevano tardato un numero di giorni sufficiente a farmi cambiare idea... Non fu semplice, cercarono di dissuadermi, ma ormai l'idea del dottorato mi si era avvinghiata come fa l'edera attorno ad un albero.
Investii quei sei mesi della mia vita per studiare. Grazie all'aiuto di Marco arrivai preparata e, alla fine, fui ammessa alla scuola di dottorato. Ed ora eccomi qui... a concludere questo ciclo della mia vita sperando che se ne riapra un altro, in questo mondo che mi tanto mi stregò qualche anno fa.

Non sono poche le persone da ringraziare!

Comincio dal mio ragazzo, che nonostante la criticità del momento, in quel lontano giugno 2013, non ha mai esitato ad ascoltare le mie paturnie, i miei monologhi, a darmi consigli, a farmi razionalizzare mentre cercavo di capire quale strada scegliere. Mi osservava stesa sul letto a fissare il soffitto, le mani sulla fronte, a parlare sola, e poi girarmi di scatto verso di lui con uno sguardo imploratore nella speranza che mi dicesse qualcosa di illuminante... grazie amore, grazie per esserci sempre stato anche quando avresti avuto tutto il diritto di dedicarti solo ai tuoi problemi!

Non posso quindi non ringraziare il prof. Gallone e Marco, che insieme mi hanno portato a capire che dovevo salire allora su questo treno in corsa. Mi resi conto che, più fosse passato il tempo, più quel treno sarebbe andato troppo veloce per poter provare a correre sulla banchina e saltare dentro una di quelle porte aperte, che sarebbero in futuro scorse così veloci da non riuscire nemmeno a vederle...

Ed è quindi, adesso, arrivato il momento di ringraziare chi invece mi ha preso per mano durante questo percorso.

Ringrazio il mio tutor, Dr. Fabrizio Castelli, un punto di riferimento stabile, un uomo tutto d'un pezzo, sempre presente nei momenti di bisogno, sempre pronto a calmarmi nei momenti di panico, a profondere consigli per ogni evenienza...

Infine, ma non per ultimo, ringrazio il Dr. Simone Cialdi, responsabile del laboratorio di Laser e Ottica Quantistica a Milano, per avermi aperto le porte del suo "territorio" ed avermi insegnato (o per lo meno ci sta provando!) a comportarmi da fisica sperimentale, per avermi rimproverato quando commettevo i miei errori, per avermi elogiato quando facevo qualcosa di buono. Mi ha trasmesso la passione per questa branca della fisica, e mi rendo conto, adesso, che in laboratorio sono diventata *rompiscatole* proprio come lui... Col tempo tenterò di diventare anche *brava* come lui, ma questo richiede tanto tanto altro lavoro che spero di avere l'opportunità di fare nel prossimo futuro...

E adesso, non posso che sorridere, pensare ai miei, guardarli e ringraziarli di non aver in alcun modo cercato di farmi cambiare idea. Questo è stato talmente importante, che mi ha dato il coraggio di affrontare quei sei mesi di studio "al buio" sapendo che, a prescindere dall'esito di questo viaggio, loro sarebbero stati con me, sempre e comunque. Grazie di esistere...

Il lavoro di tesi

Per l'ideazione e la stesura di questo lavoro ringrazio tutti e tre i miei tutor: Fabrizio, Marco e Simone. Hanno dato un apporto fondamentale, curando e ponendo l'attenzione ognuno su diversi aspetti. Fabrizio, una figura solida, attenta ad ogni mia mossa, pronto a vagliare tutta la teoria messa nella tesi, a fare critiche costruttive, ad aiutarmi a correggere i passaggi più delicati e a tenermi in studio per ore e ore, mentre si cercava il modo più corretto e allo stesso tempo elegante di affrontare determinati argomenti... Simone, che mi ha seguito nell'impostazione, la stesura e lo studio necessario per il completamento della tesi. In particolar modo nella parte centrale del lavoro (sull'ottica lineare e l'implementazione della simulazione) è stato sempre disponibile a chiarire ogni mio dubbio, a cercare con me tutti gli errori presenti nella simulazione quando qualcosa non tornava, o, ancora peggio, quando le cose tornavano ma falle subdole si nascondevano dietro ogni angolo di codice. Marco, il mio referee personale, che oltre a vegliare sul mio inglese, ha controllato, affermazione per affermazione, quanto complete e scientifiche esse fossero.

Ringrazio Sebastiano, colui che mi ha accolto al CERN, che mi ha iniziato alla vita di laboratorio, che mi ha introdotto alla realtà di una collaborazione internazionale e che ha fatto da collante tra me e gli altri collaboratori nei primi periodi lì a Ginevra, quando il mio inglese era ancora ad un livello di semplice sopravvivenza. Nell'inserimento dei dettagli relativi alla prima parte della tesi su positroni e positronio, è stata cruciale la sua risposta repentina ad ogni mia domanda sull'apparato.

L'ultimo labor limae, infine, è dovuto ai miei docenti valutatori, prof. Marco Prevedelli e Dr. Paolo Crivelli, disposti ad impegnarsi in questo duro lavoro che, nel caso del Dr. Crivelli, è stato assegnato e accettato all'ultimo momento. Con le loro correzioni, consigli e commenti hanno finalmente portato la tesi ad assumere la forma di un lavoro completo e consistente.